Origin of the chemical elements heavier than iron and of meteoritic stardust from asymptotic giant branch stars

Maria Lugaro

Konkoly Observatory
Research Centre for Astronomy and Earth Sciences
Eötvös Loránd Research Network (ELKH)
MTA Centre for Excellence

Dissertation submitted for the title of

Doctor of the Hungarian Academy of Sciences

2021

This thesis is dedicated to my parents Silvio Lugaro and Mariateresa Chiesa,
and to the memory of my aunt, Prof. Gianna Chiesa Isnardi,
who have always supported me beyond words.

Figure from Mike Pellin and Mike Savina, author unknown

Contents

Prologue

"It really is the most poetic thing I know about physics: you are all stardust."
– Lawrence M. Krauss

That energy in stars is provided by nuclear reactions is a discovery more than 80 years old (Bethe, 1939; Bethe & Critchfield, 1938), but it took another couple of decades to realise and establish that such nuclear reactions in stars also create most of the chemical elements in the Universe – from carbon up to uranium and thorium – in a process referred to as stellar *nucleosynthesis*. Research on the stellar origin of the chemical elements started in the 1940s and 1950s with the pioneering papers by Fred Hoyle (Hoyle, 1946) and Al Cameron (Cameron, 1957) and the review by Margaret Burbidge, Geoffrey Burbidge, William Fowler[1], and Fred Hoyle (Burbidge et al., 1957). The quest for the cosmic origin of the chemical elements was revolutionised in those decades because it was realised that there are stars and locations in the Milky Way Galaxy with chemical compositions different from that of the Sun and the Earth. Prior evidence instead supported the assumption that everything currently in the Galaxy had the same composition, therefore, such fixed abundances should have been produced all together during the Big Bang (Alpher et al., 1948).

The smoking gun for stellar nucleosynthesis was represented by technetium (Tc), the chemical element with 43 protons in its atomic nucleus, which lies between molybdenum (Mo) and ruthenium (Ru). Because it is fully radioactive, Tc does not exist in nature on Earth and it can only be produced artificially. Therefore, it was discovered relatively late, in 1937, by Carlo Perrier and Emilio Segrè in a sample of irradiated molybdenum. Fifteen years later, it was shown that Tc is not only made artificially by humans, but is also created in stars. In 1952, astronomer Paul Merrill observed the absorption lines corresponding to the atomic structure of Tc in the spectra of several giant stars (Merrill, 1952). Merrill was at first cautious about this result since the element he identified did not even occur naturally on Earth. This discovery was truly revolutionary: given the relatively short half lives of the Tc isotopes (a few Myr at most), the Tc lines were the first indisputable demonstration that this radioactive element was made *in situ*, i.e., inside the stars where it was observed. From that observation the theory of stellar nucleosynthesis began to take shape and garner authority.

Among the 83 stable or long-lived elements in the Universe, roughly 4/5 are heavier than iron – including the radioactive Tc observed by Merrill – and the question addressed in this thesis is[2] *how were these heavy elements from iron to uranium made?* Already in the 1950s, the

---

[1]Fowler was awarded the Nobel Prize in 1983 for his investigation of the origin of the elements.

[2]This question was listed in 2002 by the USA National Research Council Committee in their "Physics of the Universe report, Connecting Quarks with the Cosmos: 11 Science Questions for the New Century", and reported by Discover magazine as one of the "11 Greatest Unanswered Questions of Physics".

origin of the elements heavier than iron was attributed to neutron captures, simply because it is too difficult for charged particles such as protons and He atomic nuclei (i.e., α particles) to penetrate the strong Coulomb barrier of these heavy atomic nuclei, with more than 26 protons in their atomic nuclei (where 26 is the number of protons in the Fe atomic nucleus). Neutrons, instead, can be easily captured by atomic nuclei even at room temperature. The problem is that there are generally no free neutrons in the Universe, since they decay into protons with a half life of about 10 minutes. Therefore, to understand the creation the heavy elements up to U and Th, we need to investigate not only the neutron-capture processes themselves but also how large fluxes of free neutrons can be produced in astrophysical environments.

Stellar neutron-capture processes have been traditionally classified as *slow* and *rapid*, relatively to decay rates. *Slow* neutron captures produce roughly half of the cosmic abundances of the elements heavier than Fe in the Universe and occur in asymptotic giant branch (AGB) stars, such as those observed in 1952 by Paul Merrill to be enriched in Tc. *Rapid* neutron captures produce the other half of such abundances, but the first observational evidence of their production in an astronomical object was only reported very recently, in 2017, via the famous coincidence of the LIGO GW170817 neutron-star merger event with the AT 2017gfo kilonova, and the GRB 170817A short γ-ray burst (see also Section 1.3.1).

The *slow* neutron-capture process that produces elements heavier than iron in AGB stars has been the main focus of my work since I was an undergraduate student in 1996 working on my *Laurea* thesis with Prof. Roberto Gallino at the University of Torino in Italy. I became fascinated with the topic of nucleosynthesis because it combined my interests of the very large (theoretical astrophysics) and the very small (quantum mechanics and nuclear physics), and because of its solid theoretical framework, based on computational and software tools and development, which can be extensively tested with many observational constraints (as those described in Section 2.4). As I completed my PhD with Prof. John Lattanzio at Monash University in Australia, I gained access to sophisticated computational tools that allowed me to continue to investigate the *slow* neutron-capture process in AGB stars. Following my PhD, I expanded and upgraded the nuclear network used by these tools, which now covers all the elements, and their isotopes, needed to model the *slow* neutron-capture process, with 328 nuclear species. These computational tools, which I have used for the results presented in this thesis, are described in detail in Section 2.3.

While the initial focus of my research has been mostly on *slow* neutron captures, I have also moved into trying to understand the plethora of more recent observational constraints from stars that contradict the traditional picture of the *slow* and the *rapid* processes. The *intermediate* neutron-capture process was introduced in the 1970s, but it was not considered relevant until the start of the 2010s when the abundance patterns of elements heavier than iron observed in some old stars could not be explained by the *slow* and/or the *rapid* processes. My work on trying to disentangle the existence of such a new process in nature is described in Chapter 3 and it represents one of the few first efforts on this topic. The main conclusion is that the *intermediate* neutron-capture process must occur in nature, its astrophysical site(s), however, is still unknown and has become one of the most debated topics in the field of stellar nucleosynthesis.

Among observational constraints, stardust grains recovered from primitive meteorites in-

terested me from the start, when I was still a student in Torino. These are tiny (μm-size or less) minerals that formed in the cooling gas around stars and supernovae and carry the individual composition of their parent stars. I have used data from stardust grains that originated in AGB stars to understand both AGB stellar nucleosynthesis and the chemical evolution of the Milky Way Galaxy. Chapter 4 describes all my efforts on this research topic for the past 20 years. Today such investigations are becoming even more far-reaching and timely: laboratory analysis has reached extremely high precision, allowing us to discover that stardust grains imprinted the signature of their compositions in Solar System bodies, and that these signatures can be used to understand the evolution of the solar proto-planetary disk and the formation of the Solar System and its planets. For example, the Earth is more rich in *slow* neutron-capture isotopes than bodies that formed further away from the Sun and this is due to the original presence of stardust in the disk.

Finally, I decided to apply my expertise on the cosmic origin of the elements heavier than iron to nuclei that are both heavier than iron and radioactive, with half lives between roughly 1 and 100 million years. These nuclei were present at the time when the Sun formed and they tell us the story of the material that ended up in the Solar System and the circumstances at the birth of the Sun. Understanding such circumstances can lead us to discover the origin of another radioactive nucleus, lighter than iron, aluminium-26, which acted as a main heat source in the early Solar System, altering the evolution and composition of the first planetesimals. First, I started considering the origin of two radioactive nuclei produced by *slow* neutron captures in AGB stars, hafnium-182 and palladium-107, and managed to resolve a long standing discrepancy between the abundance of hafnium-182 and that of iodine-129 in the early Solar System, the latter being produced almost exclusively by *rapid* neutron captures. Then, I extended the investigation of the origin of the Solar System by including also the radioactive isotopes that are rich in protons, niobium-92 and samarium-146. My results are reported in Chapter 5 and my current work on this topic is supported by an ERC Consolidator Grant 2016, project RADIOSTAR.

As my main research topic since the completion of my PhD has been the *slow* neutron-capture process in AGB stars and its relationship to the chemical abundances of old stars, the composition of stardust grains, and the origin of radioactive nuclei in the early Solar System, in this thesis I focus on the results achieved in these three topics. I did not include in the thesis results from another three first-author papers. The first two are not included because they do not fit within the main topics listed above: Lugaro et al. (2004) investigated the production of fluorine in AGB stars, and Lugaro et al. (2012c) refuted the hypothesis that oxygen isotopic variations in Solar System bodies are due to nucleosynthesis. The third excluded first-author paper (Lugaro et al., 2012a) is on the potential origin of aluminium-26 from massive AGB stars. I did not included this paper in the thesis as do not believe it anymore to represent a relevant scenario (as discussed in more detail in Chapter 5). Other works I co-authored (not included in the thesis) cover collaborative efforts with nuclear physicists, to test the impact of uncertainties and new data related to the nuclear reaction rates relevant for the nucleosynthesis in AGB stars, astronomers and cosmochemists, to interpret the comparison between models and observations for different types of stars and stardust, and galactic astrophysicists, to include the elements produced in my AGB models into galactic chemical evolution models.

Chapter 1

Introduction

Chemical elements, as the basic constituents of the world around us, have been known since antiquity. However, only a small fraction of them, such as gold, silver, tin, copper, lead and mercury, was known before the discovery of the element phosphorus by Hennig Brand in 1649. In the following 200 years, as alchemy transformed into chemistry, a vast body of knowledge concerning the properties of the elements was acquired and, by 1869, a total of 63 elements had been discovered. In 1869, 152 years ago, Dmitri Mendeleev presented the first periodic table showing that the properties of the chemical elements follow patterns that depend on their mass. Since then, the chemical elements and their periodic system have become one of the most influential achievements in modern science, affecting not only chemistry, but also physics, biology, and other basic scientific disciplines.

In astrophysics, it is now well established that while H and ^{4}He (together with trace amounts of deuterium, ^{3}He and Li) were created in the Big Bang, the vast majority of the cosmic abundances of the chemical elements were produced in stellar objects, via nuclear processes we refer to as stellar *nucleosynthesis* (Burbidge et al., 1957). The chemical fingerprints left by the nuclear reactions that take place inside stars provide us with the opportunity not only to answer basic questions such as what are stars made of and where the chemical elements come from, but also to understand the evolution of the cosmos over a huge range of scales, from the Big Bang to life on habitable planets. Observations of the chemical composition of the oldest stars provide us with a glimpse into the early Universe and analysis of the chemical signatures of stellar populations can tell us how galaxies formed. Closer to us, investigating and interpreting the signature of stellar nuclear processes in meteoritic materials provides us with insights on how our own Solar System formed. For example, extremely high-precision laboratory analysis of extra-terrestrial materials has firmly demonstrated that the abundances of the nuclei heavier than iron produced by neutron-capture processes in giant stars are 0.01% higher in terrestrial rocks than in Solar System bodies that formed further away from the Sun than the Earth (Poole et al., 2017). How and which processes exactly in the solar proto-planetary disc produced such difference is a matter of debate.

In this thesis, I present major advances I made in the understanding of the creation of the chemical elements heavier than iron and how I have applied this knowledge to investigate the origin of stellar dust grains found in meteorites, and of radioactive nuclei heavier than iron in the Solar System.

1.1   Initial observations of the chemical elements in the cosmos

The question of the cosmic origin of the chemical elements was not confronted until the 20th century, and only after it was realised that the stars, including the Sun, produce their energy via nuclear burning. To address the question of the origin of the elements in the Universe, it was also necessary to measure their abundances in astrophysical objects, a difficult task. Joseph von Fraunhofer was the first scientist in 1813 to systematically study the dark lines seen in the spectrum of the Sun, which were found to coincide with the emission lines of various elements, such as H, Ca, Mg and Fe, seen at high temperatures in the laboratory. One such line, at 587.6 nm, was originally unidentified and named helium, only to be assigned to the actual noble gas element when it was discovered on Earth in 1895. In 1925, Cecilia Payne-Gaposchkin discovered that the strength of stellar spectral lines depends not only on the stellar surface composition, but also on the degree of atomic ionisation at a given temperature. Applying this discovery to the Sun, she found that C, Si, and other common elements seen in the solar spectrum were present in about the same relative amounts as on Earth, however, He and H were vastly more abundant in the Sun than on the Earth. While it is now well established that H and He represent roughly 99% of baryonic matter in the Universe, this was a big surprise at the time.

Another way to determine the abundances of the Sun is to analyse meteoritic rocks in the laboratory. The chemical composition of some primitive meteorites did not change significantly since their formation in the solar nebula and can thus carry accurate information on the elemental abundances of the gas from which the Sun and the planets formed. For example, carbonaceous chondrites contain a large amount of organic compounds, which indicate that they experienced very little heating (some were never heated above 50 degree Celsius). When considering the elements that condense into rocks, an extremely close match is found between the elemental compositions inferred from the solar spectrum and those measured in meteorites (see, e.g., Anders & Grevesse, 1989). The advantage of using meteorites relatively to stellar spectra is that their composition can be determined much more precisely since they can be directly studied in the laboratory using sensitive mass spectrometers. Stellar spectra, instead, need to be interpreted via models of stellar atmospheres, which are prone to systematic uncertainties due to missing physical knowledge, for example related to thermodynamic equilibrium, and dynamical and multi-dimensional effects (Asplund, 2005). Furthermore, meteoritic analysis can provide both elemental and isotopic abundances, whereas isotopic abundances are difficult or impossible to obtain from the solar spectra, and stellar spectra in general. The abundances of gaseous elements, instead, which do not preferentially condense into rocks, such as H and the noble gases, and of the major elements C, N, and O, which do not fully condense into rocks either, cannot be measured via analysis of primitive meteorites. For the abundances of these elements we must rely on the solar spectral analysis, and for the isotopic composition of the noble gases some data can also be obtained from the analysis of the solar wind.

In 1956, Hans Suess and Harold Urey (Suess & Urey, 1956) published the first table of "cosmic" abundances based on meteoritic analysis (for more recent compilations, see, e.g.,
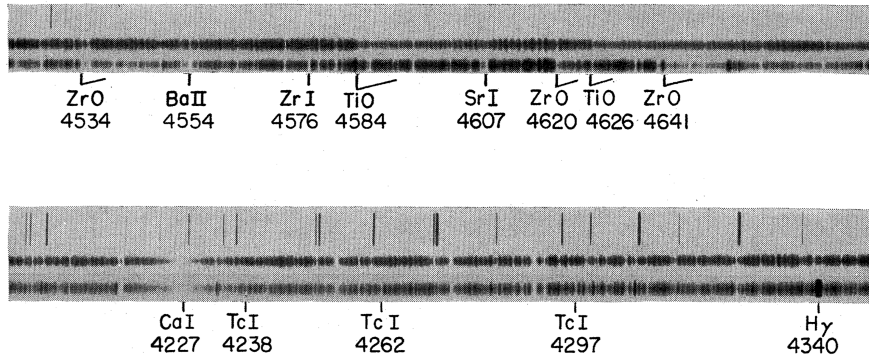
Figure 1.1: Examples of photographic spectra of stars showing similarities and differences from those of the Sun. The top and bottom sections of the figure cover spectra for two different wavelength ranges (roughly from 4520 to 4680 Åand from 4220 to 4350 Å, respectively) with the absorption lines corresponding to different elements and molecules indicated together with their wavelength. For each of the two wavelength ranges, two spectra are shown: the top spectrum is a *normal* star, i.e., with solar abundances, the bottom spectrum is an *anomalous* star with excesses in the elements heavier than iron, such as Zr (in form of the ZrO molecule), Sr, and Ba and the presence of the radioactive element Tc. (Figure from Burbidge et al., 1957).

Asplund et al., 2009; Lodders, 2010, 2020). These were actually the abundances of the Sun, as at the time it was assumed that all stars, and the whole Universe as a matter of fact, had the same chemical composition as the Sun. This was the basis of the accepted theory of the time for the origin of the elements: that all of them, from hydrogen to thorium, were produced together during the Big Bang and their abundances in the Universe were not modified by any process thereafter (Alpher et al., 1948).

In the 1950s, astronomers started to identify giant stars that show chemical compositions very different from the Sun (Figure 1.1). These anomalous stars show higher abundances of elements heavier than iron, such as Sr and Ba. Furthermore, in 1952, Paul Merrill discovered the absorption lines corresponding to the atomic structure of technetium (Tc) in the spectra of several giant stars. This result was a paradigm shift as Tc, being fully radioactive, does not even exist naturally on Earth. The isotopes of Tc have half lives of at most a few Myr, very short relatively to the life times of Gyr of the observed stars. This meant that the observed Tc could not have been present in the star when it was born, but it had been produced there. Today, we know that stars and galaxies exhibit a huge variety of differing chemical compositions, and that many nuclear processes in various types of stellar objects contribute to this diversity.

1.2 Nucleosynthetic processes in stars

Stellar interiors and stellar explosions are the ideal environments for nuclear interactions. Matter can reach extremely high temperatures (for example, 10 MK in the core of the Sun and up to GK in supernova explosions) and at the same time a high density is maintained due the force of gravity (for example, roughly 100 gr cm^{-3} in the core of the Sun and up to 10^{10}
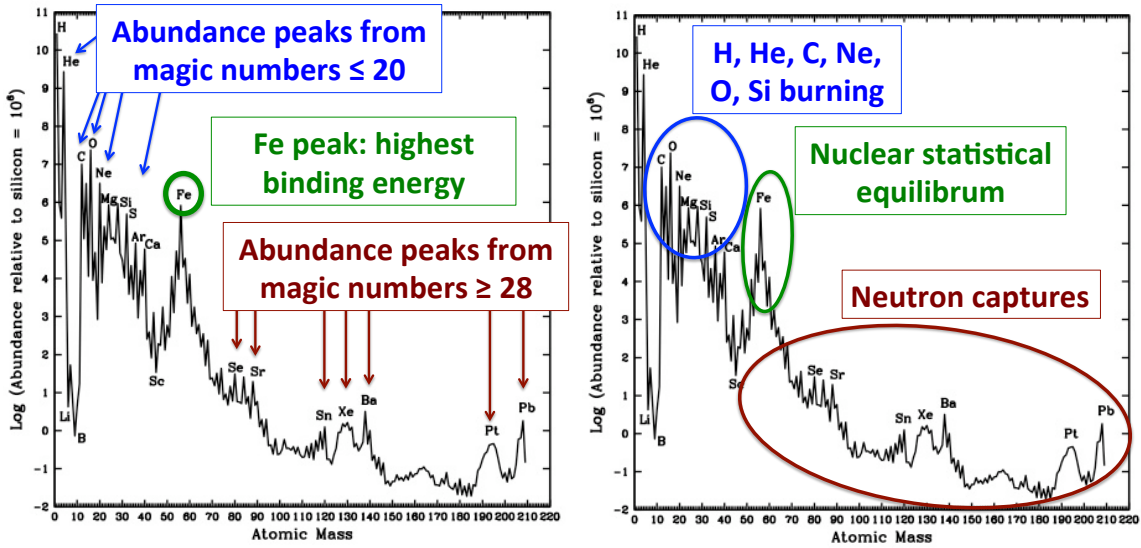
3

Figure 1.2: Isotopic abundances (by number of atoms) of the isotopes in the Solar System measured from meteorites as function of their atomic mass, with the abundance of the most abundant isotope plotted for each mass (Anders & Grevesse, 1989). Abundances are normalised such that the abundance of Si, one of the main constituents of meteoritic rocks, is set to 10^6. (Note that abundances for the solar spectrum are instead normalised such that hydrogen is set to 10^{12}.) The peaks in the distribution are indicated together with the nuclear structure features that produce them (left panel) and with the corresponding main production processes for elements with masses within different ranges (right panel).

gr cm^{-3} in supernova explosions). Nuclei are therefore forced to remain in a hot, confined volume and can react via a huge variety of nuclear interaction channels. Nuclear processes and interactions driven by the strong and weak nuclear forces result in fusion, fission, and the decay of unstable nuclei. Complex networks of such reactions can be activated depending on the temperature, the amount of the interacting nuclei, and the probability of the interactions themselves.

In the 1950s, the availability of meteoric isotopic abundances together with the growing understanding of the physical nature of the atomic nucleus, allowed us to explain the strict relationship between nuclear stability and cosmic abundances (left panel of Figure 1.2). Nuclei with nuclear magic numbers (2, 8, 20, 28, 50, 82, and 126) of proton and/or neutrons are clearly the most abundant in the Solar System. Elements up to Fe show a clear pattern resulting from the impact of the double magic nuclei ^{4}He (2p+2n) and ^{16}O (8p+8n). Isotopes with atomic mass corresponding to an integer times four (^{12}C, ^{20}Ne, ^{24}Mg, ^{28}Si, ^{32}S, ^{36}Ar, and up to ^{40}Ca[1]) reflect the strong stability of ^{4}He and are more abundant than the other isotopes in the same mass region. The total abundances of these elements are dominated by the isotopes listed, and they are often referred to in astronomy as the "α elements" (where α refers to ^{4}He, as usual). The high abundances at the iron (Fe) peak reflect the fact that in this mass region nuclei have the highest binding energy per nucleon, which effectively means that

---

[1]Titanium-48 is also sometimes considered as part of this group even if the abundance of Ti is not as high as that of the other listed elements.
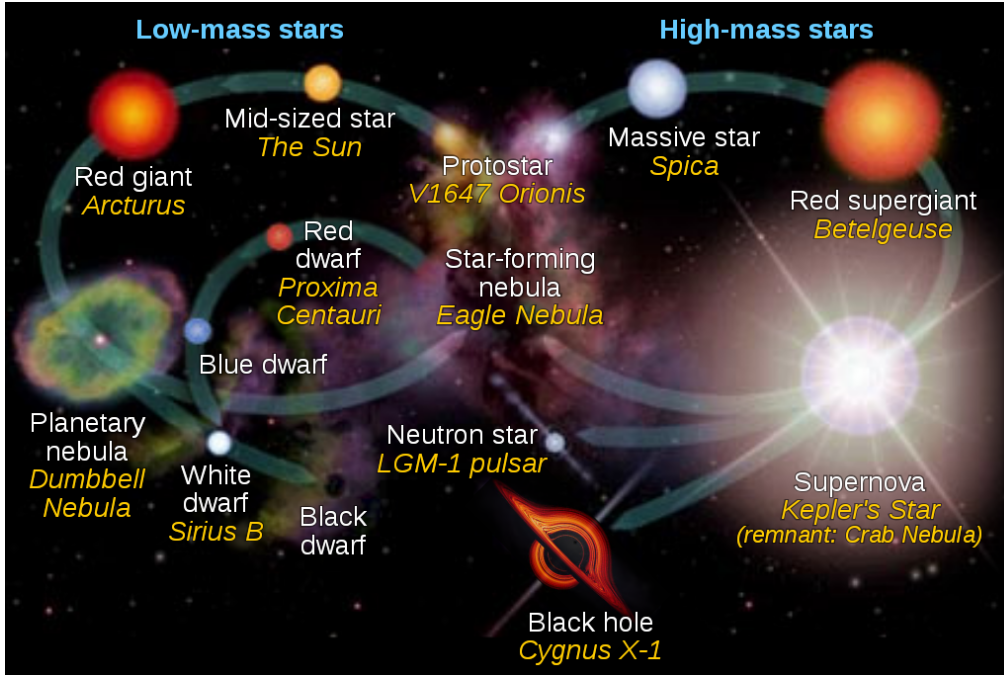
Figure 1.3: Stellar evolution of low-mass (left cycle) and high-mass (right cycle) stars, with examples in italics. (Figure from Wikipedia, author: cmglee, NASA Goddard Space Flight Center, with background images from NASA.)

in an energetic environment they are more difficult to destroy by photo-disintegration than all the other nuclei. Past the Fe peak the elemental abundances strongly decrease, although, they still show the signature of magic numbers and particularly of magic numbers of neutrons, since the main production process in this mass region is neutron captures (more details of which are presented in Section 1.3.1). In particular, the abundance peaks at Se and Sr result from the effect of the neutron magic number 50, the peaks at Xe and Ba of 82, and the peaks at Pt and Pb of 126, with ^{208}Pb being double magic (82p+126n). The enhanced abundance of Sn also reflects a magic number, in this case of protons equal to 50. Finally, the nuclear odd-even effect, by which nuclei made by an even number of nucleons are more stable than those made by an odd number of nucleons, is also reflected in the abundance distribution as a second-order zig-zag pattern along the distribution.

Based on this first analysis, it was possible to determine the main processes responsible for the production of the elements (right panel of Figure 1.2). While nuclear fusion involving H, He, C, Ne, O, and Si, both in hydrostatic and explosive stellar environments, is responsible for the production of the elements up to roughly Ti, nuclear statistical equilibrium (when fusion and fission compete) at very high temperatures results typically in material dominated by the Fe peak elements. Past the Fe peak, most of the abundances are produced by neutron captures, with minor production of proton-rich nuclei in this atomic mass region from other processes, such as charged-particle reactions and photo-disintegration (the γ process), collectively included under the label of the p process. Below I very briefly describe the processes up to the production of the Fe peak and the corresponding stellar environments. In the next section (1.3.1, I will focus on the basics of the production of the cosmic abundances of the
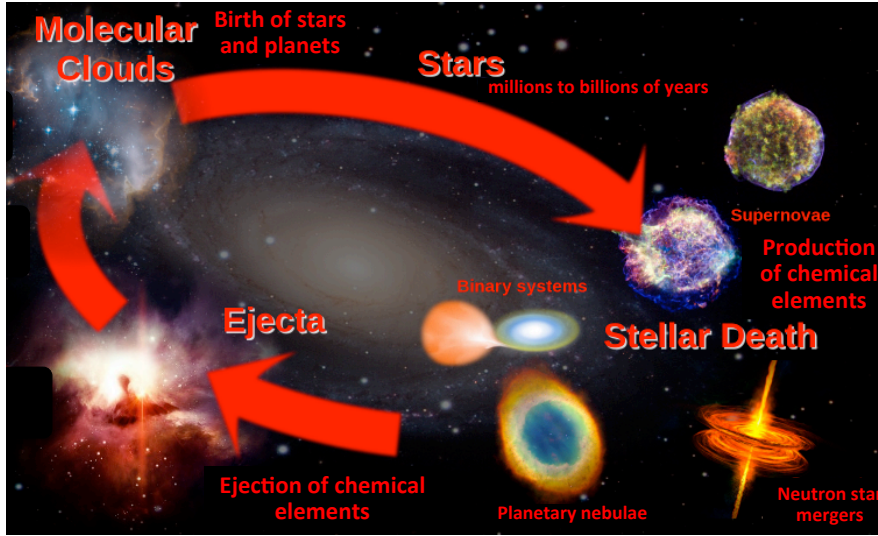
Figure 1.4: The cosmic cycle of chemical matter in a galaxy. Stars and their planetary systems are born inside cold and dense regions (molecular clouds on the upper left in the figure). Chemical elements are produced during the lives of stars and when stars die, interact, or merge, the elements are then ejected into the galactic gas via winds or explosions. When the gas cools down again, a new generation of stars is born from matter with a different chemical composition. (Figure courtesy of Richard Longland, images from NASA).

elements beyond the Fe peak, which is the main topic of this thesis.

The nuclear processes that produce the chemical elements were first systematically organised by Burbidge et al. (1957), and reviewed 40 years later by Wallerstein et al. (1997). I refer the interested reader to the textbooks by Clayton (1968) and Iliadis (2007) for more details. To support the description below, Figures 1.3 and 1.4 illustrate, respectively, the stellar evolution paths resulting in different types of stellar deaths and the cycle of chemical matter in a galaxy.

Hydrogen burning activates at temperatures starting from roughly 10 MK and is responsible for the conversion of H into He, and conversion of C and O into N. While H burning into He is the source of energy in most stars, including the Sun, the amount of He produced by stars is not as significant as that originally produced in the Big Bang: during the entire life of the Universe the He abundance has increased only by 3%, from roughly 25% to 28% of the total baryonic mass. Hydrogen burning also creates a large variety of minor isotopes, from ^{13}C and ^{17}O produced via proton captures on ^{12}C and ^{16}O, respectively, followed by the fast (order of minutes) decay of the radioactive isotopes ^{13}N and ^{17}F. Hydrogen burning occurs in the core of every star during its main sequence phase, such as in the Sun, which represents the longest phase of the life of a star. The duration of this phase strongly depends on the initial stellar mass: for stars like the Sun it is of the order of 10 Gyr, while for stars 10 times more massive it is of the order of 10 Myr.

The next phase is that of He burning, which starts in the core of the star once H has been exhausted. The star expands into a red giant (or supergiant, depending on its initial mass, and hence luminosity, see Figure 1.3) as the core contracts and reaches temperatures above 100 MK. Helium burning is mostly identified with the so-called triple-α (^{4}He + ^{4}He

+ ^{4}He) reaction producing ^{12}C, with a following α capture on ^{12}C producing ^{16}O. However, the nucleus of ^{8}Be, consisting of 2α particles, is extremely unstable, and would be expected to break up before capturing another α particle. To solve this problem and create ^{12}C, Fred Hoyle predicted that a quantum energy level must exist in the ^{12}C nucleus near the energy where the ^{8}Be + α reaction is more likely to occur in stars, i.e., a so-called "resonance" near the Gamow peak[1]. This theoretical prediction was experimentally confirmed by Cook et al. (1957). In other words, because there are no stable isotopes with mass 5 and 8, there has to be be a way to jump past these atomic masses and produce C abundantly (as is observed) from the abundant He. Without this "Hoyle resonance" no carbon would exist in the Universe, and hence no carbon-based lifeforms such as ourselves[2]. Secondary nucleosynthetic paths of He burning can lead to the production of fluorine, and to the conversion of N into ^{22}Ne, which is particularly important as it carries a "neutron excess" into the following phases of stellar evolution (it contains 2 neutrons more than protons, i.e., 10p+12n). Furthermore, during He burning, free neutrons can be released by α-capture reactions such as ^{13}C(α,n)^{16}O and ^{22}Ne(α,n)^{25}Mg, which can result in the production of elements heavier than Fe (e.g., Section 1.3.2).

In stars with mass below roughly ten times that of the Sun (left cycle in Figure 1.3), nuclear burning processes do not proceed past He burning. When the nuclear fuel is exhausted, the stellar central region becomes a degenerate, inert C-O core (the ashes of the previous He burning) while and H and He continue to burn in shells around this core. These stars can produce large amounts of the elements heavier than iron via *slow* neutron captures (Section 1.3.2). Matter is mixed from the deep layers of the star to the stellar surface and then ejected by the stellar winds that peel off the external layers of the star. These processes are most efficient during the very final phases of the lives of these stars. When most of the original stellar mass is lost, the matter expelled by the stellar winds can be illuminated by UV photons coming from the central star, producing what we observe as a colourful planetary nebula. These low-mass stars contribute most of the C, N, F, and half of the elements heavier than Fe to the chemical enrichment of the Universe. Eventually the C-O core of the star is left as a white dwarf (Figure 1.3).

In more massive stars (right cycle in Figure 1.3), after He burning the temperature in the core increases further and a larger variety of reactions can occur. These processes involve C, Ne, and O burning, and include many channels of interactions, with free protons and neutrons driving a large number of possible nucleosynthetic paths. The cosmic abundances of the "intermediate-mass" elements, roughly from Ne to Cr, are principally the results of these nuclear burning processes. Once the temperature reaches values of the order of GK, the probabilities of the fusion reactions become comparable to those of the photo-disintegration reactions and the result is a nuclear statistical equilibrium (NSE), which favours the production of nuclei with the highest binding energy per nucleon around the Fe peak, with the detailed abundance pattern depending on the temperature and density profiles as they evolve

---

[1]For charged-particle reactions, the Gamow peak is at the energy of the maximum obtained by multiplying the Maxwell-Boltzmann distribution of the particles and the efficiency of the quantum tunneling effect that allows the charged particle (e.g., ^{4}He) to penetrate the Coulomb barrier of the target (e.g., ^{8}Be).

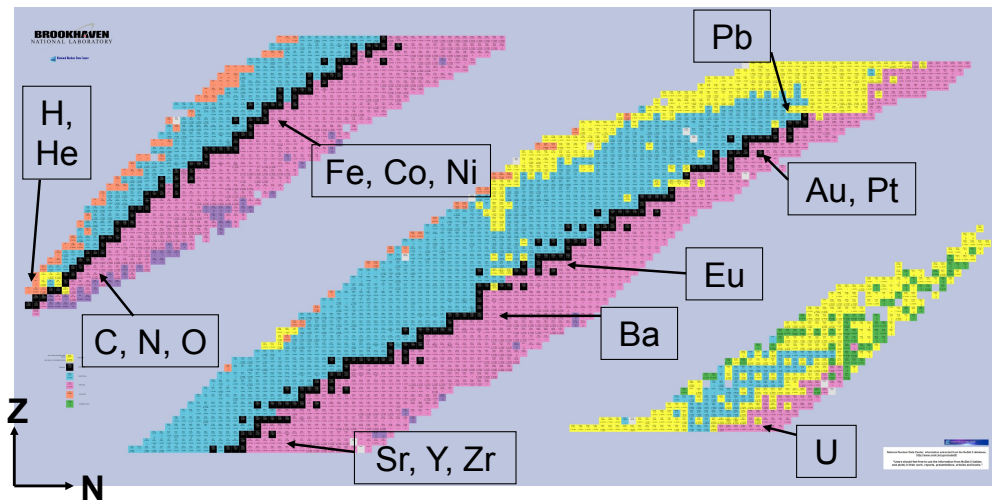[2]This is the basis on which in the 1980s it was suggested that Hoyle's prediction is anthropically significant.

Figure 1.5: General overview of the nuclide chart of nuclei, where isotopes are located as function of their proton number (Z, increasing vertically, and changing the name of the element) and their neutron number (N, increasing horizontally). Stable nuclei are represented by black boxes, unstable nuclei by coloured boxes, for example, pink, blue, and yellow represent β^-, β^+, and α decay, respectively. For stable isotopes, the nuclide chart reports the fraction each isotope contributes to the solar abundance of the element; for unstable isotopes, it reports the half lives. (Image modified from that obtained from the National Nuclear Data Center web site, www.nndc.bnl.gov.)

in time, as well as on the inherited "neutron excess" of the stellar material. These more massive stars end their lives due to the final collapse of their Fe-rich core. Once nuclear fusion processes have turned all the material in the core into Fe, neither fusion nor fission processes can release energy anymore to prevent the core collapse. As the core collapses, matter starts falling onto it, which results in a bounce shock and a final core-collapse supernova explosion. The exact mechanism of the explosion is not well known, although it has been recognised that neutrinos play a crucial role in it (Janka, 2012). The supernova leaves behind a central compact object, a neutron star or a black hole (Figure 1.3), while the material that does not fall back into this central object is ejected into the interstellar medium. This ejected material is typically rich in O and the other common elements such as Mg, Al, and Si.

Binary star interactions involving accretion onto, or mergers of, white dwarfs can also lead to explosive burning, such as novae and thermonuclear supernovae, the latter typically tearing the white dwarf apart. NSE is the main process that occurs in these supernovae, which are are responsible for producing most of the Fe peak elements in the Universe. Finally, binary interactions between neutron stars and black holes can also lead to their merging and the production of the elements heavier than iron via the *rapid* neutron capture process (see next section 1.3.1).

All together, these different processes in different types of stars lead to the chemical evolution of galaxies (Figure 1.4): they determine the composition of different stellar generations and populations, which depends on the time and place of their birth, as well as on the full history of their host galaxy.
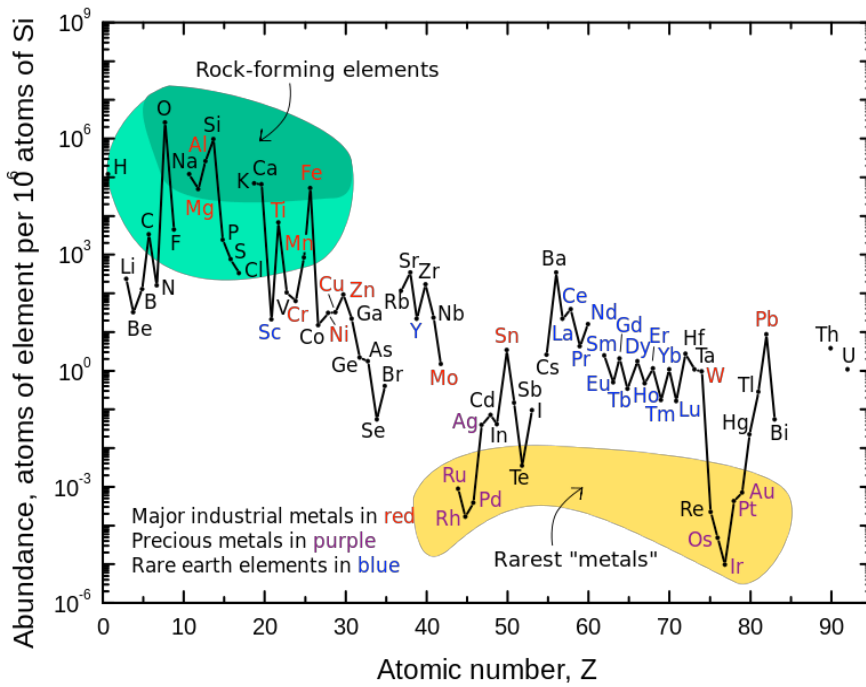
Figure 1.6: Abundances of the chemical elements in the Earth's upper continental crust as a function of atomic number, normalised to Si=10^6. (Image from Wikipedia).

1.3 Neutron-capture elements

When considering the abundances of the elements heavier than iron in the Solar System (Figure 1.2) one may wonder why it is of interest to investigate their cosmic origin given that these abundances are orders of magnitudes lower than those of the common elements, therefore, we do not expect them to make a significant contribution to the overall metallicity of the Universe. The nuclide chart of Figure 1.5, however, makes it clear that from the point of view of the chemical variety of the cosmos, the nuclei of the elements heavier than iron, with number of protons from 27 (colbalt) to 92 (uranium), make up more than 2/3 of all the atomic nuclei in the Universe. Furthermore, the abundances of the elements heavier than iron are very significant in the Earth's crust (Figure 1.6) and provide some of the crucial material on which human development is based, from major industrial metals which include of course Sn, W, and Pb, to the rare earth elements on which much of today's technology relies. The abundances of the radioactive elements U and Th strongly contribute to the heat budget of the Earth, with implications for its evolution into a habitable planet (Botelho et al., 2019; Unterborn et al., 2015). Looking at the biology of our own bodies, the element selenium (Se, 34), molybdenum (Mo, 42), and iodine (I, 53) although present only in trace amounts are, respectively, an antioxidant, part of enzymes, and part of the thyroid hormone, which helps regulate growth, development, and metabolism. "How Were the Elements from Iron to Uranium Made?" is therefore a significant question to understand the cosmos and our place within it.

Furthermore, the abundances of the elements heavier than iron can be used to trace different processes in the Universe. When determining their abundances in very old stars in the halo of our Galaxy, we can understand the nature of the first stars (e.g., Sneden et al., 2008) and when considering the evolution of their abundances in stellar systems we can study

Figure 1.7: Section of the nuclide chart from Sb to Ba showing the main s-process path along the valley of β-stability as the red line and the decay chains resulting after the operation of the r process as blue arrows. For the element Xe as an example, the two s-only isotopes (^{128,130}Xe, red boxes) cannot be reached by the r process (they are shielded by the very long-lived ^{128,130}Te), while the r-only isotope (^{134}Xe, blue box) cannot be reached by the s process. The short-lived ^{129}I discussed in detail in Chapter 5 is also an r-only isotope (blue box). ^{126}Xe (yellow box) cannot be reached by any neutron-capture process and it is a p-only isotope. (Image modified from that obtained from the National Nuclear Data Center web site, www.nndc.bnl.gov.)

the formation and evolution of galaxies and stellar populations (e.g. Skúladóttir et al., 2019; Spina et al., 2018). The analysis of their abundances in meteoritic bulk rocks and inclusions can be used to understand the formation of the Solar System and the evolution of its proto-planetary disk (e.g. Ek et al., 2020). In summary, the topic of the origin of the elements heavier than iron is intrinsically significant and carries far-reaching implications.

1.3.1 General properties of neutron-capture processes

Beyond Fe, charged-particle reactions are not efficient due to the large Coulomb barrier around heavy nuclei with the number of protons larger than 26 and neutron captures, in the form of *slow* (s) and *rapid* (r) processes[1], are the main channels for the production of the atomic nuclei up to Pb, U, and Th. The roughly 30 proton-rich nuclei heavier than iron with very low abundances require different processes than neutron captures to be produced (see, e.g., Pignatari et al., 2016a). I will not discuss these in this thesis, except for the special case of the short-lived radioactive nuclei ^{92}Nb and ^{146}Sm in Section 5.2, which are of relevance for the formation of the Solar System. The s process requires a relatively low number of neutrons ($\sim 10^{7-11}$ cm^{-3}) and is at work in low-mass giant stars, producing the Tc that has been observed in these stars since the 1950s. The r process requires a much higher number of

---

[1]A collection of the main acronyms and abbreviations used throughout the thesis can be found in Appendix A.
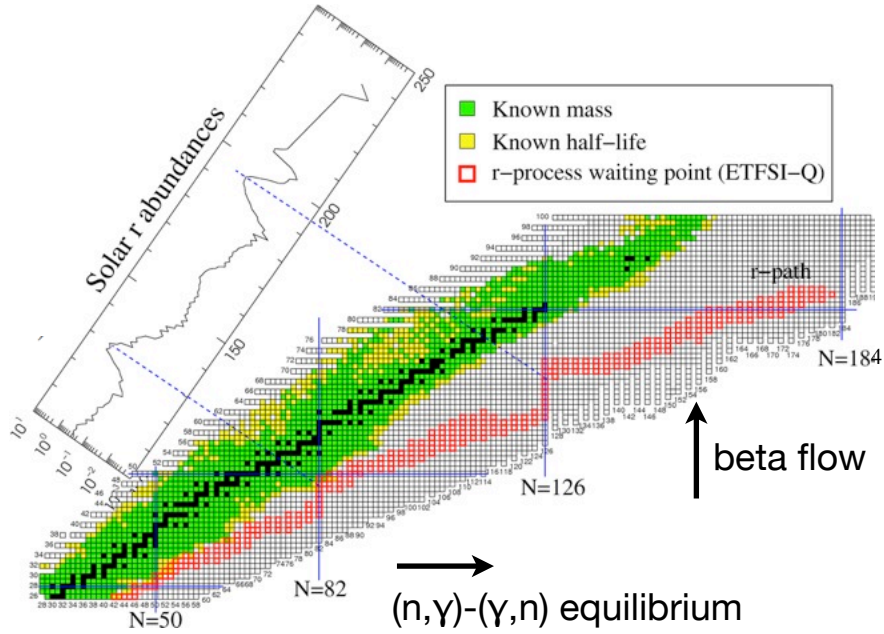
Figure 1.8: Nuclide chart indicating the location of the *r*-process path (red squares) and our knowledge of nuclear properties, illustrated by different coloured boxes as indicated in the legend, where black squares are stable isotopes, whose properties are relatively well studied. The *r*-process path moves on the nuclide chart horizontally via (n,γ) and (γ,n) reactions (the location of magic numbers where the flux accumulates is indicated by the blue solid lines), and it climbs up vertically towards heavier elements via β-decays. Also plotted on the top left corner are the *r*-process abundance contributions to the solar abundances of the elements heavier than iron as a function of atomic mass, with blue dotted lines highlighting the correspondence between neutron magic numbers and the *r*-process peaks in solar abundances. These contributions are calculated using the *r*-residual method described in the text. (Image from Grawe et al., 2007, courtesy of K.-L. Kratz and H. Schatz).

neutrons ($> 10^{20}$ cm^{-3}) and occurs in explosive neutron-rich environments. The stellar site of the *r* process has been one of the most uncertain and highly debated topics in astrophysics. Neutron star mergers are now considered as the first site where the production of the *r*-process elements is observationally proven. This evidence is based on spectra of the optical kilonova transient powered by the radioactive decay of isotopes produced by the *r*-process and associated with the 2017 gravitational wave source GW170817 (Kilpatrick et al., 2017; Watson et al., 2019). However, rare types of core-collapse supernovae, such as collapsars and magneto-rotationally driven supernovae could also contribute to the *r* process in the galaxy and they do appear to be necessary to explain observations (e.g., Côté et al., 2019c; Wehmeyer et al., 2015).

During the *s* process, the neutron density is by definition low enough that when the neutron-capture flux reaches an unstable isotope it is *slower* for it to capture a neutron than to decay, consequently the *s*-process path follows quite closely the valley of β-stability in the chart of nuclides (Figure 1.7). During the *r* process, instead, the neutron density is by definition high enough that when an unstable nucleus is produced it is more *rapid* for it to

capture another neutron than to decay. This means that the r-process path is located very far away from the valley of β-stability (Figure 1.8). Once the neutron flux is extinguished, the neutron-rich unstable nuclei decay towards the valley of β-stability until a stable isotope is produced. Some stable isotopes can only be produced by the s or the r process. The so-called r-only isotopes are those shielded from s-process production by an unstable nucleus that precedes them on the s-process path. The so-called s-only isotopes are those shielded from r-process production by a stable isotope of the same mass that precedes them on the β^--decay chain that follows the r process. Isotopes that cannot be reached by any type of neutron-capture process are proton-rich – the so-called p-only isotopes (see Figure 1.7 for examples).

Thanks to the existence of s-only isotopes it is possible to define the relative contribution of the s and r processes to the isotopes of the elements heavier than iron. Since the s-process path involves mostly nuclei located on the valley of β-stability, these can be easily used as targets in the laboratory and therefore experimental estimates of their neutron-capture cross section have been reported since the 1970s. This is very different to the case of the r process, where still today we have very little information on the nuclear properties of the nuclei involved on its path (Figure 1.8). Early parametric models of the s process (i.e., with neutron fluxes and temperatures set as free parameters) were targeted to reproduce the abundances of the s-only isotopes in the Solar System. When subtracting such contributions to the total solar abundances, the main constraint for the r-process models is derived: i.e., its expected contribution to the solar abundance distribution (e.g. Arlandini et al., 1999). This is known as the r-residual method and the resulting abundance pattern is shown in Figure 1.8[1].

There are two fundamental features of neutron-capture processes. The first is the impact of the magic number of neutrons along the neutron-capture paths. In the case of the s-process the neutron-capture path proceeds along the valley of β-stability and through stable neutron magic nuclei such as ^{88}Sr (N=50), ^{138}Ba (N=82), and ^{208}Pb (N=126). This explains why peaks are present in the distribution of the heavy elements in the Solar System (Figure 1.2) around these isotopes. Their neutron-capture cross sections are orders of magnitude lower than those of the other nuclei in the same mass regions ($\sim$ 0.1-10 mbarn, rather than 100-1000 mbarn). This means that these nuclei act as bottlenecks on the path of neutron captures. To overcome these bottlenecks, their abundances need to become high enough to make their neutron-capture rate (which is proportional to the neutron-capture cross section multiplied by the abundance) high enough that the flux can proceed. This results in a strong sensitivity of the relative abundances of the three s-process peaks listed above to the total amount of neutrons available, for any given neutron flux. The total amount of neutrons is usually expressed in terms of the neutron exposure τ, i.e., the time-integrated neutron flux ($= \int N_\mathrm{n} v \, dt$, where N_n is the neutron density and v the relative velocity, usually taken to be the thermal velocity). If τ is relatively low ($\sim$ 0.1 mbarn^{-1}, at 30 keV), more Sr than Ba is produced, for a higher flux ($\tau \sim$ 0.6 mbarn^{-1}) Ba can be produced. When the neutron exposure is so high that both

---

[1]It should be kept in mind that the residual method by definition provides us the "non-s-process" abundances of the isotopes. In recent decades it has become clear that more processes than the r process may contribute to the cosmic abundances of the isotopes heavier than Fe, particularly for those up to Ba for which different nucleosynthetic components may be present (see, e.g., Sneden et al., 2008), however, we cannot distinguish these components with the r-residual method.
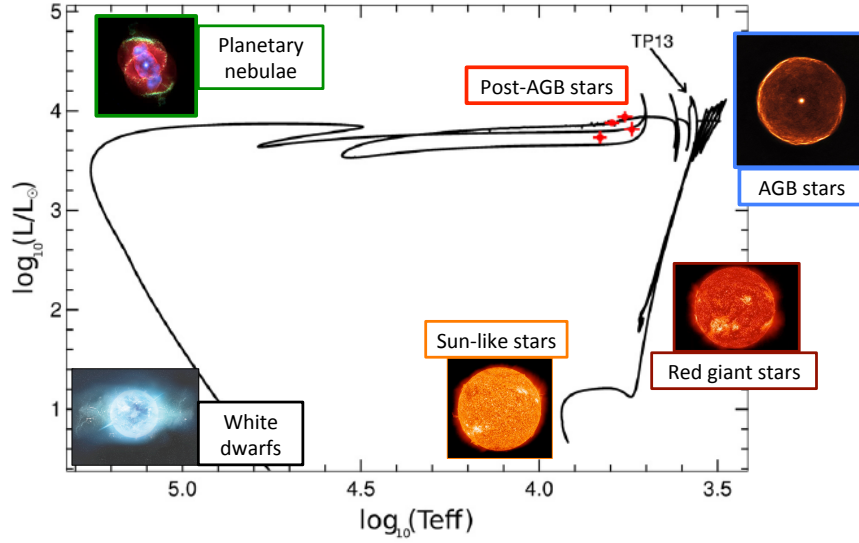
Figure 1.9: Hertzsprung-Russell (HR) diagram showing the evolution of a 1.3 $M_\odot$ star of metallicity 20 times lower than solar from the start of the main sequence (Sun-like stars) to the white dwarf cooling track, calculated by Simon Campbell using the `Stromlo` code (see Section 2.2). The star cools from the main sequence temperature to become a red giant for the first time, then loops back down in luminosity to burn He in the core, and climbs the red giant branch again as an asymptotic giant branch (AGB) star. Instabilities due to the thermal pulses (TPs) only marginally affect the surface temperature and luminosity of the star, but are noticeable as minor oscillations in the figure. The TP number 13 (indicated), 14, and 15, are already off the AGB track and are close to the locations of four post-AGB stars observed in the Large and Small Magellanic Clouds (red dots with error bars); these are discussed in Section 3.2. After the post-AGB phase the star moves to the region of planetary nebula and then to the white dwarf cooling track where both the temperature and luminosity decrease. (Images: the Sun from NASA Solar Dynamics Observatory; Red Giant from theplanets.org; AGB: see credit in Figure 1.10; X-ray/optical composite image of the Cat's Eye Nebula from J.P. Harrington and K.J. Borkowski (University of Maryland) and NASA; and white dwarf from All About Space/Imagine Publishing.)

the Sr and Ba bottlenecks are bypassed, the flux can reach Pb, which, together with Bi, also represent the end of the s-process path because beyond this point decays are always faster than neutron captures (see Figure 2.7).

A similar situation arises for the r process, as neutron magic isotopes also act as bottlenecks, however, in this case they are located far away from the valley of β-stability and the nature of the bottlenecks is that neutron captures and disintegration reach an (n,γ)-(n,γ) equilibrium, where the abundances of the magic nuclei with lower (n,γ) cross sections are favoured. Once the neutron flux is extinguished the unstable magic nuclei decay into the corresponding stable nuclei with the same mass. The resulting final r-process peaks are determined by unstable magic nuclei of mass lower than the stable nuclei with the same magic numbers of neutrons. Therefore, the r-process peaks are located at lower masses relatively to the peaks produced by the s process, i.e., at Se, Xe, and Pt (see Figures 1.2 and 1.8).

The second fundamental feature of neutron-capture processes is that while the s and the

r processes occur at neutron densities roughly ten orders of magnitudes apart, and have therefore have completely different properties, it is of course not possible to exclude that an *intermediate* (i) neutron-capture process, i.e., with neutron densities in-between those typical of the s and the r process, also exists in nature. This possibility had not been considered in depth until recent years, except for the pioneering works of Cowan & Rose (1977), in relation to the i process proper, defined to be driven by episodes of proton ingestions in He-rich layers, and Howard et al. (1992), in relation to the neutron burst in the He shells of core-collapse supernovae, called the n process. These different processes have not been popular for at least two reasons: before the widespread use of computers analytical solutions were relatively easily obtained only for the two extreme cases of the s and r processes, and also because there was no clear evidence of the need or the existence of such intermediate processes in nature. For example, the solar system abundances could be well explained by parametric models of the combination of the s and r processes and early meteoritic data on the Xe isotopes showed, already in the 1960s, the separate production of s-only and r-only isotopes of Xe (Srinivasan & Anders, 1978) demonstrating the existence in nature of the pure s- and r-process components[1]. Nowadays, however, it has become evident that some stars do show the signature of the i process, which is the thesis point presented in Chapter 3.

1.3.2   Neutron captures in AGB stars

The most prolific producers of s-process elements such as Sr, Ba, and Pb in the Universe are stars of initial mass from roughly 1 to 3-4 times the mass of the Sun, during the late phase of their life when they reach the asymptotic giant branch (AGB) after having exhausted both H and He in their cores (Figure 1.9). These are the stars whose spectra were already identified in the 1950s as showing the presence of the radioactive element Tc, as well as enhancements in Ba and Sr (Figure 1.1). As described briefly in Section 1.2, these low-mass stars evolve on long timescales of the order of Gyr and end their lives when only their C-O core remains as a white dwarf, after all their external mass is peeled off by strong stellar winds (see left panel of Figure 1.10). The outer regions of these stars are cool (~ 1000 K) and can be dense enough to form molecules and dust grains. Some of these grains travelled to the birthplace of the Solar System and are recovered today from meteorites. They carry the detailed isotopic composition of the winds of their AGB parent stars and impose strong constraints on AGB models of nucleosynthesis. I will discuss them in more detail in Section 2.4.2 and Chapter 4.

In terms of the nucleosynthesis itself, what is relevant is the material very close to the core of AGB stars, where the temperature and densities are high enough to drive nuclear interactions. In particular, the He-rich intershell located between the H- and the He-burning shells (see right panel of Figure 1.10) is the perfect region for (α,n) neutron-source reactions to be activated. A mechanism is also required to carry the material produced in the deep layers of the He-rich intershell to the stellar surface, where it is observed. The process of

---

[1]Although it should be noted that the measured abundance of the r-only isotopes of Xe are not produced by solar proportions, their origin is still mysterious (Amari, 2009), and motivated investigations of an n process in core-collapse supernovae (Howard et al., 1992). The measured abundance of the s-only isotopes show a typical s-process signature, when considering a minor possible contribution of the p process to ^{128}Xe.
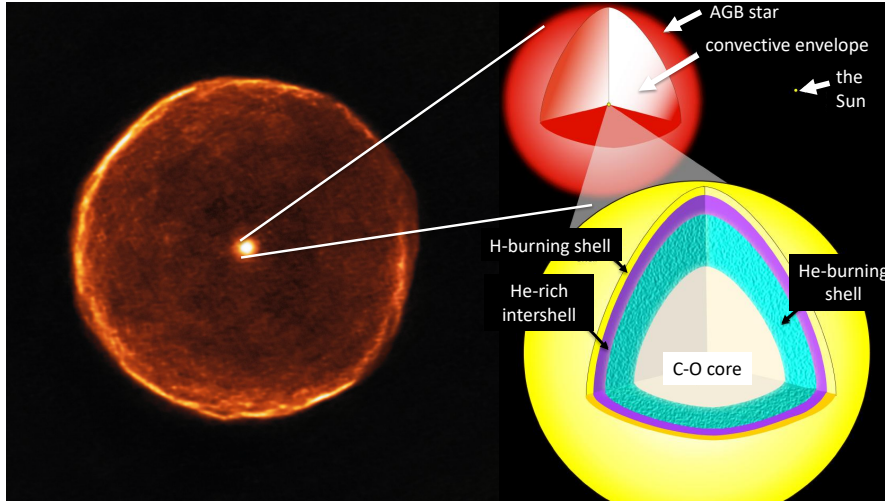
Figure 1.10: Image of the AGB star U Antliae (left) obtained with the Atacama Large Millimeter/submillimeter Array ALMA telescope (Kerschbaum et al., 2017) showing a thin shell of material that was lost by the star 2700 yr ago. The actual star is the central emission. A schematic of its theoretical structure (right) shows that the star is a red giant with an extended convective envelope. Just above the C-O core, the H- and a He-burning shells are activated, and the region in-between the two shells (the He-rich intershell) is where the neutron captures can occur. (Left figure modified from that obtained from Amanda Karakas, original author unknown.)

nucleosynthesis and mixing in AGB stars is illustrated in detail in Figure 1.11, which focuses on the evolution in time of the He-rich intershell region.

The evolution of AGB stars is complicated by the fact that H and He burning do not occur at the same time. Theoretical models predict a cycle made of a relatively long phase of H burning, during which H from the envelope is converted into He in the intershell and the H-burning shell moves up to a higher location in masses, interrupted (every $\sim 10^4$ yr or so, depending on the stellar mass) by a burst of He burning, a so-called *thermal pulse* (TP). A TP lasts for $\sim 10^2$ yr or so, and releases a large amount of energy at the base of the He-rich intershell, which cannot be carried outwards by radiation alone. Therefore, a convective region (or *convective pulse*) develops, which engulfs the whole intershell. After the convective pulse is extinguished, and while He is still burning at the base of the intershell, the envelope penetrates the internal layers of the stars that were previously exposed to the convective pulse. Once the mixing has reached its deepest extent, the relatively long phase of H burning stars again and the cycle above is repeated, in total from a few to hundreds of times, depending on the initial mass and the strength of the mass loss. The recurrent mixing episodes that may follow the convective pulse are collectively known as the *third dredge-up*[1] (TDU) and allow materials produced by nuclear reactions in the intershell to be carried to the stellar surface, where it is observed. This intershell material includes the elements heavier than iron produced via neutron captures, and a large amount of carbon, produced by partial

---

[1]The first and second dredge-ups occur after H and He core, respectively, see e.g. the review by Karakas & Lattanzio (2014) for more details.
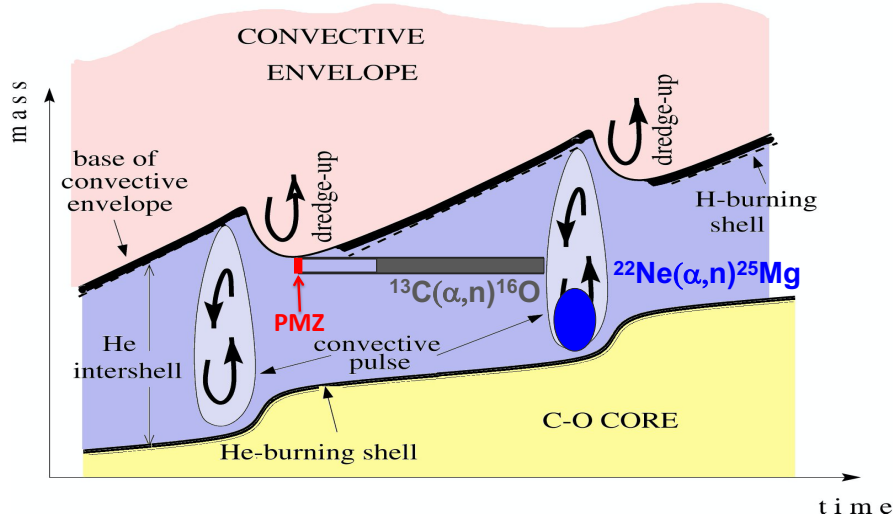
Figure 1.11: Schematic picture of the structure of the inner region of an AGB star (bottom right of Figure 1.10) as a function of time. The regions where the main reactions that produce free neutrons are activated are indicated, with the ^{13}C (grey region) and ^{22}Ne (blue regions) nuclei as the neutron sources, and the location of the partial mixing zone (PMZ, in red) leading to the formation of the ^{13}C pocket.

He burning[1]. Some AGB stars can eventually become C-rich at the stellar surface, i.e., the amount of carbon atoms can exceed that of oxygen atoms (C>O), which is a rare occurrence in the Universe (e.g., the Solar System is made of O-rich material, Figure 1.2) and it has fundamental implications on the type of molecules that can form in the envelopes of these stars, and in turn the types of dust.

In AGB stars of mass above roughly 3.5 - 4 M$_\odot$, the base of the extended H-rich convective envelope (see Figure 1.10) can become hot enough for proton captures to occur, a process usually referred to as hot bottom burning (HBB). As the mixing timescale of the convective envelope is relatively short, of the order of days, the products of this burning are quickly carried to the stellar surface, which results in the observational signatures of CNO burning. These include the destruction of carbon (so that these stars remain O-rich) and the enhancements of He and N. Proton captures on the Ne, Na, Mg, and Al isotopes (the NeNa and MgAl cycles) can also occur leading, for example, to enhancements in Na and in the radioactive nucleus ^{26}Al.

The neutron captures that result in *s*-process nucleosynthesis in AGB stars can occur in two locations of the He-rich intershell. One source of neutrons is the ^{22}Ne(α,n)^{25}Mg reaction, acting on the ^{22}Ne produced in the convective pulse via double α-capture on the abundant ^{14}N ingested from the ashes of H burning. This neutron source can only be activated at relatively high temperatures, above $\sim$300 MK, which are reached only in the convective pulses of AGB stars of initial mass above 3 - 4 M$_\odot$. Another neutron source is therefore required to explain the strong enhancements of neutron-capture elements observed in AGB stars, and the ^{13}C(α,n)^{16}O is an ideal candidate because it is already activated at temperatures around 90

---

[1] i.e, the triple-α reaction is activated, but the TP finishes before the ^{12}C(α,γ)^{16}O reaction is also efficiently activated.

MK. However, there is not enough ^{13}C in the H-burning ashes to produce the strong neutron flux required to match the observations and, furthermore, the H-burning ashes also contain large quantities of ^{14}N, which is a neutron poison via the ^{14}N(n,p)^{14}C reaction (with a neutron capture cross section of around 2 mbarn, Wallner et al., 2016).

A solution to this problem was found by assuming that at the deepest extent of each TDU episode, when a sharp discontinuity is present between the convective H-rich envelope and the radiative He-rich region, a partial mixing region (PMZ) could form where protons and a high ^{12}C abundance are present together. The proton-capture chain ^{12}C(p,γ)^{13}N(β^+)^{13}C would then lead to the formation of a so-called ^{13}C *pocket* (more details can be found in Section 2.3.4). While there is no consensus on the exact mixing mechanism, this model is robust enough to be able to reproduce the observational data. In the current models the temperature is high enough in the ^{13}C pocket such that the neutrons are produced before the onset of the next convective pulse, and the pocket becomes rich in the abundances of the elements heavier than iron before it is ingested in the convective pulse, and subsequently dredged-up to the stellar surface and carried out into the stellar surrounding via the stellar winds.

There are crucial differences between the neutron fluxes from these two main neutron sources (Figure 1.12). The ^{13}C neutron source is active during the interpulse periods over long times scales, of the order of 10^4 yr. This results in relatively slow burning and a neutron flux with a relatively low peak neutron density, of the order of 10^7 n cm^{-3}. The ^{13}C nuclei are completely burnt, and the neutron exposure reaches relatively high values, up to 1 mbarn^{-1} or even higher in low-metallicity AGB stars, where the abundance of iron nuclei that capture the free neutrons is lower. The ^{22}Ne neutron source is active instead during the thermal pulses over shorter times scales, of the order of a few years only, following sudden increase in temperature of the thermal pulse. This results in relatively fast burning and a neutron flux with a relatively high peak neutron density, of the order of 10^{11} n cm^{-3}, and up to 10^{13} n cm^{-3} in stars more massive than the 3 M$_\odot$ case shown in Figure 1.12 (Fishlock et al., 2014; van Raai et al., 2012). As only a few percent of the ^{22}Ne nuclei burn, the neutron exposure has relatively low values, typically up to 0.1 mbarn^{-1}. This means that the ^{13}C neutron source is responsible for producing the bulk of the *s*-process elements in the Galaxy, whereas the ^{22}Ne neutron source has a marginal affect on the elemental abundance pattern; its activation results in abundance variations of the isotopes that are involved in the operation of *branching* points.

Branching points are located at unstable isotopes along the *s*-process path, where, given an high enough neutron density, the probability of capturing a neutron becomes comparable or even higher than that of β decaying. These are typically isotopes with a half life of at least a few days (see Appendix of Lugaro & Chieffi, 2018, for a full list). Famous branching points that can be activated by the ^{22}Ne neutron source are, for example, the unstable isotopes ^{85}Kr and ^{86}Rb, which lead to the production of stable neutron magic isotopes ^{86}Kr and ^{87}Rb, the unstable ^{95}Zr, which leads to the production of stable ^{96}Zr (measured in stardust grains, Figure 4.1), and the unstable ^{134}Cs leading to the production of the short-lived isotope ^{135}Cs (with half life of 2 Myr) and variation to the ratio of the *s*-only isotopes ^{134,136}Ba measured in stardust grains (Figure 4.4).

Figure 1.12: Example of the evolution of the neutron density with time in a typical case of a 3 $M_\odot$ star of solar metallicity calculated with three different stellar evolutionary codes when the neutron source is ^{13}C (left panel) or ^{22}Ne (right panel). (Figure adapted from Lugaro et al., 2003b).

Branching points therefore reflect the behaviour of the two neutron sources and have been used effectively to constrain the s process in AGB stars of different masses. In fact, AGB stars of initial stellar mass above ~ 4 $M_\odot$ are predicted to experience hotter convective pulses and smaller ^{13}C pockets, therefore, a stronger activation of the ^{22}Ne neutron source relative to the ^{13}C source than AGB stars of lower masses. This prediction has been verified using the abundance of Rb relative to Zr observed in massive AGB stars, which confirmed that the predominant neutron source in this mass range is ^{22}Ne (Garcia-Hernandez et al., 2006; García-Hernández et al., 2009). Another example is meteoritic stardust SiC grains from AGB stars, which have ^{96}Zr/^{94}Zr ratios lower than solar: this is a clear signature of the ^{13}C neutron source and the origin of thse grains from low-mass AGB stars (Section 4.1).

1.4 Open questions and motivations

While the principal features of the knowledge described above are relatively well established, there are many aspects of the production of the elements heavier than iron and of the nucleosynthesis in AGB stars in general that are not understood. For example, two of the most crucial physical processes in AGB stars remain highly uncertain: the efficiency of the mass loss, which determines the lifetime of an AGB star and the total ejected chemical yields, and the mixing processes leading to both the TDU and the formation of the ^{13}C pocket.

Mixing can also occur within the ^{13}C pocket itself due, for example, to rotationally induced instabilities (Herwig et al., 2003; Piersanti et al., 2013; Siess et al., 2004) or diffusion processes acting on long timescales (Battino et al., 2019). Mixing inside the ^{13}C pocket is crucial for the s-process predictions because it can carry the neutron poison ^{14}N into the region where the free neutrons are released. The number of free neutrons therefore decreases as they are captured by ^{14}N and the s process is much less efficient in producing the elements heavier than iron. In some models, the s process can even completely disappear when the rotational mixing inside the pocket is included (Herwig et al., 2003). On the basis of spectroscopic (Cseh et al., 2018) and asteroseismology (den Hartogh et al., 2019) observations it has been established that strong mixing effects on the s process due to rotation should not occur in AGB stars, however, weak effects, which may also be driven by slow diffusive processes, could

still play a role.

Many different aspects of the the s process are determined by the neutron source reactions. For example, a slower $^{13}C(\alpha,n)^{16}O$ rate would result in models in which some fraction of ^{13}C in the ^{13}C pocket would not burn during the interpulse period and be ingested in the following convective pulse. This may change both the overall elemental distribution and the isotopic abundances. A stronger $^{22}Ne(\alpha,n)^{25}Mg$ rate would activate more efficiently the branching points and modify the resulting isotopic pattern. While the rates of these neutron source reactions are still not well known; significant efforts are currently on-going to provide better estimates. The $^{13}C(\alpha,n)^{16}O$ reaction has been recently analysed underground at the Laboratory for Underground Nuclear Astrophysics (LUNA) and the paper on the results has been submitted. More analyses are also planned at other underground laboratories in China and the USA. The $^{22}Ne(\alpha,n)^{25}Mg$ reaction has been the topic of several works (see, e.g., Adsley et al., 2021; Bisterzo et al., 2015; Karakas et al., 2006; Longland et al., 2012), and is the current topic of the ERC Starting Grant project[1] of Andreas Best at the University of Naples, who plans to measure this reaction with LUNA underground directly in the energy region of stellar He burning.

Neutron-capture cross sections of course also play a role in obtaining accurate s-process results. These are currently the focus of various experimental campaigns of the n_TOF (Neutron Time of Flight) facility at CERN, and in many cases the experimental measurements are given with an uncertainty of less than 5%. However, especially for nuclei with masses above ~ 140, the stellar neutron-capture cross section is determined not only by the value measured by laboratory experiments, which necessarily target the nucleus in its ground state, but also by the contribution of the neutron captures occurring while the nucleus is excited to higher energy levels within a stellar plasma at temperatures of hundreds of MK. These contributions cannot be measured in the laboratory and introduce further theoretical uncertainties, in some cases up to a factor of two, on the determination of total cross section as the temperature increases (Rauscher, 2012). Moreover, most of the unstable nuclei that control the operation of branching points have half lives too short to be used as laboratory targets and theoretical models or indirect measurements are needed to derive their neutron-capture cross sections, which carry large uncertainties, typically also up to a factor of two (see, e.g., Yan et al., 2017, for the case of ^{95}Zr). Some of these nuclei also carry a temperature (and, potentially, density) dependence in their β-decay or electron-capture rates, which can only be evaluated using theoretical models (Goriely, 1999; Li et al., 2016; Takahashi & Yokoi, 1987).

Another major fundamental question is that of the existence of the intermediate i process and its possible occurrence in nature. The i process is probably driven by proton ingestion into a He-burning region, which allows production of the neutron source ^{13}C via proton captures on ^{12}C and the release of neutrons over a very short time scale (Cowan & Rose, 1977). This mixing and burning mechanism can act in low-mass core He-burning stars (Campbell et al., 2010), post-AGB stars (Herwig et al., 2011), AGB stars of low metallicity (Cristallo et al., 2009a), super-AGB stars[2] (Jones et al., 2016), and even more massive stars (Banerjee et al.,

---

[1]SHADES: Scintillator-He3 Array for Deep-underground Experiments on the s process, https://cordis.europa.eu/project/id/852016

[2]i.e., initially massive AGB stars that evolve on the AGB with a NeO core produced by C burning (e.g.

2018; Clarkson et al., 2018). All of these may be sites for the i process, and produce very different abundance patterns from those produced by the s and the r processes (Hampel et al., 2019, 2016).

Meteoritic stardust grains from AGB stars provide extremely powerful high-precision constraints on AGB nucleosynthesis (Section 2.4.2). They carry anomalies in major and trace elements, including many refractory elements heavier than iron. We know that the vast majority of this stardust originated in AGB stars, where dust formation is observed, however, the grains do not carry direct information on the mass and metallicity of their parent stars (as it is possible to derive instead from spectroscopic observations, Section 2.4.1). Therefore, we need to accurately and precisely identify the mass and metallicity of their AGB parent stars.

Another question to be addressed by AGB nucleosynthesis is the long-standing problem of the origin of short-lived radioactive nuclei in the early Solar System (Section 2.4.3). Single nearby sources have been invoked for these nuclei since the 1970s, and include AGB (Trigo-Rodríguez et al., 2009; Vescovi et al., 2018; Wasserburg et al., 2006, 2017) and Super-AGB stars (Lugaro et al., 2012a). Furthermore, AGB stars are the main source within the Galaxy of short-lived radioactive nuclei produced by the s process and their role still needs to be fully exploited to better understand the events in the prehistory of the matter in the Solar System, as will be discussed in detail in Chapter 5.

1.5   Main objectives and overview of the thesis

The main objectives of this work are to exploit observational data of three different types (stars, stardust, and radioactivity) to obtain a complete and self-consistent picture of the s-process nucleosynthesis that occurs in AGB stars of different masses and metallicities. My goals are to identify both the short-comings of the current scenario, for example, the need for the i process to complement the s and r processes, and the far-reaching implications of such a scenario, for example, on the types of stardust grains present in the solar proto-planetary disk and the circumstances of the birth of the Sun.

In Chapter 2, I illustrate the computational method and the stellar models I used to perform the theoretical calculations presented in the thesis (Section 2.3). Predictions from such models are compared to a wide set of observational evidence in the following result chapters. The observational evidence I have used is also described in this chapter, ranging from stellar spectroscopic abundances (Section 2.4.1), to stardust grains from meteorites (Section 2.4.2), and short-lived radioactive nuclei in the early Solar System, whose abundances are also inferred from meteoritic analysis (Section 2.4.3).

In Chapter 3, I discuss the need for an i process in nature. There, I verify if the s process is enough, or the i process is required, to cover data from spectroscopic observations of post-AGB stars in the Large and Small Magellanic Clouds (of metallicity roughly $1/10^{\text{th}}$ of solar, Section 3.2) and of the binary companions of AGB stars at low metallicity (roughly $1/100^{\text{th}}$ of solar, Section 3.1), the carbon-enhanced metal-poor (CEMP) stars, which show excesses in

Doherty et al., 2014a).

the abundances of elements heavier than iron accreted from a former AGB companion, that has since become a white dwarf.

In Chapter 4, I consider stardust grains recovered from meteorites that originated around AGB stars. I analyse O-rich (such as corundum and silicates) and C-rich (specifically silicon carbide, SiC) dust. The O-rich stardust formed both in low-mass AGB stars (roughly < 3 $M_\odot$) before the star turned C-rich, and in more massive AGB stars, where H burning at the base of the convective envelope (hot bottom burning, HBB) destroys carbon and keeps the star O-rich. The C-rich stardust formed in the outer layers of C-rich AGB stars and present strong signatures of neutron captures in the isotopic composition of the elements heavier than iron, from Sr, Mo, and Zr up to Ba, W, and Hf. In particular, I investigate the origin of O-rich grains with strong depletion of ^{18}O using the first underground measurement of the $^{17}O(p,\alpha)^{14}N$ reaction (Section 4.4), and of C-rich SiC grains, by comparing their compositions to that predicted by my models and observed in the binary companions of AGB stars at high metallicity, the so-called Ba stars (Sections 4.1, 4.2, and 4.3.1).

In Chapter 5, I consider short-lived radioactive nuclei heavier than iron in the early Solar System. First, I analyse the information that the r- and s-process short-lived radioactive nuclei carry to us in relation to the events that predated the formation of the Sun (Section 5.1). Then, I include short-lived radioactive nuclei produced by the p process within the same framework (Section 5.2).

Each result chapter (3, 4, and 5) is concluded with a section on the implications of my results and an outlook of the progress that we will achieve in the next years and decades. The summary of the theses is presented in Chapter 6.

Chapter 2

Methodology

The vast majority of the work presented in this thesis is based on the comparison between theoretical, computational model predictions of the evolution and nucleosynthesis of AGB stars and a variety of observational constraints. In the first part of this chapter I describe in detail the computational tools, nuclear reaction networks, and input physics, including the nuclear reaction rates, used to calculate the theoretical predictions. In the second part, I provide the background related to the different observational constraints, some of which derive from spectroscopy of different types of stars, and others from the laboratory analysis of meteorites. Observational evidence from these various types of objects is obtained using completely different methodologies. Therefore, comparing these to the model predictions requires different approaches for the differing observational constraints. One of the main strengths of my work is the ability to exploit these many different sources of information.

2.1 The stellar evolution and nucleosynthesis codes

In my methodology, calculating predictions for stellar abundances involves two steps. First, the evolution of the stellar structure is calculated (in one dimension) by a stellar structure evolution code that solves the four standard equations of stellar structure (hydrostatic equilibrium, energy transport, and mass and energy conservation). The detailed information of the stellar structure solution at each time step is recorded so that a second code, containing the nuclear reaction network, can use the stellar structure to determine the nuclear burning details. This second *post-processing* code calculates the stellar abundances and tabulates them at each time step and in each mass shell of the star. In stellar structure and nucleosynthesis codes, abundances can be represented by mass fractions, i.e., for each nuclear species (isotope) i, $X_i = M_i/M_{\text{total}}$, where M_i is the mass of the species i in the given computational mass shell, and M_{total} the total mass of the shell, or by normalised number abundances: $Y_i = X_i/A_i$, where A_i is the mass of the isotope. In the codes described below the latter representation is used.

The first step of the computational method calculates how each region of a low-mass star (1 $M_\odot$< M < 8 $M_\odot$) evolves in time as the star moves from the main sequence phase to the red giant and the AGB phase, until it becomes a white dwarf. These calculations are performed using the Fortran 77 `Stromlo` stellar evolution code (named after Mount Stromlo,

where the Institute of Astronomy of the Australian National University is located), which was developed by Australian astronomers in the 1970s and 1980s, and in particular my PhD supervisor John Lattanzio (Lattanzio, 1991). The code includes only the 6 nuclear species needed to calculate the contribution of nuclear energy production to the stellar structure via H and He burning: H, ^{3}He, ^{4}He, ^{12}C, ^{14}N, and ^{16}O. During the calculations, the stellar evolution code records the details of the physics of the evolution in time of the entire star, particularly its thermodynamics (temperature and density) and mixing (convective velocities and mixing length) features. Most of the stellar evolution models used in this thesis were calculated by my close collaborator Amanda Karakas at Monash University, Australia (Section 2.2), except for one model presented in Section 3.2 (and Figure 1.9), which was calculated by Simon Campbell (Monash University, both Karakas and Campell were also PhD students of John Lattanzio).

The post-processing nucleosynthesis code `dppns45`, which stands for double-precision post-processing nucleosynthesis,[1] was developed in the 1990s by John Lattanzio and Robert Cannon from the University of Cambridge (UK), on the basis of Cannon's nucleosynthesis code originally developed to study the production of p-only isotopes in a type of exotic stellar object: a red giant star with a neutron star at its core (Thorne-Żytkow objects, Cannon, 1993). Given a stellar structural evolution as input, the code calculates the changes in the abundances of a large number of nuclear species due to nuclear burning and mixing. A main advantage of `dppns45` over competing codes is that the equations that represent the abundance changes include both nuclear burning and mixing. In other words, of the three main stellar physical processes to be solved – structure, nucleosynthesis, and mixing – the last two are coupled. This is crucial, for example, in the case of H burning at the base of the envelope of massive AGB stars (hot bottom burning, HBB), where lithium production and destruction occurs on the same timescale as convective mixing (Lattanzio et al., 1996). Other codes, for example, the version of the `FRANEC` code that was used for the FRUITY database of nucleosynthesis in AGB stars (Cristallo et al., 2009b) combines structure and nucleosynthesis, but not mixing. To my knowledge, there are no codes for AGB nucleosynthesis that can solve simultaneously all the three processes. The `dppns45` code can handle any number of isotopes, although, the larger the number, the longer the running time.

My main contributions to the development of this method have been to extend the nuclear network from the original 77 species to the current 328. To the original network I added the isotopes from sulphur (S, atomic number 16) via Fe (26) to Pb, Bi, and Po (82, 83, 84, respectively) so that it can now calculate s-process nucleosynthesis (Section 2.3.2). I have also continually updated and tested the input of nuclear reaction rates (Section 2.3.3).

2.2 Stellar structure models

While I refer the interested reader to Karakas (2014) for the full details of the input physics and methodology used by Amanda Karakas to calculate the `Stromlo` evolution of the stellar structure used as input for the `dppns45` nucleosynthesis calculations, I summarise here the input physics most relevant to the stellar nucleosynthesis.

---

[1]The code is half written in Fortran 77 and half in Fortran 90 (specifically in relation to dynamic allocation of memory), hence the 90/2=45 at the end.

Figure 2.1: Total mass dredged-up as a function of the initial stellar mass in AGB stars of metallicity a factor of two around solar (where solar $Z = 0.014$, from Karakas & Lugaro, 2016, left panel) and of metallicity 1/100th solar (from Lugaro et al., 2012b, right panel). The left panel includes only results from the `Stromlo` code, the right panel includes both results from the `Stromlo` and the `stars` stellar codes.
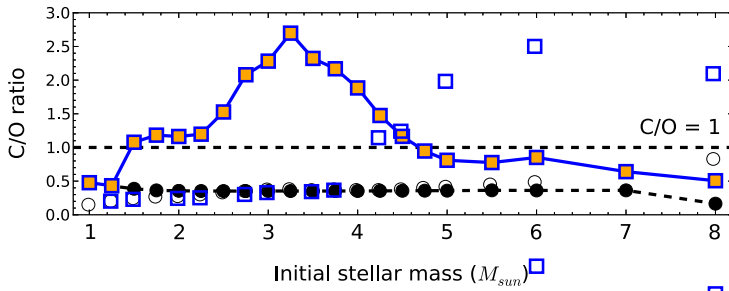
Figure 2.2: The C/O ratio after the first and the last thermal pulses (circles and squares, respectively) as a function of the stellar mass from `Stromlo` models calculated with initial solar metallicity $Z = 0.014$. (Figure from Karakas & Lugaro, 2016).

No mass loss is included on the red giant branch and the Vassiliadis & Wood (1993) mass-loss rate is used on the AGB phase. The mixing-length theory of convection with a mixing-length parameter $\alpha = 1.86$ is employed and instantaneous mixing is assumed in convective regions. No convective overshoot is included in the calculations prior to the AGB phase. Dealing with the borders between radiative and convective regions in stellar interiors is a major uncertainty. An algorithm is implemented in the `Stromlo` code to search for a neutrally stable point from the formal Schwarzschild boundary as described by Lattanzio (1986). This method has been shown to somewhat increase the efficiency of TDU (Lattanzio, 1989).

The models typically cover the complete range of AGB masses from 1 $M_\odot$ to the upper limit for producing a CO core, around 7-8 $M_\odot$, depending on the metallicity. Some models at upper mass boundary produce a hybrid CO(Ne) core and experience off-centre carbon flashes, but the temperature in the core is not high enough to ignite a carbon flame that reaches the centre (e.g., as described by Siess, 2006). Above these masses, stars will become ONe super-AGB stars or neutron stars (Doherty et al., 2014b,c, 2015).

The relevant properties of the AGB models considered here are tabulated in Lugaro et al. (2012b), Karakas (2014), and Karakas & Lugaro (2016) and are reported in this thesis only when relevant to the specific results discussed in the following chapters. The efficiency of the

TDU, together with the evolution and absolute values of the temperature profile near the core of the star are the main determinant of the final abundance distributions at the stellar surface. In Figure 2.1 I show the total amount of mass carried to the stellar surface by the TDU episodes. The TDU efficiency shows three main features: (i) it increases with the stellar mass, reaches a maximum around 3 $M_\odot$ and then decreases again, although the decrease is not always linear as a second maximum is found around 5 $M_\odot$ (the exact location and height of the peak depends on the metallicity). The second maximum is due to the effect of the mass loss, as these stars experience many more thermal pulses, and thus more TDU episodes. (ii) It increases with decreasing metallicity; and (iii) it is heavily model dependent, as different assumptions on mixing at the border of convective regions can change the results. To illustrate this, in the left panel of Figure 2.1, the results of the `Stromlo` models are compared to those from the `stars` models (Stancliffe et al., 2005), which I will use together with the `Stromlo` models in Section 3.1 .

The TDU efficiency also controls the potential transition of AGB stars from O-rich to C-rich, which is crucial for the production of C-rich stardust (Section 2.4.2 and Chapter 4). In Figure 2.2 I show typical results for the C/O ratio from the `Stromlo` models of solar metallicity. The C/O value reaches a maximum at around 3 $M_\odot$, due to the fact that at this mass the TDU efficiency is the highest for $Z = 0.014$ (see Figure 2.1). For higher masses, hot bottom burning (HBB) is activated and the star remains O rich. In the models by Karakas (2014) the theoretical minimum initial mass for producing a solar metallicity, C-rich star is 2 $M_\odot$, because below this mass the TDU is not efficient enough. The minimum mass for C-stars in the Galaxy is not accurately known and probably lies somewhere between 1.4 and 2 $M_\odot$ with the most recent determination of 1.65 $M_\odot$ derived from observations of C-O white dwarfs in old open clusters of the Milky Way (Marigo et al., 2020). Motivated by these uncertainties, some C-rich, low-mass AGB models were also calculated by including convective overshoot at the base of the convective envelope using the prescription from Karakas (2010) and Kamath et al. (2012), which extends the base of the convective envelope by multiplying the pressure scale heights during the TDU by a free integer parameter (called N_{ov}). These models are used in Section 4.1.

2.3 The `dppns45` code

There are several pros and cons to consider when using a post-processing code like `dppns45` for nucleosynthesis calculations. The main advantage is that the running time is much more manageable than if the stellar structure is also solved at the same time as the nucleosynthesis. I am able to run detailed nucleosynthesis calculations of the elements up to Po for the whole life of a star by a time between a few days and a few weeks, depending on the stellar mass. The higher the stellar mass the longer the running time as it is not the main sequence phase (which is shorter for higher masses) that is the most computationally demanding, but the AGB phase, due to the thermal instabilities that need to be followed in both the structure and the nucleosynthesis codes with high temporal and spatial resolution. As the stellar mass increases, the interpulse period decreases and there are many more thermal pulses. For example, at solar metallicity, a 3 $M_\odot$ star typically experiences 10-20 TPs, while a 6 $M_\odot$ star can experience more
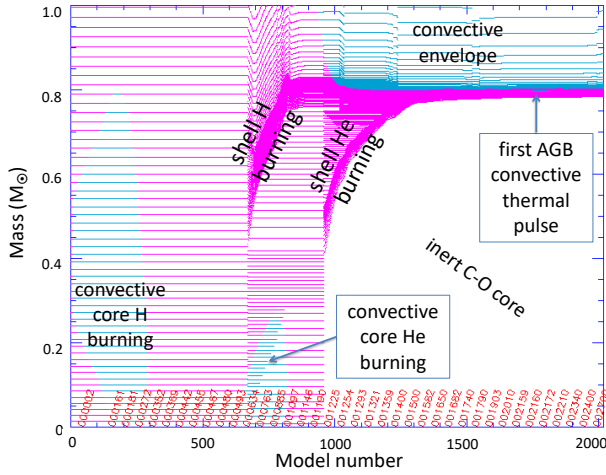
Figure 2.3: Example of the distribution and evolution of the mesh points (represented by lines) along the internal mass (y-axis) in the `dppns45` code for the evolution of a star like the Sun from the main sequence phase to the first AGB thermal pulse, as a function of model number (which represent the time evolution, on the x-axis are the `dppns45` models, the red numbers on top are the original `Stromlo` models). Cyan and pink lines represent convective and radiative mesh points, respectively. The H and He burning shells are more resolved in mass than the other regions of the star as this is where chemical abundances are changing the most. The code does not follow the degenerate, inert, C-O core (white region).

than 50, depending also on the choice of the mass-loss rate. Decreasing the computational time required by stellar evolution and nucleosynthesis codes is difficult, especially as they are not easily amenable to parallel processing. Currently, `dppns45` in particular runs on one CPU only, as the equations to solve involve time evolution, i.e., each step requires the previous step to be solved first. Some part of the calculations could be parallelized, such as the calculation of the nuclear reaction rates, however, this has not been done for `dppns45` yet. Another possibility to improve efficiency is to use an adaptive nuclear network, where the code decides at each time step which nuclear reactions are activated efficiently enough that it is worth including them in the solution. This is done, for example, in the `kepler` code (Heger et al., 2000), but is not yet implemented in `dppns45`, which instead uses a fixed nuclear network.

Other, related advantages of a two-step process are that reaction rate updates and uncertainties can be easily tested without running the structure evolution again, and that the nucleosynthesis code can choose its own time step and its own mass mesh (i.e., the spatial resolution) to solve each model (see Figure 2.3 for an example of a star like the Sun as seen by `dppns45`). Choosing a mass mesh based on the chemical composition instead of based on pressure gradients, as in an evolutionary code, is an advantage as fewer mesh points may be needed for every model. Having a separate time step and mass mesh is also crucial when the nuclear reactions we need to follow for the nucleosynthesis are insignificant for the stellar structure. In fact, in `dppns45` time steps are determined by changes in nuclear burning, not by changes in the structure, and the code is slower when the stellar composition is changing. This means that, for example, the evolutionary code slows down during the AGB H-burning interpulse phases, while the nucleosynthesis code slows down during the thermal pulse phases.

The main disadvantage of using a post-processing code is that if a change in a nuclear reaction rate also affects the structure, this will be ignored by the nucleosynthesis code: the two-step process is obviously not fully self-consistent. Most of the time the nuclear reactions that are important for nucleosynthesis (e.g., neutron captures) do not significantly
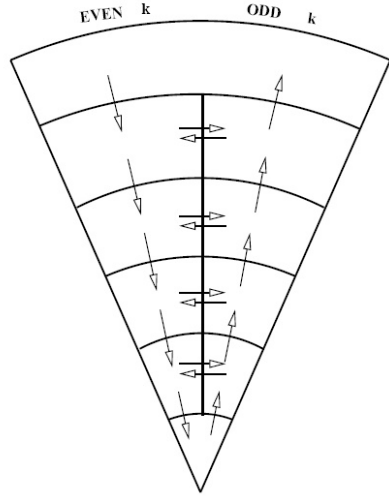
Figure 2.4: Scheme of the advective mixing employed by the `dppns45` code to simulate convective regions in a star. All the nuclear species at each time are represented by a two-dimensional variable h(i,k), where i represents the nuclear species, and even and odd values of k representing to abundance in the downward and upward flows, respectively (Figure from Cannon, 1993).

affect the stellar structure, however, one always needs to keep this caveat in mind. An important example is that of the neutron source reaction ^{13}C$(\alpha,$n$)^{16}$O. If the rate of this reaction were much lower than that currently recommended by nuclear physics colleagues, based on experimental and theoretical investigations, some ^{13}C may remain in the He-rich intershell at the time of the development of the thermal pulse, be ingested into the convective pulse, and affect the energy within the pulse. Other interesting cases that cannot be solved with a two-step computational method are those related to possible ingestion of protons into convective pulses, which are of interest for the i process. In these cases, H burning within the convective pulse could generate enough energy to split the convective region in two (Herwig et al., 2011). These special cases are not treated in this thesis, they require different computational tools.

2.3.1 Mixing

The other advantage of `dppns45` is that, as mentioned above, it includes time-dependent mixing within the equations to be solved, while the evolution code treats mixing as instantaneous. In other words, once the stellar `Stromlo` code has converged on a solution for a given time step, it finds the borders of the convective regions and instantaneously homogenises all the material in that region so that it all has the same composition. In `dppns45`, instead, material in convective regions may not be completely homogenised because the mixing occurs on the same timescale as the nuclear burning. This is crucial for Li production, as mentioned above, but also for neutrons released inside the convective pulse, since the timescale for the neutrons to be captured is much shorter than the convective overturn of the pulse. The neutron abundance, therefore, shows a distribution within the convective region, with the peak neutron density located at the base of the pulse where the temperature is highest and the ^{22}Ne$(\alpha,$n$)^{25}$Mg neutron source is most efficiently activated.

The mixing scheme employed by `dppns45` is presented schematically in 2.4, which shows how the code includes two different streams of material: one going up, and one coming down.

Horizontal diffusion between streams is also allowed so that the final composition of each shell depends on both vertical and horizontal mixing. Knowing the velocity, density, and mass we can solve for the vertical mass flux through each cell, while the horizontal mixing is controlled by the gradient in the vertical flow plus a fraction from diffusion.

2.3.2 Nuclear networks

Most of the AGB nucleosynthesis models presented in this thesis were calculated with two different networks: I used a "light" network of N=77 nuclear species, when the focus was on the elements lighter than iron and the calculations could be run faster (the running time is roughly proportional to N^2, since the implicit method of `dppns45` solves a N×N matrix); and a "heavy" network of N=328 (320 before the year 2014) including all the isotopes on the s-process path, up to Po, with some short-cuts to remove some species, as described below[1].

The initial abundances used in all the calculations are the solar abundances from Asplund et al. (2009), scaled to the stellar metallicity of the model considered[2]. Specifically, they are the pre-solar[3] isotopic nebula values from Table 3 of Asplund et al. (2009), with solar spectroscopic abundances of C, N, O, Ne, Mg, Si, S, Ar, and Fe, the meteoritic value of F from Table 1 of the same paper (chosen because it has a lower uncertainty than the spectroscopic abundance), and the meteoritic values for the solar abundances of the elements heavier than Fe. The small network originally developed by John Lattanzio involves 77 species and includes all the light elements up to S, then it skips the elements from Cl to Mn, but includes some Fe-peak elements. This choice was made to make sure that even if the s process is not covered in this network the amount of free neutrons would be realistic thanks to the inclusion of all the major neutron sources, neutron poisons, and the Fe-peak seeds, which are relatively abundant and have relatively large neutron capture cross sections (∼10 barn).

To build up the 328-species nuclear network I used the following criteria:

1. The network should follow the whole s-process path from Fe to Po, as well as the main branching points along the path;

2. It should include all the light and intermediate-mass nuclei (i.e., below Fe) of interest both as neutron sources and neutron absorbers. While AGB stars are not main sources of these elements in the Galaxy, their isotopic abundances can be modified by neutron captures, and predictions can be compared to measurements of stardust grains. Futhermore, they contribute to the accurate calculation of the amount of free neutron since they can capture and "steal" the free neutrons from the s process;

3. The number of species should be minimised to reduce computing time if possible. Therefore, I excluded from the network most of the p-only isotopes, as well as the r-only nuclei that cannot be reached by the activation of the s-process branching points listed by Lugaro & Chieffi (2018), i.e., typically connected to unstable isotopes with half lives shorter

---

[1]The full networks are listed in Appendix A.

[2]For example, for a star of half-solar or twice-solar metallicity the initial abundances of all the isotopes except H and He, are divided or multiplied by two, respectively. The total sum of the mass fraction X_i of each isotope i is always equal to one, as required by definition.

[3]i.e., the current abundances of long-lived radioactive isotopes such as ^{40}K, ^{87}Rb, and ^{235,238}U are increases to their value before decay using the current age of the Solar System of 4.6 Gyr.
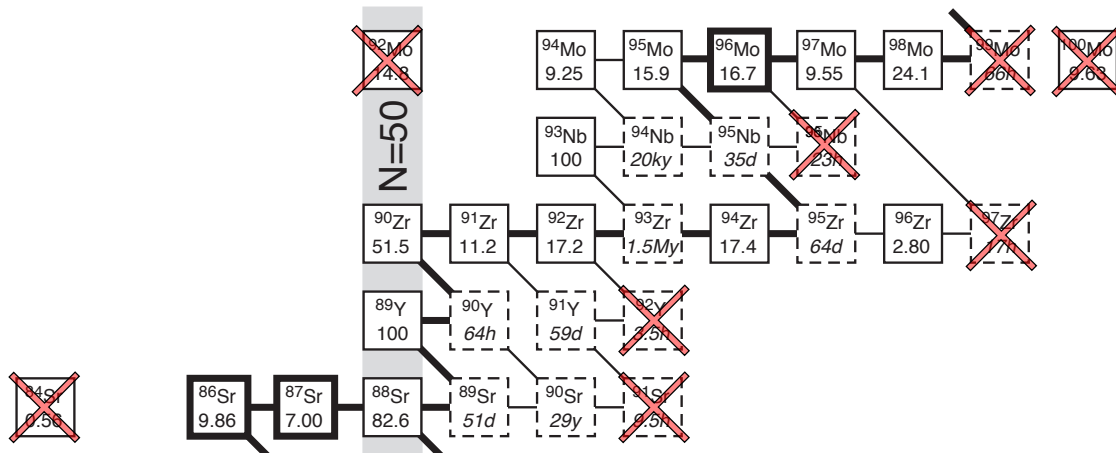
Figure 2.5: Section of the nuclide chart showing the *s*-process nucleosynthesis path in the region of the first *s*-process peak at N=50 magic number of neutrons (grey vertical band) at Sr, Y, Zr. Thick lines connecting isotopes show the main flow of the *s* process, and thinner lines show branches; *s*-only isotopes are in bold boxes and unstable isotopes in dashed-line boxes. For each isotope either the percent of the element in the solar abundance in form of each isotope, or the half-life, in italics, is given. Red crosses cover the isotopes that are not included in my nuclear network: the *p*-only stable isotopes ^{84}Sr and ^{92}Mo, the *r*-only stable isotope ^{100}Mo, and unstable isotopes with half lives short enough to allow the short-cut described in the text. For example, ^{92}Y is not included in the network and the chain of reactions ^{91}Y(n,γ)^{92}Y(β^-)^{92}Zr is substituted by ^{91}Y(n,γ)^{92}Zr. (Figure modified from Lugaro et al., 2003a, courtesy of Andrew Davis.).

than a day[1].

To minimise the network, and therefore the computational time, I also short-cut several chains of reactions involving a neutron capture and a β decay to avoid including unstable nuclei with half lives of less than a day. For example: I modified the ^{96}Zr(n,γ)^{97}Zr(β^-)^{96}Mo reaction chain into an artificial ^{96}Zr(n,γ)^{96}Mo reaction to avoid including ^{97}Zr in the network. This allowed me to remove roughly 60 nuclear species. Examples of the network above Fe around the first, second, and third *s*-process peaks are shown in Figures 2.5, 2.6, and 2.7, respectively.

I needed to include two different energy states for the ^{26}Al and the ^{85}Kr unstable nuclei: the ground and the isomeric states. For these nuclei, these states are not in thermal equilibrium in stellar environments, therefore, they need to be treated as separate isotopes, each with its own associated nuclear reactions. Accurate predictions for the abundance of the ^{26}Al isotope, with half life of 0.717 Myr, are fundamental to compare to the ^{26}Al/^{27}Al ratio inferred in stardust grains (Section 4.4). The ^{85}Kr isotope represents a crucial branching point on the *s*-process path, affecting the ^{86}Kr/^{82}Kr isotopic ratio, which is also measured in stardust grains. Note that the two different isomers of ^{26}Al are included in standard `reaclib` tables described in the next section, while this is not the case for ^{85}Kr, which I therefore included specifically in

---

[1]In a few cases, this resulted in removing the most abundant isotopes of a given element, for example, in the case of Te, the most abundant isotopes are ^{128}Te and ^{130}Te, which are *r*-only nuclei. This point needs to be kept in mind when comparing results to observations because it means that also the abundance of Te in the envelope of our models is artificially lower than solar.
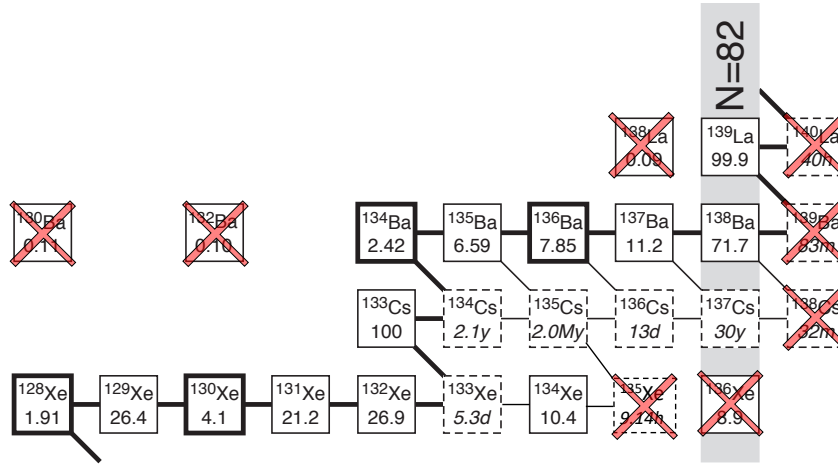
Figure 2.6: Same as Figure 2.5 but for the region of the second *s*-process peak at N=82 magic number of neutrons (grey vertical band) at Ba and La (compare to Figure 1.5). The isotopes that are not included in my nuclear network in this region are the *p*-only stable isotopes ^{130,132}Ba and ^{138}La, the *r*-only stable isotope ^{136}Xe, and unstable isotopes that have half lives short enough to allow the short-cut described in the text. For example, ^{139}Ba is not included in the network and the chain of reactions ^{138}Ba(n,γ)^{139}Ba(β^-)^{139}La is substituted by ^{138}Ba(n,γ)^{139}La. (Figure modified from Lugaro et al., 2003a, courtesy of Andrew Davis.).

my network.

2.3.3 Nuclear reactions

The nuclear reaction network of `dppns45` is based on the `reaclib` package provided by Friedel Thielemann and Thomas Rauscher (University of Basel), where all the reaction rates are expressed by the analytic formula below with 7 coefficients, from which the rate can be calculated at any given temperature T9, i.e., in units of 10^9 K:

$$\text{rate} = exp\left(\text{a1} + \text{a2 T9}^{-1} + \text{a3 T9}^{-1/3} + \text{a4 T9}^{1/3} + \text{a5 T9} + \text{a6 T9}^{5/3} + \text{a7} \, ln[\text{T9}]\right)$$

Each rate is represented by one set of 7 coefficients or by several sets, which need to be summed up. The `reaclib` formula has the advantage of making it easy to built huge databases of theoretically calculated nuclear reaction rates, furthermore, it comes with a set of codes that allow you easily select the rates needed for the nuclear network that the user wishes to build, and updates are provided by JINA (reaclib.jinaweb.org). However, for rates that are determined experimentally it is sometimes difficult to find good fits, and variations up to 10%-20% of the fit from the actual rate are sometimes inevitable. Many other stellar codes, such as the `Kepler` code and the open-source `MESA` code, also use the `reaclib` tables provided in the JINA database. However, if the focus of a study is to test new reaction rates, their uncertainties and their impact on the final abundances, then the `reaclib` fits are not the best approach. For this reason in 2007 my Master student Mark van Raai (University of Utrecht) added a routine to the `dppns45` code that allows us to include specific reaction rates as tabulated values instead of a `reaclib` fit. Thanks to this implementation it was possible
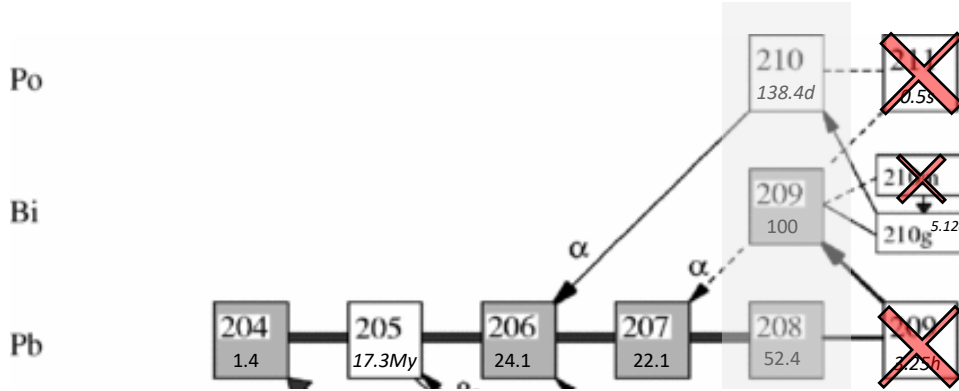
Figure 2.7: Similar to Figures 2.5 and 2.6 but for the region of the third *s*-process peak at N=126 magic number of neutrons (grey shaded band) at Pb and Bi, and the reaction network at the end of the *s*-process path at the unstable Po isotopes. Stable isotopes are indicated with grey boxes. The isotopes that are not included in my nuclear network in this region are ^{209}Pb and ^{211}Po (e.g., the chain of reactions ^{208}Pb(n,γ)^{209}Pb(β^-)^{209}Bi is substituted by ^{208}Pb(n,γ)^{209}Bi). The isomeric state of ^{210}Bi is also not included, because at *s*-process temperatures it quickly decays to the ground state. Most of the reaction flow is trapped at ^{208}Pb and ^{209}Bi because of the small neutron-capture cross sections of these neutron magic nuclei. (Figure modified from Ratzel et al., 2004).

for me to study accurately the effect of many reaction rates on AGB nucleosynthesis (e.g., Section 4.4 and Guo et al., 2012; Lugaro et al., 2014a; Raut et al., 2013; Yan et al., 2017).

Moreover, the neutron-capture reactions that make the *s*-process behave completely differently to charged-particle reactions: neutron-capture rates do not significantly vary with temperature, while charged-particle capture rates have temperature variations of orders of magnitude, as in the latter case the particles need enough energy to overcome the Coulomb barrier. The mild temperature dependence of neutron-capture rates is sometimes difficult to reproduce with the `reaclib` formula, especially within the whole range of temperatures of interest for AGB stars from 10^6 to 10^9 K, and one needs to exercise great caution when using such fits for neutron captures. In the version of the `dppns45` code used to produce most of the results presented in this thesis, neutron-capture rates where included in the calculations based on the JINA `reaclib` fits of the `KADoNiS` database of neutron captures (version 0.2, Dillmann et al., 2006). However, I checked all the rates and if the deviation of the fits from the `kadonis` tables were above roughly 10%, then I implemented the tabulated rate in the calculations.

The other important reactions for the *s*-process, the neutron source reactions ^{13}C(α,n)^{16}O and ^{22}Ne(α,n)^{25}Mg, are included in most of the calculations presented in this thesis as `reaclib` fits of the recommended values of Heil et al. (2008) and Iliadis et al. (2010), respectively. While many indirect estimates of the ^{13}C(α,n)^{16}O reaction are available in the literature, I chose to use Heil et al. (2008), who presented direct measurements and a fit to all the available data. In the case of the ^{22}Ne(α,n)^{25}Mg, the Iliadis et al. (2010) compilation of reaction rates provides rates calculated using a statistical Monte Carlo analysis of the available experimental data.

Another problem is that `reaclib` libraries do not include the temperature dependence for decay rates, nor any density dependence. The latter is not relevant for most reactions

rates, since the cross section itself of a given reaction rate does not intrinsically depend on the density (it is just the probability, for example in the case of a two-body reaction, that one projectile particle reacts with one target particle). The density dependence is included in the calculation of the overall rate within a certain volume simply by multiplying by ρ in case of a decay, ρ^2 in case of a two-body reaction, etc. However, some β-decay rates, and most electron-capture rates, are intrinsically density dependent. For electron-capture rates this is because the electron density determines the probability that a bare nucleus inside a stellar plasma captures an electron. Calculations of electron captures in stellar environments are among the most difficult problems to solve in the field, as atomic and nuclear physics need to be combined as in reality nuclei can be also part of an ionised atom (see, e.g., Simonucci et al., 2013, for the case of ^{7}Be). In general, `reaclib` tables cannot be used for decay rates; different tables are needed. For the isotopes up to Fe these are provided within the `reaclib` package as a different file mostly based on Fuller et al. (1982, however, this is not yet implemented in `dppns45`) and for the nuclei heavier than iron of the standard rates are those from Takahashi & Yokoi (1987) or the `NETGEN` library (Xu et al., 2013). Because of the significance of decay rates both in the treatment of branching points and short-lived radioactive nuclei, in 2014 I started to include analytical formulas for some selected decay rates within the `dppns45` code based on populating the excited energy levels of the unstable nucleus and the theoretical decay rates of such excited levels. I included in the code formulas for the temperature dependence of the decay rates of 11 isotopes (^{107}Pd, ^{128,129}I, ^{134,135,137}Cs, ^{154,155}Eu, ^{160}Tb, and ^{181,182}Hf), which allowed me to accurately calculate the results presented in Section 4.1 and 5.1. Currently, Andrés Yägue, a post-doctoral fellow in my group has been implementing a better and more flexible description of decay rates in the `dppns45` code, including both temperature and density dependence. Therefore, from now on I will be able to perform many more accurate investigations of the behaviour of branching points and of the production of radioactive nuclei in AGB stars.

2.3.4   The inclusion of the ^{13}C pocket

As introduced in Section 1.3.2, to match the observations that AGB stars are enriched in the s-process elements (see Section 2.4.1 and, e.g., Abia et al., 2002; Busso et al., 2001), a large number of neutrons are needed to be released in the intershell by the ^{13}C(α,n)^{16}O reaction. To achieve this a ^{13}C pocket is commonly assumed to form in the region located below the deepest point in mass reached by each TDU episode (Figure 1.11). In the work presented in this thesis, protons are inserted in this region by including an artificial, parametrised partial mixing zone (PMZ) in the post-processing `dppns45` calculations. The protons are partially mixed over a mass extent in the intershell denoted by M_{PMZ}, normally using an exponentially declining profile such that at the base of the envelope the proton abundance is the envelope H abundance $X_{\mathrm{p}} \simeq 0.7$ and in the intershell, at M_{PMZ} below the base of the convective envelope, it is $X_{\mathrm{p}} = 1 \times 10^{-4}$. Below this point in mass, $X_{\mathrm{p}} = 0$. The structure of this standard proton profile and the resulting ^{13}C pocket are shown in Figure 2.8.

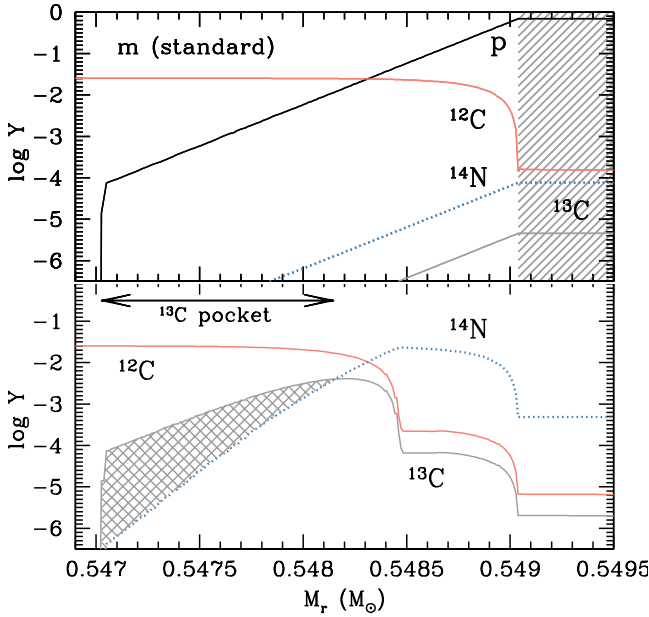This method differs from those used, for example, by Cristallo et al. (2009b) to produce

Figure 2.8: Abundance profiles of selected isotopes as a function of mass, showing the formation of the ^{13}C pocket when using our standard exponential mixing function applied to a 1.25 M$_\odot$ Z = 0.01 model at the deepest extent of the first TDU episode. Top panel: the proton profile just after insertion of a PMZ with $M_{\mathrm{PMZ}} = 2 \times 10^{-3}$ M$_\odot$, the shaded region represents the convective envelope. Bottom panel: the ^{13}C pocket formed after all protons have burnt. The cross hatched region represents the total mass of the pocket where the abundance of ^{13}C is higher than that of ^{14}N, and free neutrons are available for the s process. This is typically half the size in mass of the M_{PMZ}, although the exact fraction depends on the mixing profile. (Figure from Buntain et al., 2017, courtesy of Carolyn Doherty.)

the FRUITY database[1] and by the NuGRID collaboration[2] (Battino et al., 2016, 2019), both of which are based on the inclusion time-dependent convective overshoot at the base of the envelope. This overshoot leads to the mixing of protons in the intershell, below the deepest point in mass reached by each TDU episode, that produces the ^{13}C pocket. The overshoot method involves a main free parameter, the *overshoot* parameter, which scales the exponential decline of the velocity, or the diffusion coefficient, depending on the exact method. Overshoot is still a more self-consistent method than that used in `dppns45` as it tries to describe the physical process that leads to the proton abundance profile, rather than including the mixing in an artificial way. Nevertheless, it turns out that the s-process results from `dppns45` for AGB stars of low mass, where ^{13}C is the main neutron source, are reasonably similar to those of FRUITY (Cristallo et al., 2009b), as discussed by Lugaro et al. (2012b), Fishlock et al. (2014), and Karakas & Lugaro (2016). This demonstrates that the `dppns45` parametric approach is a good reproduction of the more self-consistent model that uses time-dependent convective overshoot. The `dppns45` results and those from FRUITY differ from NuGRID mostly due to the fact that NuGRID additional includes time-dependent convective overshoot also at the base of the convective pulses. This results in higher abundances of ^{12}C in the intershell, leading to higher abundances of ^{13}C and therefore of the neutron exposure in the pockets, as well as higher temperatures in the convective pulses, as discussed in detail in my PhD thesis (Lugaro et al., 2003b). Overall, while the `dppns45` method bypasses the actual physical mechanism responsible for the mixing, and ignores possible effects on the stellar structure, it has the advantages that it allows me to study more freely the specific impact of the mixing on the

---

[1]http://fruity.oa-abruzzo.inaf.it/

[2]https://nugrid.github.io/content/data

model predictions, and provides me with the opportunity to constrain the physical mechanism from the observation. For example, the PhD thesis of my student Joelene Buntain at Monash University analysed the effect of changing the shape of the exponential mixing profile. The principal result was that only when the profile is modified by orders of magnitude is there a strong effect on the s-process nucleosynthesis (Buntain et al., 2017).

In this thesis I present only models calculated with the standard profile, however, I varied the M_{PMZ} parameter as function of the stellar mass according to Karakas & Lugaro (2016). Depending on the intial stellar mass different standard values were used: (1) for stars of initial mass ≤ 3 M$_\odot$ $M_{\mathrm{PMZ}} = 0.002$ M$_\odot$ (as in Figure 2.8), which results in a ^{13}C pocket mass typically roughly 1/10 to 1/20 of the total mass of the He-rich intershell. As demonstrated early by, e.g., Gallino et al. (1998), such M_{PMZ} values are required to match the strong observational constraint that AGB stars of metallicity close to solar are enhanced in s-process elements by up to one order of magnitude. (2) For stars of initial mass $3 < M \leq 4$ M$_\odot$, I used $M_{\mathrm{PMZ}} = 0.001$ M$_\odot$. This is because the mass of the intershell decreases with the initial stellar mass and the FRUITY calculations mentioned above, where the pocket is formed by including time-dependent overshoot (Cristallo et al., 2009b), indicate that M_{PMZ} follows such a decrease, due to the steeper pressure profile between the core and the envelope. (3) For initial masses $4 < M \leq 5$ M$_\odot$, I set $M_{\mathrm{PMZ}} = 0.0001$ M$_\odot$, an order of magnitude smaller than for the lower masses, again due to the shrinking of the mass of the intershell. (4) For intermediate-mass AGB models with mass > 5 M$_\odot$, I did not include a ^{13}C pocket, following indications both from theory (Cristallo et al., 2015; Goriely & Siess, 2004) and observations (García-Hernández et al., 2013) that the ^{13}C pocket is insignificant in this mass range. Instead, in these models the s process proceeds through activation of the ^{22}Ne reaction inside the TP, with temperatures above 300 MK (Karakas et al., 2012; van Raai et al., 2012), and produces excesses in Rb, as has been observed (Garcia-Hernandez et al., 2006). The main limitation of the models presented in this thesis is that both the exponential proton profile and the value of M_{PMZ} are constant for all the ^{13}C pockets in a given model[1]. This is in contrast to the findings of Cristallo et al. (2009b) that the extent in mass of the ^{13}C pocket decreases for any given model as the star evolves on the AGB phase, again due to the shrinking of the He-rich region, like it occurs in the more massive stars. Furthermore, the variation of M_{PMZ} with the stellar mass described above and implemented in my models is quite crude. Therefore, in some selected models I also experimented with a range of values of M_{PMZ}, which allowed me to progress beyond these limitations in a simple way.

Finally, rotation (and magnetic fields) were not included in the models I present in this thesis. I refer to co-authored papers by Cseh et al. (2018) and den Hartogh et al. (2019) for the justification, drawn from observational constraints related to spectroscopic observations of Ba stars and to asteroseismology, of the fact that stellar rotation should not play a major role in the predictions of the s-process abundances.

---

[1]I remind here that PMZ is introduced in correspondence to each TDU episode, therefore it is a recurrent feature in each model.

2.4   Observational constraints

There are two main types of observations directly related to AGB s-process models: (i) spectroscopic observations of AGB stars, their companions, and their progeny, and (ii) stardust grains that formed in AGB stars, travelled to the birthplace of the Sun formed and where trapped inside meteorites, from which they are now extracted and analysed. Both types of observations have advantages and disadvantages and to build a self-consistent picture it is, therefore, imperative to consider them together (Section 4.2). One main difference is that spectroscopic data provide almost exclusively elemental ratios, while stardust grain data provide exclusively isotopic ratios. The reason is that on the one hand stellar spectra are produced by atomic physics and differences in the spectra produced by atoms of different isotopes of the same element are very difficult, and often impossible to pin down. On the other hand, elemental abundances in stardust grains are almost exclusively determined by the chemical processes that drive the formation of such dust around AGB stars, rather than by the nucleosynthesis that produces such elements. Therefore, elemental data can be used to understand dust formation in such environments (e.g., Lodders & Fegley, 1997), but it does not provide very stringent constraints on the nuclear processes inside the star. Isotopic ratios of stardust grains provide detailed constraints on stellar models. For example, the activation of many branching points along the s-process path can be investigated using stardust, while only the branching points that produce ^{87}Rb in AGB stars can be investigated using stellar spectra, because the elemental abundance of Rb is affected by these branching points.

One key advantage of stardust grains over spectroscopic observations is that the composition of stardust is derived directly from laboratory analysis using mass spectrometers and the main uncertainty is the statistical counting[1], whereas, the composition of stars derived from spectra is dependent on the models of stellar atmospheres employed to analyse the spectra. Multi-dimensional and non-local equilibrium effects are known to play significant roles even in the composition of the Sun (Asplund, 2005), and introduce potentially large systematic uncertainties. Overall, typical uncertainties for stardust grain data are a few percent, while for spectroscopically derived abundances they are approximately 50% for the hotter post-AGB and AGB binary companions (see, e.g., Cseh et al., 2018; de Castro et al., 2016; De Smedt et al., 2012). In the case of direct observations of the cooler, dynamical, molecule- and dust-producing atmospheres of AGB stars, uncertainties on spectral abundances can be as large as an order of magnitude (see, e.g., Abia et al., 2002; Garcia-Hernandez et al., 2006; Pérez-Mesa et al., 2017).

The main drawback of stardust is that we do not know its origin a priori. Each grain can originate from a different star and we do not know the initial mass and metallicity of each parent stars. In the case of stellar observations, instead, it is typically possible to derived the metallicity, usually as Fe/H, as the Fe lines are quite easy to observe (de Castro et al., 2016). Often the stellar mass is also observable, for example, by considering binary properties (Jorissen et al., 2019), or qualitative and/or semi-empirical considerations related to the mass

---

[1]In some cases pollution of material of solar origin and composition cannot be excluded, which represent a further systematic uncertainty, see, e.g., the discussion in Section 4.4 for the ^{18}O/^{16}O isotopic ratio and the case of Fe in Section 4.1 (Trappitsch et al., 2018).
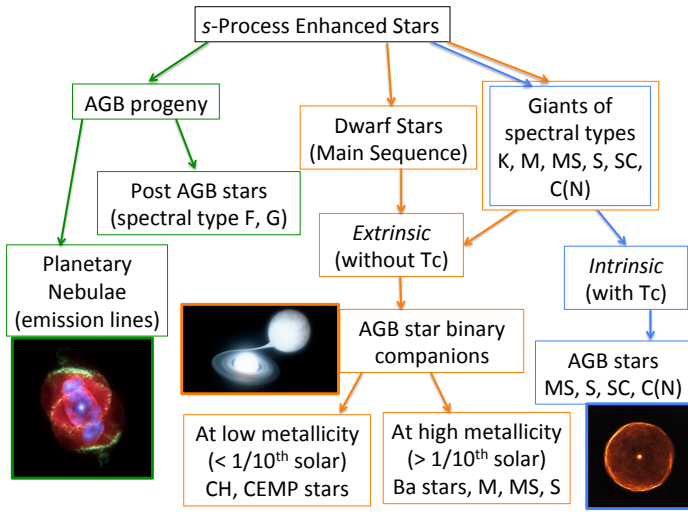
Figure 2.9: Schematic illustration of the different types of stars that show *s*-process enhancements. Direct observation of AGB stars are indicated as blue arrows, observed objects related to stellar evolution past the AGB phase, specifically the AGB progeny as indicated by green arrows. Stars that are enriched by an AGB companion are connected with orange arrows. This scheme should be taken only as a general guideline because mixed objects may also exists. (Image credits as in Figure 1.9, except: binary interaction image, credit: Caltech.)

loss, the wind speed, and the location in the Galaxy (Garcia-Hernandez et al., 2006). By considering stardust and stars together in Section 4.2, I exploit all the advantages provided by these two different observational objects.

Another observational source related to the *s*-process in AGB stars is the presence at the time of the formation of the Solar System of short-lived radioactive nuclei (SLR), i.e., nuclei with half lives ($T_{1/2}$) of the order of a few 0.1 to 100 Myr. The abundances of these nuclei are inferred from meteoritic analysis. They can be used as cosmic chronometers for the history of the matter that ended up in the Solar System and as nuclear fingerprints to understand the environment where the Sun formed. In some cases, such as that of ^{26}Al (0.7 Myr) they also contributed to the thermal evolution of proto-planets with implications on the habitability of terrestrial planets (see review by Lichtenberg et al., 2019; Lugaro et al., 2018b). Four of these nuclei, ^{107}Pd ($T_{1/2}$=6.5 Myr), ^{135}Cs ($T_{1/2}$=2.3 Myr), ^{182}Hf ($T_{1/2}$=8.9 Myr), and ^{205}Pb ($T_{1/2}$=17.3 Myr), are produced by the *s* process in AGB stars and model predictions of their abundances can be applied to investigate the presolar history of the Solar System matter (Section 5.1).

Below I present a more detailed introduction to these three types of observational constraints, which I will use in the following results chapters: spectroscopic observations in Chapter 3, stardust grains in Chapter 4, and radioactive nuclei in Chapter 5.

2.4.1 Stellar spectroscopy

As described in the Introduction, spectroscopy in the 1950s already allowed the identification of stars whose spectra showed the signature of excesses relative to the Sun of the abundances of elements heavier than iron produced by the *s* process (Figure 1.1). Since then, a large number of astrophysical objects have been discovered that present such chemically peculiar features, belonging to a variety of evolutionary phases. This diversity is schematically illustrated in Figure 2.9.

The main distinction in the group of giant stars is if the star is an *intrinsic* or *extrinsic* *s*-process enhanced star. The intrinsic stars are true AGB stars experiencing the TDU and
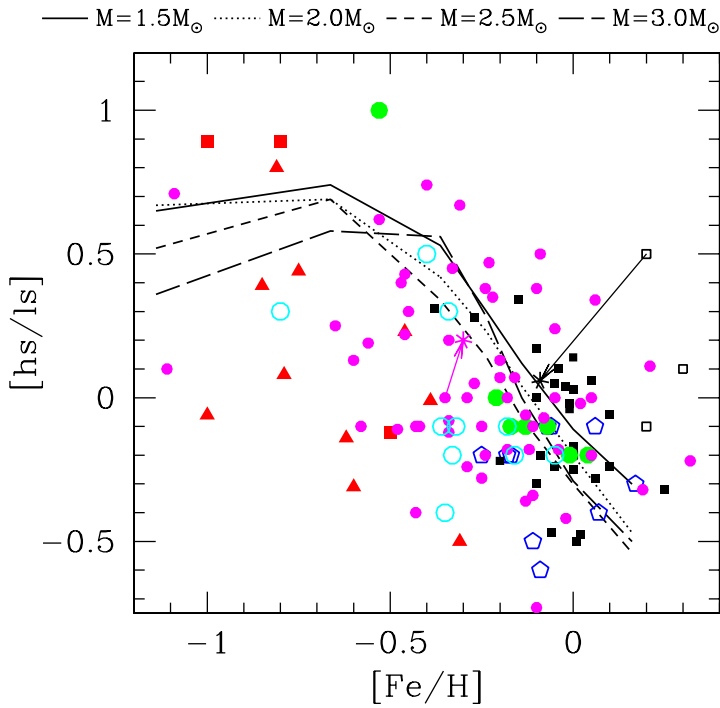
Figure 2.10: Figure 12 from Cristallo et al. (2011) showing a collection of spectroscopic data available from 22 different studies prior to 2016 in the metallicity range [Fe/H] from solar to roughly 1/10th of solar. The different symbols represent different classes of intrinsic (squares and pentagons), extrinsic (circles), and post-AGB (triangles) stars. The lines represent model predictions from FRUITY for the indicated masses. The black and pink arrows indicate the results of the re-analysis of the composition of two specific stars.

showing Tc at their surface. At around solar metallicity, they are also typically C-rich, i.e., they belong to the spectroscopic classes, SC and C(N), which show the signatures of C-rich molecules such as CH in their spectra. The extrinsic stars are giant and dwarf stars in binary systems that accreted s-process material from a more massive binary companion already evolved through the AGB phase and now a white dwarf. Recently, *bitrinsic* stars, i.e. AGB stars that also accreted from a former AGB companion, have also been discovered (Shetye et al., 2020). At solar metallicity, there is a larger amount of O initially in the stellar envelope than at lower metallicities and binary interaction does not typically transfer enough C-rich material to make a C-rich star. These binary companion stars, which remain O-rich, comprise the class of Ba (barium) stars (usually K and M giants, but also dwarfs) as well as more evolved MS and S giants. As the metallicity decreases it is much more difficult to observe intrinsic s-process-rich AGB stars. This is because AGB stars have masses typically above 1 $M_\odot$, therefore they evolve into white dwarfs by less than 9 Gyr, which is shorter than the age of the Galaxy. Instead, s-process-enriched stars at low metallicities are observable as extrinsic AGB binary companions. These stars are C-rich, because it is much easier to transfer enough C to overcome the lower initial O abundance, and the efficiency of the TDU increases with decreasing stellar metallicity (Figure 2.1). Such s-process enhanced stars at low metallicity represent a large fraction of the so-called CEMP (Carbon-Enhanced Metal-Poor) stars and in particular the groups originally referred to as CEMP-s and CEMP-s/r, which I will discuss in detail in Section 3.1.

The atmospheres of intrinsic AGB stars themselves direct constrain the absolute abundances resulting from nucleosynthesis but are very difficult to model due to the presence of molecules, dust, winds, and pulsations (Höfner & Olofsson, 2018). Even if uncertainties are large, it is expected that stellar AGB models at solar metallicity should produce enough Ba to reach roughly an order of magnitude higher than the solar value of Ba in their envelopes

(Abia et al., 2002) and theoretical models are typically calibrated in terms of choices of the ^{13}C pocket to match such a constraint (e.g., Section 2.3.4). The existence of hotter, binary, extrinsic companions allows us to obtain more precise spectroscopic data. One disadvantage of binary systems is that there are still major uncertainties in the process of binary interaction (see, e.g., Section 5.4 of De Marco & Izzard, 2017). For nucleosynthesis purposes, we can rely on ratios of *s*-process elements belonging to the different *s*-process peaks, such as Ce/Y, since the abundances of both elements, to a first approximation, would have experienced the same amount of dilution during the binary transfer. Elemental ratios, therefore, do not carry binary uncertainties and directly represent the features of the neutron exposure in the original AGB parent star (see discussion in, e.g. Cseh et al., 2018, and in Section 3.1.3).

As AGB stars evolve through the post-AGB phase, their atmospheres cool down again and it is easier to derive the surface abundances for these stars than for their progenitors. This has been done extensively, and these abundances have been compared to AGB theoretical models (e.g. Reyniers et al., 2004). However, recently it has become clear that the abundances observed in post-AGB stars, and in particular their Pb deficiency, are not compatible with AGB model predictions. This puzzle, which I will discuss at length in Section 3.2, also highlights the danger of assuming that different AGB-related stellar objects are affected by the same physics.

Finally, since the pioneering work of Dinerstein (2001), the abundances of elements heavier than iron and specifically those elements that do not condense into dust, such as the noble gases Kr and Xe, as well as Se, Rb, and Cd, have been observed thanks to analysis of the emission lines of planetary nebulae (e.g. Madonna et al., 2018; Sterling & Dinerstein, 2008, and references therein). There are large uncertainties related to the modelling of ion populations in the UV-illuminated gas that constitute a planetary nebula, which were produced during the previous AGB mass-loss phase and carry the signature of the *s* process. There are also significant uncertainties in our understanding of planetary nebulae, for example, their often asymmetric shapes cannot be reconciled with simple single star evolution – binary channel interactions are probably required (see, e.g., Section 6.3 of De Marco & Izzard, 2017). Nevertheless, observations of planetary nebulae represent direct and complementary constraints along with observations of stellar atmospheres, especially given that the elements observable in planetary nebulae are not observable in stellar atmospheres, and vice versa.

Early studies aimed at comparing *s*-process AGB models to spectroscopic observations (Busso et al., 2001; Cristallo et al., 2011) had to rely on very limited data sets. To resolve this problem all the available observations were considered together, not only AGB stars themselves, but also their binary companions, and post-AGB stars. However, different observations obtained from different telescopes and different spectral analysis are inconsistent with each other, furthermore, different types of stars may present the signature of different physics. On top of issues related to different samples and different objects, there are problems related to the traditional usage of the *ls* and *hs* indices. By definition, *hs* represents the average of the abundances of the *heavy s*-process elements, i.e., belonging to the second peak, Ba, La, Ce (but also in some cases Nd, Pr, and Sm, although these are not predominantly *s*-process elements) and *ls* represents the average of the abundances of the *light s*-process elements,

i.e., belonging to the first peak (Sr, Y, and Zr). For example, [hs/Fe][1]=1/2([Ba/Fe]+[La/Fe]), [ls/Fe]=1/2([Y/Fe]+[Zr/Fe]), both depending on which elements are available from the observations, and obviously [hs/ls]=[hs/Fe]-[ls/Fe]. One problem is that the elements chosen to calculate hs and ls may be different in different studies, depending on the accuracy of elemental abundances from the available spectra. While the s-process model predictions do not vary significantly when different elements are chosen, there are still basic inconsistencies between different studies, which use different elements to calculate [ls/Fe] and [hs/Fe]. More inconsistencies appear if the initial composition of the stellar model is, for example, artificially enhanced in the r-process abundances(as done by Bisterzo et al., 2011, see also Figure 3.3), in which case Nd and Sm, whose abundances have a relatively important contribution by the r process ($\sim$50% and 70%, respectively, in the Solar System) should not be used as s-process indicators. Furthermore, because of the definitions of [hs/ls], it is not straightforward to calculate the observational uncertainties, and generic error bars of ± 0.25 dex have usually been given.

Figure 2.10 represents an attempt at comparing AGB s-process model predictions to spectroscopic observations from different studies and different types of stars and illustrates the limitations of such an approach. It is not possible to decide if the models are a good match to the data. On the one hand, the predictions do not cover the whole spread of the data of roughly one order of magnitude at any given metallicity, since variations in the stellar mass only allow a spread of roughly 0.2 dex. On the other hand, it is not possible to determine if the observational spread is real or if it is an artefact of the problems related to the mixed data sets. Furthermore, because no error bars are reported for individual stars, one cannot clearly compare the spread with the observational uncertainties. The new abundances reported for the two stars indicated by the two arrows in the figure are a further indication of problems with systematic uncertainties when considering different studies.

More recently, all these problems have been resolved, at least in the metallicity region of Ba stars, thanks to a large ($\simeq$170) self-consistent data set of high-resolution spectra of Ba stars obtained with the Fiberfed Extended Range Optical Spectrograph (FEROS) installed at the 1.52 m and 2.2 m telescopes of ESO at La Silla (Chile), with a spectral resolving power of R = 48000 and wavelength coverage from 3800 Å to 9200 Å (de Castro et al., 2016; Pereira et al., 2011). Using these breakthrough measurements it has been possible for my group, in collaboration with Brazilian colleagues, to better constrain AGB models by removing the need for the use of the outdated hs and ls indexes and deriving accurate error bars for each individual star (Cseh et al., 2018). Thanks to these new data, we understood that rotational mixing should not play a major role in the s process in AGB stars and that the main feature of the process is the predicted and observed increase of the neutron exposure with decreasing the stellar metallicity. In Section 4.2 I build on these recent advances from spectroscopic Ba star data to pin down the origin of stardust grains.
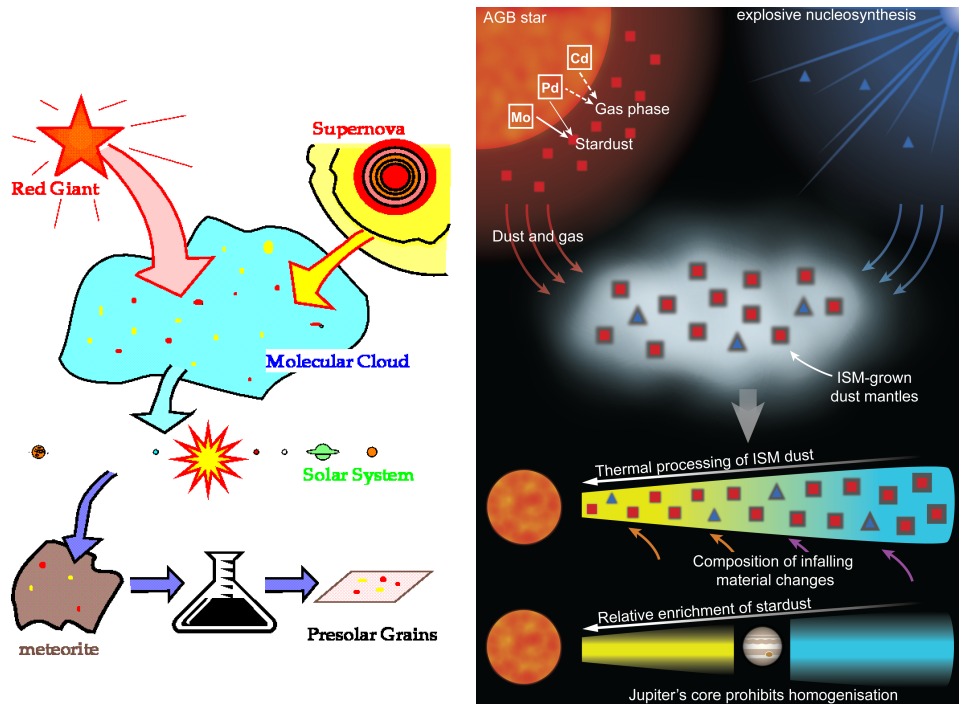
Figure 2.11: Left panel: Schematic cartoon of the journey of stardust grains from the stars to the laboratory (courtesy of Larry Nittler). Right panel: Figure 3 of Ek et al. (2020) extending the picture on the left to illustrate possible implications of the presence of stardust in the solar proto-planetary disk. In dense molecular clouds, dust/ice mantles (dark grey) condense onto pre-existing stardust grains from AGB stars (red squares) and core-collapse supernovae (blue triangles). If the mantles are preferentially destroyed in regions closer to the Sun, a relative enrichment of stardust results in these regions, as reflected in *s*-process enrichment of the Earth. The observed isotopic dichotomy between the inner and outer Solar System may have been caused by compositional changes of the in-falling material and the early formation of a possibly Jupiter-related barrier (see, e.g. Brasser & Mojzsis, 2020; Kruijer et al., 2017; Nanne et al., 2019).

2.4.2 Stardust grains

The first hint of the existence of stardust grains appeared in the 1960s when analysis of the composition of the noble gases Ne (Black & Pepin, 1969) and Xe (Reynolds & Turner, 1964) trapped inside old carbonaceous meteorites showed the presence of exotic components with isotopic compositions completely different to the bulk of Solar System material. However, it took more than 20 years to isolate the carriers of such anomalous compositions. In 1987, microscopic dust grains were finally recovered from meteorites, displaying enormous anomalies in their isotopic compositions of up to four orders of magnitude relative to the bulk solar composition. These are too large to be attributed to chemical or physical fractionation and could only have been produced by nuclear reactions in stars. After being ejected into the interstellar medium, these stardust grains were incorporated in the proto-solar nebula and then

---

[1]The usual spectroscopic notation is used throughout the thesis, where abundances relative for example to iron are represented as $[X/Fe] = log_{10}[(X/Fe)_{star}/(X/Fe)_{\odot}]$, and the unit is referred to as *dex*.
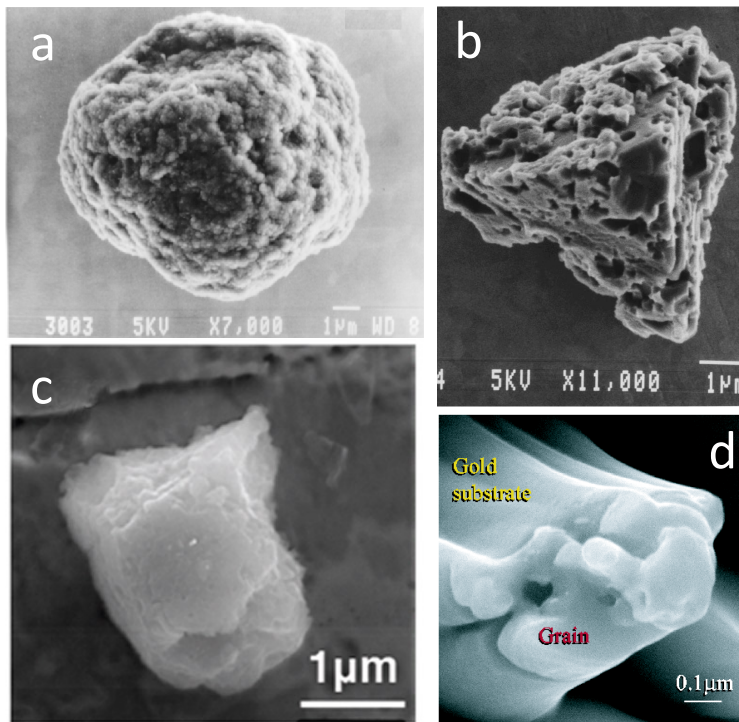
Figure 2.12: Electron microscope images of stardust grains: **a)** a graphite grain of cauliflower type (courtesy S. Amari); **b)** a silicon carbide (SiC) grain (courtesy S. Amari); **c)** a corundum (Al_2O_3), i.e., sapphire grain (courtesy A. Takigawa); **d)** a spinel ($MgAl_2O_4$), i.e., ruby grain (courtesy L. R. Nittler). The size scale is at the bottom right of each panel; the ruby grain is ten times smaller than the other three grains. Sizes below 1 μm are most typical for stardust grains, but grains > 1 μm are easier to analyse in the laboratory. All the grains shown here formed around AGB stars, except for the graphite grain, which came from a core-collapse supernova.

survived the formation of the Solar System without being destroyed. Reviews on meteoritic stardust grains can be found in Clayton & Nittler (2004a); Nittler & Ciesla (2016); Zinner (2014), and a more detail description can be found in my textbook (Lugaro, 2005). Here I only report a brief introduction.

A cartoon depiction of the journey of stardust grains from their stellar site of formation to the laboratory is shown in the left panel of Figure 2.11. It begins with their birth as dust grains in the gas surrounding stars. One of the most favourable, and observationally confirmed, location for the formation of dust are the wind-driven, extended envelopes of AGB stars, and the majority of the known stardust grains came from such stars. Another astrophysical site where dust is observed to form is the cooled ejecta of core-collapse supernova explosions. Together with most of the gas that formed the star, the stardust is ejected into the interstellar medium by the stellar winds or the supernova explosion. When the Sun formed in a molecular cloud, some of the stardust grains that had travelled from their formation site to the proto-solar nebula were trapped inside asteroids, the parent bodies of the meteorites from which they are recovered today. Since stardust grains carry the detailed signature of the isotopic composition of the gas that surrounds stars, they are effectively tiny specks of stars. While the bulk of the solar material (Figure 1.2) came from many different stars because of the chemical evolution of the Galaxy (Figure 1.4), each stardust grain instead carries the signature of the particular site of its formation and gives us the unique opportunity to study the detailed isotopic composition of a single star or supernova, rather than a mixture of them.

The right panel of Figure 2.11 is an updated depiction of the journey undertaken by meteoritic stardust, including details of their possible effect within the solar proto-planetary disk. In recent years, thanks to significant advances in the development of chemical procedures dedicated to the extraction of the specific chemical elements and their high-precision

laboratory analysis, it has been possible to measure isotopic variations down to parts per ten thousand, or even parts per million, with extremely high precision in different Solar System bodies. These analyses have demonstrated, for example, that the Earth is more rich in s-process isotopes than bodies that formed further away from the Sun (Dauphas et al., 2004; Ek et al., 2020). The presence of stardust is most likely responsible for these tiny anomalies; the right panel of Figure 2.11 shows a proposed explanation of the data. It involves dust mantles, which grow on top of stardust in the interstellar medium and, unlike the original stardust, do not carry the pure nucleosynthetic signature of a stellar environment since they are formed from material already homogenised in the interstellar medium. Thermal processing in the proto-solar disc distinguishes between mantles and stardust, such that, closer to the Sun, the stardust becomes enriched relative to the mantles. Finally, the formation of a barrier possibly related to Jupiter may have prevented further mixing, resulting in the observed dichotomy between materials from the outer and from the inner Solar System showing the presence or lack, respectively, of the signature of explosive nucleosynthesis (see Kleine et al., 2020, for an accessible review).

Table 2.1: Types of stardust grains, in order of decreasing typical abundances in meteorites, in parts per million by mass (ppm), their typical size range and C/O condition for formation, where C stands for C/O> 1 and O for O/C> 1. Adapted from Table 1.1 of Clayton & Nittler (2004b), see references therein.

Type	Abundance (ppm)	Size (μm)	C/O condition
Diamond	1400	0.002	C
Silicates[a]	500 (in IDPs[b])	$0.3 - 1$	O
Silicon Carbide (SiC)[c]	14	$0.1 - 20$	C
Graphite	10	$1 - 20$	C
Spinel ($MgAl_2O_4$)[a]	1	$0.1 - 3$	O
Corundum (Al_2O_3)[a]	~ 0.1	$0.1 - 3$	O
Silicon Nitride (Si_3N_4)	>0.002	~ 1	C
Hibonite ($CaAl_{12}O_{19}$)	0.002	~ 2	O
TiC, ZrC, MoC, RuC, FeC, Fe-Ni	sub-grains	$0.005 - 0.22$	C

[a]Will be compared to AGB models and discussed in Section 4.4.
[b]Interplanetary dust particles.
[c]Will be compared to AGB models and discussed in Sections 4.1, 4.2, and 4.3.

Table 2.1 lists the types of stardust grains recovered so far and Figure 2.12 shows some images of them. Stardust grains are strongly refractory materials, which can condense directly from the gas phase at high temperatures, roughly between 1300 and 2000 K. The condensation sequence of minerals depends on the initial composition of the gas, and predominantly on the C/O ratio. If C/O < 1, all the carbon is locked up in carbon monoxide (CO) molecules, which have a very strong bond and are stable at high temperatures, and the condensed minerals are mostly oxides and silicates (like in the Solar System, where C/O $\simeq$ 0.4). If C/O > 1, instead, all the oxygen is locked up in CO molecules and carbon compounds can condense, such as graphite and carbides.

The most abundant stardust grains are very small diamonds of the size of nanometers, called *nanodiamonds*. Because of their small size, it has not been possible so far to analyse them as single grains. They carry the exotic Xe-HL component potentially related to p- and r-process nucleosynthesis. Since these processes are predicted to occur in explosive conditions, presolar diamonds have been attributed a supernova origin. Silicate grains are the second most abundant stardust grains and were discovered only in 2004 (Nguyen & Zinner, 2004). The lack of stardust silicates before 2004 was puzzling as the major oxides observed around AGB stars are silicates (Demyk et al., 2000; Waters et al., 1996) while no stardust silicates were to be found in meteorites. The reasons of this mismatch were that silicates are more likely to be destroyed by chemical processing during the life of the meteorite, and that presolar silicates are very difficult to locate among the abundant silicates of solar origin that constitute the main part of meteorites. Moreover, silicates are destroyed by most of the chemical treatments used to prepare meteoritic residues and stardust silicates were also difficult to detect because of their small size. With the NanoSIMS instrument (a mass spectrometer with a primary beam of nanometer size) it is now possible to identify and analyse stardust grains of smaller sizes and this led directly to the discovery of presolar silicates.

Among the carbon-bearing minerals, silicon carbide (SiC) grains are large enough (from a fraction to a few tens of μm) to allow the analysis of single grains. They are also relatively easy to extract from meteorites, with respect to the other types of stardust grains, and several thousand of them have been analysed to date[1]. SiC grains typically have shapes bounded by crystal planes, with pitted surfaces likely due to the harsh treatments to which they are exposed during their extraction (Figure 2.12b). Based on their C and Si compositions, SiC grains have been classified into several populations, the largest of which (*mainstream* SiC) comprises more than 90% of the grains and are believed to have originated in C-rich AGB stars of approximately solar metallicity (Hoppe & Ott, 1997; Lugaro et al., 1999) and will be discussed in Sections 4.1, 4.2, and 4.3. The remaining SiC grains are classified in another four small populations: A+B of unclear origin (Amari et al., 2001b; Liu et al., 2017a,b), X from core-collapse supernovae (e.g Liu et al., 2018b; Pignatari et al., 2013a), and Y and Z from C-rich AGB stars of metallicity lower than solar (Amari et al., 2001a; Hoppe et al., 1997; Zinner et al., 2006), although there are some inconsistencies with such an interpretation (Lewis et al., 2013; Liu et al., 2019). Some SiC grains have also been interpreted as material originating from nova explosions (José et al., 2016).

Stardust SiC grains contain impurities that can also be analysed for their isotopic composition, which are dominated by N, Al and Ti, and trace elements with low concentrations such as Mg, Ca, Sr, Zr, Mo, Ru, Ba, and Nd. One of the main proofs of evidence of their origin in AGB stars is that these grains are the carriers of the so-called "Xe-S" meteoritic exotic component (Reynolds & Turner, 1964), which is produced by s-process nucleosynthesis. In fact, the emission line at 11 μm – characteristic of SiC – is observed spectroscopically in these stars (Clément et al., 2003; Speck & Hofmeister, 2004; Speck et al., 1999; Treffers & Cohen, 1974). Since the start of the 2000s, a new analytical technique: Resonant Ionisation Mass

---

[1]Stardust grain data has been collected and can be retrieved from the Presolar Grain Database at presolar.physics.wustl.edu/presolar-grain-database/ (Hynes & Gyngard, 2009) of the Laboratory for Space Sciences of Washington University in St Louis (USA).

Spectrometer (RIMS) has been applied at the University of Chicago (the CHARISMA and the more recent CHILI instruments, see detailed descriptions in Savina et al., 2003; Stephan et al., 2016) to the analysis of relatively large ($\simeq \mu$m) single stardust SiC grains to obtain the isotopic composition of the trace elements. Ions are extracted from the sample via lasers, tuned such that only the atoms of a selected element are ionised and therefore accelerated by an electric field, and allowed to enter the mass spectrometer. In this way it is possible not only to increase the efficiency of the ion extraction, but also to avoid analysing isotopes of different elements with the same mass, which cannot be distinguished in the mass spectrometer. This has allowed unprecedented precision in the derivation of the isotopic ratios of the elements heavier than Fe in SiC grains. Comparison between these data and AGB models is discussed in detail in Section 4.1.

Like the SiC grains, also the graphite grains are large enough to be analysed singularly. However, their extraction procedure is more complex than that of other grains since graphite has chemical and physical properties similar to those of other carbonaceous compounds present in the meteorites. Moreover, trace elements are present in extremely low abundances, which makes their analysis challenging. A few hundred graphite grains have been analysed to date and have been classified according to their morphology and density. Round grains, which comprise more than 90% of graphite grains, have anomalous carbon isotopic ratios and are clearly of stellar origin. Their density is in the range 1.6 - 2.2 g/cm^3 and they have two different external appearances: cauliflower-like, consisting of aggregates of smaller grains (Figure 2.12a), which are more abundant among grains of low density, and onion-like, consisting of concentric layers of carbon, which are more abundant among grains of high density. About one third of stardust graphite grains have low densities (1.6 - 2.05 g/cm^3) and appear to have originated from core-collapse supernova explosions (Hoppe et al., 1995; Pignatari et al., 2013a; Travaglio et al., 1999). Higher-density grains may have originated from a range of stellar environments (Amari et al., 2014). Stardust silicon nitride grains (Si_3N_4) have also been identified during the analysis of meteoritic residues (Nittler et al., 1995). The condensation of silicon nitride requires C/O > 1 and a high nitrogen concentration. The composition of this type of grain is very similar to that of SiC grains belonging to the X population and points to a core-collapse supernova origin of Si_3N_4 grains. Graphite and SiC grains also contain tiny subgrains of Ti, Zr, Mo, Ru and Fe-carbides (Bernatowicz et al., 1996) as well as subgrains of Fe-Ni metals (Croat et al., 2003).

Until 2003, corundum (sapphire and ruby, Al_2O_3, Figure 2.12c) was believed to be the most abundant stardust oxide grain. However, with the NanoSIMS instrument it is now possible to identify and analyse presolar grains of smaller sizes. Thanks to these advances, it has been recently found that spinel ($MgAl_2O_4$, Figure 2.12d) is the most abundant (by mass) type of stardust oxide grains (Zinner et al., 2003), while having, on average, a smaller size than corundum grains. A few hibonite grains (with composition $CaAl_{12}O_{19}$) and one titanium oxide grain (TiO_2) of stellar origin have also been recovered (Choi et al., 1999; Nittler et al., 1997). Oxide grains are resistant to the chemical treatments used to isolate the carbonaceous grains and they are present in meteoritic residues together with SiC grains. However, stardust oxide grains, like silicate grains, are more difficult to locate because the majority of those grains in meteorites formed in the Solar System, where C/O < 1. Only a small fraction of oxide and

silicate grains are of stellar origin and special techniques have been developed to recognise them (Nguyen et al., 2007). Oxide and silicate grains have been separated into distinct groups, mostly based on their oxygen isotopic ratios. Also the $^{26}\text{Al}/^{27}\text{Al}$ ratio can be derived in some of the grains (where ^{26}Al is a short-lived radioactive isotope with half life of 0.7 Myr) for the time when the grain formed. The initial abundance of ^{26}Al can be inferred from the radiogenic abundance of the daughter nucleus ^{26}Mg. The composition of most of these grains suggests that they have formed around O-rich AGB stars, as will be discussed in detail in Section 4.4.

2.4.3   Short-lived radioactive nuclei in the early Solar System

Analysis of meteoritic whole rocks and separate inclusions allows us to derive the abundances of short-lived radioactive nuclei (SLRs, with half lives between 0.1 and 100 Myr) in the *early Solar System* (ESS), defined as the time of the formation of the oldest solids found in meteorites. These solids are the calcium-aluminium-rich inclusions (CAIs, left panel of Figure. 2.13) that represent up to several % of most primitive meteorites: the carbonaceous and unequilibrated ordinary chondrites[1], which are used to obtain the Solar System abundances (Figure 1.2). The oldest solids in the Solar System were found among CAIs via their U to Pb radioactive dating (Amelin et al., 2010) and they are used to set the age of the Sun at 4.67 Gyr.
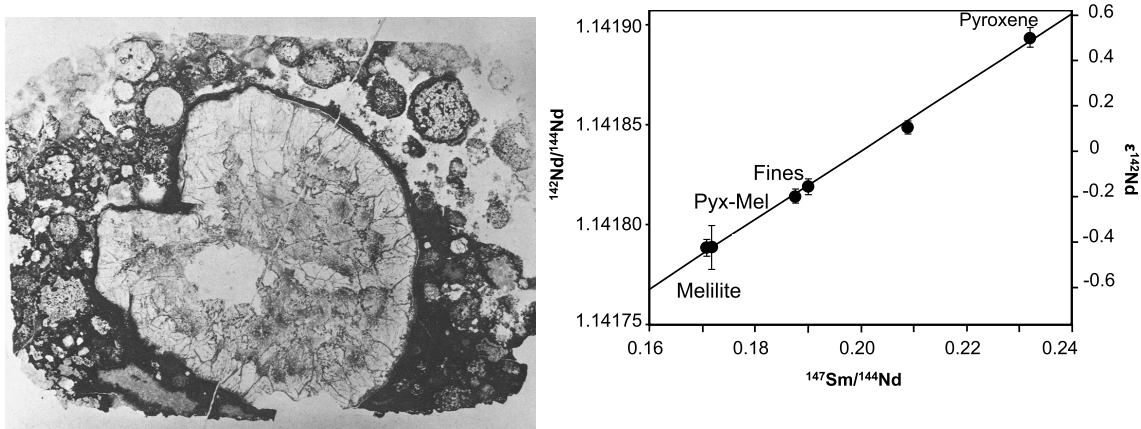
Figure 2.13: Left panel: Photomicrograph (of 22 × 17 mm) of the CAI named Al3S4. The different minerals within the CAI were analysed by Marks et al. (2014) for excesses in ^{142}Nd with respect to another abundant isotope of the same element, ^{144}Nd. Right panel: The y-axis reports the measured excess of $^{142}\text{Nd}/^{144}\text{Nd}$ in the different minerals within Al3S4, both as ratio (left y-axis) and as ϵ-value (see Eq. 2.1, right y-axis). The x-axis reports the isotopic ratio of $^{147}\text{Sm}/^{144}\text{Nd}$, two isotopes taken to represent the relative abundances of the two elements involved (Sm and Nd), which is controlled by the chemistry and mineralogy of the sample. The initial $^{146}\text{Sm}/^{147}\text{Sm}$ ratio is represented by the slope of the black line fit to the data (Figures from Marks et al., 2014).

---

[1]These consist mainly of silicate minerals in the form of *chondrules*, solidified melt droplets that gave these meteorites their name, and *matrix*, an amalgam of amorphous material and crystals of very small dimensions ($\sim \mu$m, where the stardust grains are found).

Table 2.2: Daughter nuclei (D), stable or long-lived reference isotopes (R), $T_{1/2}$ and τ in Myr from the National Nuclear Data Center website (www.nndc.bnl.gov, including errors on the last digits in brackets, except for ^{146}Sm, see table footnotes), stellar nucleosynthetic production processes (where expl. stands for explosive, and NSE for nuclear statistical equilibrium) and ESS ratios with statistical 2σ uncertainties, for which references can be found in Table 2 of Lugaro et al. (2018b) for the nine SLRs of interest in Chapter 5.

SLR	D	R	$T_{1/2}$	τ	Process	ESS ratio
^{26}Al	^{26}Mg	^{27}Al	0.717(24)	1.035	H burning O/Ne expl.	$(5.23 \pm 0.13) \times 10^{-5}$
^{53}Mn	^{53}Cr	^{55}Mn	3.74(4)	5.40	NSE	$(7 \pm 1) \times 10^{-6}$
^{60}Fe	^{60}Ni	^{56}Fe	2.62(4)	3.78	n captures	$(1.01 \pm 0.27) \times 10^{-8}$
^{92}Nb	^{92}Zr	^{93}Nb	34.7(2.4)	50.1	p process	$(1.57 \pm 0.09) \times 10^{-5}$
		^{92}Mo^a				$(3.2 \pm 0.3) \times 10^{-5}$
^{107}Pd	^{107}Ag	^{108}Pd	6.5(3)	9.4	s and r	$(6.6 \pm 0.4) \times 10^{-5}$
^{129}I	^{129}Xe	^{127}I	15.7(4)	22.6	r	$(1.28 \pm 0.03) \times 10^{-4}$
^{146}Sm	^{142}Nd	^{144}Sm	$68^b/103^c$	$98^c/149^d$	p	$(8.28 \pm 0.44) \times 10^{-3}$
^{182}Hf	^{182}W	^{180}Hf	8.90(9)	12.8	s and r	$(1.018 \pm 0.043) \times 10^{-4}$
^{247}Cm	^{235}U	^{235}U	15.6(5)	22.5	r	$(5.6 \pm 0.3) \times 10^{-5}$

^{a}Renormalised using Solar System abundances (Burkhardt et al., 2011; Lodders et al., 2009).
^{b}According to Kinoshita et al. (2012). ^{c}According to Marks et al. (2014).

Given that the Sun is 4.67 Gyr old and the SLRs we consider here live less than 100 Myr, even if they were abundantly present when the Sun was born, today they are completely extinct and their abundances in the ESS cannot be measured directly. Instead, they are inferred from analysis of meteoritic samples via the identification of an excess in the daughter nucleus into which each SLR decays. For example, excesses in ^{60}Ni in meteorities, with respect to its normal abundance ratios relative to ^{58}Ni, can be the product of the radioactive decay of ^{60}Fe ($T_{1/2}$=2.6 Myr). Such an excess represents extinct ^{60}Fe and potentially the fingerprint of one or more supernovae that occurred more than 4.6 Gyr ago. Note that this is conceptually very different from observing, as was done recently, live ^{60}Fe in the Earth's deep sea crust (Wallner et al., 2016), in fossilised bacteria (Ludwig et al., 2016), and on the Moon (Fimiani et al., 2016). This live ^{60}Fe is instead the fingerprint of a recent injection, roughly 2 Myr ago, from one or more supernova (Breitschwerdt et al., 2016). Also, fifteen atoms of live ^{60}Fe have been counted in accelerated particles (cosmic rays) that reach the Earth (Binns et al., 2016). These live ^{60}Fe atoms are also the fingerprint of recent production events in massive (OB) star associations from where the cosmic rays are believed to originate.

In the case of the ESS abundances, to make more evident the radiogenic origin of the observed excesses, it is necessary to analyse materials with variable amounts of the element to which the SLR isotope belongs relative to the element to which the daughter isotope belongs. For example, the Sm/Nd in the case of ^{146}Sm (which α-decays into ^{142}Nd with a debated half life of $T_{1/2}$=68 or 103 Myr) illustrated in the right panel of Figure 2.13. True radiogenic excesses should be more evident in materials with the highest elemental ratios. These materials are advantageous in disentangling the radiogenic excesses from other effects

that may cause unusual isotopic ratios, such as statistical flukes and instrumental and natural mass fractionation. Excesses in the daughter nuclei are usually measured relative to the most abundant isotope of the same element, and to better highlight their nature as excesses, they are reported in the form of δ-values or ϵ-values, i.e., per mil or per ten thousand, respectively, variations with respect to the corresponding laboratory standard ratio. For example, in the case of the ^{142}Nd/^{144}Nd ratio the ϵ-value shown in the right panel of Figure 2.13 is:

$$\epsilon(^{142}\mathrm{Nd}/^{144}\mathrm{Nd}) = \left(\frac{(^{142}\mathrm{Nd}/^{144}\mathrm{Nd})_{\mathrm{measured}}}{(^{142}\mathrm{Nd}/^{144}\mathrm{Nd})_{\mathrm{standard}}} - 1 \right) \times 10000. \tag{2.1}$$

A linear correlation between the excess and the elemental ratio (e.g., the solid line in the right panel of Figure 2.13) proves that the SLR ^{146}Sm was incorporated in the samples while still alive (see also Lee et al., 1977, for the early development of this method in relation to the SLR ^{26}Al). The slope of the line defined by the data points gives the abundance ratio of the SLR to the stable reference isotope at the time after which the system was not disturbed anymore by any redistribution of isotopes or elements, the only change coming from radiogenic decay. This line is referred to as an *isochrone*, since data points located on a given line have by definition the same ratio of the SLR to its reference isotope, i.e., their closure time is the same. Any younger sample, i.e., one that closed after some time, would lie on a line with a reduced slope, since it would contain a lower initial abundance of the SLR due to its decay during the given time interval. Using this method, SLRs can be used to derive relative ages for Solar System samples, from which we can infer the history of the formation of planetesimals and planets (Dauphas & Chaussidon, 2011).

Clearly, the best samples to derive the SLRs abundances in the ESS are the oldest possible materials, the CAIs, as in the case shown in Figure 2.13. In some cases, however, analysis of a given element in CAIs is not possible, and other materials younger than CAIs must be used. This is the case, for example, for ^{60}Fe, due to the fact that not much Fe is present in CAIs. The age difference between the analysed sample and the CAIs can be measured using other radioactive systems and then be used to extrapolate back from the abundance measured in the sample to the ESS value. In Table 2.2 (adapted from Tables 2 and 3 of Lugaro et al., 2018b) I present the list of SLRs that will be discussed in more detail in Chapter 5. For ^{92}Nb I provide both the experimental ^{92}Nb/^{93}Nb ratio and the ratio re-normalised to a different stable isotope, ^{92}Mo. The reason for this renormalisation is that ^{92}Nb is produced by the p process, while ^{93}Nb, the only stable isotope of Nb, is produced mainly by the s process. To obtain a ratio that is possible to interpret within the framework of stellar nucleosynthesis it is necessary to re-normalise the measured ratio to a stable isotope also produced by the p process, such as the neighbouring nucleus ^{92}Mo. Overall, the extremely low uncertainties associated with the ESS SLRs allows us to use these isotopes as one of the best available observational tools to understand the formation of the Sun, with implications on the formation of its terrestrial planets including the Earth, as I will discuss in Chapter 5.

Chapter 3

Neutron captures in AGB stars of low metallicity

In this first chapter of results, I compare models of s-process nucleosynthesis in AGB stars to a category of stellar objects, the so-called carbon-enhanced metal-poor (CEMP) stars, that has become the focus of much research in the past two decades as they represent relics of the early Universe. These stars are located in the Galactic halo, have low mass[1] and a very low content of metals, specifically their Fe abundances are as low as 1/100 solar or less. This low Fe content means that these stars were born out of material that had not experienced substantial enrichment from previous stellar generations via the cycle of matter in the Galaxy (Figure 1.4). Most interestingly, a relatively large number of these old stars show enhancements in carbon, and are therefore called CEMP stars, and many of these CEMPs are also enriched in the elements heavier than iron. The peculiar chemical compositions of these stars have sparked many investigations into the abundance analysis of their spectra and the nucleosynthetic models of stars of low metallicity required to interpret them (e.g., Beers & Christlieb, 2005; Sneden et al., 2008). Such investigations are providing significant constraints on the evolution and nucleosynthesis of low-metallicity stars that existed in the early Galaxy, which are compact object not directly observable. By interpreting the chemical composition of CEMP stars in the light of stellar nucleosynthesis models, we derive clues on the sites and nature of the first nucleosynthetic processes in the Galaxy.

In the first part of this chapter I analyse in detail whether the composition of all CEMP stars enhanced in the elements heavier than iron can be explained by enrichment of s-process elements due to mass transfer from a binary companion that previously evolved to the AGB phase and is now a white dwarf (Section 3.1). I conclude that this is not possible because some of the observed signatures are incompatible with s-process nucleosynthesis. I obtain the same conclusion in the second part of the chapter (Section 3.2), where I compare the AGB s-process models to observations of post-AGB stars in the Magellanic Clouds. My overall conclusion is that, therefore, a different type of neutron-capture process must to exist in nature, with features in-between the s and the r processes, i.e., the intermediate i process. I finish the

---

[1]A star of roughly 0.9 the mass of the Sun becomes a giant (more luminous than a main-sequence star like the Sun and therefore easier to observe) after a time of roughly 13 Gyr, corresponding to the age of the Milky Way Galaxy.

chapter with a brief summary and the follow-up studies motivated by the main conclusions reported here (Section 3.3).

3.1 Neutron captures in AGB stars and the origin of CEMP stars

Lugaro et al. 2012, The Astrophysical Journal, 747, 1

3.1.1 Motivation

Roughly 10% to 20% (Carollo et al., 2012; Cohen et al., 2005; Lucatello et al., 2006) of all observed old halo stars are enriched in carbon (i.e., their C abundance is more than 10 times higher than of the Sun, relative to Fe: [C/Fe] > 1). Roughly 2/3 of these CEMP stars also show enrichment in the elements heavier than iron produced by neutron-capture processes (Aoki et al., 2007; Sneden et al., 2008). These enhancements range from pure *s*-process in the case of CEMP-*s* stars, with [Ba/Fe] > 1 (where Ba is a typical *s*-process second peak element), to *s*- and *r*-process enhancements, in the case of the originally named CEMP-*s/r* stars, with [Eu/Fe] > 1 (where Eu is a typical *r*-process element), and [Ba/Eu] > 0 (Jonsell et al., 2006).

Qualitatively, the C and *s*-process enhancements in CEMP-*s* and CEMP-*s/r* stars can be explained by the presence of an initially more massive binary companion, which produced C and *s*-process elements during its AGB phase and transferred them onto its companion via mass transfer (Lucatello et al., 2005). Roughly 50% of all CEMP stars are CEMP-*s/r*, which is puzzling given that we believe the *s*- and the *r*-processes to be independent events occurring in different astrophysical sites (AGB stars for the *s* process and compact mergers or rare types of supernovae for the *r* process, Section 1.3.1). Many scenarios have been proposed (as summarized by Jonsell et al., 2006; Lugaro et al., 2009) and most of them appear unlikely. Here I discuss models of the *s*-process in AGB stars of low metallicity to understand if AGB nucleosynthesis can explain the composition of CEMP-*s* stars, and also of CEMP-*s/r* stars when adding an *r*-process component to the abundances.

3.1.2 Methodology

Before my work in 2012, the range of published models of the *s*-process in AGB stars of 1/100 solar or lower metallicity was limited as *s*-process predictions were only available for stellar masses between 1.3 and 2 $M_\odot$ from Bisterzo et al. (2010), and of 2 $M_\odot$ from Cristallo et al. (2009b). In the work presented here I investigated for the first time AGB stars of metallicity 1/200 solar for masses from 0.9 to 6 $M_\odot$, using different physical and numerical approaches.

Stellar evolutionary inputs into the post-processing `dppns45` code were calculated using two different evolutionary codes: the `Stromlo` (Section 2.1) and the `stars` (Stancliffe, 2009) codes for stars of mass between 0.9 and 6 $M_\odot$, and between 1 and 3 $M_\odot$, respectively. The basic inputs used by my collaborator Amanda Karakas, needed to calculate the evolutionary sequences of the `Stromlo` models, were reported in Section 2.2 with the main differences here

being that these low-metallicity models were calculated with (i) a mixing-length parameter of 1.75 (instead of 1.86), (ii) the mass loss before the AGB phase based on the Reimers (1975) prescription, with the free parameter $\eta = 0.4$ (this does not affect the following AGB evolution), and (iii) the mass loss also during the AGB phase based the Reimers (1975) prescription (instead of Vassiliadis & Wood, 1993) with η values that vary with mass, for models above 3 $M_\odot$ (see discussion in Karakas, 2010). The reason for this different choice of mass loss is computational: at low metallicity the mass loss from Vassiliadis & Wood (1993), used as standard in the `Stromlo` code, becomes extremely low, and the evolution of the AGB star extremely long, with hundreds to thousands thermal pulses. This renders the calculations, also of the post-process nucleosynthesis, difficult to manage, particularly for a large set of models. The computation of the AGB phase with the `stars` code was performed by Richard Stancliffe and has been described in detail in Stancliffe et al. (2004). Mass loss is included as in the `Stromlo` code. Also as in the `Stromlo` code, convective overshoot is not included at any stage throughout the evolution, however, a different mixing length parameter (equal to 2) is employed. The two main differences between the stellar structures computed with the two codes are that: (i) there are fewer TPs in the `stars` than in the `Stromlo` models due to a different treatment of the opacities, which influences the mass loss and this results in a smaller amount of TDU mass (Figure 2.1); and (ii) the temperature in the convective thermal pulse is lower in the `stars` calculations, for the same initial stellar mass, which means that the ^{22}Ne neutron source is activated less strongly than in the `Stromlo` models.

I extended the nuclear network from the networks previously available[1] to run `dppns45` to include 320 species and reach up to Pb and Bi[2]. Then, Amanda Karakas executed the calculations for the nucleosynthesis of the elements up to Bi by feeding the stellar evolutionary sequences described above into the `dppns45` post-processing code described in Section 2.3. For the initial composition of most nucleosynthesis models the solar distribution of abundances from Asplund et al. (2009), reported in Appendix B, were taken and scaled down to [Fe/H] = -2.3 (i.e., Z=0.00007, 1/200 the solar value of Z=0.014). Some post-processing models were also calculated by varying the initial composition to: (i) the values predicted by galactic chemical evolution models for solar neighbourhood stars of metallicity [Fe/H] = -2.3 from Kobayashi et al. (2011) - this values affect only the initial composition of the elements up to Zn, and the final results are almost unchanged, so I will not discuss it further; (ii) the values obtained assuming that the star was already born with an r-process enrichment and, in some cases, also an s-process enrichment. To compute these initial r- and s-process enhancements we used the s and r contributions to the solar abundances given by Sneden et al. (2008). The ^{13}C pockets were included as described in detail in Section 2.3.4 and a number of tests were performed varying the M_{PMZ} parameter for a selected set of stellar masses.

---

[1] i.e, the light 77-species network described in Appendix B and another 166-species network, reaching up to the first s-process peak at Zr and used by Karakas et al. (2012); van Raai et al. (2012) to study the production of Rb, but not used in this thesis.

[2] The 8 more species I further introduced in the network in 2014 to reach the 328 species list described in Section 2.3.2 and Appendix B are: ^{128,129}I and ^{181,182}Hf, related to the production of the SLR nuclei ^{129}I and ^{182}Hf, which will be discussed in detail in Section 5.1, and ^{159,160}Gd and ^{160,161}Tb, for the inclusion of branching points on the s-process that could affect predictions for the isotopic composition of the element Dy, which is potentially measurable in stardust SiC grains.
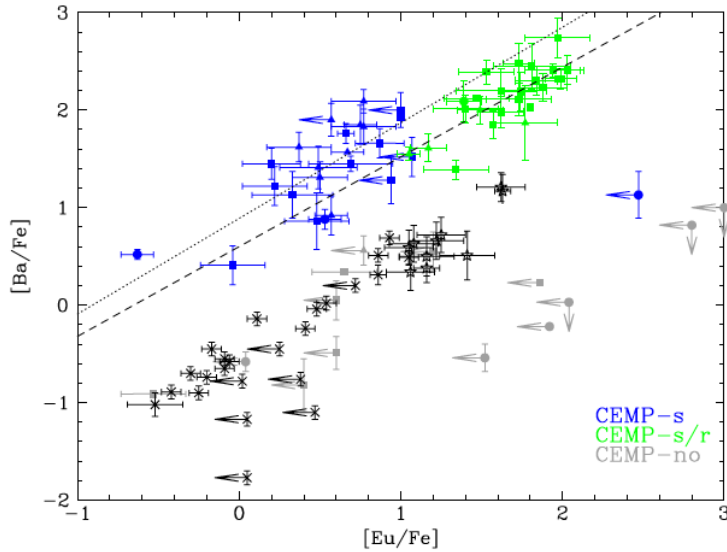
3.1 Neutron captures and the origin of CEMP stars

Figure 3.1: Observational data for CEMP stars colour-coded as in the legend. Black crosses and stars are weak and strong, respectively, r-process-enhanced low-metallicity (which are not CEMP stars). For the CEMP stars, triangles, squares and circles represent stars with $[Fe/H] > 2$, $3 < [Fe/H] < 2$, and $[Fe/H] < 3$, respectively. The short-dashed and long-dashed lines represent the correlation lines through the CEMP-s and the CEMP-s/r populations, respectively. (Figure from Lugaro et al., 2012b, courtesy of Carlos Rijs.)

Together with Richard Stancliffe[1], I then compared our model predictions to the abundances of CEMP stars using the compilation of CEMP star compositions from Masseron et al. (2010). We compared our models to the composition of CEMP stars as a population, rather than to single objects, keeping in mind that all the models were computed with the same metallicity, $[Fe/H] = -2.3$, which represents the peak of the metallicity distribution of the CEMP stars enhanced in neutron-capture elements, while the overall CEMP metallicity range covers $3.5 < [Fe/H] < 1$ (see, e.g., Figure 7 of Aoki et al., 2007). Figure 3.1 presents an overview of the observational data for CEMP stars and carbon-normal metal-poor stars enhanced in r-process elements, following the data and classification of Masseron et al. (2010) (except that, for the sake of simplicity, their CEMP-low-s stars are included in the CEMP-s group). The CEMP-no stars have no enhancements in elements heavier than iron. In this and the following figures different symbols are used for stars in different metallicity ranges, as indicated in the caption. Stars with different metallicities show no noticeable differences in their abundance distribution, however, there are more CEMP-s than CEMP-s/r stars with $[Fe/H] > 2$, and more CEMP stars with no enhancement in the elements heavier then Fe (CEMP-no) with $[Fe/H] < 3$ than CEMP stars with such enhancement.

The two groups of CEMP-s and CEMP-s/r are clearly distinct: CEMP-s/r have higher $[Eu/Fe]$ ratio than CEMP-s in absolute terms, and also higher $[Ba/Fe]$, on average. In the figure we also plot the correlation lines of the two groups. Because the scale of the plot is logarithmic, the similar gradients of around unity (0.98 and 0.92, respectively for CEMP-s and CEMP-s/r) indicate that for both classes the linear dependence is preserved in a non-logarithmic scale. The y-intercept corresponds to $[Ba/Eu]$ and defines the slope of the linear correlation between the two variables in a non-logarithmic scale: the process responsible for their compositions produced on average $[Ba/Eu]=0.89$ and $[Ba/Eu]=0.60$, (which translates into around 400 and 200 times more Ba than Eu) for CEMP-s and CEMP-s/r stars, respectively, and with a spread of a factor of about two in both cases (r~0.6). Unsurprisingly,

---

[1]Carlos Rijs, the fourth author of the paper handled the data and produced the figures.

Table 3.1: Selected key heavy elemental abundance ratios at the stellar surface at the end of the computed evolution for the selected `stars` and `Stromlo` models plotted in Figure 3.2. The masses are indicated in Column 1 (units of $M_\odot$) and the selected values of the partial mixing region M_{PMZ} leading to the formation of the ^{13}C pocket in Column 2 (units of 10^{-3} $M_\odot$) .

M	M_{PMZ}	[Sr/Fe]	[Ba/Fe]	[Eu/Fe]	[Pb/Fe]	[Ba/Sr]	[Ba/Eu]	[Pb/Ba]
				stars				
1.25	2	1.65	1.59	0.69	2.75	-0.06	0.90	1.16
2.0	2	1.34	2.04	1.12	3.03	0.70	0.92	0.99
				Stromlo				
1.0	0^a	1.14	2.05	1.08	2.29	0.91	0.97	0.24
	2	1.10	2.03	1.11	2.46	0.93	0.92	0.43
1.25	2	1.51	2.17	1.08	2.76	0.66	1.09	0.59
2.0	2	1.78	2.42	1.51	3.24	0.64	0.91	0.82
5.0	0	1.67	1.35	0.20	0.63	-0.32	1.15	-0.72
5.5	0^a	1.84	1.54	0.29	0.82	-0.30	1.25	-0.72
	0.1^a	1.76	1.60	0.50	2.49	-0.16	1.10	0.89

^{a}Not plotted in Figure 3.2, but reported here to support the description of the four regimes in the text.

the r-process enhanced stars (black symbols) also display a correlation of around unity and they have a y-intercept [Ba/Eu] of approximately -0.6, corresponding to the solar r-process Ba/Eu ratio of roughly 10.

The [Ba/Eu]=0.89 value of the CEMP-s stars agrees very well with the [Ba/Eu] ratios of around unity typically produced by s-process models (see Table 3.1). In fact, this is the value expected by the s-process at $\sigma_A N_A \simeq$ constant equilibrium[1], where σ_A is the neutron-capture cross section of the isotope of mass A and N_A its s-process abundance. When considering that the neutron-capture cross section of the neutron magic ^{138}Ba is 650 times lower than the neutron-capture cross section of ^{153}Eu, and that the ^{138}Ba solar abundance is $\sim$65 times higher than that of ^{153}Eu, following the relation above and the definition of the square bracket notation, [Ba/Eu] is equal to approximately $\mathrm{Log}_{10}(650/65)$. Instead, the [Ba/Eu] value of CEMP-s/r of $+0.6$ poses a puzzle: it does not agree with any of the AGB models that produce [Ba/Fe] > 1, and it is also very far from the r-process value of -0.6.

3.1.3 Model results

We calculated 17 `stars` and 30 `Stromlo` stellar models of different initial masses and masses of the partial mixing zone leading to the formation of the ^{13}C pocket, of M_{PMZ} (Section 2.3.4). The results are shown here for a selection of these models, as ratios relative to Fe for selected elements (in Table 3.1), and for all (in Figure 3.2) the elements heavier than iron at the stellar surface at the end of each AGB evolutionary sequence[2]. For Table 3.1 I selected three

---

[1]This rule can be applied here as a first approximation because the Eu abundance in s-process conditions follows that of Ba, the element with the magic nucleus ^{138}Ba that precedes it in mass.

[2]Note that the end of the evolution for AGB models is often determined by convergence issues due to the very fast mass loss. While this problem has been discussed at length, for example, by Karakas & Lattanzio
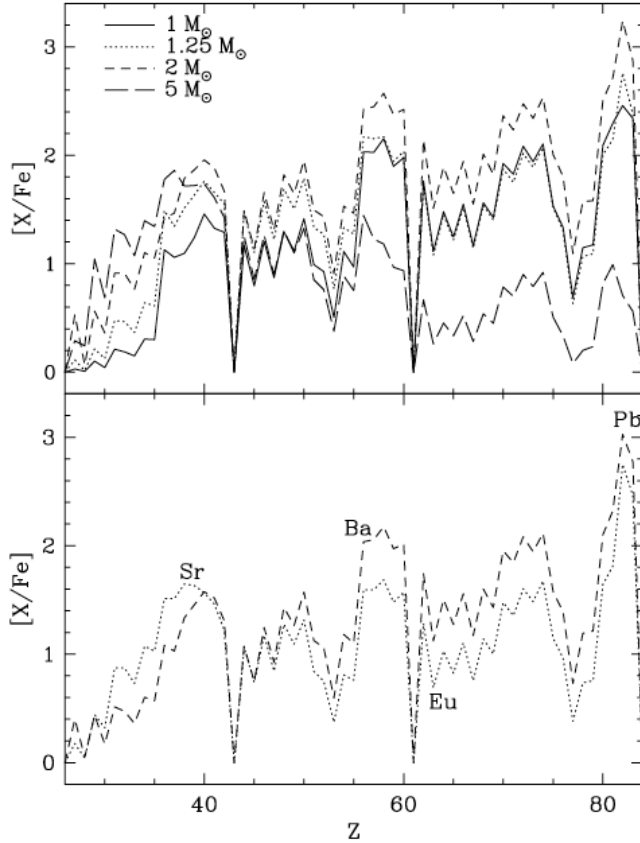
Figure 3.2: [X/Fe] surface ratios after the last computed TDU, as a function of the atomic number (Z), for the elements heavier than Fe, for the selected `Stromlo` (upper panel) and `stars` (lower panel) models listed in Table 3.1. (Figure from Lugaro et al., 2012b, courtesy of Carlos Rijs.)

typical *s*-process elements belonging to the first (Sr), second (Ba), and third (Pb) peaks, as well as the typical *r*-process element Eu. The relative ratios between these elements (e.g., Ba/Eu) illustrate the abundance distributions. The ratios are presented relative to Fe, which is unaffected by AGB nucleosynthesis: it is mildly depleted in the *s*-process regions, as the seed for neutron captures that transmutes into heavier elements, however, this depletion has almost no impact on the high surface abundance of Fe, which reflects the initial composition of the star. The reported ratios illustrate the operation of the possible four regimes of neutron fluxes experienced by AGB stars described below.

Regime 1. The ^{22}Ne neutron source operates inside convective pulses when the temperature at the base of the TP increases above 300 MK, i.e., according to the structure models, when the initial stellar mass is higher than roughly 2 - 2.5 M$_\odot$. The temperature in any case is never high enough to completely burn all the ^{22}Ne, at most its abundance decreases by a factor of 1/3. The free neutrons are released inside the convective pulse (see Figure 1.11) and are distributed over the entire intershell. The number of neutrons per Fe seed is relatively low, which favours the production of the lighter *s*-process elements (e.g., Sr) with respect to the heavier *s*-process elements (e.g., Ba and Pb) and the [Ba/Sr] and [Pb/Ba] ratios are negative (see the 5 and 5.5 M$_\odot$ models). For very short times the neutron density can reach up to peaks above $\simeq 10^{13}$ cm^{-3}, therefore the branching points are affected, for example Kr and Rb (at atomic number 36 and 37,

---

(2003) and van Raai et al. (2012), it does not strongly affect the results presented here as only a very limited number of TDU episodes may have been missed by these models.

respectively) are overproduced, relatively to the s-process first peak elements, due to the activation of the branching points at ^{85}Kr and ^{86}Rb feeding the magic nuclei ^{86}Kr and ^{87}Rb, respectively. The overall distribution remains in any case a typical s-process distribution, with a [Ba/Eu] ratio close to unity.

Regime 2. The ^{13}C neutron source is produced via the inclusion of the pocket (cases with $M_{\mathrm{PMZ}} \neq 0$) and releases neutrons in radiative conditions, as is typical in AGB stars with initial masses between roughly 1.75 and 3 $M_\odot$. In this regime the ^{13}C nuclei burn completely in radiative conditions during the interpulse periods and the neutrons are captured locally in the thin ^{13}C pocket. Overall, the high number of neutrons per Fe seed produces an s-process distribution weighed toward Pb, with [Pb/Ba] ratios in some cases around unity and $0 < $ [Ba/Sr] < 1 (see the 2 $M_\odot$ models). While, as explained in Section 2.3.4, the standard choice here is to not include the ^{13}C pocket in massive AGB models, a test case was run including a small (10^{-4} $M_\odot$) mixing region in the 5.5 $M_\odot$ model to check its potential effect. The main result was a strong increase in the production of Pb, by a factor of $\simeq$50 (see Table 3.1), in agreement with the explanation above that the main feature of the ^{13}C neutron source is the the high number of neutrons per Fe seed. As in Regime 1 described above, efficient activation of the ^{13}C neutron source produces the typical s-process [Ba/Eu] ratios close to unity.

Regime 3. The ^{13}C neutron source is produced via the inclusion of the pocket (cases with $M_{\mathrm{PMZ}} \neq 0$) but, unlike Regime 2 described above, it is ingested in the following convective pulse and releases neutrons in convective conditions. This is because the temperature in the ^{13}C pocket is not high enough to completely burn the ^{13}C before the onset of the following convective pulse. This regime characterises the first two or three ^{13}C pockets in the lowest mass models, such as the two ^{13}C pockets of the 1 $M_\odot$ `Stromlo` model and the first three ^{13}C pockets of the 1.25 $M_\odot$ `Stromlo` model. These ^{13}C pockets are ingested in the following convective pulse still containing a number of ^{13}C nuclei higher than 10^{-4}. These ^{13}C nuclei release the neutrons over material in the whole intershell region and they are mixed with the ^{14}N poison both from the ^{13}C pocket and from the H-burning ashes. Therefore, the overall number of neutrons per Fe seed is lower with respect to the Regime 2, where ^{13}C burns completely in radiative conditions. A main result is that the [Pb/Ba] ratio is lower in these models. Nevertheless, also in Regime 3 the [Ba/Eu] ratio is close to unity.

Regime 4. The ^{13}C neutron source is produced by the ingestion of a small number of protons in the convective pulse (low-mass cases with $M_{\mathrm{PMZ}} = 0$) and releases neutrons in convective conditions, during the first few TPs of models with masses roughly less than 2.5 $M_\odot$. In our models, the convective TP reaches the point in mass where the H mass fraction is 0.01, and the convective region does not split into two separate convective regions after the proton ingestion. This splitting, which is due to the energy released by H burning in the middle of the convective region, has been fund to occur in some studies at lower metallicities than that considered here (e.g. Campbell & Lattanzio, 2008; Cristallo et al., 2009a; Lau et al., 2009; Suda & Fujimoto, 2010). We should treat these cases with much

caution, however, because it is well known that such proton-ingestion events strongly depend on the treatment of convection and of the convective mixing scheme employed, and that one-dimensional models such as those presented here are not well suited to investigate them (Herwig et al., 2014). Furthermore, in the `Stromlo` code convective regions are instantaneously mixed at each iteration, which is not the appropriate method to model situations such as these proton-ingestion episodes when mixing and burning timescales are comparable. In the `stars` code instead a diffusive mixing scheme is used (Eggleton, 1972), which should be able to resolve the splitting of the convective region, if it occurred. Three-dimensional simulations of AGB proton-ingestion episodes suggest that advective mixing (such as that implemented in the `dppns45` code) may be more appropriate than diffusive mixing to describe these processes and that the splitting of the convective TP does not occur (Stancliffe et al., 2011). With these caveats in mind, we find that if proton-ingestion episodes do occur, they can be expected to lead to favourable conditions for s-process nucleosynthesis and to favour the production of the s-process elements lighter than Pb, for the same reasons related to Regime 3 discussed above. For models with mass higher than $\simeq 1.9$ $M_\odot$, the effect of these events is dwarfed by the presence of the ^{13}C pocket. In the lower mass models, instead, the proton-ingestion events alone can result in significant production of s-process elements (see the 1 $M_\odot$ model with $M_{PMZ} = 0$ in Table 3.1) resulting in relatively low [Pb/Ba] ratios and the usual s-process [Ba/Eu] ratio near unity. The final [Ba/Sr] ratio in these low-mass models depends on the detailed features of the proton-ingestion episodes, with ingestion of a smaller number of protons favouring the production of Sr, as well as on the amount of ^{13}C from the pocket that is left over to burn in the following TP (Regime 3). In some `stars` models the final result is a negative [Ba/Sr] ratio.

To summarise, in Figure 3.2, the 5 $M_\odot$ model represents Regime 1, where all neutrons are released by the ^{22}Ne neutron source in the TPs. The 2 $M_\odot$ models represent Regime 2, where most neutrons are released under radiative conditions during the interpulse periods by the ^{13}C neutron source. The `stars` 1.25 $M_\odot$ model represents a case where Regime 2 – i.e., the neutrons released in radiative conditions by the ^{13}C neutron source – primarily determine [Pb/Ba], while [Ba/Sr] is also affected by Regimes 3 and 4 – i.e., the ^{13}C burning convectively. Finally, the `Stromlo` 1 $M_\odot$ and 1.25 $M_\odot$ models also represent a mix of regimes (Regimes 3 and 4) where most of the neutrons are released in the convective TPs by the ^{13}C neutron source. All the other models show behaviours in-between the selected models and are not included in Table 3.1 and Figure 3.2 for the sake of clarity.

To conclude, the four regimes described above are all present in both the `Stromlo` and `stars` models, however, they predominate in slightly different mass ranges. Therefore, the relative distribution of the s-process elements (represented in Table 3.1 by the [Ba/Sr] and [Pb/Ba] ratios) may be different for models of the same stellar mass but calculated with the two different codes (compare, e.g., the distributions from the `Stromlo` and `stars` models of same mass 1.25 $M_\odot$.) The other main difference is that the absolute abundances with respect to Fe, i.e., [X/Fe], are typically smaller in the `stars` results, with respect to the `Stromlo` results, because, as shown in Section 2.2, the `stars` models have a smaller number of TDU episodes. This is the effect of the different implementation of the molecular opacities in the
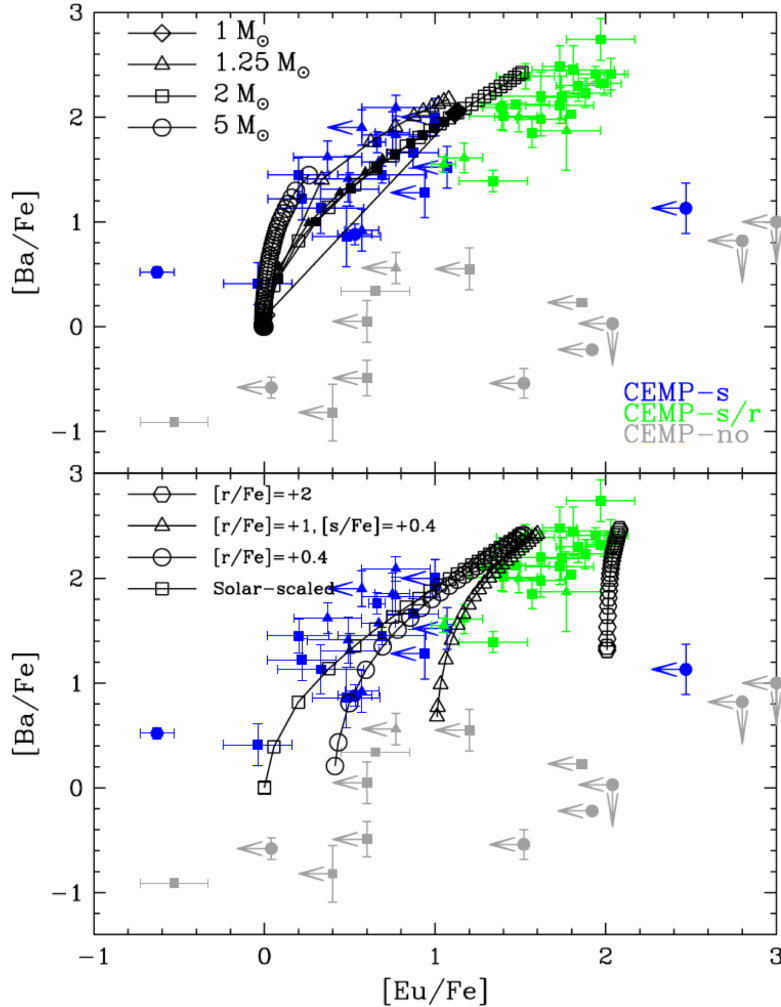
Figure 3.3: Top panel: the CEMP data from Figure 3.1 is plotted together with the selection of our model predictions, where open and black symbols refer to the `Stromlo` and the `stars` models, respectively. The prediction lines represent the evolution of the stellar surface composition of the AGB stars and each symbol on each line represents a TDU episode. Bottom panel: same as the top panel, but with the `Stromlo` models of 2 $M_\odot$ with varied initial enhancements of the s- and r-process elements, with values indicated in the legend. (Figure from Lugaro et al., 2012b, courtesy of Carlos Rijs.)

`stars` codes, which vary with the envelope composition and result in shorter AGB lifetimes than those resulting in the `Stromlo` calculations.

3.1.4 Comparison with the observations

The top panel of Figure 3.3 includes the selection of our model predictions shown in Figure 3.2 together with the CEMP star data shown in Figure 3.1. Note that the prediction lines are not straight because the composition of the s-process material carried from the He intershell to the stellar surface changes with time, and because the variables are shown on a logarithmic scale. For sake of readability, the process of transferring and mixing material from the AGB star onto the companion star, now observed as a CEMP stars, is not plotted in the figure. This process would result in mixing lines located close to the plotted AGB evolution lines and connecting, at each point in time, the AGB composition to the initial composition.

All the models produce both Ba and Eu and the prediction lines closely follow the trend of the CEMP-s group, however, they do not reach the high [Eu/Fe] between 1.5 and 2 observed in many CEMP-s/r stars. One way to resolve this may be to increase the initial [r/Fe] abundance by up to +2 dex, under the assumption that the r-process enrichment was primordial, i.e., it was present in the material from which the stars in the binary system formed. This may be

possible if the molecular clouds where the CEMP-s/r stars formed were polluted by r-process elements from a nearby r-process event. The results of such models, shown as open hexagon symbols in the bottom panel of Figure 3.3, demonstrate that this scenario can provide a solution for the highest measured [Eu/Fe] abundances in CEMP-s/r stars (as discussed in detail by Bisterzo et al., 2011). However, it comes with two major problems (as also pointed out by, e.g., Jonsell et al., 2006; Lugaro et al., 2009): (1) the initial, enhanced [r/Fe] value affects the initial but not the final [Ba/Fe] value, which remains constant, at roughly +2.5 dex in the case plotted in Figure 3.3; therefore, the linear correlation between the Eu and Ba enhancements observed in the CEMP-s/r sample cannot be reproduced. (2) The number of known, strong r-process-enhanced stars ($\simeq$10) is smaller than the number of CEMP-s/r stars ($\simeq$30), therefore it is unlikely that CEMP-s/r stars represent the companions of a subgroup of r-process-enhanced stars in binary systems because in this case CEMP-s/r stars should represent a fraction of r-process-enhanced stars, instead of the other way around. This does not appear to be an observational bias since stellar surveys, such as the Hamburg/ESO R-process-Enhanced Stars, have specifically targeted r-process enhanced stars. Furthermore, the metallicity distribution is different: [Fe/H] is centred at $\simeq -2.5$ for CEMP-s/r stars and at $\simeq -2.8$ for the strong r-process enhanced stars.

Finally, I note from Figure 3.3 that not only do CEMP-s/r stars have more Eu than CEMP-s stars, but they also have, on average, more Ba than CEMP-s stars. The AGB models predict that such enhancements should be accompanied by higher Sr abundances as well. In fact, AGB models produce [Ba/Sr] < 1, whereas, CEMP-s/r have [Ba/Sr] up to $\simeq 2$.

3.1.5 Summary and conclusions

I have presented results for s-process nucleosynthesis from a large set of stellar models at metallicity [Fe/H] $= -2.3$ using two different evolutionary codes. There are four regimes of neutron-capture processes in AGB stars and which regime dominates depends on the initial stellar mass: for the highest mass models the ^{22}Ne neutron source (Regime 1) is dominant; for models of mass < 3.5 M$_\odot$, ^{13}C nuclei are the main neutron source (Regime 2, 3, and 4). For masses $\simeq 2$ M$_\odot$, the ^{13}C nuclei burn in radiative layers in the ^{13}C pocket during the interpulse periods (Regime 2). For lower masses, ^{13}C can also burn in the convective region when the first few ^{13}C pockets are engulfed in the following TPs before ^{13}C is completely burnt during the interpulse period (Regime 3). For the lowest masses, proton-ingestion episodes associated with the first few TPs can also produce ^{13}C, which burns in the convective region inside the TPs (Regime 4). Neutrons released during convective TPs produce lower [Pb/Ba] ratios than neutrons released in the ^{13}C pocket in radiative layers, and also higher [Sr/Ba] ratios, if an even smaller number of protons are ingested. It should be kept in mind that proton-ingestion episodes are extremely sensitive to the adopted convective mixing scheme, and their occurrence and features are very uncertain. The AGB models, especially those with ^{13}C burning in radiative layers, present a very good match to the composition of CEMP-s stars. However, they cannot match the compositions of CEMP-s/r stars, since they cannot produce the observed Eu enhancements up to one order of magnitude higher than in CEMP-s stars. If the s-process and r-process components, making Ba and Eu, respectively, in CEMP-s/r

stars are completely independent, as in the scenario we explored where the r enrichment is primordial, it is difficult to explain why the observed Ba and Eu are correlated, and also why there are more CEMP-s/r than strong r-process-enhanced stars in the halo. Moreover, the models predict [Ba/Sr]<1, while CEMP-s/r stars are relatively more enhanced in Ba, reaching [Ba/Sr] up to 2. In conclusion, to explain the composition of CEMP-s/r stars I invoke the possibility of a different type of neutron-capture process with neutron densities in between the s- and the r-processes.

3.2 Neutron captures in post-AGB stars in the Large and Small Magellanic Clouds

Lugaro et al. 2015, Astronomy & Astrophysics, 583, A77

3.2.1 Motivation

During the past decades, significant information has been gathered on the chemical compositions of post-AGB stars, i.e., in the evolutionary phase following the AGB (Figure 2.9), in the Milky Way. This has led to the discovery of a class of post-AGB stars that have C/O > 1 and display extreme enrichments in the abundances of the elements heavier than Fe produced by the s-process (Reyniers & Van Winckel, 2003; Reyniers et al., 2004; Van Winckel & Reyniers, 2000). It is natural to interpret these post-AGB observations as the signature of the nucleosynthesis and mixing events that occurred during the preceding AGB phase. As discussed in Section 1.3.2, many details of these processes are very uncertain and observations of post-AGB stars can provide strong constraints, particularly since post-AGB stars are hotter than their AGB precursors (Figure 1.9), and therefore their spectral analysis is not disturbed by the presence of molecules, nor by the dynamical pulsations and the strong, dense, dusty winds experienced by AGB stars (see Section 1.3.2).

However, observations of the chemical composition of four low-metallicity ([Fe/H] = 1.15 - 1.34), s-process-rich, C-rich, post-AGB stars in the Large (3 stars) and Small (1 star) Magellanic Clouds (LMC and SMC, respectively) have provided a big challenge (De Smedt et al., 2014, 2012; van Aarle et al., 2013). Since we know the distance of the LMC and SMC, using H-R diagram tracks as those shown in Figure 1.9, it is possible to determine from the observed luminosity that the initial mass of these stars was in the range 1-1.5 M$_\odot$. Stellar AGB models in this range of mass and metallicity produce the high observed abundances of the s-process elements, e.g., 1 < [Zr/Fe] < 2 and 1 < [La/Fe] < 3, if a deeper TDU, than that usually experienced by the models, is assumed to occur after the final TP. However, the models produce values around unity for [Pb/La], while the observed upper limits are [Pb/La]< 0 (De Smedt et al., 2014). Therefore, the question arises: do any possible modifications of the current AGB s-process scenario exist that are able to explain the unexpected neutron-capture abundance patterns observed in these MC post-AGB stars?

3.2 Neutron captures in post-AGB stars in the LMC and SMC

Table 3.2: Properties of the ^{13}C-pocket models and artificial TDU mass (M_{TDU}) imposed to match the [La/Fe] observed in each of the four stars.

	Y_{p}	$M_{\mathrm{PMZ}}(\mathrm{M}_\odot)$		$M_{\mathrm{TDU}}(10^{-3}\,\mathrm{M}_\odot)$		
star name			J004441[a]	J050632	J052043	J053250
pocket_case1	$standard^b$	1.8×10^{-3}	45.3	1.05	3.13	4.16
pocket_case2[c]	$standard^b$	1.0×10^{-3}	3.77	0.18	0.51	0.67
pocket_case3[d]	0.70×10^{-4}	1.8×10^{-3}	87	1.33	4.03	5.40
pocket_case4[d]	1.05×10^{-4}	1.8×10^{-3}	6.04	0.27	0.78	1.02
pocket_case5[d]	1.05×10^{-4}	3.6×10^{-3}	2.76	0.14	0.39	0.50

[a]This is the only star in the SMC, the other three stars are in the LMC. [b]Refers to a proton abundance Y_{p} that decreases exponentially with the mass depth from the envelope value to 10^{-4} at a mass depth M_{PMZ} below the base of the envelope (as described in Section 2.3.4).
[c]A case where I forced the ^{13}C to be ingested in the following TP and burn in convective conditions (Regime 3 of Section 3.1.3) by artificially keeping the temperature below 70 MK in the ^{13}C pocket, which is not enough to activate the ^{13}C(α,n)^{16}O reaction.
[d]A case where I set the proton abundance to a constant. This physically corresponds to assuming some mixing to occur inside the ^{13}C pocket during the interpulse period. This mixing may be due to potential rotational and/or diffusive instabilities as explored, for example, by Battino et al. (2019).

3.2.2 Methodology

The structural evolution of a star of initial mass 1.3 M$_\odot$ and [Fe/H] = 1.3 was calculated by Simon Campbell using the version of the `Stromlo` code updated by Campbell & Lattanzio (2008) to introduce the low-temperature opacities from Lederer & Aringer (2009). No overshoot was applied beyond the border defined by convective neutrality. This resulted in a small number of TDU episodes: five in total following the 8$^{\mathrm{th}}$ to the 12$^{\mathrm{th}}$ TPs, out of a total of 15. The total mass carried to the envelope by TDU is of a few 10^{-3} M$_\odot$ and the last three TPs (13, 14, and 15) occurred after the star had left the AGB track. The evolution of this particular star is plotted in Figure 1.9, which shows that during the 15$^{\mathrm{th}}$ TP the post-AGB star, which had already moved far away from the AGB track, turned around and became a "born-again" AGB star. The stellar evolution model did not experience any proton-ingestion episode of the H-rich envelope (of mass $\simeq 0.002$ M$_\odot$) during this "born-again" phase, as is found in some models in the literature, and explains the existence of H-deficient post-AGB stars (see review by Blöcker, 2001). However, the post-AGB stars considered here do not belong to this category since their H surface abundance is not observed to be depleted. I calculated the s-process nucleosynthesis using `dppns45` with initial abundances from Asplund et al. (2009), scaled to the required [Fe/H], except for O, which was enhanced such that [O/Fe] = +0.4, both in the evolutionary and in the nucleosynthetic calculations[1].

I tested several possible models for the activation of the ^{13}C neutron source[2] using the various free parameters summarised in Table 3.2. I varied the abundance of protons Y_{p} in

---

[1]This initial enhancement is observed in stars in the LMC and SMC and in general in low-metallicity environments, and it is due to the fact that O in the Galaxy originates mostly from massive stars, which have short lifetimes, and is therefore more enhanced at low metallicity relative to Fe, which instead originates from Type Ia supernovae, which have longer lifetimes.
[2]The stellar mass is not high enough to activate the ^{22}Ne neutron source in these stars, see Section 3.1.3).

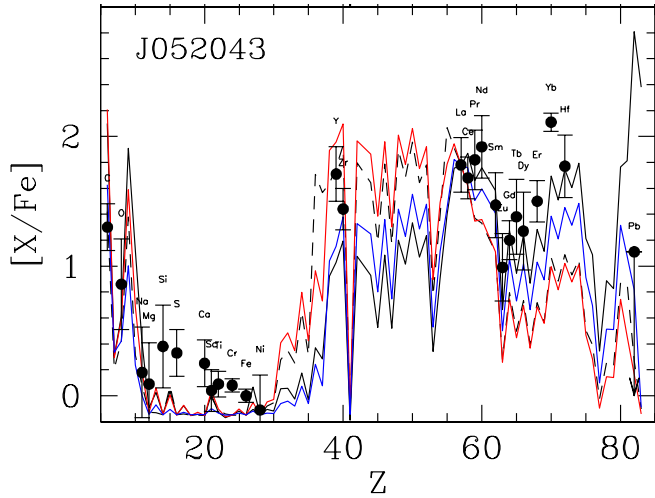## 3.2 Neutron captures in post-AGB stars in the LMC and SMC

Figure 3.4: [X/Fe] ratios as a function of the atomic number Z predicted at the stellar surface by the models listed in Table 3.2, where one ^{13}C pocket is introduced at the end of the TDU episode after the 12th TP, as compared to the LMC post-AGB star J052043. The black solid and dashed lines represents "pocket_case1" and "pocket_case2", respectively. The red and blue lines represent "pocket_case3" and "pocket_case4", respectively. (Figure from Lugaro et al., 2015).

the PMZ leading to the formation of the ^{13}C pocket and its mass extent M_{PMZ}, and the temperature in the pocket, to simulate the ^{13}C burning radiatively or convectively (Regimes 2 and 3 in Section 3.1.3, respectively). Because the amount of TDU calculated by the evolution model does not allow us to match the absolute abundances of the s-process elements observed in these stars, I imposed an artificial final TDU episode with the mass carried to the stellar surface set to the value that allowed me to match the observed [La/Fe] ratio for each star, as reported in Table 3.2. Even if the stellar evolution model experienced 5 TDU episodes, and therefore could have experienced 5 ^{13}C pockets, I only included one ^{13}C pocket, after the last TDU episode (corresponding to the 12th TP). I had to make this choice because when I included more than one ^{13}C pocket it was impossible to match the main constraint, i.e., the observed negative [Pb/La]. With more than one ^{13}C pockets the material is recurrently exposed to several neutron fluxes, which necessarily push the abundance pattern towards Pb and increase the [Pb/La] ratio above zero. For comparison, "pocket_case2" and "pocket_case4" in Table 3.2, represent examples of Regimes 2 and 3, respectively. They have similar neutron exposure of ~0.5 mbarn^{-1}, but, in the ^{13}C pocket radiative case (Regime 3, "pocket_case4") the neutron flux lasts roughly 30000 yr and the neutron density reaches a maximum of 5×10^6 cm^{-3}, while in the ^{13}C pocket convective case (Regime 2, "pocket_case2") the neutron flux lasts only roughly 10 yr and the neutron density reaches a maximum of 2×10^{11} cm^{-3}.

3.2.3   Results

Figure 3.4 shows the comparison[1] between models and observations for the ^{13}C-pocket cases of Table 3.2. The standard "pocket_case1" predicts an elemental pattern very similar to that previously presented by De Smedt et al. (2014), with a Pb abundance almost two orders of magnitude higher than observed. I designed the other three models to decrease the neutron flux and therefore the Pb abundance. While I was successful in this aim, I still found two

---

[1]I normalises both model predictions and observations to meteoritic rather than photospheric solar abundances for the elements heavier than Fe (Asplund et al., 2009). Most importantly, this modifies the observed [Pb/Fe] upper limits reported by De Smedt et al. (2014) by −0.3 dex.

main problems with the comparison between any of the models and the observations: (1) all the four stars show positive [Y/Zr] while all the models predict negative values. I did not pursue this issue further because there may be a systematic error in the observations since the Y abundance is based on a limited number of spectral lines; (2) the models that produce [Pb/Fe] below the observational upper limits, together with [Y/Fe] and [Zr/Fe] reasonably close to the observations, under-produce the observed abundances of the elements between Eu and Pb, such as Dy, Er, Lu, Yb, Hf, and W. The number of lines used to determine the abundances of these elements are limited and often blended, but there is no strong evidence that I should ascribe this general mismatch to observational issues since all the four stars clearly show this problem for several of these elements. For example, the LMC star shown in Figure 3.4 has Pr, Nd, Tb, Er, Yb, and Hf, all clearly above the prediction lines than can match the Pb upper limit.

3.2.4   Discussion and conclusions

The main conclusion of this study is that the major problem (2) reported above cannot be explained by any s-process models because the s-process cannot produce high abundances of the elements from Eu to W together with a Pb deficiency. This follows from the nuclear properties of the nuclei along the s-process path. Once the bottleneck at the nuclei with the magic number of neutrons 82 (^{138}Ba and ^{139}La) is bypassed, the s-process neutron-capture flux proceeds through each isotope to reach the next magic isotope ^{208}Pb, according to its neutron-capture cross section. In other words, the abundance pattern between the magic neutron numbers at Ba and at Pb is almost completely determined by the neutron-capture cross sections of the isotopes involved. These are relatively well known (Bao et al., 2000), and that their values cannot be drastically changed is also demonstrated by the fact that the s-process has no major problems (within 10-20%) in reproducing the solar abundances of the isotopes of the elements between Ba and Pb that are exclusively produced by the s-process, i.e., the s-only nuclei such as ^{154}Gd, ^{160}Dy, and ^{170}Yb (Arlandini et al., 1999; Bisterzo et al., 2010).

I found a similar problem in five out of the nine CEMP-s/r stars for which observations for the elements between Eu and Pb are available. As in the case of the four post-AGB stars, the observed abundances are higher than model predictions, and this is true even if the initial r-process abundances are enhanced (Bisterzo et al., 2011). As I suggested already in Section 3.1.5 for the CEMP-s/r stars, an intermediate neutron-capture process, with neutron densities between the s and the r-process may have also shaped the abundance pattern in the post-AGB stars. To avoid overproduction of Pb, such a process should experience similar neutron exposures as those experienced by the models presented here, however, the neutrons should be distributed among the elements between Eu and Pb differently from the s-process pattern. This may be possible if the neutron density was generally (and not just at the peak) a few orders of magnitude higher than in our models and the overall path of neutron captures was shifted farther away from the valley of β stability than the s-process path.

The fact that all four post-AGB stars of low mass and low metallicity considered here show similar abundance patterns in the elements heavier than Fe suggests that this intermediate

neutron-capture process may be of common occurrence in low-mass AGB stars up to [Fe/H] ~ 1. Since stars in this mass range are common, this conclusion may have important implications for the stellar yields that drive the chemical evolution of stellar clusters and galaxies. Investigation of similarities and differences in the neutron-capture pattern of the CEMP-s/r and post-AGB stars, which sample different metallicity ranges, will provide fundamental constraints to determine the metallicity dependence of the intermediate process and its effect on the chemical evolution of stellar systems.

3.3   Implications and outlook

Follow-up work of the investigations presented in this chapter include the papers by Abate et al. (2015, 2018) (the PhD thesis of Carlo Abate at the University of Nijmegen), where the binary interactions that produced CEMP stars were modelled in more detail and coupled together with the s-process nucleosynthesis yields from Lugaro et al. (2012b). The conclusion of these works was again that the chemical patterns of CEMP-s/r could not be explained by s-process nucleosynthesis only.

As part of her master's thesis at the University of Bonn, and in collaboration with me, Melanie Hampel further studied whether the abundance patterns of CEMP-s/r stars can arise from the nucleosynthesis of an intermediate neutron-capture process (the i process) characterised by neutron densities between those of the s and the r processes. Using nuclear network calculations, we studied neutron capture nucleosynthesis at different constant neutron densities ranging from 10^7 cm^{-3} (typical of the s process) to 10^{15} cm^{-3} (typical of the i process). Comparison to the surface abundances of the sample of 20 CEMP-s/r stars selected already by Carlo Abate demonstrated that our predicted i-process abundances successfully reproduce the observed abundance patterns of the CEMP-s/r stars. Because the i-process models fit the abundances of CEMP-s/r stars so well, we proposed that this class should be renamed as CEMP-i, and this label has now become the standard in the community (Hampel et al., 2016, a paper with more than 20 independent citations within the first two years of publication). In a subsequent work (Hampel et al., 2019), which is part of Melanie Hampel's PhD thesis (at Monash University) we verified that the i-process models can also explain the heavy-element abundance patterns measured in the Magellanic Cloud post-AGB stars, including their puzzlingly low Pb abundances. Furthermore, we found that the lower-metallicity CEMP-i stars ([Fe/H]< -2.5) have heavy-element abundances best matched by models with higher neutron densities and exposures $\tau > 2.0$ mbarn^{-1}, as compared to the higher-metallicity ([Fe/H]$\simeq -1.3$) post-AGB stars, $\tau < 1.3$ mbarn^{-1}), and demonstrated that the responsible process operates on timescales of the order of a few years or less. Proton ingestion episodes leading to the i process may occur in the thermal pulses of AGB stars (Cowan & Rose, 1977) and post-AGB stars (Herwig et al., 2011), but also on the surface of accreting white dwarfs (Denissenkov et al., 2015), in super-AGB stars (Jones et al., 2016) and in more massive stars (Banerjee et al., 2018; Clarkson et al., 2018). It is still unknown which may be the dominant site and at which metallicity.

With the support of the MTA Lendület (LP17/2014) and of the NKFI grant KH_18 130405, I have extended the analysis of the composition of s-process enhanced stars to consider

observational data for stars of higher metallicities than those investigated in this chapter. These are the Ba stars, the companion of AGB stars with [Fe/H] in the range roughly from -0.6 to $+0.3$, i.e., the equivalent of CEMP stars at higher metallicities. A global population analysis of the data previously published by de Castro et al. (2016) for 180 Ba stars allowed our group to determine that stellar metallicity is the main parameter that controls the observed relative abundance distribution of the elements at the first and second peaks made by the s process (Cseh et al., 2018). We are now proceeding with the analysis of a sub-sample of roughly 30 out of these 180 Ba stars, for which a mass determination is also available (Cseh et al. 2021, in prep). The aim is to determine if AGB s-process models of the corresponding mass are successful at matching each of these stars individually, or if the signature of the i process appears also at solar metallicity. For the moment, we have not seen any strong evidence for the need of the i process to match Ba stars.

In the meantime, together with Amanda Karakas and using the `Stromlo` and `dppns45` codes with my nuclear network, we have published further extensions of the Lugaro et al. (2012b) study, which was focused at Z=0.0001 only, and presented extensive sets of s-process stellar AGB yields at different metallicities: Z=0.001 (Fishlock et al., 2014), Z=0.007, 0.014, and 0.03 (Karakas & Lugaro, 2016, a paper with more than 20 independent citations within the first two years of publication), and Z=0.0028 (Karakas et al., 2018). These studies form the base of our paper led by Chiaki Kobayashi that analyses the chemical evolution of the elements from carbon to uranium in the Milky Way Galaxy (Kobayashi et al., 2020, which received 18 independent citations in the first 3 months after publication). The combination of the yields produced by Karakas & Lugaro (2016) and the Ba star analysis of Cseh et al. (2018) are at the basis of the investigations of stardust SiC grains presented in the next chapter.

Chapter 4

Origin of meteoritic stardust from AGB stars

As introduced in Section 2.4.2, a small fraction (of the order of 1-100 parts per million by mass) of the matrix of primitive meteorites is composed of stardust grains. The isotopic composition of these grains can be measured in the laboratory with high precision using various mass spectrometry techniques. Chemistry cannot affect isotopic ratios to the level observed in the grains[1]. Therefore, the measured isotopic composition represents an accurate record of the nuclear reactions that occurred in the deep layers of the parent stars and supernovae of the grains, and of the mixing processes that carried such material to the external regions where dust can form (Lugaro, 2005; Zinner, 2014). In this chapter I begin by addressing specifically the origin of the vast majority (>90%, the "mainstream") of SiC grains (Sections 4.1, 4.2, and 4.3). These grains are believed to come from C-rich AGB stars of metallicity around solar because these stars are the closest match to the isotopic composition of both their light (e.g., C, Ne, Si) and heavy (e.g., Sr, Zr, Ba) elements. Futhermore, SiC dust particles are predicted to form (Dell'Agli et al., 2015; Ferrarotti & Gail, 2006; Nanni et al., 2013) and are observed to be present around AGB stars (e.g., Speck et al., 2005), and the isotopic signatures of mainstream SiC grains qualitatively agree with those expected from nuclear reactions and mixing in these stars (Hoppe & Ott, 1997; Lugaro et al., 2003a, 1999). I investigated both (i) the composition of the elements heavier than iron in the grains and how it compares to AGB models and Ba star observations (Sections 4.1 and 4.2), and (ii) the composition of the main light element Si, which is mostly unaffected by AGB nucleosynthesis and represent the initial composition of the SiC parent star, and how it compares to galactic chemical evolution models and observations of the age-metallicity relation in the solar neighbourhood (Section 4.3). In both cases, I derive strong indications that the majority of the large (roughly μm-sized) SiC grains should have originated from AGB stars of metallicity higher than solar. In Section 4.4, I discuss the origin of a subgroup (the so-called "Group II") of O-rich oxide and silicate stardust minerals, which have the characteristic of a strong deficit in ^{18}O, most likely linked to H burning in AGB stars. The origin of these Group II grains was mysterious, and I have found a new solution where these grains formed around massive AGB stars. This solution is based on a new underground measurement performed at LUNA of the proton-capture reaction

---

[1]Although, see recent work by Robert et al. (2020) on the titanium isotopes.

of the ^{17}O isotope.

4.1 Neutron-capture elements in mainstream SiC grains

Lugaro et al. 2003, The Astrophysical Journal, 593, 486
Lugaro et al. 2014, The Astrophysical Journal, 780, 95
Lugaro et al. 2018, Geochimica et Cosmochimica Acta, 221, 6

4.1.1 Motivation

Mainstream SiC grains show indisputable evidence that the *s* process occurred in their parent stars: isotopes that are produced exclusively or predominantly by the *s* process are enhanced in these grains. For example, SiC grains carry the famous Xe-S component, which shows excesses mostly in the two isotopes of Xe, ^{128}Xe and ^{130}Xe, that can only be produced by the *s* process (Srinivasan & Anders, 1978). Since the 1990s, a large fraction of the meteoritic SiC grain data has been reported in the literature from experiments on stardust isolated by acid dissolution of the Murchison CM2 meteorite, and specifically from the K series extracted by Amari et al. (1994). These authors used a centrifugation method to separate SiC grains of different size ranges; and named the different samples KJA to KJH, in order of increasing grain size (as will be reported and discussed in Table 4.2). The first analyses of the isotopic composition of elements heavier than iron present in SiC grains in trace amounts were possible only on bulk samples, i.e., on large (millions of grains) collections of SiC grains of a given fraction (i.e., size). With the development of Resonant Ionisation Mass Spectrometry (RIMS, Savina et al., 2003; Stephan et al., 2016) it has become possible to analyse with statistical significance the composition of trace elements in single SiC grains. The RIMS high-precision data provide the composition of each AGB parent star of each single grain, rather than the average over a whole population of AGB parent stars as for the bulk analysis. However, only relatively large grains ($> 1\mu$m) contain enough atoms to be analyzed individually via RIMS.

I, and other authors, have used extensively the data provided both from bulk SiC grains via Secondary Ion Mass Spectromery (SIMS, e.g., Ávila et al., 2013b) and from single SiC grains via RIMS (e.g., Liu et al., 2014a,b) to constrain the various features of the modelling of the *s* process in AGB stars. Examples include nuclear reaction cross sections, both neutron-capture cross sections (Lugaro et al., 2003a, 2014a) and neutron source reaction rates, especially the ^{22}Ne$(\alpha,$n$)^{25}$Mg reaction (e.g., Liu et al., 2015; Lugaro et al., 2003a), the mass range of the parent stars of the grains (Lugaro et al., 2003a), and the size of the ^{13}C pocket and the efficiency of the neutron flux within it (Liu et al., 2014a, 2018a; Lugaro et al., 2003a). The Sr, Zr, and Ba isotopic ratios measured in single grains (Liu et al., 2014a,b, 2015) are particularly effective in constraining the neutron flux in the ^{13}C pocket. This is because the isotopic ratios that involve the magic or close-to-magic nuclei, ^{88}Sr, ^{90,91,92}Zr, and ^{138}Ba, essentially depend on the neutron exposure, i.e., the time-integrated total number of free neutrons released in the ^{13}C pocket. This, in turn, obviously depends on the formation and the activation of the ^{13}C neutron source itself.

Lugaro et al. (2003a) investigated AGB stellar models of metallicity around solar and mass in the range for which C>O is achieved at the surface, the condition for the formation of SiC (Section 2.4.2), i.e., around 2-4 $M_\odot$. The result was that these models are able to cover the isotopic spread observed in SiC grains only if a large variety of ^{13}C-pocket mass sizes and ^{13}C abundance profiles is considered (see also Liu et al., 2014a, 2015). One problem is that self-consistent investigations of the effect of the initial stellar mass and metallicity have been so far limited to solar metallicities, i.e., Z=0.014, or 0.02, following Asplund et al. (2009) or the earlier Anders & Grevesse (1989) compilation, respectively. Recent comparisons (Liu et al., 2014a, 2015) have still been made only with models of metallicities only up to Z=0.02, using the FRUITY database (Cristallo et al., 2009b, 2011). The main reason for this lack of analysis was that AGB models of higher metallicity were not yet available. Karakas (2014) published a new set of evolutionary models for metal-rich AGB stars up to Z=0.03 using the `Stromlo` code, and in Karakas & Lugaro (2016) we presented the full s-process nucleosynthesis using `dppns45`. Here, I explore the comparison of predictions from these models to the composition of Ni, Zr, Sr, and Ba in single SiC grains.

4.1.2   Methodology

From Karakas & Lugaro (2016), I selected a subset of models of solar (assuming the most recent Z=0.014 value) and roughly twice-solar (Z=0.03) metallicity that become C-rich. The initial masses range from 2 to 4.5 $M_\odot$ because below 2 $M_\odot$ the TDU is not efficient enough to produce a C-rich envelope, while above roughly 4.5 $M_\odot$ the envelope remains O-rich due to the activation of HBB (see Section 1.3.2).

Table 4.1 reports the main features of interest here for the models I selected. The structure models with Z=0.03 and initial mass 2.5, 2.75, and 3 $M_\odot$ were computed including overshoot at the base of the convective envelope to force enough TDU to make these stars become C-rich. To include overshoot during the TDU the base of the envelope was extended by $N_{\rm ov}$ pressure scale heights (Kamath et al., 2012; Karakas, 2010), using the value reported in the footnotes of Table 4.1 and keeping it constant throughout the entire AGB evolution. When overshoot is included, the lowest calculated initial mass at which an AGB star becomes C-rich at Z=0.03 reduces from 3.25 to 2.5 $M_\odot$. As the stellar mass increases, $T_{\rm TP}^{\rm max}$ increases to above 300 MK for masses larger than $\simeq 3$ $M_\odot$. This effect depends also on the metallicity: for the same initial mass, AGB stars with Z=0.03 are generally cooler than those with Z=0.014 due to the higher opacities, e.g., 324 MK versus 348 MK, respectively, for the 4 $M_\odot$ stars. In relation to the inclusion of the ^{13}C pocket, the standard choice of the $M_{\rm PMZ}$ parameter (as described in Section 2.3.4) is also reported in Table 4.1. In the following, I also comment on the results I obtained by running `dppns45` models with varying $M_{\rm PMZ}$.

4.1.3   Results

In the following subsections I present the comparison between models and data for the four elements: Zr, Sr, Ba, and Ni. The grain data considered here come exclusively from single grain analysis with RIMS, therefore, they are derived from grains of size large enough ($\sim \mu$m)
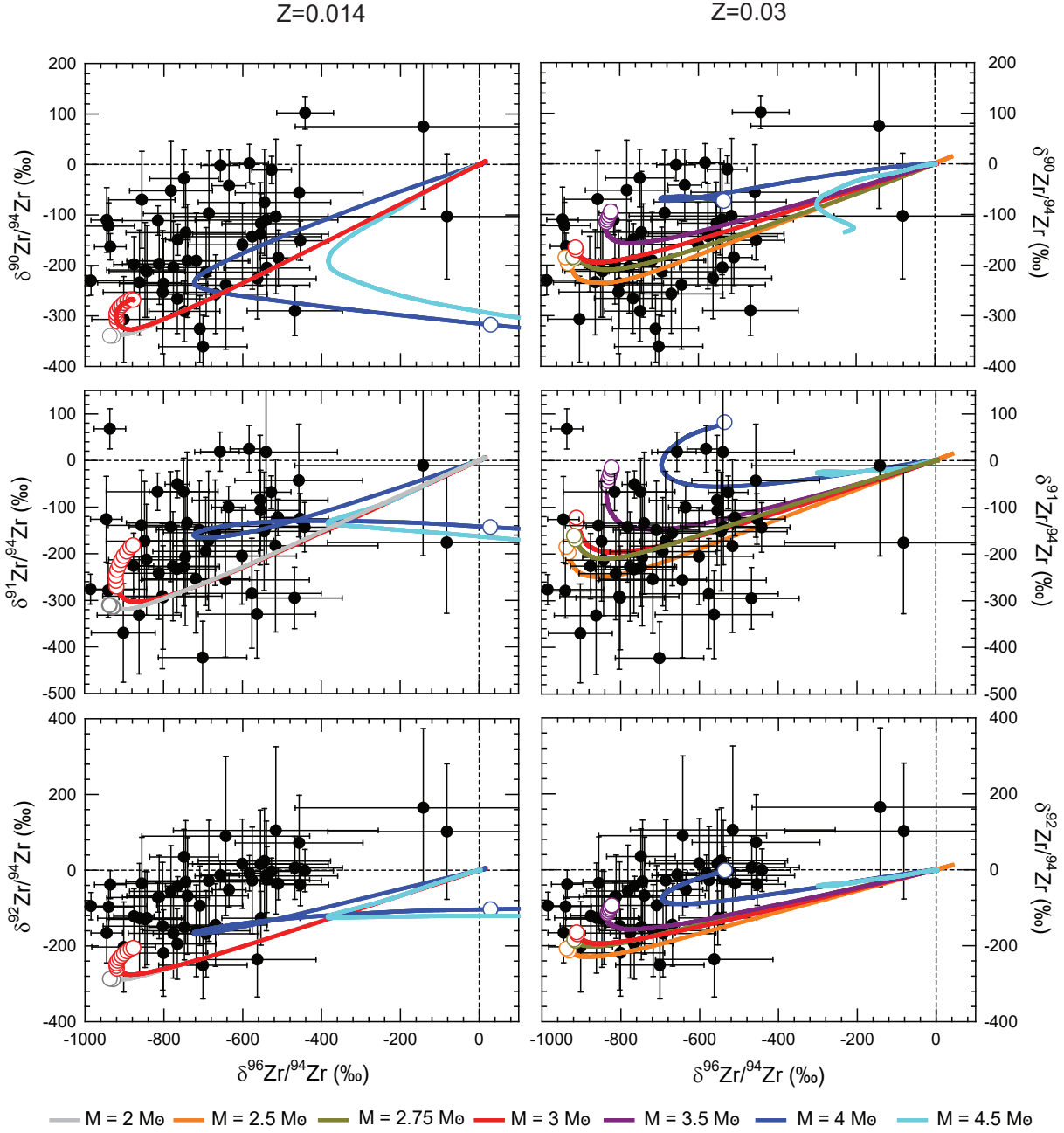
Figure 4.1: The RIMS SiC grain data for Zr (black circles with 2σ error bars, for references see Liu et al., 2014a) are compared to the surface evolution of stellar models of solar metallicity (left panels) and of twice-solar metallicity (right panels) of different masses from 2 to 4.5 $M_\odot$ and the standard choice of the M_{PMZ} parameter (Table 4.1). The dashed lines represent the solar composition, with $\delta = 0$ by definition. Each coloured line represents the evolution of a model of different initial mass and open circles on the lines represent the composition after each TDU when C/O>1 in the envelope. Note that the 4.5 $M_\odot$, Z=0.03 model does not become C-rich but is included in the plot to indicate the trend above 4 $M_\odot$. (Figure from Lugaro et al., 2018a, courtesy of Mária Pető.)

4.1 Neutron-capture elements in mainstream SiC grains

Table 4.1: Selected features of the stellar models calculated by Amanda Karakas of initial mass M reported in Column 1 and composition as indicated by Z (the metallicity) and Y (the He abundance, which increases with metallicity): total number of thermal pulses (No.TP), total mass dredged-up (M_{TDU}), maximum temperature reached during TPs ($T_{\text{TP}}^{\text{max}}$, which controls the activation of the $^{22}\text{Ne}(\alpha,\text{n})^{25}\text{Mg}$ neutron source), number of TPs during which the envelope is C rich (No.TP with C/O>1), final C/O ratio ($(\text{C/O})_{\text{fin}}$), and standard choice of the extension in mass of the partial mixing zone (PMZ) leading to the formation of the ^{13}C pocket in our models (M_{PMZ}, as described in detail in Section 2.3.4).

M($M_\odot$)	No.TP	$M_{\text{TDU}}(M_\odot)$	$T_{\text{TP}}^{\text{max}}$(MK)	No.TP with C/O>1	$(\text{C/O})_{\text{fin}}$	$M_{\text{PMZ}}(M_\odot)$ standard
			Z=0.014, Y=0.28			
2.00	25	0.024	280	2	1.16	2×10^{-3}
3.00	28	0.099	302	10	2.28	2×10^{-3}
4.00	23	0.088	348	8	1.75	1×10^{-3}
4.50	31	0.096	356	1	1.16	1×10^{-4}
			Z=0.03, Y=0.30			
2.50[a]	30	0.060	282	1	1.08	2×10^{-3}
2.75[a]	33	0.073	289	2	1.15	2×10^{-3}
3.00[a]	33	0.071	294	2	1.10	2×10^{-3}
3.50	33	0.112	308	6	1.30	1×10^{-3}
4.00	24	0.083	324	1	1.06	1×10^{-3}
4.50	20	0.040	335	0	0.76	1×10^{-4}

[a]In these models the base of the envelope was artificially extended by N_{ov} = 2.5, 2, and 1 pressure scale heights, respectively, to allow enough TDU to occur for the star to become C rich.

to allow single grains analysis. The isotopic ratios are usually expressed in form of δ values, i.e., per mil variations with respect to the solar ratio, which is zero by definition in δ value (see Section 2.4.3 for the formula). Positive/negative δ values indicate ratios higher/lower than solar and, e.g., $\delta(^{88}\text{Sr}/^{86}\text{Sr})=+500$ means that the measured $^{88}\text{Sr}/^{86}\text{Sr}$ ratio is 1.5 higher than the solar ratio, while $\delta(^{88}\text{Sr}/^{86}\text{Sr})= -500$ means that the measured $^{88}\text{Sr}/^{86}\text{Sr}$ ratio is 0.5 of the solar ratio.

To interpret the model predictions in the discussion below we need to keep in mind the two main effects resulting from increasing the metallicity from solar to twice solar: the higher opacities make the star generally cooler at higher metallicities, and the Fe abundance is obviously twice the solar value. The higher Fe abundance leads to a lower neutron exposure, or equivalently, a lower number of neutrons captured per Fe seed in the ^{13}C pocket. This is also a consequence of the fact that the number of neutrons produced does not vary with the metallicity because the abundance of the ^{13}C neutron source does not depend on the metallicity. It is made, in fact, by the capture of protons initially present in the star by
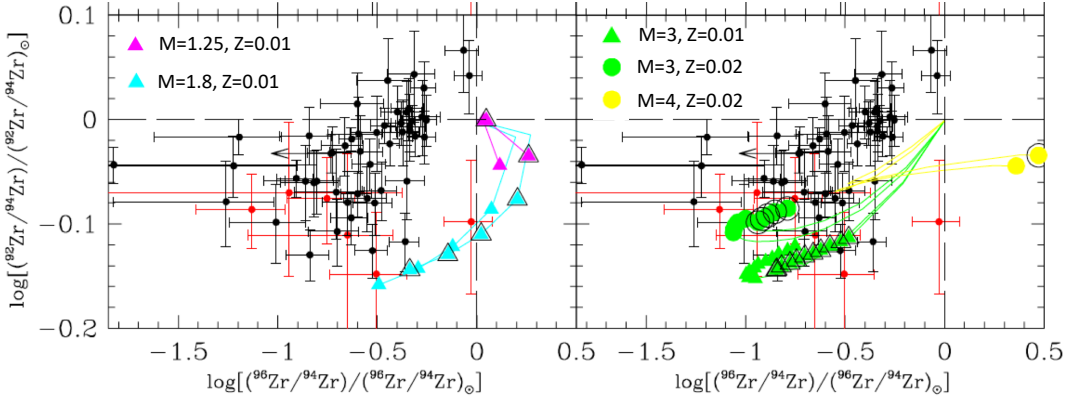
Figure 4.2: Zr isotopic ratios involving ^{92}Zr, ^{94}Zr, and ^{96}Zr measured in single SiC grains (black dots, with 2σ error bars) and in six high-density graphite grains (red dots, also with 2σ error bars from Nicolussi et al., 1998) compared to those predicted by the `Stromlo` AGB models available in 2014, with masses and metallicities as indicated in the labels. The coloured symbols represent the composition at the stellar surface after each TDU episode when C/O > 1. All the models were computed with the standard M_{PMZ} of 0.002 M$_\odot$, but using different cross-section values for the Zr isotopes: from the n_TOF experiments (coloured symbols without the black contour) and from Bao et al. (2000) (coloured symbols with the black contour). Note that, unlike all the other figures in this chapter, here I presented the data, relative to solar, in the $\log_{10}$ notation usually employed in spectroscopic studies, instead of the linear δ-notation. (Figure from Lugaro et al., 2014a).

the ^{12}C produced during He burning, which is relatively constant with metallicity (Clayton, 1988). Therefore, the number of neutron captures per Fe seed decreases with metallicity since there are more Fe nuclei. This number of neutrons captured per Fe seed mostly affects the ratios of isotopes with a magic (^{88}Sr/^{86}Sr and ^{138}Ba/^{136}Ba) or close-to-magic (^{90,91,92}Zr/^{94}Zr) number of neutrons.

Zirconium

As illustrated in Figure 2.5, Zr has 5 stable isotopes, of which 4 are on the main s-process path - at masses 90 (with a magic number of neutrons of 50), 91, 92, and 94; and one is at mass 96, and potentially produced by a branching point at mass 95. ^{94}Zr is the most abundant and therefore is used as the reference isotope for the RIMS analysis. We have then 4 isotopic ratios for which data and models can be plotted against each other, as in Figure 4.1. The left panels of the figure show the predictions for the solar metallicity models and demonstrate two results well known since Lugaro et al. (2003a, 2014a): (1) only stellar models of mass lower than roughly 3 M$_\odot$ can be considered as potential parent stars of the mainstream SiC grains. Higher mass stars are excluded because they experience temperatures up to 360 MK during their TPs (Table 4.1), which are well above the activation temperature of the ^{22}Ne(α,n)^{25}Mg reaction. This results in high neutron densities, which leads to an overproduction of ^{96}Zr relative to the grain data: therefore, the predicted ^{96}Zr/^{94}Zr ratio is higher, rather than lower than solar, as observed in the grains. (2) No models overlap

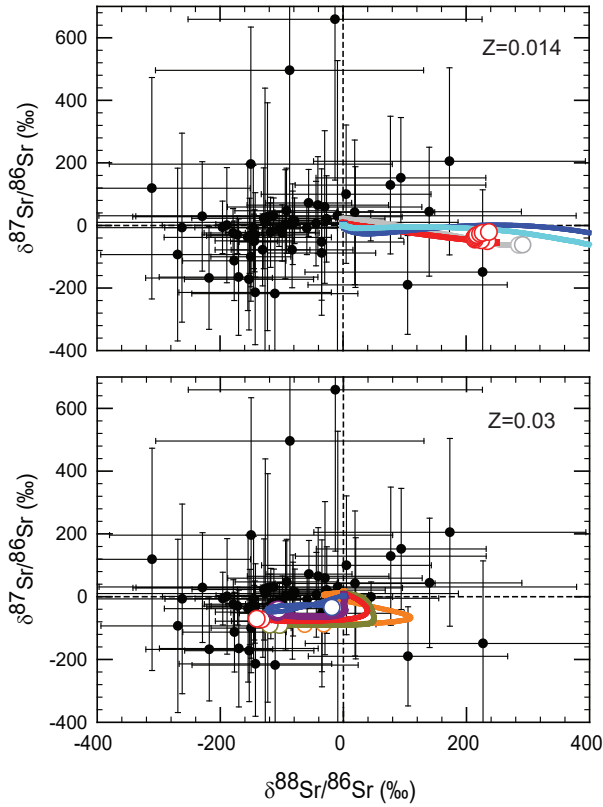**4.1 Neutron-capture elements in mainstream SiC grains**

Figure 4.3: Same as Figure 4.1, for the Sr isotopic ratios and the RIMS SiC grain data from Liu et al. (2015), and with the models of solar and twice-solar metallicity in the upper and lower panels, respectively. (Figure modified from Lugaro et al., 2018a, courtesy of Mária Pető.)

with grains than have ^{90,91,92}Zr/^{94}Zr ratios close to solar. I reported this problem first in 2003 (Lugaro et al., 2003a), where we concluded that a revision of the neutron-capture cross sections of the Zr isotopes was needed to be able to address this mismatch. Such revision was subsequently performed via detailed experiments at the n_TOF facility at CERN, where the cross sections of all the stable Zr isotopes (plus the radioactive ^{93}Zr) were revised (Tagliente et al., 2008a,b, 2010, 2011a,b). In the light of these new results, in 2014, in collaboration with Giuseppe Tagliente, I evaluated the impact of the new rates on the comparison between SiC grain data and AGB models (Lugaro et al., 2014a). The principal result is presented in Figure 4.2: the new cross sections do not significantly change the model predictions and therefore do not help to resolve the problem of the predicted ^{92}Zr/^{94}Zr ratio being too low relative to the SiC grain data distribution. Further experiments performed at JRC-GELINA (Geel, Belgium) confirmed the value of the cross section of ^{92}Zr to be within a few percent of the n_TOF experiment (G. Tagliente, personal communication). In summary, these results eliminated the possibility of attributing the mismatch between models and SiC grain data to the nuclear physics inputs. Note that the cross sections are given with an error bar of 10% at 2σ, which translates roughly into a variation of ± 100 per mil in the δ notation, which is not enough to cover the data (Figure 4.1). In view of this long-standing problem, Liu et al. (2014a) proposed that, to achieve a match between SiC grain data and AGB models, large variations need to be assumed and fined-tuned for both the mass extent and the abundance profiles within the ^{13}C pocket.

The right panels of Figure 4.1 show the predictions for the twice-solar metallicity models. The situation here is very different. Stars of mass < 3.5 M$_\odot$ produce results quite similar

to their solar-metallicity counterparts, however, in contrast to their counterparts at Z=0.014, models of mass between roughly 3 and 4 $M_\odot$ at Z=0.03 are also potentially good candidates to be parent stars of the grains. In fact, stars of initial mass between 3 and 4 $M_\odot$ even provide a good match to the grains showing ^{90,91,92}Zr/^{94}Zr ratios close to solar, which as discussed above are difficult to cover with any models at solar metallicity.

This successful result is a combination of several different effects. First, as mentioned above, the ^{22}Ne(α,n)^{25}Mg reaction is not activated as efficiently at Z=0.03 as at Z=0.014, and therefore the ^{96}Zr/^{94}Zr ratio remains negative even for the 4 $M_\odot$ model, as required to cover the grains. Second, the ^{22}Ne neutron source re-adjusts the ^{92}Zr/^{94}Zr ratio to its equilibrium value, given by the inverse ratio of the neutron-capture rates, at the temperature at which the ^{22}Ne source is activated ($\simeq$300 MK), which is higher than the temperature at which the ^{13}C source is activated ($\simeq$90 MK). The neutron-capture rate of ^{92}Zr is a relatively special case because it decreases as the temperature increases[1]. This decrease results in higher ^{92}Zr/^{94}Zr ratios during the activation of the ^{22}Ne neutron source than during the activation of the ^{13}C neutron source. The fact that the ^{13}C pocket is assumed to be smaller in models of mass larger than roughly 3 $M_\odot$ (Table 4.1) results in a larger relative weight of the ^{22}Ne neutron source on the determination of the final surface abundances. In the case of the ^{92}Zr/^{94}Zr ratio, the final effect is a significantly higher value at the stellar surface. Note that this same temperature effect is also the basis of the alternative solution proposed by Liu et al. (2014a) within lower-mass AGB stars. In contrast to that work, however, I did not fine-tuned the features of the ^{13}C pocket to make it smaller and match the grains data. The fact that the pocket should be smaller for higher masses is an assumption made *a priori*, independently of the grain data. It was based on different considerations and constraints, both theoretical and observational (as discussed in detail in Section 2.3.4) and it later turned out to result in a solution for the grains.

I experimented with varying the extent of the $M_{\rm PMZ}$ in the Z=0.03 models and the effects were not significant, with the main difference being a shift towards the solar values for a smaller $M_{\rm PMZ}$, due to the fact that lower absolute s-process abundances are produced for smaller values of $M_{\rm PMZ}$, which helps to better cover the ^{96}Zr/^{94}Zr data spread.

Strontium

As illustrated in Figure 2.5, Sr has 4 stable isotopes, of which 3 on the main s-process path and are included in my nuclear network - at masses 86, 87, and 88 (with a magic number of neutrons of 50). While the magic ^{88}Sr is the most abundant isotope of Sr, ^{86}Sr and ^{87}Ba are s-only isotopes, which cannot be made by the r process, being shielded by ^{86}Kr and ^{87}Rb, respectively. Therefore, one of them, ^{86}Sr is used as the reference isotope for grain analysis and we have 2 isotopic ratios for which data and models can be plotted against each other, as in Figure 4.3, where solar and twice-solar metallicity models are shown in the top and lower panels, respectively. The effect of decreasing the number of neutrons captured by each Fe seed, when increasing the stellar metallicity, is to lower the ^{88}Sr/^{86}Sr ratios from above

---

[1]Usually neutron-capture rates are relatively constant with the temperature because neutrons do not need the energy required to overcome the Coulomb barrier of the nucleus.
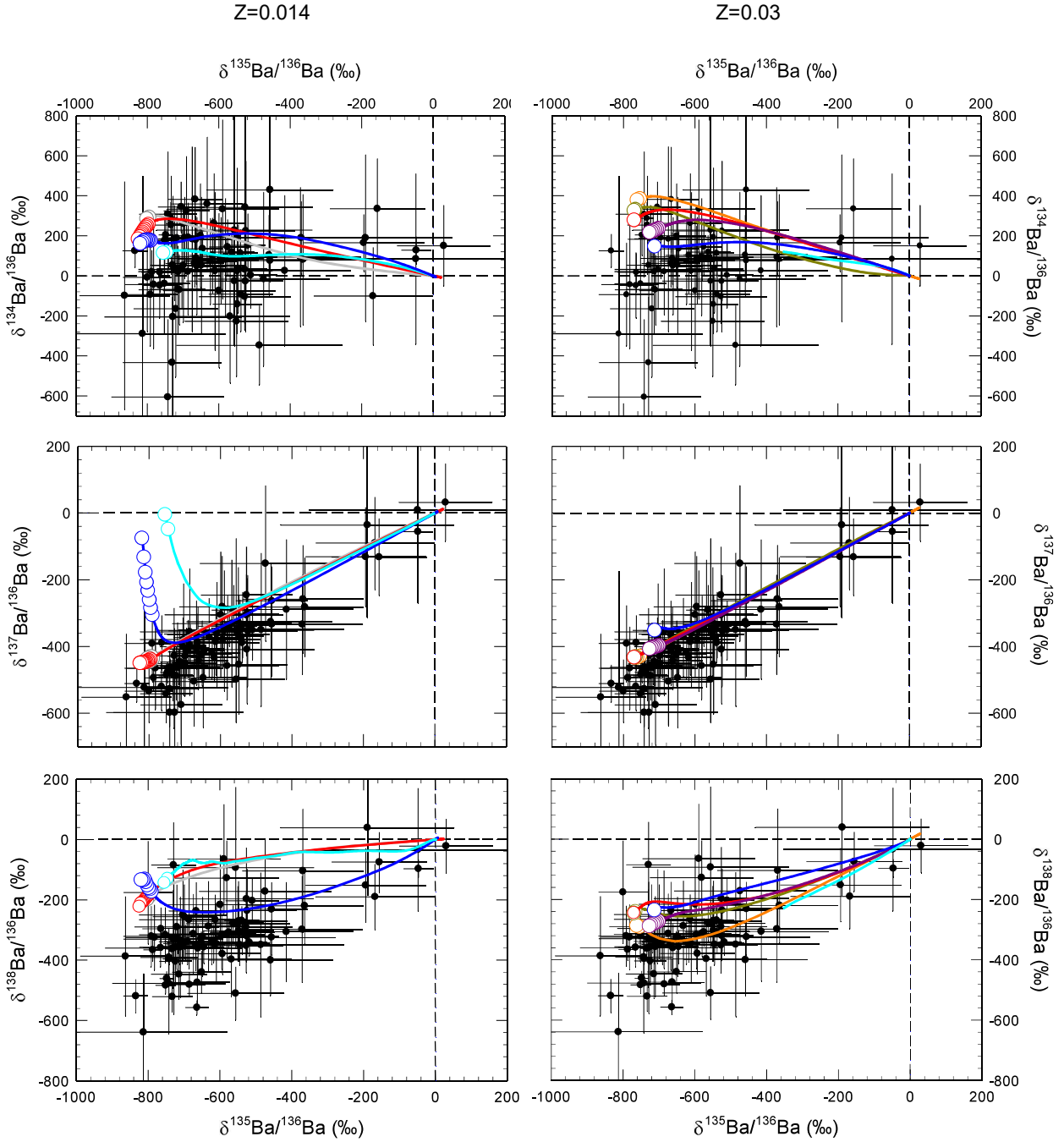
Figure 4.4: Same as Figure 4.1, for the Ba isotopic ratios and the RIMS SiC grain data from Liu et al. (2014b) and Liu et al. (2015). (Figure from Lugaro et al., 2018a, courtesy of Mária Pető.)
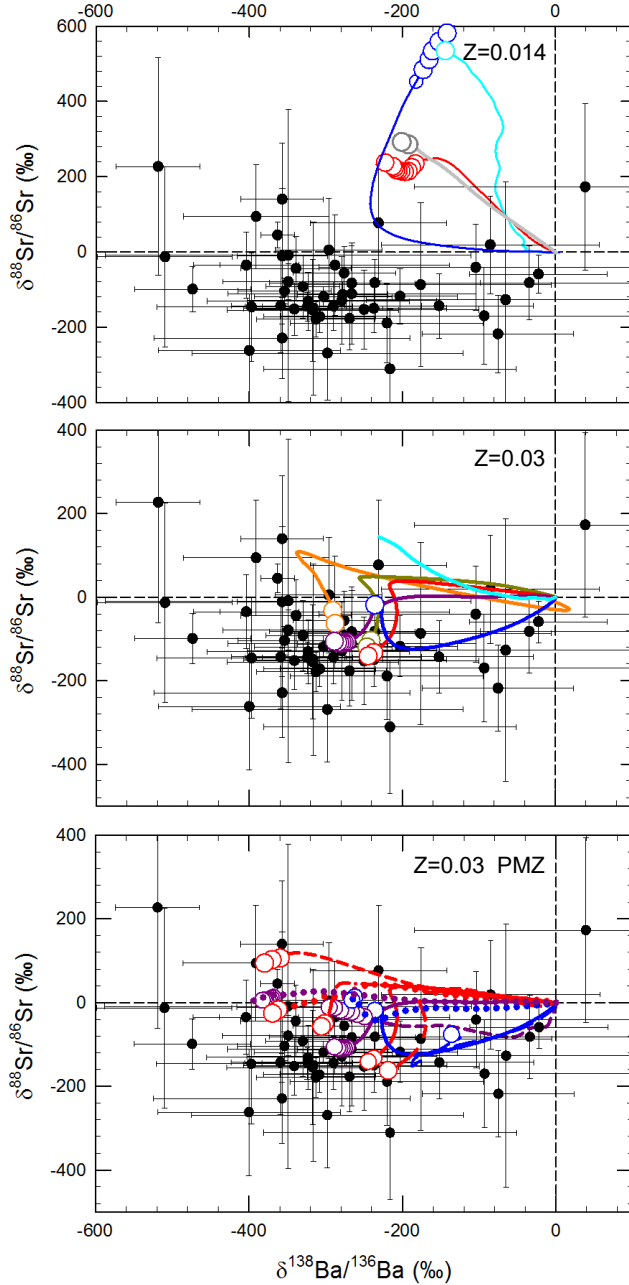
Figure 4.5: Same as Figure 4.3, for the correlated $^{138}Ba/^{136}Ba$ versus $^{88}Sr/^{86}Sr$ ratios (data from Liu et al., 2015, black circles with 2σ error bars and excluding the grains classified as "contaminated"). The lowest panel shows the 3, 3.5, and 4 $M_\odot$ Z=0.03 models calculated with the standard M_{PMZ} (Table 4.1, solid lines) and with other non-standard choices of M_{PMZ} (all in units of $M_\odot$): short-dashed lines for 2×10^{-4} (for the 3 and 3.5 $M_\odot$); dotted lines for 5×10^{-4} (for all three masses); dashed-dotted lines for 1×10^{-3} (for the 3 $M_\odot$); long-dashed lines for 2×10^{-3} (for the 4 $M_\odot$); and long/short-dashed line for 3×10^{-3} (for the 3 $M_\odot$). (Figure from Lugaro et al., 2018a, courtesy of Mária Pető.)

solar (at Z=0.014) to below solar (at Z=0.03), i.e., the corresponding δ values switch from positive to negative. Most of the single grain data present ^{88}Sr/^{86}Sr ratios that are lower than solar, as predicted by the twice-solar metallicity models. Only a small number of grains show ^{88}Sr/^{86}Sr ratios higher than solar, as expected from the solar metallicity models, although the error bars are very large. For the ^{87}Sr/^{86}Sr ratio, mass and metallicity do not play a major role, since this ratio is mostly defined by the local equilibrium abundances controlled by the neutron-capture cross sections of ^{86}Sr and ^{87}Sr. As for Zr, variations in the extent of M_{PMZ} in the Z=0.03 models do not result in major changes for Sr.

Barium

As illustrated in Figure 2.6, Ba has 7 stable isotopes, of which 5 are on the main s-process path and are included in my nuclear network - at masses 134, 135, 136, 137, and 138 (with a magic number of neutrons of 82). While the magic ^{138}Ba is the most abundant isotope of Ba, ^{134}Ba and ^{136}Ba are s-only isotopes, which cannot be made by the r process, being shielded by ^{134}Xe and ^{136}Xe, respectively. Therefore, one of them, ^{136}Ba is used as the reference isotope for grain analysis and we have 4 isotopic ratios for which data and models can be plotted against each other, as in Figure 4.4. The ^{134}Ba/^{136}Ba ratios (top panels) are similar between the solar and twice-solar metallicity models, but they both only cover the grains with ratios higher than solar. The ^{134}Ba/^{136}Ba ratio is controlled by the operation of the branching point at ^{134}Cs and in particular to the temperature dependence of its decay rate into ^{134}Ba. A recent evaluation of this nuclear physics input (based on the nuclear model of Li et al., 2016) resulted in a value lower than that used in the calculations presented here, which leads to a lower abundance of ^{134}Ba and a better match with the grain data (Li, Qi, Lugaro, et al. 2021, submitted to ApJL).

The case of the ^{137}Ba/^{136}Ba ratio is similar to that of the ^{96}Zr/^{94}Zr ratio, where models of mass larger than 3 M$_\odot$ at solar metallicity are excluded as candidates to match the observed ratio because of the activation of the branching points at ^{134,135,136}Cs. This results in an enhanced production of the unstable ^{137}Cs, which decays into ^{137}Ba with a half life of 30 yr. At Z=0.03, instead, all the masses presented in Figure 4.4 are consistent with the data. Finally, as with the case of the ^{88}Sr/^{86}Sr ratio, the lower number of neutrons captured by each Fe seed in stars of twice-solar metallicity decreases the ^{138}Ba/^{136}Ba ratios to the typical values seen in the grains, while the solar metallicity models produce ratios somewhat higher than those observed. Variations in the extent of M_{PMZ} in the Z=0.03 models results in a broadening of the spread in the ^{135}Ba/^{136}Ba ratios, which helps to cover the full set of data. Furthermore, the 3.5 M$_\odot$ model with $M_{\mathrm{PMZ}} = 2 \times 10^{-4}$ M$_\odot$ predicts values of $\delta(^{138}$Ba/^{136}Ba) down to -400, which helps to cover the lower end of the observed range (see also Figure 4.5).

Since Sr and Ba data are available for the same single SiC grains (Liu et al., 2015), I was able to perform a self-consistency check using the observed correlation between the ^{138}Ba/^{136}Ba and ^{88}Sr/^{86}Sr ratios, which are both controlled mainly by the number of neutrons captured by each Fe seed in the ^{13}C pocket. Figure 4.5 confirms the general compatibility of the data with the twice-solar metallicity models, and their general incompatibility with the solar metallicity models. In the lowest panel of Figure 4.5, I show the variations resulting from
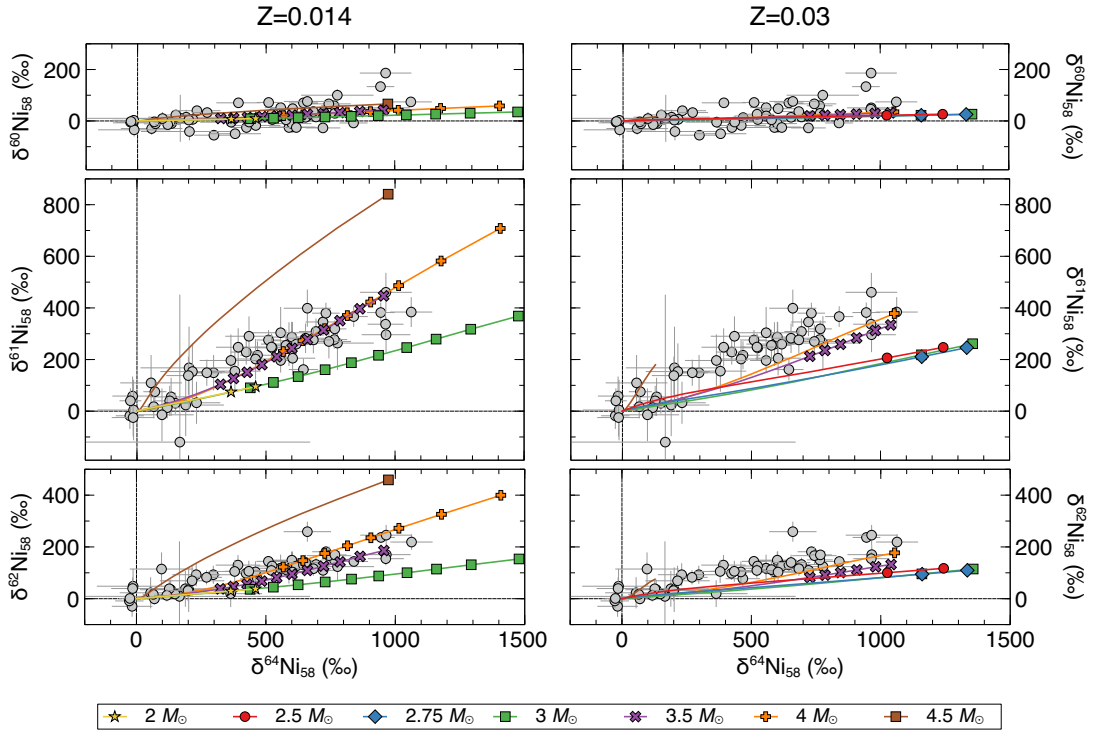
Figure 4.6: Same as Figure 4.1, for the Ni isotopic ratios and the RIMS SiC grain data from Trappitsch et al. (2018) (grey symbols with 2σ error bars). (Figure from Lugaro et al., 2020, courtesy of Reto Trappitsch.)

varying M_{PMZ} in the Z=0.03 models. An interesting trend that requires future investigation is represented by the 3 and 3.5 M$_\odot$ models with the lowest M_{PMZ} values, which predict the $\delta(^{138}\mathrm{Ba}/^{136}\mathrm{Ba})$ decrease to be accompanied by an increase of $\delta(^{88}\mathrm{Sr}/^{86}\mathrm{Sr})$.

Nickel

Nickel is located just above Fe and Co and it is therefore a Fe-peak element not predominantly made by the s process. However, neutron captures can affect its isotopic composition. It has 5 stable isotopes, of which $^{58}\mathrm{Ni}$ is the most abundant and a typical product of explosive nucleosynthesis; together with $^{60}\mathrm{Ni}$, they is not affected by nucleosynthesis in AGB stars. The rare isotopes at masses 61, 62, and 64, instead, can be produced by neutron captures on the abundant $^{58}\mathrm{Ni}$ and $^{60}\mathrm{Ni}$. The SiC grain isotopic ratios are reported relative to $^{58}\mathrm{Ni}$ and the 4 deriving ratios can be plotted against each other, as in Figure 4.6. A match can generally be achieved between data and models both at solar and twice-solar metallicity. For both metallicities, the most massive models (3.5 to 4 M$_\odot$) present the best match, however, the 4 and 4.5 M$_\odot$ models of Z = 0.014 should be excluded because they predict $^{96}\mathrm{Zr}/^{94}\mathrm{Zr}$ ratios higher than solar, instead of lower as seen in the grains (as discussed above, see Figure 4.1). The 3.5 M$_\odot$, Z = 0.014 and the 3.5 and 4 M$_\odot$, Z= 0.03 models provide a possible match to the measured $^{96}\mathrm{Zr}/^{94}\mathrm{Zr}$ ratios, within the nuclear uncertainties. Variations in the extent of M_{PMZ} in the Z=0.03 models result in a broadening of the spread in the $^{64}\mathrm{Ni}/^{58}\mathrm{Ni}$ ratio, which

helps to cover the full set of data[1].

4.1.4   Discussion and conclusions

My comparison of stardust SiC grain data with AGB models shows that AGB models of twice-solar metallicity generally perform better than models of solar metallicity in covering self-consistently the Zr, Sr, Ba, and Ni isotopic ratios observed in the single, relatively large SiC grains measured by the RIMS technique. In particular, these metal-rich models can cover the significant fraction of grains with ^{90,91,92}Zr/^{94}Zr ratios close to solar, together with the observed ^{88}Sr/^{86}Sr and ^{138}Ba/^{136}Ba ratios, and without the need to invoke any specific features of the ^{13}C pocket. Some variations in M_{PMZ} give a better coverage of the data, and this approach is potentially more realistic than keeping M_{PMZ} as a constant given the limitation of our models in this respect, described in Section 2.3.4. From these results the main question arises: is it possible that large meteoritic stardust SiC grains originated in AGB stars on average of twice-solar metallicity? In the next section I answer this question by comparing stardust data to spectroscopic data of Ba stars.

4.2   Origin of μm-sized SiC grains from AGB stars of super-solar metallicity

Lugaro et al. 2020, The Astrophysical Journal, 898, 96

4.2.1   Motivation

As illustrated in the section above, it was recognized early that the vast majority of mainstream SiC grains originate from a population of AGB stars of low mass, typically in the range 1.5 to 4 M$_\odot$ (Lugaro et al., 2003a). However, the exact mass and metallicity range of the AGB parent stars of stardust SiC grains has been so far difficult to determine accurately. In fact, while high-precision data are available for stardust, both in bulk and as single grains, unambiguous identification of their exact AGB origin is hampered by the fact that various uncertainties related to the modelling of stellar physical processes can mimic variations in stellar mass and metallicity. This results in multiple solutions that can be found to match the same observed composition.

These main stellar physics uncertainties include: the treatment of convective mixing in all phases of the evolution, stellar rotation, the rate of the mass loss from the stellar surface, and the mixing processes leading both to the dredge-up of carbon and the *s*-process elements to the stellar surface, and to the production of the ^{13}C pocket, see discussion in, e.g., Battino et al. (2019); Cristallo et al. (2009b); den Hartogh et al. (2019); Karakas & Lugaro (2016); Liu et al. (2018a); Piersanti et al. (2013); Trippella et al. (2016). Therefore, in spite of their outstandingly high precision, isotopic measurements of SiC stardust cannot

---

[1]Note that while Trappitsch et al. (2018) also measured the Fe isotopic ratios, I do not consider them here because they are affected by contamination with material of solar composition.

4.2 Origin of μm-sized SiC grains from AGB stars of super-solar metallicity

yet be used to strongly constrain the uncertainties in stellar modelling. In fact, although in the previous section I presented a good match for the composition of Sr, Zr, Ba, and Ni in SiC grains considering AGB stars of metallicity higher than solar (Z = 0.03) and keeping a basic exponential mixing profile to generate the ^{13}C pockets (Lugaro et al., 2018a), Palmerini et al. (2018) also successfully matched most of the Sr, Zr, and Ba SiC grain data by instead considering solar metallicity models and ^{13}C pockets generated by magnetically-induced mixing. Liu et al. (2018a) demonstrated that using a specific parametrization of the ^{13}C pocket, aimed at modelling the effect of such magnetically-induced mixing, also produces a match to the Ni and Sr data, and Battino et al. (2019) presented yet another possible solution for the Sr data by including some slow diffusive mixing within the ^{13}C pockets. This multiplicity of available solutions illustrates that a variety of hypotheses can cover the grain data and demonstrates that it is not possible to constrain the ^{13}C pockets, or the stellar metallicity, or the mixing processes only by comparing the grain data to the stellar models. However, I note that so far only our `Stromlo/dppns45` AGB models of 3.5-4 M$_\odot$ and $Z = 0.03$ have been able to explain the ^{92}Zr/^{94}Zr values around and larger than solar measured in many mainstream SiC grains without affecting the match to any other isotopic ratios. In any case, a better approach to identifying the parent stars of the SiC grains is provided instead by comparing the stardust data directly to the abundances derived from the spectra of AGB stars and their binary companions, for which we know the stellar mass and metallicity.

Recently, a consistent spectroscopic data set for a large ($\simeq$180) sample of giant barium (Ba) stars, i.e., stars that accreted s-process elements from an AGB companion (see Figure 2.9) has become available (de Castro et al., 2016) with improved calculations of the uncertainties (Cseh et al., 2018). This new data set has already allowed us to determine, for example, that stellar metallicity is the main determinant of the distribution of the elements heavier than Fe in AGB stars and that other effects such as rotation should play a secondary role (Cseh et al., 2018); this is in agreement with inferences we derived by comparing s-process models to asteroseismology observations (den Hartogh et al., 2019). Here, I further exploit the Ba star spectroscopic data to determine more accurately and reliably the origin of stardust SiC grains.

4.2.2   Methodology

My aim is to compare observational data from the spectra of Ba stars to high-precision laboratory analysis of SiC grains. The problem is that the analysis of stellar spectra mostly provides s-process constraints in terms of elemental abundances (e.g., the Ba/Eu ratio discussed in Chapter 3), while analysis of stardust grains mostly provides s-process constraints in terms of isotopic ratios (e.g., the ^{138}Ba/^{136}Ba ratio discussed in Section 4.1.3). This is because elemental abundances in stardust SiC are predominantly controlled by the chemistry of dust formation, rather than by their nucleosynthesis. Therefore, I need to develop a method to relate elemental abundance ratios observed in Ba stars to isotopic ratios measured in SiC grains. I selected two main s-process observable ratios, one related to Ba stars and one related to SiC stardust. The comparison is meaningful because the AGB parent stars of the SiC grains and the Ba-star AGB companions should belong to the same population, in terms

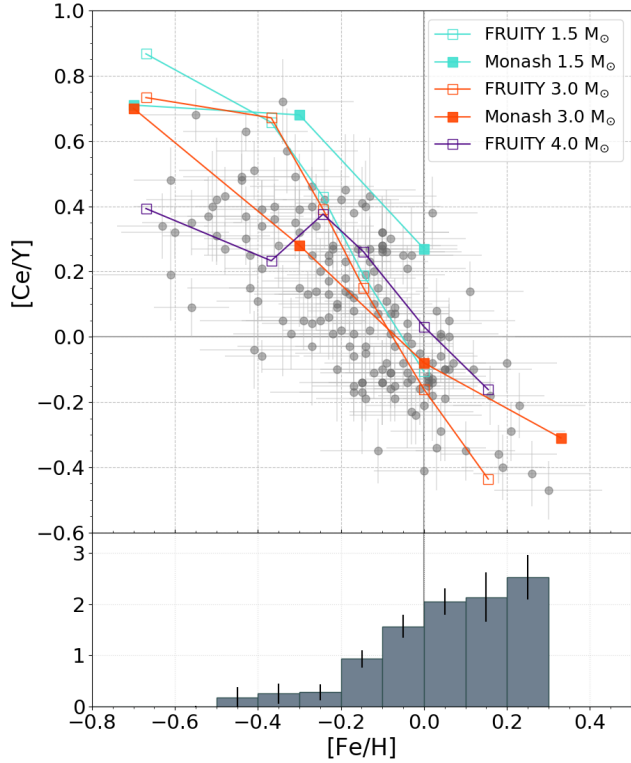## 4.2 Origin of μm-sized SiC grains from AGB stars of super-solar metallicity

Figure 4.7: Upper panel: the [Ce/Y] ratio observed in Ba stars (grey circles) as a function of the metallicity [Fe/H] from Pereira et al. (2011) and de Castro et al. (2016). The coloured lines show the results from a selection of the AGB models presented in Figure 4.8. Lower panel: the distribution of Ba stars with [Ce/Y]<0, represented by the fraction of stars with negative [Ce/Y] in each metallicity bin, divided by the fraction of all the stars in each metallicity bin. The error bars on the bins are calculated by applying the bootstrap method (see Section 4.2.2).(Figure from Lugaro et al., 2020, courtesy of Borbála Cseh and Blanka Világos).

of the mass and metallicity. In fact, the AGB parent stars of the SiC grains correspond to stars born between 5 and 8 Gyr ago, as obtained by summing (i) the age of the Sun of 4.6 Gyr, (ii) the interstellar lifetime of the grains, mostly <0.3 Gyr, occasionally up to 3 Gyr (Heck et al., 2020), and (iii) the lifetime of a star of mass between 1.5 and 4 $M_\odot$, roughly between 0.2 and 3 Gyr. The Ba stars probably represent a younger population since their companion stars are not required to have evolved to the AGB phase before the formation of the Sun, but before today. Their corresponding ages should be roughly between 0.2 and 3 Gyr, plus the time elapsed since the mass transfer event that produced the Ba stars, which is unknown. In any case, the main features (mass and metallicity) of the AGB parent stars of the SiC grains are comparable to those of the Ba star AGB companions because we do not expect major variations in the initial mass function over the past 8 Gyr, nor do we observe major changes in the metallicity distribution, see, e.g., Figure 16 of Casagrande et al. (2011) and Figure 10 of Hayden et al. (2015). Better observations of the age-metallicity relationship in solar-type stars (Nissen et al., 2020) are currently providing a more accurate picture of the solar neighbourhood; the implications of this will be discussed in the outlook Section 4.5.

4.2 Origin of μm-sized SiC grains from AGB stars of super-solar metallicity

The [Ce/Y] ratio in Ba stars

For Ba stars, I consider the [Ce/Y][1] ratio derived from spectroscopic observations because Ce and Y are s-process elements belonging to the s-process second (isotopes with magic number of neutrons 82) and first (magic number of 50) peaks, respectively. This means that their relative abundances are a measure of the number of neutrons captured per Fe seed during the s process (Section 1.3.1). The [Ce/Y] ratios for the large sample of Ba stars from Pereira et al. (2011) and de Castro et al. (2016) are plotted against metallicity in the top panel of Figure 4.7, with metallicities ranging from roughly 1/4 of solar ([Fe/H]$= -0.6$) to twice solar ([Fe/H]$= +0.3$). The [Ce/Y] errors were calculated for all of the sample stars as described in Cseh et al. (2018). Observationally, the main trend of the [Ce/Y] ratio in Ba stars is that it decrease with increasing metallicity. This agrees with the main feature of low-mass AGB s-process models (some examples of which are shown in the top panel of Figure 4.7), which is that the abundance of the main neutron-source nuclei, ^{13}C, does not depend on metallicity, while the abundance of the main neutron-capturing nuclei, ^{56}Fe, obviously increases with increasing metallicity (Clayton, 1988; Gallino et al., 1998). As explained in Section 4.1.3, this results in a decrease of the number of neutrons captured per each Fe seed at higher metallicities, because the number of neutrons produced remains the same (as the number of ^{13}C nuclei) but as Fe increases, for each Fe atom there are fewer neutrons available to capture. Overall, at higher metallicities the final atomic mass reached by the neutron-capture process is lower and it is more difficult to reach the second s-process peak. This leads to higher Sr, Y, and Zr abundances as compared to Ba, La, and Ce. The same trend shown by [Ce/Y] in Figure 4.7 is also shown by other second-peak to first-peak elemental ratios. Here, I decided to use [Ce/Y] because it shows the smallest uncertainty in the observational data (Cseh et al., 2018).

The $\delta(^{88}$Sr$/^{86}$Sr$)$ in stardust SiC grains

For SiC grains, it was noticed, since the first analyses in the 1990s, that the average isotopic composition of several elements vary with the grain size, as shown in Table 4.2. This indicates that nucleosynthetic and dust-growth processes somewhat correlate in AGB stars. In the case of Sr, $\delta(^{88}$Sr$/^{86}$Sr$)$ varies from positive in the small size fractions, to negative in large size fractions (Table 4.2), with an overall variation of 6% (Podosek et al., 2004). RIMS measurements of individual relatively large 1-3 μm SiC grains (typically KJG) are mostly located in the region between -200 and 0 (Liu et al., 2018a, 2015). For $\delta(^{138}$Ba$/^{136}$Ba$)$, also a decreasing trend was found moving from small to large sizes (Table 4.2). Because both $\delta(^{88}$Sr$/^{86}$Sr$)$ and $\delta(^{138}$Ba$/^{136}$Ba$)$ involve a nucleus with a magic number of neutrons it was recognized early that the number of neutrons captured per Fe seed should play a role in such variations, with the parent stars of the larger grains somehow experiencing a lower number of neutrons captured per Fe seed (see also discussion in Gallino et al., 1997; Ott & Begemann, 1990; Zinner et al., 1991). The bulk grain $\delta(^{88}$Sr$/^{86}$Sr$)$ shows more significant variations with respect to the data from single large grains than $\delta(^{138}$Ba$/^{136}$Ba$)$ does: in the large (KJE and

---

[1]As a reminder from Chapters 1 and 3, to express elemental ratios I use the square bracket notation, which represents the $\log_{10}$ of the observed abundance ratios relative to the solar ratio, which is zero by definition.

4.2 Origin of μm-sized SiC grains from AGB stars of super-solar metallicity

Table 4.2: Mass-weighted mean particle size and abundance in parts per million by mass (ppm) for the KJ SiC grain fractions extracted from the Murchison meteorite (Amari et al., 1994) for which data are available for either $\delta(^{29}\text{Si}/^{28}\text{Si})$, $\delta(^{88}\text{Sr}/^{86}\text{Sr})$, and/or $\delta(^{138}\text{Ba}/^{136}\text{Ba})$. (Fractions KJF and KJH also exist but no such data are available.) All the data represent the composition measured by analysing millions of grains together (i.e., in bulk), except in the case of the large (KJG) grains for which data for single grain data are also available. The latter are indicated in italics and in parenthesis as a reminder that they should not be quantitatively compared to the bulk data.

Fraction	Size[a]	Abundance	$\delta(^{29}\text{Si}/^{28}\text{Si})$[b]	$\delta(^{88}\text{Sr}/^{86}\text{Sr})$[c]	$\delta(^{138}\text{Ba}/^{136}\text{Ba})$[e]
	(μm)	(ppm)			
KJA	0.24 - 0.65	0.25	22.2 ± 1.6		
KJB	0.32 - 0.70	1.97	24.6 ± 1.3	20 ± 15	
KJC	0.42 - 1.02	1.11	29.0 ± 2.1	3 ± 14	-319 ± 9
KJD	0.54 - 1.23	1.21	27.0 ± 2.5	-18 ± 18	-321 ± 10
KJE	0.70 - 1.65	0.97	31.8 ± 3.0	-40 ± 15	-348 ± 10
			39.7 ± 3.6[d]		
KJG	2.1 - 4.5	0.36	50.0 ± 5.6	*(0 to -200[f])*	*(-200 to -400[f])*

[a]Observed range containing 90% of the mass (omitting top and bottom 5%). [b]Amari et al. (2000), except where indicated otherwise . [c]s-process component of bulk data (Podosek et al., 2004). [d]Hoppe et al. (1996). [e]s-process component of bulk data (Prombo et al., 1993). [f]Range where the single grain data are concentrated (Liu et al., 2018a).

KJG) grains it is mostly negative both for the bulk and the single grains, while the bulk value of the small grains (KJB) is clearly positive. For $\delta(^{138}\text{Ba}/^{136}\text{Ba})$, instead, the distinction is not as clear because the large (KJG) single grains cover the whole δ range observed in the different grain size fractions from KJC to KJE (Table 4.2).

Therefore, among all the available measured isotopic ratios of elements heavier than iron in SiC grains, I selected the $^{88}\text{Sr}/^{86}\text{Sr}$ ratio because it shows the largest variations both with the grain size (Table 4.2) and in the model predictions (Figure 4.3), where the ratio substantially increases when increasing the number of neutron captures per Fe seed, with its δ moving from negative to positive, like the [Ce/Y] ratio. Increasing the neutron density has also the potential effect of increasing the value of $\delta(^{88}\text{Sr}/^{86}\text{Sr})$ because the branching points at ^{85}Kr and ^{86}Rb can open when the neutron density reaches above 5×10^8 and 10^9 cm^{-3}, respectively, therefore by-passing the production of ^{86}Sr (see, e.g., Bisterzo et al., 2015; van Raai et al., 2012). I will discuss the impact of this secondary effect in the next section.

Translating stardust $\delta(^{88}\text{Sr}/^{86}\text{Sr})$ values into Ba-star [Ce/Y] ratios

To identify which AGB stars, among the companions of the observed Ba stars, the parent stars of the SiC grains, I investigate the correlation between $\delta(^{88}\text{Sr}/^{86}\text{Sr})$ and [Ce/Y] predicted by models of the s process. I consider and discuss both (1) a simple parametric model of the s process with one neutron flux of constant neutron density and (2) more realistic predictions for the surface composition of AGB stars. Both approaches (1) and (2) are necessary: on the one hand, the more general model (1) produces a more robust prediction for the inves-

4.2 Origin of μm-sized SiC grains from AGB stars of super-solar metallicity

tigated correlation because it is not affected by the stellar model uncertainties mentioned in Section 4.2.1. On the other hand, models (2) are much more accurate in describing the complex combination of processes that results in the s-process enrichment in AGB stars (see Section 1.3.2). Figure 4.8 shows all these different models and demonstrates that, while the simple parametric neutron-capture model (1, black line in the figure) cannot produce realistic predictions for the surface composition of AGB stars, it still provide limits within which s-process stellar model predictions (2, coloured lines in the figure) are located. Below, I describe the different models in more detail.

The black line in Figure 4.8 shows the result of a parametric model of s-process nucleosynthesis calculated by Melanie Hampel by feeding a constant neutron density to a nuclear network using the NucNetTools (Meyer, 2012) and the JINA Reaclib database (Cyburt, 2010). (More information and details on these models can be found in Hampel et al., 2019, 2016). The neutron density is a constant in this model, set to 10^7 neutrons cm^{-3}, and the simulation was run for 60,000 yr, which is typical for the neutron flux in the ^{13}C pocket (see left panel of Figure 1.12). If the value of the neutron density was larger, the branching points at ^{85}Kr and ^{86}Rb would activate and $\delta(^{88}$Sr/^{86}Sr$)$ may increase. For example, a model run with a neutron density of 10^8 cm^{-3} produces an increase of the maximum value of $\delta(^{88}$Sr/^{86}Sr$)$ in the top right quadrant of Figure 4.8 up to $\simeq 12,000$. As explained in Section 1.3.2, in models of AGB stars with mass typically higher than 3 M$_\odot$, the activation of the ^{22}Ne(α,n)^{25}Mg reaction during recurrent episodes of He burning may produce a further neutron burst with higher neutron densities than those within the ^{13}C pocket (see right panel of Figure 1.12), potentially activating the branching points at ^{85}Kr and ^{86}Rb and increasing the value of $\delta(^{88}$Sr/^{86}Sr$)$. Because this neutron burst provides a small amount of neutrons and only contributes to the production of the first peak s-process elements[1], it can marginally decrease the [Ce/Y] ratio. Overall, the maximum impact, on each of the points on the black line shown in Figure 4.8, of an additional neutron burst like those produced by the ^{22}Ne neutron source, is represented by an upward shift of +300 to +400 in $\delta(^{88}$Sr/^{86}Sr$)$ and a decrease in [Ce/Y] of at most -0.1 dex (see discussion in Cseh et al., 2018). The temperature and density are set to 0.9×10^8 K and 1000 g/cm^3, respectively, in the parametric simulation, which are also typical for the ^{13}C pocket. These specific choices do not have a significant effect on the final results because the production of neutrons itself (which is temperature and density dependent) is not included in the model, and neutron-capture reaction rates are typically only mildly dependent on the temperature, given that the neutron-capture cross sections are roughly proportional to the inverse of the velocity and the reaction rate is given by the cross section multiplied by the velocity. If the temperature in the model is increased to 1.5×10^8 K there is a minor effect only on the maximum $\delta(^{88}$Sr/^{86}Sr$)$ value, which decreases from 3300 to roughly 2500.

The results from the parametric model described above are controlled almost exclusively by the general properties of neutron-capture cross sections of the isotopes on the s-process path, and specifically by the presence of isotopes with magic numbers of neutrons (see Section 1.3.1). As time passes, more and more neutrons are fed into the network and elements heavier than Fe

---

[1]This is correct for AGB stars of metallicity around solar, which are the best candidate parent stars of the stardust grains, for stars of lower metallicity this neutron burst can also reach the second peak, as discussed in Section 3.1.

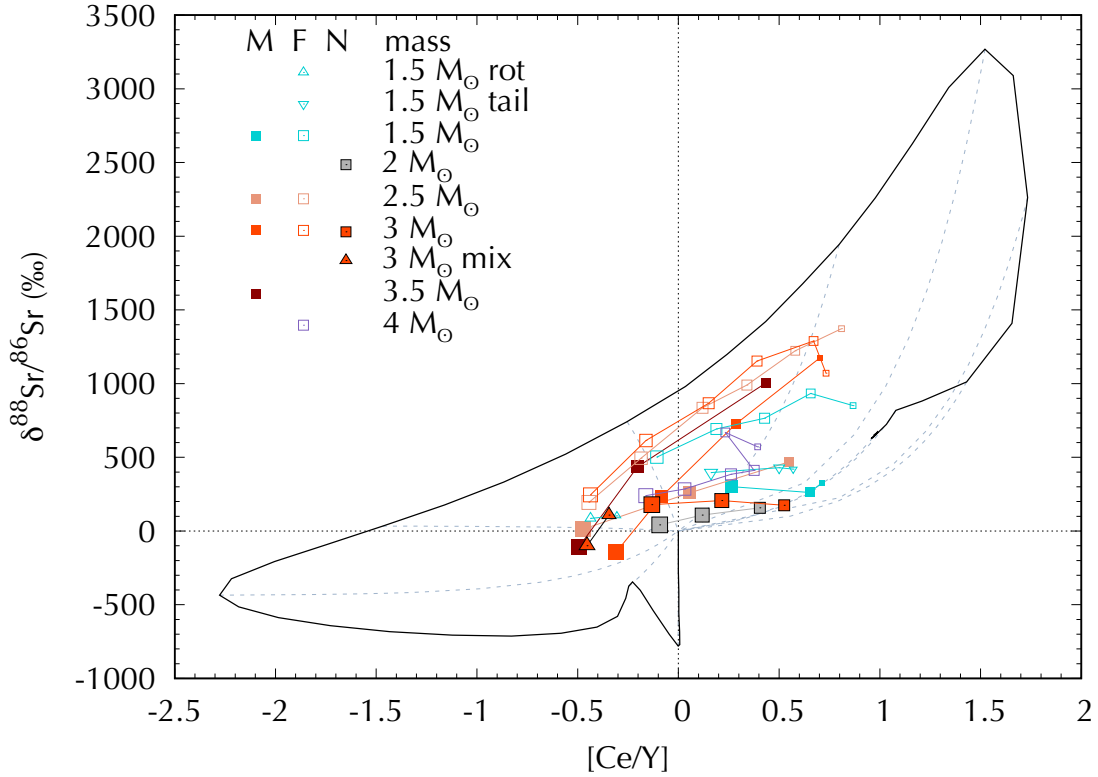## 4.2 Origin of μm-sized SiC grains from AGB stars of super-solar metallicity

Figure 4.8: The black line represents $\delta(^{88}\mathrm{Sr}/^{86}\mathrm{Sr})$ as a function of the [Ce/Y] ratio predicted by a parametric model of neutron captures with initial abundances scaled to solar (the origin in the plot) and neutron density of 10^7 cm^{-3}. The coloured symbols and lines represent the composition of the stellar surface at the end of the evolution from different sets of calculations of AGB stars of different initial masses (see legend). The same symbols of different sizes (connected by the solid, coloured lines) indicate different initial metallicities (in the range listed below for each set of models), with increasing symbol size representing increasing metallicity. As discussed in Section 4.2.2, the general trend is that higher metallicity models typically predict lower [Ce/Y] ratios. The models included are from the FRUITY database (label "F", Z = 0.003 - 0.03 where "rot" refers to models rotating with initial velocity 60 km/s, and "tail" to models calculated with a different mixing profile leading to the formation of the ^{13}C pocket, Cristallo et al., 2015), the `Stromlo/dppns45` codes (label "M" for Monash University, Z = 0.0028 - 0.03 and with the standard extent of the partial mixing zone leading to the formation of the ^{13}C pocket as described in detail in Section 2.3.4), and the NuGrid collaboration (label "N", Z = 0.01 - 0.03, where "mix" represents the case where a constant slow mixing is included inside the ^{13}C pocket, Battino et al., 2019). Several other models were presented by Battino et al. (2019), but they are not included in the figure for sake of clarity as they overlap with the other models. Examples of mixing lines between a selection of points from the parametric model and the solar composition are shown as dashed, grey lines. All the stellar model results are located within such mixing lines. (Figure from Lugaro et al., 2020, courtesy of Borbála Cseh).

82

4.2 Origin of μm-sized SiC grains from AGB stars of super-solar metallicity

are produced. Up to roughly 6000 yr (a neutron exposure $\simeq 0.23$ mbarn^{-1}), the first s-process peak elements, represented by Y, accumulate, since their magic number of neutrons results in relatively small neutron-capture cross sections ($\simeq$ a few mbarn), and [Ce/Y] is negative (bottom left quadrant of Figure 4.8). After this time, the abundance of ^{89}Y (the only stable isotope of Y) becomes large enough that this nucleus also starts capturing neutrons (top left quadrant of Figure 4.8), producing the second-peak elements (e.g., Ce). Eventually, [Ce/Y] becomes positive (top right quadrant of Figure 4.8). When Ce also becomes abundant enough to start capturing neutrons, the flux reaches the third peak at Pb (magic number of neutrons 126) and [Ce/Y] settles on an equilibrium value of roughly +0.8 dex.

At the same time $\delta(^{88}$Sr$/^{86}$Sr$)$ also evolves: it remains negative, together with the [Ce/Y] ratio (bottom left quadrant of Figure 4.8), but becomes positive before the [Ce/Y] ratio does (top left quadrant of Figure 4.8). When the [Ce/Y] ratio reaches zero, $\delta(^{88}$Sr$/^{86}$Sr$)$ is already $\sim +1000$. It reaches a maximum of roughly +3300 and then turns down to settle into the equilibrium value of roughly +600 (top left quadrant of Figure 4.8). The main result is that, during the s process, negative $\delta(^{88}$Sr$/^{86}$Sr$)$ values are always accompanied by negative [Ce/Y], i.e., there are no model predictions in the bottom right quadrant of Figure 4.8. This is simply because the second s-process peak at Ce is populated only after the first s-process peak at Sr, Y, and Zr. In other words, before the flux can proceed to the second peak, ^{88}Sr needs to be overproduced relative to ^{86}Sr, relative to solar. The potential activation of the ^{85}Kr and ^{86}Rb branching points mentioned above does not change this overall conclusion since their only possible effect on the result of Figure 4.8 would be to increase the value of $\delta(^{88}$Sr$/^{86}$Sr$)$.

Examples of predicted final surface compositions from three different sets of AGB stellar models are also shown in Figure 4.8 as coloured lines. Summarising from Section 1.3.2, these models are much more complex and realistic than the parametric model because:

1. The material in the He-rich intershell, where the s process occurs, is not the result of a single episode of neutron captures, but of the combination of many cycles of neutron captures. In fact, a ^{13}C pocket forms as a consequence of each TDU episode, of which there are typically 10-20 for C-rich stars in the low-mass AGB range considered here.

2. A marginal neutron flux can also occur within the recurrent convective instabilities during the episodes of He burning in the intershell due to the activation of the ^{22}Ne reaction. This can also affect the final intershell composition, particularly for the higher range of stellar masses when considering the effect of the neutron density and the related operation of the branching points at ^{85}Kr and ^{86}Rb on the $\delta(^{88}$Sr$/^{86}$Sr$)$ as discussed above.

3. The material from the intershell is recursively carried to the stellar surface by the TDU, and thus is diluted with the envelope material.

As expected, when considering the third point above, the results from the stellar models lie on the intersection of mixing lines connecting the envelope abundances (with a distribution assumed to be close to solar) to the compositions produced by different amounts of neutrons within the parametric models. In other words, the AGB s-process models are constrained

4.2 Origin of μm-sized SiC grains from AGB stars of super-solar metallicity

to lie within the area covered by the "butterfly" shape produced by the parametric neutron-capture model and its mixing lines with solar composition. Only a few of the plotted stellar models reach the region of negative $\delta(^{88}Sr/^{88}Sr)$ observed in the large SiC grains (bottom left quadrant of Figure 4.8): the 3 and 3.5 M$_\odot$ Monash models with $Z = 0.03$ and the 3 M$_\odot$ NuGrid models of $Z = 0.03$ that include slow mixing in the ^{13}C pocket. Several other models with negative $\delta(^{88}Sr/^{88}Sr)$ were presented by Liu et al. (2018a) (from the Torino post-processing code, based on FRANEC code evolutionary calculations, e.g. Bisterzo et al., 2014). These models also have negative [Ce/Y] (Nan Liu, personal communication) and support the results of Figure 4.8.

4.2.3   Results

Overall, the evidence from Figure 4.8 is that the negative $\delta(^{88}Sr/^{86}Sr)$ values observed in the large SiC grains are necessarily accompanied in their parent stars by negative values of [Ce/Y]. Therefore, to identify the parent stars of such grains we need to search for the AGB stars that correspond to the companions of Ba stars with [Ce/Y] less than zero. Actually, this is a very conservative limit because the condition that [Ce/Y] is less than zero is necessary but not sufficient, given that it is possible to find neutron-capture results that show [Ce/Y] less than zero but $\delta(^{88}Sr/^{86}Sr)$ ratios higher than zero (top left quadrant of Figure 4.8).

The bottom panel of Figure 4.7 shows the normalized distribution of the number of Ba stars that show negative [Ce/Y] for the different metallicity bins. Each bin corresponds to a range of 0.1 dex in [Fe/H] and the error bars on each bin were calculated by Borbála Cseh and Blanka Világos using the bootstrap method (Efron, 1979) as follows: 10,000 samples were simulated, with 182 randomly chosen stars for each simulation by applying the so-called "random sampling with replacement" on the whole data of 182 stars. This means that in each simulated sample some stars can appear more than once, while others can be missing. For each selected star, the [Ce/Y] ratio was chosen randomly from a normal distribution with a width corresponding to the error bar of its given [Ce/Y]. Finally, the number of stars was calculated in each metallicity bin for all runs. The final error on the height of a bin is the standard deviation of the 10,000 runs.

The distribution of Ba stars with sub-solar [Ce/Y] ratios, i.e., the candidate parent stars of the large SiC grains, is heavily skewed towards stars of higher-than-solar metallicity, whose companions therefore appear to be the favoured site of formation of the grains with negative $\delta(^{88}Sr/^{86}Sr)$. For example, stars of metallicity from 1.6 to 2 times solar, i.e., [Fe/H]=+0.2 to +0.3, or Z$\simeq$0.02 to 0.03 (using the solar metallicity of 0.014 from Asplund et al., 2009) are roughly 70% more likely to be the parent stars of the large grains than are stars from solar to 25% lower than solar metallicity (i.e., [Fe/H]=−0.1 to 0, or Z$\simeq$0.01 to 0.014); and roughly 2.5 times more likely than stars with metallicity between 60 and 80% of solar (i.e., [Fe/H]=−0.2 to −0.1, or Z$\simeq$0.009 to 0.01). As mentioned above, this estimate is a conservative lower limit because as the number of neutrons captured by each Fe seed increases, $\delta(^{88}Sr/^{86}Sr)$ becomes positive before the [Ce/Y] ratio does (top left quadrant of Figure 4.8). Because both the observational and theoretical [Ce/Y] versus [Fe/H] trends show that the number of neutrons captured per Fe seed increases as the metallicity decreases, it is more likely that stars of

4.2 Origin of μm-sized SiC grains from AGB stars of super-solar metallicity

higher rather than lower metallicity may have a negative [Ce/Y] accompanied by a negative $\delta(^{88}\mathrm{Sr}/^{86}\mathrm{Sr})$, as observed in the large SiC grains.

4.2.4   Discussion and conclusions

In summary, it appears that the larger ($\simeq \mu$m sized) mainstream SiC grains showing negative $\delta(^{88}\mathrm{Sr}/^{86}\mathrm{Sr})$ values should form in AGB stars of higher metallicity than the AGB star sources of the smaller SiC grains showing positive $\delta(^{88}\mathrm{Sr}/^{86}\mathrm{Sr})$ values. Several other lines of evidence related to the origin of stardust of different sizes are discussed below.

1. Barium isotopic data from even larger SiC grains (7-58 μm from the LS + LU fractions of Amari et al., 1994) showing no Ba nucleosynthetic variation (Ávila et al., 2013a) would then follow this trend and originate in AGB stars of even higher metallicity, such that the Ba isotopes remain mostly unaffected by s-process nucleosynthesis. However, they might still show variations in the composition of s-process elements belonging or close to the first s-process peak, e.g., Sr, Zr, and Mo, which have not been yet analysed in these grains.

2. The hypothesis that larger grains should come from more metal-rich AGB stars also predicts that the Si isotopic ratios should present some variations with the grain size not due to nucleosynthetic processes, as for Sr and Ba, but due to galactic chemical evolution models, which predict that $\delta(^{29}\mathrm{Si}/^{28}\mathrm{Si})$ increases with the metallicity (Kobayashi et al., 2011; Lewis et al., 2013; Timmes & Clayton, 1996). Even though heterogeneities in the interstellar medium could somewhat smear out such an increase (Lugaro et al., 1999; Nittler, 2005), the expected trend is observed in the bulk data of SiC in grains of different sizes. These measurements show in fact that $\delta(^{29}\mathrm{Si}/^{28}\mathrm{Si})$ increases with the grain size (Table 4.2). Among the Ti isotopic ratios, the least affected by neutron captures in AGB stars is $\delta(^{47}\mathrm{Ti}/^{48}\mathrm{Ti})$, therefore, this ratio should also carry the signature of the initial composition of the star. While an increase with grain size is observed in the Murchison meteorite size fractions KJA/KJB grains towards the KJF grains, the KJG and KJH grains show a decline, although contamination problems could have affected the data (Amari et al., 2000).

3. In relation to the lighter elements C and N, interesting isotopic trends with grain size are present (Hoppe et al., 1994, 1996), however, they need to be discussed in a separate work because the isotopic compositions of these elements are affected by mixing processes in red giant and AGB stars, some of which are still not well understood (see, e.g. Karakas & Lattanzio, 2014), and N may in some cases be severely affected by terrestrial contamination. The presence of the radioactive nucleus $^{26}\mathrm{Al}$ in SiC grains (Groopman et al., 2015) also needs to be analysed in the light of the different grain sizes together with its production in AGB models of different metallicity. Both the `Stromlo/dppns45` and the FRUITY models predict increasing $^{26}\mathrm{Al}/^{27}\mathrm{Al}$ ratios with increasing stellar metallicity (Cristallo et al., 2011; Karakas & Lugaro, 2016).

4. Disentangling possible trends of metallicity versus grain size from observations of elemental abundances in SiC grains is more difficult than from isotopic ratios because, as mentioned at the start of Section 4.2.2, elemental abundances are also affected by the chemistry of dust condensation around AGB stars of different metallicity (Amari et al., 1995). In any case, available measurements may be in agreement with the metallicity versus size trend proposed here: (i) rare earth elemental abundances measured in bulk KJB grains are in agreement with models of metallicity around solar (Ireland et al., 2018), (ii) larger (KJH) grains contain, in general, lower elemental abundances than smaller grains (Amari et al., 1995, 2000), and (iii) KJH grains with the highest $\delta(^{29}\mathrm{Si}/^{28}\mathrm{Si})$ ratios have also the lowest abundances of Ce relatively to Y (see Figure 3 of Amari et al., 1995).

Now, the main question arises: why should larger grains come from higher-metallicity stars? Actually, we may not expect a large number of low-mass stars of such metallicity to have evolved prior to the formation of the Sun (Cristallo et al., 2020; Gail et al., 2009). A first consideration is that a simple picture of galactic chemical evolution (GCE) where metallicity increases with age is well known to be inaccurate. Observations of large stellar samples show that there is no strong correlation between age and metallicity in the Galaxy. These surveys show that stars with ages between that of the Sun and roughly 8 Gyr have a spread in metallicity from 0.3 to 2.5 solar (Bensby et al., 2014; Hayden et al., 2015; Mishenina et al., 2013). This is currently explained by inhomogeneous GCE models, which predict a large spread in metallicity with age (e.g., Kobayashi & Nakasato, 2011) and/or the effect of stellar migration in the Galaxy (e.g., Spitoni et al., 2015). To compare in more detail the age-metallicity relationship of the parent stars of the SiC grains to that of stars in the solar neighbourhood we can further use the information from the Si isotopic ratios of the grains. I address this independent evidence in the next section.

4.3 Si isotopic anomalies in stardust SiC grains and the age-metallicity relationship of their parent stars

Lugaro et al. 1999, The Astrophysical Journal, 527, 369
Lewis, Lugaro et al., 2013, The Astrophysical Journal Letters, 768, 19

4.3.1 Motivation

Much high-precision Si isotopic data from stardust SiC have been collected in the past 30 years (Figure 4.9); their distribution, however, can not be understood in the framework of AGB nucleosynthesis. This is illustrated in Figure 4.10, which shows the evolution of the Si isotopic ratios in the envelope of AGB of different masses and metallicities calculated by Lugaro et al. (1999) using the Torino models. Nucleosynthesis in low-mass AGB stars of metallicity around solar does not significantly modify the Si isotopic ratios (left panel of Figure 4.10), but, the mainstream grains show instead changes of up to +20%. Nucleosynthesis in AGB stars of higher masses and/or metallicity lower than solar instead can significantly modify the Si
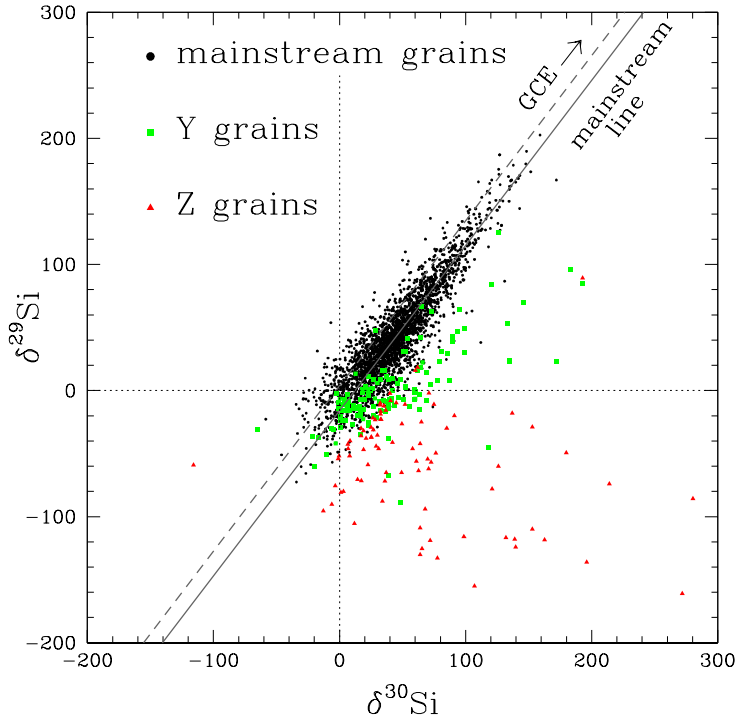
Figure 4.9: Si isotopic compositions (in δ notation) of SiC mainstream, Y, and Z grains with 1σ error bars <15 per mil. The solid black line is the best fit through the mainstream SiC data (the "mainstream line") of slope 1.31 and intercept -15.9 per mil. The dashed line is the mainstream line shifted to the left by 15 per mil in $\delta(^{30}\text{Si}/^{28}\text{Si})$ to pass through the solar ratio, at δ=0 (dotted lines). The shift represents the average contribution of AGB nucleosynthesis to the Si isotopic ratios in the grains, and therefore, the shifted line represents the GCE of the Si isotopic ratios, i.e., the initial composition of the AGB star, with values of δ increasing with the initial metallicity of the star. (Figure from Lewis et al., 2013).
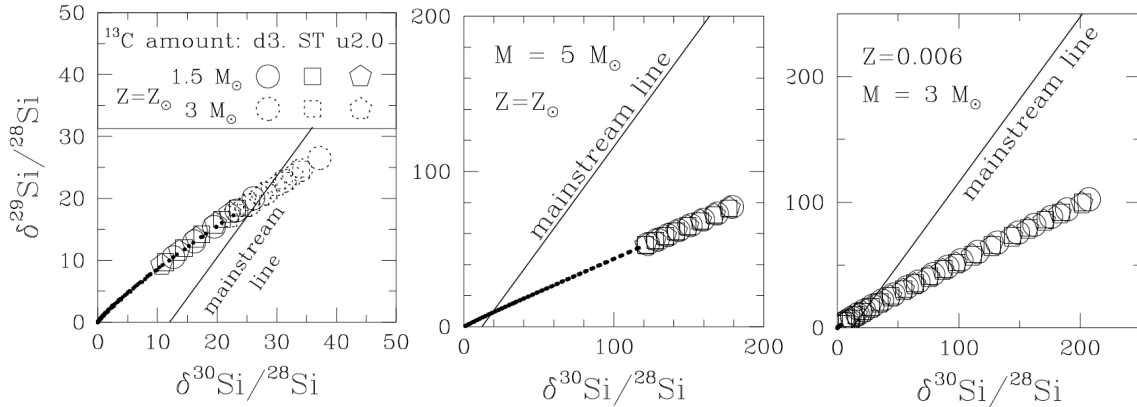

Figure 4.10: Silicon isotopic ratios (plotted as δ-values) predicted by the Torino models for the envelopes of AGB stars of mass 1.5 and 3 M$_\odot$ and metallicity $Z = 0.02$ (left panel), of mass 5 M$_\odot$ and $Z = 0.02$ (middle panel), and of mass 3 M$_\odot$ and $Z = 0.006$ (right panel) for three different choices of the abundance of ^{13}C in the ^{13}C pocket, where the label "ST" stands for the standard choice of Gallino et al. (1998), while "d3." and "u2.0" represent the ST case divided by 3 and multiplied by 2, respectively (see Lugaro et al., 1999, for more details). Each symbol represents the composition after a TDU episode and open symbols are used when the star is C-rich (C>O). In all the panels the correlation line of the mainstream grains (see Figure 4.9) is also indicated as a solid black line. (Figure from Lugaro et al., 1999).

isotopic ratios (middle and right panel of Figure 4.10). However, the changes are not in the direction of the composition of the mainstream grains, where ^{29}Si is more abundant than ^{30}Si, relative to solar (and the slope of the mainstream line in Figure 4.9 is larger than one), but in the direction of the composition of the Y and Z grains, where ^{30}Si is relatively more abundant than ^{29}Si.

As also shown in the Figure 4.10, the Si isotopic ratios are essentially independent of the amount of ^{13}C in the ^{13}C pocket. They are instead mostly affected by the activation of the ^{22}Ne neutron source. This is because the neutron-capture cross sections of the Si isotopes are very small ($\simeq$1-10 mbarn), as compared to those of the elements beyond iron. This means that a large number of Si nuclei needs to be exposed to a neutron flux for its composition to be affected significantly. This can only occur when the whole He-rich intershell is exposed to the ^{22}Ne neutron source during the convective thermal pulse.

The comparison between the predicted Si isotopic ratios to the ratios measured in mainstream grains (Figure 4.9) clearly shows that the mainstream grain Si data cannot be explained by nucleosynthesis in AGB stars of metallicity around solar (left panel of Figure 4.10) since predicted variations are much smaller than observed. As the stellar mass increases (middle panel of Figure 4.10) or the metallicity decreases (right panel), the temperature increases inside the thermal pulses and the ^{22}Ne neutron source becomes more activated, resulting in a more significant production of the neutron-rich isotopes of Si. However, as mentioned above, contrary to what is observed in the mainstream SiC grains, ^{30}Si is always produced more than ^{29}Si, relatively to solar, in AGB models. This is because both isotopes are affected by the ^{28}Si(n,γ)^{29}Si(n,γ)^{30}Si(n,γ)^{31}Si reaction chain, while ^{30}Si is also produced by the ^{32}S(n,γ)^{33}Si(n,α)^{30}Si reaction chain.

Note that I assumed the starting composition of all the models shown in Figure 4.10 to be solar, although in the low metallicity stars (left panel) an initial excess in ^{28}Si relative to ^{29,30}Si would be expected. This is because ^{28}Si is an α-nucleus (i.e., it has a mass equal to an integer multiple of 4, Section 1.2) whose production does not depend on the initial metallicity of the star, unlike ^{29,30}Si. A different initial composition would not significantly change the effect of neutron capture, but, it would shift the whole prediction lines to lower δ-values. This feature make the low-metallicity AGB stars potential good candidates to explain the composition of Y and especially Z grains, which typically lay below and to the right of the mainstream line (Figure 4.9 Amari et al., 2001a; Hoppe et al., 1997; Zinner et al., 2006).

Since AGB nucleosynthesis cannot explain the Si composition of mainstream SiC grains, another effect has been considered that affects the Si isotopic ratios. This is the initial composition of the parent star, where stars of different metallicity and/or ages are expected to have different compositions due to the chemical evolution of the Galaxy (see Figure 1.4). A particularly irksome problem has been that most mainstream grains have ^{29}Si/^{28}Si and ^{30}Si/^{28}Si larger than solar, while according to galactic chemical evolution (GCE) models, the ^{29}Si/^{28}Si and ^{30}Si/^{28}Si ratios increase with metallicity, which, in a simplified picture, increases over time (Timmes & Clayton, 1996). In other words: the conundrum was that since the grains have Si isotopic ratios higher than solar, they must have formed in stars of metallicity higher than solar, however, their parent stars must have died before the Solar System formed. Several possible explanations have been proposed for this apparent paradox, from a simple
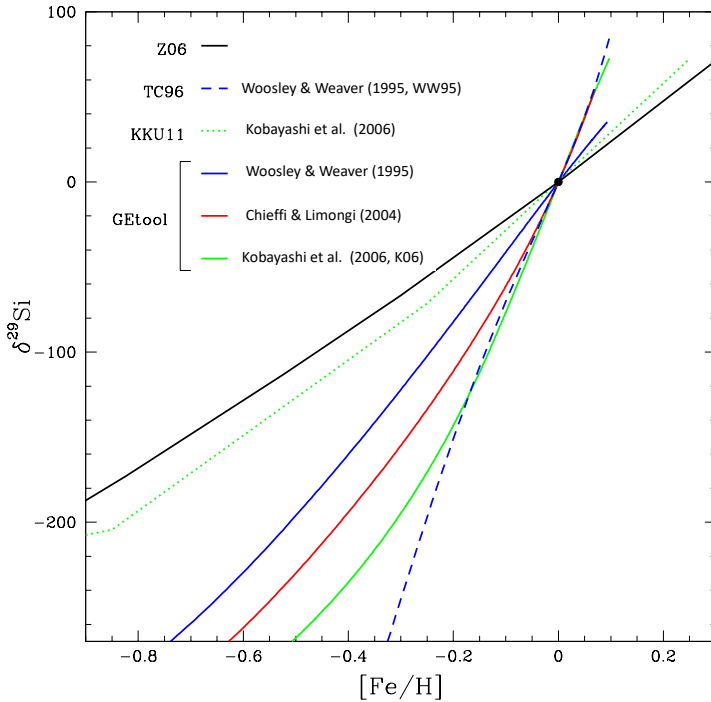
Figure 4.11: $\delta(^{29}Si/^{28}Si)$ (written here simply as $\delta^{29}Si$) versus [Fe/H] predicted from different GCE models: TC96 (Timmes & Clayton, 1996), KKU11 (Kobayashi et al., 2011), and GEtool (Fenner et al., 2003) using the yields from different core-collapse supernova models (the main sources of Si in the Galaxy) indicated on the left of each line in the legend. The black line indicated as Z06 (Zinner et al., 2006) is derived from the simple assumption that $^{29,30}Si$ scale with metallicity, while ^{28}Si is over-produced in lower metallicity stars, in such a way that ^{28}Si is, for example, 1/8 of its solar abundance when the metallicity is 1/10 of solar. (Figure from Lewis et al., 2013) .

model of stellar migration from the inner part of the Galaxy (Clayton & Timmes, 1997), which has some difficulties in reproducing the observed distribution (Nittler & Alexander, 1999), to inhomogeneities in the interstellar medium (Lugaro et al., 1999), which is at odds with the correlation between the Si and Ti isotopic composition of the grains (Nittler, 2005), to a starburst triggered by the merging of our Galaxy with another galaxy (Clayton, 2003).

In summary, the main effect that may explain the Si isotopic composition for mainstream SiC grains is the initial composition of the star due to GCE. In the case of Y and Z grains, both GCE and AGB nucleosynthesis play a role. To resolve these problems and the paradox described above, I combined the SiC grain data with GCE and AGB models to derive the age-metallicity relation (AMR) of the parent stars of the SiC grains, and compared this relation to that of stars observed in large surveys of the solar neighbourhood. In the next section, I explain the methodology I developed to integrate all these sources of information to investigate the origin of SiC grains.

4.3.2 Methodology

I used the measured $^{29}Si/^{28}Si$ and $^{30}Si/^{28}Si$ ratios of SiC grains from AGB stars (Figure 4.9) together with the predicted GCE evolution (Figure 4.11) and AGB nucleosynthesis (Figure 4.10) of the Si isotopes. I selected from the Presolar Grain Database[1] (Hynes & Gyngard, 2009) 2732 mainstream, 133 Y, and 92 Z grains with 1σ error bars lower than 1.5%. I used their $\delta(^{29}Si/^{28}Si)$ to infer the initial composition of the star (the [Fe/H], Step 1 below) and $\delta(^{30}Si/^{28}Si)$ – which is more affected than $\delta(^{30}Si/^{28}Si)$ by neutron-captures in AGB stars – to

---

[1]https://presolar.physics.wustl.edu/presolar-grain-database/

infer the mass of the AGB parent star (and therefore the age, Step 3 below) via the effect of AGB nucleosynthesis (Step 4 below). I conceptualised the following steps, to be applied to each grains, and Karen Lewis computed them [1].

1. The metallicity [Fe/H] (as usual defined as the logarithm of the Fe/H ratio, with respect to solar) of the parent star of each SiC grain is inferred from the relationship between $\delta(^{29}\text{Si}/^{28}\text{Si})$ and [Fe/H] predicted by the different GCE models shown in Figure 4.11, with the GEtool models calculated by Brad Gibson and Kate Pilkington. All the models were renormalized so that at the time of the formation of the Sun, 8.5 Gyr in these models of the Galaxy, [Fe/H] = 0 and $\delta(^{29}\text{Si}/^{28}\text{Si})=0$, by definition. Before renormalization, all the models predict $\delta(^{29}\text{Si}/^{28}\text{Si})$ between -600 and -400 at [Fe/H] = 0, a long-standing problem probably related to the rates of the nuclear reactions that produce ^{29}Si in core-collapse supernovae (Hoppe et al., 2009).

2. The change in $\delta(^{30}\text{Si}/^{28}\text{Si})$ resulting from AGB nucleosynthesis is estimated as the distance $\Delta(^{30}\text{Si}/^{28}\text{Si})$ between the measured $\delta(^{30}\text{Si}/^{28}\text{Si})$ and the value obtained from the GCE line at the corresponding $\delta(^{29}\text{Si}/^{28}\text{Si})$. The GCE line is shown in Figure 4.9 and is obtained by forcing the mainstream line to pass through the solar composition. This shifted line is in agreement with the Si composition of stardust silicate grains from AGB stars, which represents the Si composition of O-rich AGB stars and is less altered by nucleosynthesis and dredge-up than the Si composition of SiC grains from C-rich AGB stars (Mostefaoui & Hoppe, 2004; Nguyen et al., 2010).

3. The age of each parent star is derived from its mass as obtained from $\Delta(^{30}\text{Si}/^{28}\text{Si})$ using the set of Torino C-rich AGB models presented in Zinner et al. (2006)[2] with the neutron-capture cross sections of the Si isotopes by Guber et al. (2003). To the age of the parent star we added the age of the Sun. In the Torino models the mass-loss rate was included using the parametrisation given by Reimers (1975). For the 1.5 and 2 $M_\odot$ models, results were presented for different values of the associated free parameter $\eta = 0.1$, 0.3, 0.5, and I choose to average the results for each mass. A range of $\Delta(^{30}\text{Si}/^{28}\text{Si})$ is allowed during the C-rich phase of each model since $\Delta(^{30}\text{Si}/^{28}\text{Si})$ increases with the number of TDU episodes. This results in different possible initial stellar masses associated to the same $\Delta(^{30}\text{Si}/^{28}\text{Si})$, especially when its value is small. We chose to remove this degeneracy by taking as the best representative of each model the Si composition reported after the last computed TDU episode. Most SiC grains probably formed after the final few TDUs since the largest fraction of the envelope mass is lost in the final phases. I did not include in the age determination the grain residence time in the interstellar medium, which is up to a few Gyr, but typically <300 Myr (Gyngard et al., 2009; Heck et al., 2020), while the age of the Sun was of course included since the parent stars of the grains died before the Sun was born.

---

[1]As stated in the acknowledgements of Lewis et al. (2013) "The first two authors have equally contributed to this paper."

[2]I did not use the `Stromlo/dppns45` models because the extensive sets of yields mentioned in Section 3.3 were not published yet at the time of this work. Note that one main difference between the `Stromlo/dppns45` and the Torino/FRANEC results is that at solar metallicity, stars of 5 $M_\odot$ do not become C-rich in the former set models, due to the activation of HBB, while in the latter set HBB only appears at higher masses.
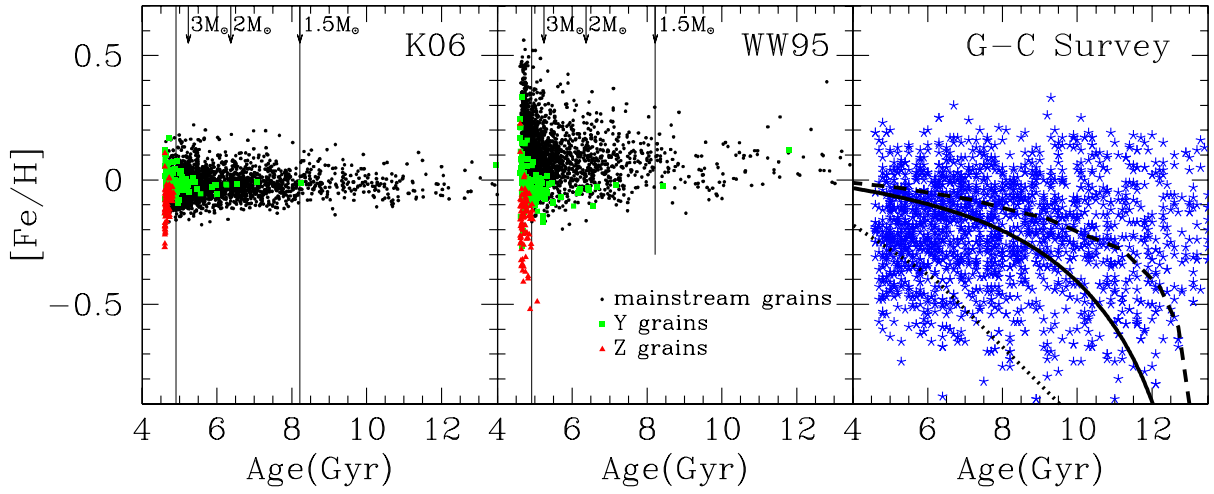
Figure 4.12: AMR derived for the parent stars of SiC mainstream, Y, and Z grains using GEtool results with the K06 (left panel) and WW95 (middle panel) supernova yields. All the plotted ages are lower limits. Indicative expected age range of the parent stars of the grains, corresponding to initial masses between 1.5 and 4 M$_\odot$, are shown as vertical thin black lines, with the mass values indicated at the top of the panels. The right panel shows the AMR obtained from the Geneva-Copenhagen (G-C) survey for 2037 stars in the solar neighbourhood with age uncertainties lower than 25%, compared to the AMRs predicted by the different GCE models: GEtool (solid line); TC96 (dashed line); and KKU11 (dotted line). (Figure from Lewis et al., 2013, courtesy of Karen Lewis.)

4. Since also $\delta(^{29}Si/^{28}Si)$ can be marginally affected by AGB nucleosynthesis, we improved the estimates of age and metallicity by repeating the procedure above with a new initial $\delta(^{29}Si/^{28}Si)_{new} = \delta(^{29}Si/^{28}Si)$ - $\Delta(^{29}Si/^{28}Si)$, with $\Delta(^{29}Si/^{28}Si)$ derived from the same AGB model predictions used to match $\Delta(^{30}Si/^{28}Si)$.

4.3.3 Results and discussion

The age-metallicity relationship (AMR) of the parent stars of SiC grains

The SiC AMR resulting from our method is plotted in Figure 4.12 together with the AMR derived for stars in the solar neighbourhood from the Geneva-Copenhagen (G-C) survey (Holmberg et al., 2007). The latter was updated by Casagrande et al. (2011) (see their Figure 16), but the large metallicity spread present at most ages remained similar. Only AGB stars in the initial mass range between roughly 1.5 M$_\odot$ and 4 M$_\odot$ are expected to become C-rich and therefore produce SiC grains (Gail et al., 2009; Groenewegen et al., 1995), with the lower limit of this range recently being more accurately determined by Marigo et al. (2020) to be around 1.65 M$_\odot$. This mass range corresponds to ages as reported in Figure 4.12 from around the age of the Sun to 8 Gyr.

The [Fe/H] distribution of the SiC grains is determined by the steepness of the $\delta(^{29}Si/^{28}Si)$ versus [Fe/H] relationship, which varies with the choice of the core-collapse supernova yields and the GCE model (Figure 4.11). In Figure 4.12 we plot the two SiC AMRs obtained using the most and the least steep $\delta(^{29}Si/^{28}Si)$ versus [Fe/H] relationships from the GEtool

simulations. As a consistency check, in the right panel of Figure 4.12 the AMRs predicted by the different GCE models are compared to the G-C stars. None of the models can fully recover the observed AMR. A better match may be found by recent models that consider dynamics together with the chemical evolution in the Galaxy (Kobayashi & Nakasato, 2011; Pilkington et al., 2012). Scattering and radial migration must have played an important role in determining the properties of stars in the solar neighbourhood (as predicted by Clayton & Timmes, 1997, in relation to SiC grains) and this is supported by observational studies (Boeche et al., 2013; Mishenina et al., 2019; Ramírez et al., 2013). Stellar migration can significantly effect the AMR in the solar neighbourhood as, for example, stars can migrate outward from the inner parts of the Galaxy, which are more metal rich (Spitoni et al., 2015). However, GCE models including migration have not been extended yet to include the evolution of isotopic abundances. Overall, the SiC grain data confirm the result of the G-C survey that stars exist with ages older than the Sun and metallicities higher than the Sun.

The SiC grain ages calculated via the method described above are affected by several uncertainties. First, there are uncertainties related to the measurement error bars. We have made the conservative choice to plot the lower limits of the ages derived from adding the experimental 2σ error bar to $\delta(^{30}\text{Si}/^{28}\text{Si})$. The upper limits of the ages are either undetermined, because of negative $\Delta(^{30}\text{Si}/^{28}\text{Si})$, or >13 Gyr, the age of the Universe, for 54% and 26% of the mainstream grains, respectively. Instead, they are <6 Gyr for 86% of the Z grains. Second, there are errors related to the possible effect of inhomogeneities in the interstellar medium, which may change the Si composition of any given parent star by $\delta \simeq \pm 50$ (Lugaro et al., 1999; Nittler, 2005) not explicitly included in our method. If we assume that they are distributed symmetrically, then the age and the metallicity calculated for the grains at the peak of the distribution should be reliable. Third, there are systematic uncertainties related to both the choice of the line taken to represent the GCE in the Si isotope plot (Figure 4.9) and the AGB model predictions. for example, the GCE line could be shifted further away from the mainstream line than what I have done here, and still be in agreement with the silicate data. In this case higher masses would be needed to reproduce the same $\Delta(^{30}\text{Si}/^{28}\text{Si})$ resulting in shorter ages. Instead, it is not known if the uncertainty related to the AGB models would result in smaller or larger stellar ages since both larger and smaller $\Delta(^{30}\text{Si}/^{28}\text{Si})$, for a given stellar mass, are possible within the uncertainties wrought by, e.g., the mass-loss rate, the efficiency of the TDU, and the neutron-capture cross section of the Si isotopes.

Notwithstanding the uncertainties discussed above, when we consider the ages derived here relative to each other, it is clear that the ages derived for the parent stars of the Y grains are similar to those of the mainstream grains, while those derived for the Z grains cover a much narrower range. This indicates that on average Z grains have parent stars of higher mass than mainstream and Y grains and supports hot bottom burning (HBB) in massive AGB stars as the process responsible for lowering the $^{12}\text{C}/^{13}\text{C}$ ratios in the Z grains (ranging from 20 to 100) with respect to those observed in the Y grains (>100, by definition of Y grains). If this interpretation is correct then, on the one hand, GCE models are not required to match the $\delta(^{29}\text{Si}/^{28}\text{Si})$ versus [Fe/H] relationship of Zinner et al. (2006) (their Figure 2), which was derived using mainstream, Y, and Z grains and AGB models of fixed mass, lower than $\simeq 3\ \text{M}_\odot$, given that the Z grains come from higher mass AGB stars. On the other hand,
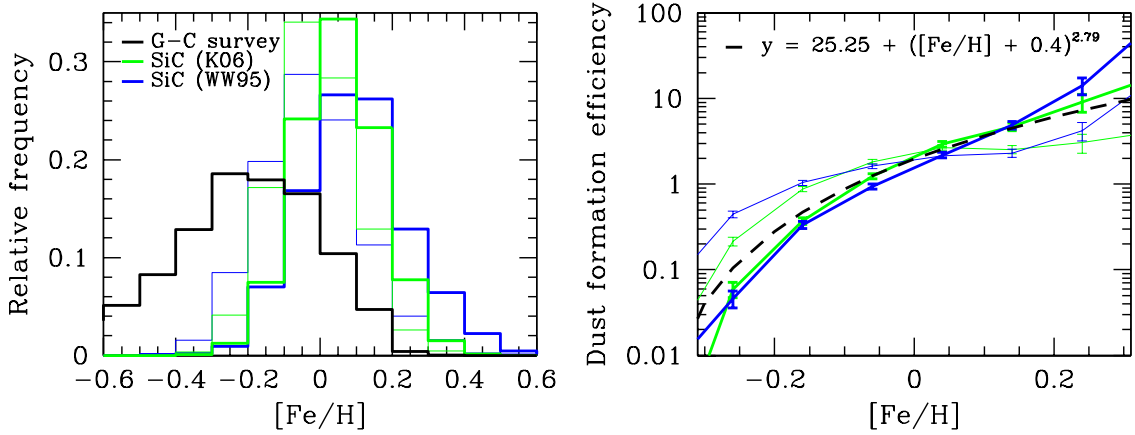
Figure 4.13: Left panel: Metallicity distribution function (MDF) of the parent stars of mainstream SiC grains derived using GEtool and the two different sets of SNII yields, WW95 and K06, as compared to that obtained for stars from the Geneva-Copenhagen (G-C) survey. Right panel: The SiC grain relative formation efficiency (RFE) as a function of [Fe/H], with the proposed power-law fit plotted as a black dashed line. The thin lines are obtained by renormalising $\delta(^{29}Si/^{28}Si) = 50$ per mil at [Fe/H] = 0. (Figure from Lewis et al., 2013, courtesy of Karen Lewis.)

one may wonder why there are no SiC grains from low-metallicity and low-mass parent stars. A possibility is that the very high C/O ratio reached in these stars (up to 20-30) favours production of amorphous carbon dust rather than SiC dust (Sloan et al., 2008).

The metallicity distribution function and the SiC dust formation efficiency

To make a quantitative comparison of the metallicity distribution functions (MDF) derived for the SiC grain parent stars and for the G-C stars, we restrict ourselves to the mainstream SiC grains as they represent the least biased sample, since the numbers of Y and Z grains are probably overestimated due to specific searches dedicated to identifying these types of grains. In the left panel of Figure 4.13 we compare the MDF obtained from the SiC AMR to that obtained from the G-C survey. Because the 1σ error bars of the [Fe/H] derived for each grain, from the experimental uncertainty of $\delta(^{29}Si/^{28}Si)$, is much smaller (<0.03 dex) than that of the stellar [Fe/H] ($\simeq 0.1$ dex), for better comparison we convoluted the grain [Fe/H] data with a Gaussian of $\sigma = 0.1$[1].

The main difference between the grain and the stellar MDF is that the mean metallicity of the parent stars of the mainstream SiC grains is $\sim 50\%$ higher than that of the G-C stars. We can interpret this as a selection effect between the grain and the stellar samples, indicating that formation of SiC dust is favoured in higher metallicity stars. This is in qualitative agreement with observations of C-rich AGB stars in the Large and Small Magellanic Clouds (Sloan et al., 2008), which indicate that their mid-infrared emission from SiC and silicate dust decreases with the metallicity, while the emission from amorphous carbon dust does not. We

---

[1]i.e., we took the [Fe/H] of each grain and added to, or removed from, it a number between -0.1 and +0.1 randomly drawn from a Gaussian distribution.
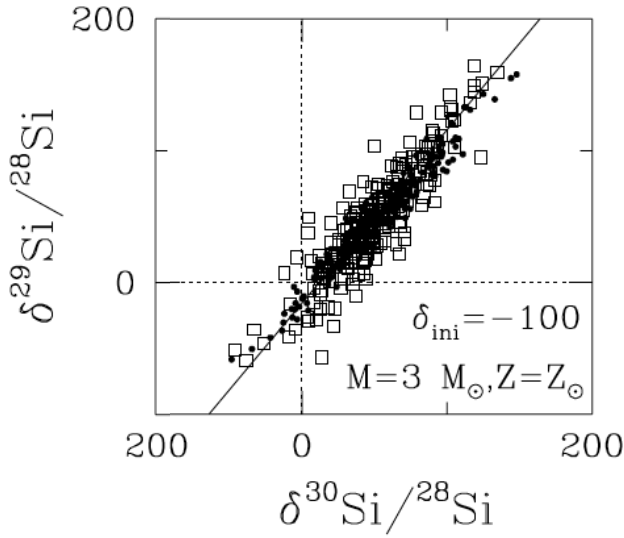
Figure 4.14: Silicon isotopic ratios measured in mainstream SiC grains and plotted as δ-values (open squares) compared with the results from Monte Carlo example (black circles) with starting composition $\delta^{29,30}\text{Si}/^{28}\text{Si} = -100$ and the isotopic shift predicted for AGB models of 3 $M_\odot$ and Z=0.02, where the range of shifts predicted under the condition C>O (see Figure 4.10) was added also in a random way. (Figure from Lugaro et al., 1999).

define the SiC relative formation efficiency (RFE) as the ratio between the normalized number of mainstream SiC grains and of G-C stars in each metallicity bin and plot these values in the right panel of Figure 4.13. The SiC RFE is unitless and its values are not absolute, but have a meaning only when considered relative to each other. We infer that the SiC RFE can be represented by a power law in metallicity. The relationship is well defined only for values of [Fe/H] between ± 0.3 dex, because in this range there are sufficient numbers of both mainstream SiC grains and G-C stars to make their ratio statistically meaningful.

An important systematic uncertainty in the derivation of the SiC RFE is related to the renormalised value of $\delta(^{29}\text{Si}/^{28}\text{Si}) = 0$ at [Fe/H] = 0 (Step 1 of Section 4.3.2). Such renormalization may easily be wrong by a few percent, in particular due to the effect of inhomogeneities in the interstellar medium, which may produce variations in $\delta(^{29}\text{Si}/^{28}\text{Si})$. In Lugaro et al. (1999), following a suggestion of Ernst Zinner, I developed a Monte Carlo model to account for inhomogeneous mixing of supernova ejecta in the interstellar medium. The physics behind this model is that the addition of contributions from individual supernovae, which are responsible for the Si isotopic ratios of a certain region of the interstellar medium, is instrinsically a stochastic process, and we do not expect that material from these contributions is instantly homogenized with pre-existing material. Fluctuations therefore result from the fact that individual supernova sources are predicted to produce yields with different Si isotopic compositions due to their different initial stellar mass. In the model, material is added from a limited number of discrete supernova sources in a statistical way, by randomly selecting the mass of each stellar source based on the initial mass function, to material with an arbitrary (but reasonable) starting isotopic composition. This model, of which an example result is shown in Figure 4.14, allowed us to show that the Si isotopic distribution of the mainstream SiC grains can be explained as the result of statistical fluctuations. In other words, it can be the result of local heterogeneities in the regions where low-mass AGB stars, the sources of mainstream grains, were born.

Further work by Nittler (2005) considered the Ti SiC data together with the Si data and demonstrated that the correlation between the isotopic ratios of these two elements allows for the effect of inhomogeneities to reach, at the very most, 70 per mil, for a given [Fe/H] within

± 0.01. This mean that both the intrinsic GCE trend and the effect of inhomogeneities have an impact on the distribution of Si in SiC. If I renormalize $\delta(^{29}\text{Si}/^{28}\text{Si})$ to a positive value, instead of to zero, clearly the grain MDF shifts closer to that of the G-C survey and the derived SiC RFE is less steep. In Figure 4.13, I also present the results obtained by setting, for example, $\delta(^{29}\text{Si}/^{28}\text{Si}) = 50$ at [Fe/H] = 0. The SiC RFE still increases with the metallicity, although the increase is less pronounced and disappears between $0 < [\text{Fe/H}] < 0.1$. I consider this example as an upper limit: a choice of $\delta(^{29}\text{Si}/^{28}\text{Si}) \simeq 30$ per mil at [Fe/H] = 0 may be more realistic, being the value shown by the largest number of SiC grains, see Figure 13 of Nittler (2005) and Figure 4c of Boujibar et al. (2021).

4.3.4 Conclusions

Under the hypothesis that the shift of the SiC MDF to metallicities higher than the G-C survey is a dust formation selection effect, I predict that the MDF of stardust silicates (Hoppe et al., 2018; Mostefaoui & Hoppe, 2004; Nguyen et al., 2010) should be similar to that of SiC grains, since SiO should also depend on the absolute abundance of Si, while the MDF of stardust graphite grains from C-rich AGB stars (Jadhav et al., 2008) should be similar to that of the G-C survey. It should also be noted that stardust oxide and silicate grains are more likely to come from lower-mass O-rich stars than SiC grains (Gail et al., 2009), which may result in a somewhat different AMR. More high-precision Si data for these different types of stardust will provide further independent information to be exploited by future investigations.

4.4 Origin of Group II oxide and silicate stardust from intermediate-mass AGB stars

Lugaro et al. 2007, Astronomy & Astrophysics, 461, 657
Lugaro et al. (The LUNA collaboration), 2017, Nature Astronomy, 1, 0027

4.4.1 Motivation

I now move the focus from C-rich SiC grains to O-rich oxide and silicate grains. These grains are classified into different groups mostly based on their oxygen isotopic compositions (Nittler et al., 1997). Group I grains make up the majority (75%) of oxide and silicate grains and show excesses in ^{17}O characteristic of the first dredge-up in red giant stars of initial mass roughly 1-3 $M_\odot$, with a maximum ^{17}O/^{16}O ratio of $\simeq 3 \times 10^{-3}$ (while solar is 3.8×10^{-4}). Their origin is generally well understood and attributed to the O-rich phases of the subsequent dust-rich AGB phase. Group II grains represent roughly 10% of all stardust oxide grains, although this is a lower limit since their extreme compositions may suffer from isotopic dilution during ion probe analysis[1]. Like Group I grains, Group II grains display excesses in ^{17}O (^{17}O/^{16}O up to $\simeq 1.5 \times 10^{-3}$), but are also highly depleted in ^{18}O, with ^{18}O/^{16}O ratios up to two

---

[1]The less abundant Group III and IV grains have an unclear origin, potentially related to core-collapse supernovae for Group IV (Nittler et al., 2008)
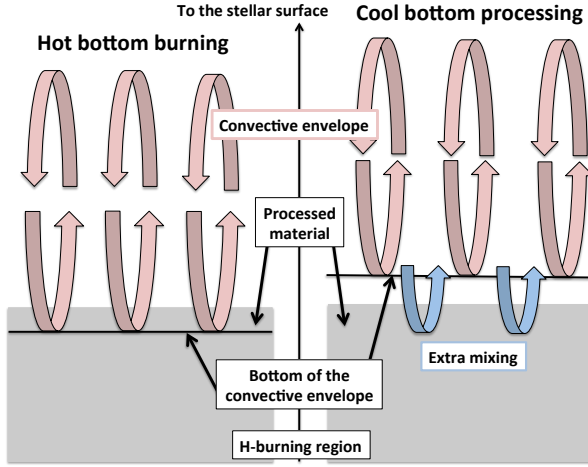
Figure 4.15: Schematic of the internal structure of AGB stars at the interface between the H-burning region and the convective envelope. Hot bottom burning (HBB, left side) and cool bottom processing (CBP, right side) take place in massive and low-mass AGB stars, respectively, and carry material processed in the H-burning region to the stellar surface. The main differences are that, in HBB, material is processed at higher temperatures but lower densities then in CPB and that mixing occurs via convection, whereas in CBP non-convective extra mixing needs to be invoked. (Figure from Lugaro et al., 2017).

orders of magnitude less than the corresponding solar value of 2×10^{-3}. The initial ratio of the radioactive ^{26}Al to the stable ^{27}Al, inferred from ^{26}Mg excesses, reaches 0.1 in Group II grains, almost an order of magnitude higher than the average ratio for Group I grains. While this composition is the indisputable signature of H burning, which produces ^{17}O and ^{26}Al and destroys ^{18}O (via the ^{16}O(p,γ)^{17}F(β^+)^{17}O(p,α)^{14}N reaction chain, and the ^{25}Mg(p,γ)^{26}Al and ^{18}O(p,α)^{15}N reactions, respectively), hypotheses on the exact site of formation of the Group II grains have so far been tentative.

Hydrogen burning affects the surface composition of massive (>4 M$_\odot$) AGB stars when the base of the convective envelope becomes hot enough for proton-capture nucleosynthesis to occur (e.g., Ventura et al., 2013) ("hot bottom burning", HBB; see Section 1.3.2 and Figure 4.15, left side). These are the brightest AGB stars, and the fact that they mostly show C/O$<$1 is attributed to the operation of the CN cycle during HBB (Wood et al., 1983), which depletes carbon into N via the ^{12}C(p,γ)^{13}N(β^+)^{13}C(p,γ)^{14}N reaction chain. In contrast, their less bright AGB counterparts mostly show C/O $>$ 1 as a result of the TDU and are the parent stars of the SiC grains discussed in the previous sections. Characteristic temperatures of HBB exceed $\simeq$ 60 MK and, thanks to the fast convective turnover time ($\simeq$ 1 yr), the composition of the whole envelope, including the stellar surface, is quickly changed into the H-burning equilibrium abundances produced at the base of the envelope. Massive AGB stars are observed to generate significant amounts of dust and, based on current models of galactic dust evolution, are expected to have contributed almost half of the O-rich dust of AGB origin in the Solar System (Gail et al., 2009; Zhukovska et al., 2015). However, no stardust grains have been found to show the signature of HBB because, although Group II grains show the highly depleted ^{18}O/^{16}O ratios qualitatively expected from HBB, their ^{17}O/^{16}O ratios are roughly twice lower than predicted using available reaction rates (Iliadis et al., 2010).

In Lugaro et al. (2007), I analysed in detail the composition of a spinel grain, named OC2, possible showing the signature of an origin in a massive AGB star. This origin was suggested due to the fact that this grain belongs to the extreme fraction of Group II grains
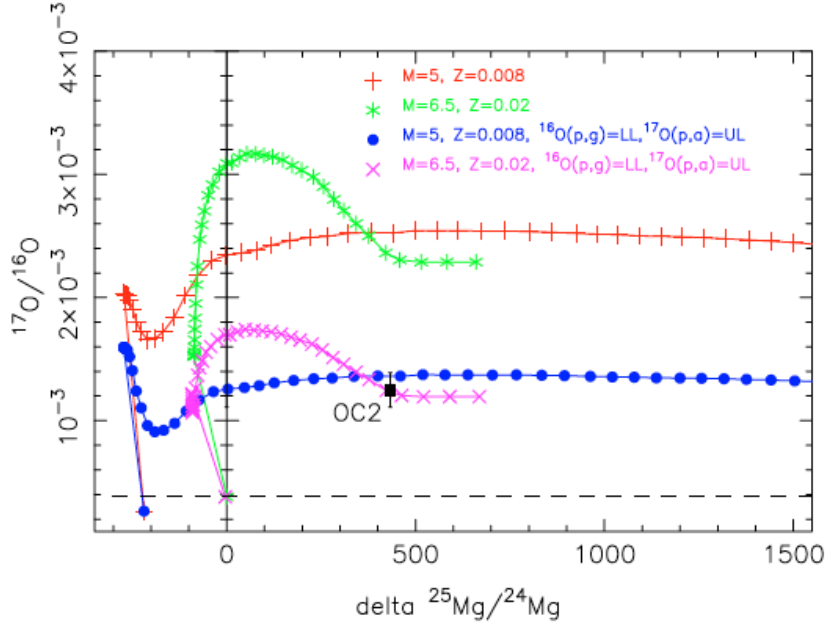
Figure 4.16: Predictions for massive AGB stars suffering HBB (as indicated, with each symbol corresponding to the surface composition following a TDU episode) compared to the composition of grain OC2 belonging to Group II (black square with 2σ error bars). Two of the models are calculated using the lower limit (LL) and the upper limit (UL) of the $^{16}O(p,\gamma)^{17}F$ and the $^{17}O(p,\alpha)^{14}N$ reaction rates, respectively, from the NACRE compilation (Angulo et al., 1999). (Figure from Lugaro et al., 2007).

and shows the ^{25}Mg excess predicted in massive AGB stars from the TDU of ^{25}Mg produced by the $^{22}Ne(\alpha,n)^{25}Mg$ reaction. By taking the lower and upper limits of the $^{16}O(p,\gamma)^{17}F$ and the $^{17}O(p,\alpha)^{14}N$ reactions, respectively, I was able to match the $^{17}O/^{16}O$ ratio of the grain (Figure 4.16). However, a year later Christian Iliadis updated and much reduced the uncertainty of the $^{16}O(p,\gamma)^{17}F$ reaction: the old error bars allowed for a 30% decrease of the $^{16}O(p,\gamma)^{17}F$ reaction in the temperature range of interest, the new error bars only allowed for a decrease of less than 10%. When I calculated new models with such updated uncertainty, I found that it was impossible to cover the composition of grain OC2, or of any other Group II grain, using massive AGB models (Iliadis et al., 2008).

The other suggestion for the origin of Group II grains is that they formed in AGB stars of low mass (<1.5 $M_\odot$) that did not dredge-up enough carbon to become C-rich but experienced extra mixing below the bottom of the convective envelope ("cool bottom processing", CBP, Nollett et al., 2003; Palmerini et al., 2011, Figure 4.15, right panel). In this scenario, material from the bottom of the convective envelope penetrates the thin radiative region located between the base of the convective envelope and the top of the H-burning shell, where the temperature and density increase steeply with mass depth, and proton captures can occur. While several mechanisms have been proposed for the physical process driving this extra mixing (e.g., Nucci & Busso, 2014), the current models of CBP are mostly parametric: the rate of the extra mixing and the depth reached are treated as free parameters, with the depth adjusted to reach temperatures in the range of 40-55 MK.

Among the reactions that control the O isotopic ratio during H burning, the rate of the $^{17}O(p,\alpha)^{14}N$ reaction has been re-evaluated from a direct underground measurement of the strength of the 64.5 keV resonance (Bruno et al., 2016) that dominates the rate at temper-
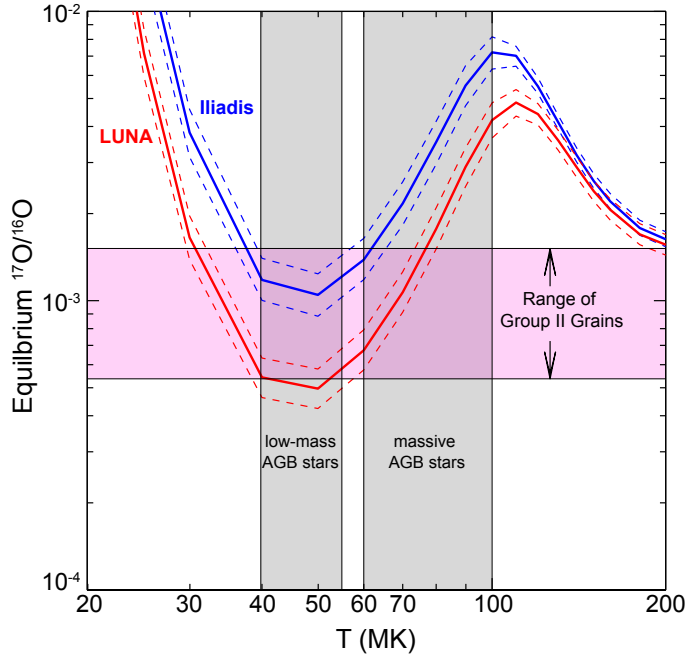
Figure 4.17: The equilibrium $^{17}O/^{16}O$ ratio defined as the ratio of the production to destruction rates of ^{17}O (i.e., $^{16}O(p,\gamma)^{17}F$ and $^{17}O(p,\alpha)^{14}N$, respectively) in the temperature range of interest for AGB stars. I used the recommended (thick solid lines) and the lower and upper limits (thin dashed lines, essentially corresponding to the 1σ experimental uncertainty of the strength of the 64.5 keV resonance) of the $^{17}O(p,\alpha)^{14}N$ reaction rate from LUNA (Bruno et al., 2016) and from Iliadis et al. (2010). The horizontal pink band shows the range of $^{17}O/^{16}O$ values observed in Group II grains. The typical temperature ranges for CBP in low-mass AGB stars and for HBB in massive AGB stars are also indicated as grey vertical bands. (Figure from Lugaro et al., 2017).

atures between 10 and 100 MK, i.e., the entire range of interest here. The experiment took place at the Laboratory for Underground Nuclear Astrophysics (LUNA) at Gran Sasso, Italy, where improved experimental procedures, coupled with an underground background for α-particle detection 15 times lower than in surface laboratories, allowed for the most sensitive measurement to date. The new rate was reported to be 2.0 - 2.5 times higher than previous evaluations by Iliadis et al. (2010) and Buckner et al. (2015). I investigated the impact of the new rate on the predictions from the scenarios above to derive stronger constraints on the origin of Group II oxide grains.

4.4.2 Methodology and results

Temperature dependence of the $^{17}O/^{16}O$ ratio

Whichever scenario we consider, the equilibrium $^{17}O/^{16}O$ ratio produced by H burning is determined by the competition between the processes that generate and destroy ^{17}O. Specifically, it depends on the ratio between the rate of the $^{16}O(p,\gamma)^{17}F$ reaction, which produces ^{17}O following the beta decay of ^{17}F (with a half life of 64 s) and is known to within 7% (Iliadis et al., 2008, 2010), and of the $^{17}O(p,\alpha)^{14}N$ reaction, which destroys ^{17}O, and has been measured at LUNA underground. (The $^{17}O(p,\gamma)^{18}F$ reaction rate is comparatively negligible at all temperatures considered here.) I plot the ratio of the two rates in Figure 4.17. At temperatures typical of CBP (40-55 MK), the new rate reproduces only the lowest $^{17}O/^{16}O$ values observed in Group II grains, while at 60-80 MK, the typical temperatures for HBB, the new rate reproduces most of the observed $^{17}O/^{16}O$ range, revealing for the first time the clear signature of HBB in this type of stardust grain. HBB temperatures higher than $\simeq 80$
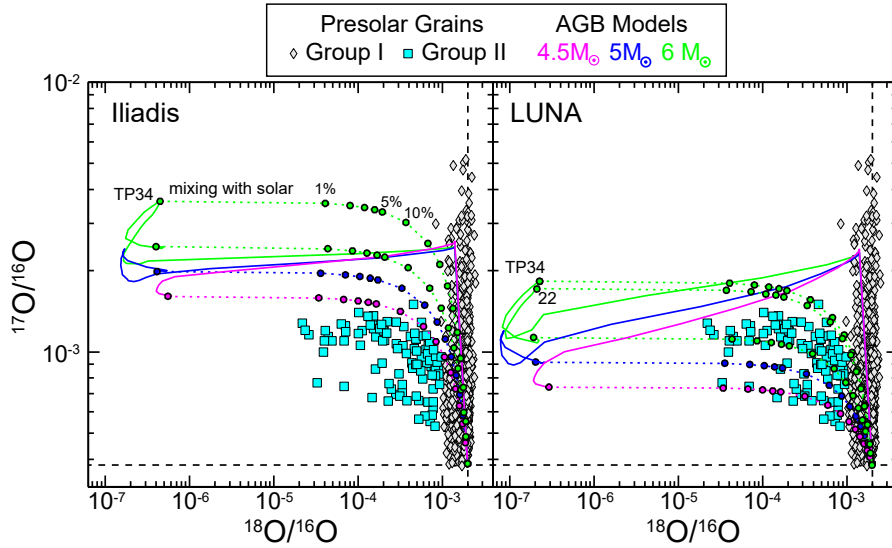
Figure 4.18: Evolution (solid lines) of the O isotopic ratios at the surface of AGB models of different masses (see top panel) calculated using the old (Iliadis et al., 2010, left panel) and new (Bruno et al., 2016, right panel) $^{17}O(p,\alpha)^{14}N$ reaction rate, as compared to Group I and II grains (with error bars at 1σ typically within the size of the symbol). The dotted lines represent the composition obtained by diluting AGB material at the end of the evolution (and at the TPs 22 and 34 out of the total 53 computed for the 6.0 $M_\odot$ star) with a solar material fractional amount indicated for the different circles on the dotted lines. Black, dashed vertical and horizontal lines indicate the solar ratios. (Figure from Lugaro et al., 2017).

MK are excluded in the parent stars of the grains. Although the initial stellar mass and metallicity ranges at which HBB occurs, as well as the AGB lifetime, are model dependent (Cristallo et al., 2015; Karakas & Lugaro, 2016; Ventura et al., 2013), this result is robust because any massive AGB model experiencing HBB with temperatures between 60 and 80 MK will necessarily produce $^{17}O/^{16}O$ ratios in agreement with those observed in most Group II grains.

Comparison to massive AGB models

Figure 4.18 compares the observed isotopic ratios for Group II stardust grains to the surface evolution of the O isotopic ratios for three AGB models that experience HBB (initial mass 4.5, 5.0 and 6.0 $M_\odot$ and solar metallicity, Z=0.014). The stellar structure evolution was calculated by Amanda Karakas using the `Stromlo` code and I calculated the nucleosynthesis using the `dppns45` code. The models evolve through the first and second dredge-ups at the end of core H and He burning, respectively, which increase the $^{17}O/^{16}O$ ratio by roughly a factor of five leaving the $^{18}O/^{16}O$ ratio very close to solar. During the subsequent AGB phase, HBB quickly (for example, for the 6 $M_\odot$ star, after about 1/5 of its total AGB lifetime) shifts the O isotopic composition to the equilibrium values corresponding to the HBB burning temperature of the model. Using the LUNA rate, the $^{17}O/^{16}O$ ratio produced by HBB is roughly a factor of two lower than that obtained with the previous rate of Iliadis et al. (2010). Uncertainties quoted on either rate translates into changes in the $^{17}O/^{16}O$ ratio by at most 20%, which are smaller
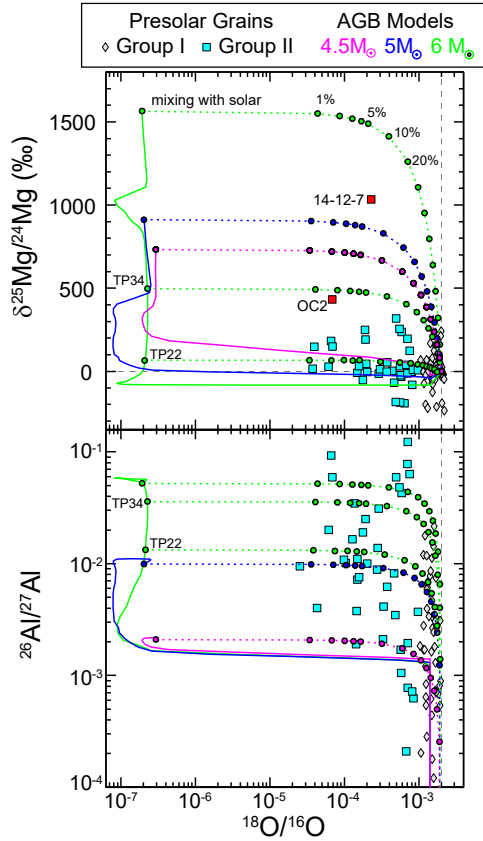
Figure 4.19: Same as Figure 4.18, but for the Mg and Al isotopic ratios as a function of $^{18}O/^{16}O$ and only showing models calculated using the LUNA rate. Top panel: Evolution of $\delta(^{25}Mg/^{24}Mg)$ versus $^{18}O/^{16}O$. The two spinel grains with the strongest excess in ^{25}Mg (OC2 and 14-12-7) are highlighted in red. Bottom panel: Evolution of the $^{26}Al/^{27}Al$ ratio versus $^{18}O/^{16}O$. (Figure from Lugaro et al., 2017).

than the differences between the stellar models of various mass.

If AGB material is diluted with material of solar composition, then the models calculated with the LUNA rate can well reproduce the oxygen ratios observed in Group II grains. The dilution is required because HBB, at the equilibrium, depletes ^{18}O too strongly relative to its abundance in the grains. This strong depletion is in agreement with the non-detection of ^{18}O in bright O-rich AGB stars (Justtanont et al., 2015), but results in $^{18}O/^{16}O$ ratios more than two orders of magnitude lower than those observed in Group II grains. Dilution with solar material is particularly effective at increasing the $^{18}O/^{16}O$ ratio: for example, 99% of HBB material mixed with only 1% of solar material increases the $^{18}O/^{16}O$ ratio by two orders of magnitude. Dilution has a comparatively minor effect on other isotopes measured in the grains (such as ^{17}O, ^{25}Mg, and ^{26}Al) because they are produced rather than destroyed in massive AGB stars. For example, it takes dilution with 50% of Solar System material to decrease the $^{18}O/^{16}O$ and $^{25}Mg/^{24}Mg$ ratios by a factor of two.

The other isotopic pairs measured in Group II grains are also consistent with an origin in massive AGB stars (Figure 4.19). The $^{25}Mg/^{24}Mg$ ratios are enhanced in massive AGB stars by the TDU of material from the He inter-shell, where the $^{22}Ne(\alpha,n)^{25}Mg$ reaction is activated, and such a signature is seen in some presolar spinel ($MgAl_2O_4$) grains. Specifically, the value observed in a spinel grain named 14-12-7 (twice the solar $^{25}Mg/^{24}Mg$ ratio; Gyngard et al., 2010) is close to that obtained in the final composition of the 5 $M_\odot$ model. However, grain OC2, already discussed above (Lugaro et al., 2007), and the majority of the other grains show a spread in the $^{25}Mg/^{24}Mg$ ratio from 1.0 to 1.5 times the solar value, that is, lower than

predicted by the dilution computed using the final AGB composition. This may reflect partial redistribution of Mg isotopes in the grains themselves (Nittler et al., 2008). Alternatively, the lower ^{25}Mg/^{24}Mg ratios may be explained by truncating the AGB evolution to one-half or one-third of the total computed evolution (as illustrated in Figures 4.18 and 4.19 by the dotted lines starting at points TP22 and TP34). This could result from a higher mass-loss rate and/or the effect of binary interactions. Another solution allowed within current model uncertainties is a TDU that is less efficient than that calculated in our models, therefore, carrying less ^{25}Mg to the stellar surface. Finally, the high ^{26}Al/^{27}Al ratios typical of Group II grains (up to $\simeq 0.1$) are also consistent with HBB (Figure 4.19), although a more accurate analysis toward matching the few grains with ^{26}Al/^{27}Al > 0.07 is currently hampered by the uncertainties in the ^{25}Mg and ^{26}Al proton-capture rates (Iliadis et al., 2010; Straniero et al., 2013).

4.4.3 Discussion and conclusions

I have discovered that the new ^{17}O(p,α)^{14}N rate measured by the LUNA underground laboratory favours the scenario where the low ^{18}O/^{16}O ratios measured in Group II oxide grains are produced by HBB in massive AGB stars, relative to the scenario were they are produced by CBP in low-mass AGB stars. This evidence that some meteoritic stardust grains exist whose O, Mg and Al isotopic compositions are best accounted for by H-burning conditions characteristic of massive AGB stars, proves for the first time that these stars were contributors of dust to the early Solar System, as expected and predicted by models of dust evolution in the Galaxy. Such evidence further provides us with a new tool to understand physical processes in massive AGB stars, for which observational constraints are still scarce. To explain the measured ^{18}O/^{16}O ratio together with the ^{17}O/^{16}O ratio, some dilution of the composition predicted by massive AGB models with material of solar composition is necessary. This can be caused by percent-level traces of contaminant oxygen (for example, from terrestrial or solar material) during isotopic measurements, which can result in ^{18}O/^{16}O up to $\sim 10^4$; however, laboratory contamination cannot easily explain grains with higher ^{18}O/^{16}O ratio values. For these, a dilution of the HBB signature composition with solar material at the level of up to a few tens of percent is required. Even higher dilution would result in a fraction of Group I grains also originating from massive AGB stars. Possible processes that could result in such dilution involve mixing with previously ejected gas within the dust formation region and/or with material in the interstellar medium prior to the grain formation. These hypotheses need to be tested.

4.5 Implications and outlook

The composition of stardust grains has provided me with amazingly high-precision data to test models of AGB stars, both for the s-process and for the production of lighter isotopes such as those of O, Mg, and Al. Detailed comparisons between data (including spectroscopic observations of Ba stars) and models has allowed me to pin down more accurately the origin of large SiC grains from AGB stars of metallicity higher than solar. Determining the origin of the

presolar dust inventory of the protosolar nebula has huge implications because an *s*-process dust carrier, such as SiC, is required to explain why different Solar System bodies show tiny anomalies in the isotopes produced by the *s*-process (see, e.g., review by Kleine et al., 2020). It has been discovered that the Earth is enriched in *s*-process isotopes relative to bodies that formed further away from the Sun, and this can be attributed to selective thermal destruction of different types of dust. In brief, the mineralogy of the dust produced in the interstellar medium that does not carry *s*-process anomalies would made it easier to destroy such dust closer to the Sun than the SiC dust produced in AGB stars carrying the *s*-process anomalies. As we published in Nature Astronomy (Ek et al., 2020), the best candidate dust to have carried such anomalies are the large SiC grains, which I identified as originating in AGB stars of metallicity higher than solar. The reason for this is that, in these stars, production of the *s*-process elements belonging to the second peak is lower, relative to the elements belonging to the first peak, which can explain why, in the Solar System bodies, we see *s*-process variation in first peak elements, and not in second peak elements. To achieve this, large SiC grains must have been a dominant component in terms of mass in the protosolar cloud, relative to the smaller grains. Observationally, it is difficult to determine the size distribution of the full inventory of the presolar SiC grains from meteorites and further studies are needed. In my future work on nucleosynthetic anomalies in meteorites I plan to address the recent discovery that different types of meteorites show a strong dichotomy in the composition of several elements, including Ti, Cr, Ni, and Mo, which has been attributed to two different reservoirs of material (the outer and the inner Solar System), which were kept well separated in the first few million years perhaps by the formation of Jupiter (Kruijer et al., 2017) or other related processes (Brasser & Mojzsis, 2020). Such a dichotomy is revealed by the fact that outer Solar System material shows the presence of nucleosynthesis tracers typically associated to supernovae, such as ^{58}Ni, and neutron-captures, such as ^{54}Cr. I want to analyse in more detail the observed signatures, in relation to models of nucleosynthesis in core-collpase supernovae, to determine the exact origin of such material and how it was incorporated in the pre-solar nebula. This will also provide independent and complementary constraints to circumstances surrounding the birth of the Sun, which I address in the next chapter using radioactive rather than stable nuclei.

Finally, if many of the stardust grains in the meteoritic inventory originated in AGB stars of metallicity higher than solar, this will have implications on our understanding of the evolution of the solar neighbourhood within the Milky Way Galaxy. Nissen et al. (2020) recently determined and accurate age-metallicity relationship for 72 nearby solar-type stars (Figure 4.20). They found two distinct population sequences, both with metallicity decreasing with age and with the older population showing a steeper increase in metallicity at age around 6-7 Gyr. As this is the time just before the formation of the Sun it seems plausible that AGB stars of such age and high metallicity contributed dust to the protosolar nebula, as I argued in Section 4.2 based on the Ba star data. This means that these high-metallicity stars should have been in the solar neighbourhood already at the time when the Sun formed, and not migrated there later on from another region of the Galaxy. The implication is that they record the chemical evolution of the solar neighbourhood, instead of that of another region of the Galaxy. An exciting future plan will be to reanalyse the investigation presented in
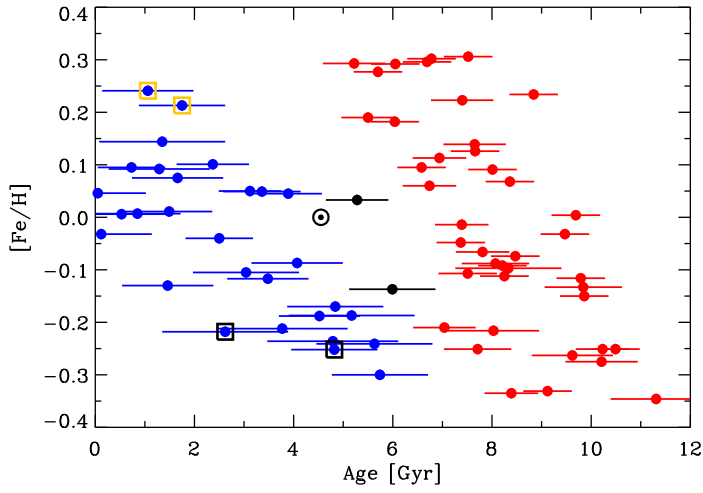
Figure 4.20: Figure from Nissen et al. (2020) showing their observed [Fe/H] versus stellar age. The stars have been divided into two groups: an older sequence (red circles) and a younger sequence (blue circles). Two stars with intermediate ages are shown with filled black circles and the Sun with the ⊙ symbol. The components of a visual binary are marked with black squares and two Na-rich stars with yellow squares.

Section 4.3 in the light of these new age-metallicity relationship observations in the solar neighbourhood, considering separately the grains of different sizes.

Chapter 5

Short-lived radioactive nuclei and the origin of Solar System matter

Radioactivity, a term coined by Marie Skłodowska Curie at the end of the nineteenth century to indicate the emission of radiation and particles from peculiar nuclei, has had a profound impact in many fields of science and technology, including astrophysics (Diehl et al., 2018). Radioactive nuclei power the light of supernovae and their radiation can be mapped throughout the Galaxy via satellites for γ-ray spectroscopy. Radioactivity is also a powerful clock for measuring cosmic times, from the ages of old stars in the halo of our Galaxy (Frebel et al., 2007), to the age of the Solar System (Amelin et al., 2010; Connelly et al., 2012) and the Earth (Wilde et al., 2001), and the timing of planetary growth (Dauphas & Chaussidon, 2011). Here, I use radioactive nuclei to calculate the age of astronomical objects and events specifically related to the birth of our Sun and its planetary system. The ultimate aim is to compare this birth to that of other stars and their planetary systems. The radioactive chronometers of the required sensitivity have half-lives $T_{1/2} \sim 0.1$ to 100 Myr and are the so-called "short-lived" radionuclides (SLRs). For radionuclides with shorter half lives, the nuclei would almost completely disappear by the time we measure their abundances; for those with longer half lives, their abundances would have barely changed, and we would not be able to detect any variation.

In this chapter I first describe the background and the specific methodology aimed at using radioactive decay to measure the timing of the events that predated the birth of the Sun. Then I apply this methodology to two types of SLRs heavier than iron whose abundances are well know for the early Solar Systems (as explained in Section 2.4.3): those made by the s process, specifically ^{107}Pd and ^{182}Hf, also considering their relationship with ^{129}I and ^{247}Cm, which are made by the r process (Section 5.1); and those made by the p process, ^{92}Nb and ^{146}Sm (Section 5.2). I discovered that nuclear physics inputs based on recent experimental work have a crucial effect in boosting the s-process production of ^{182}Hf from AGB stars, and thanks to this I was able to resolve a long-standing discrepancy between the origin of ^{182}Hf and of ^{129}I in the early Solar System. In relation to the p nuclei, the situation is more uncertain because their origin is still debated between core-collapse supernovae (CCSNe) and Type Ia supernovae. I conclude that it is likely that the abundances of at least the lighter p nuclei (such as ^{92}Nb) have a CCSNe component, while those of the heavier p nuclei (such as ^{146}Sm)

may be mostly made by Type Ia supernovae.

Background and specific aims

As is well known, radioactive decay can be used as an accurate clock because the rate in time at which the number of nuclei of a radioactive species, hereafter N_{SLR}, decreases is a linear function of the abundance itself:

$$\frac{dN_{\mathrm{SLR}}}{dt} = -\lambda\, N_{\mathrm{SLR}}, \tag{5.1}$$

where λ (usually given in 1/s) is a constant of proportionality referred to as the decay rate. To investigate the time t_1 of an event that predated the birth of the Sun, set as time t_0, a quick integration between t_1 and t_0 (as $t_0 > t_1$) delivers:

$$N_{\mathrm{SLR}}(t_0) = N_{\mathrm{SLR}}(t_1)e^{-\lambda(t_0-t_1)}, \tag{5.2}$$

which can also be written as

$$t_0 - t_1 = \tau[\ln(N_{\mathrm{SLR}}(t_1)) - \ln(N_{\mathrm{SLR}}(t_0))], \tag{5.3}$$

where $\tau = 1/\lambda = T_{1/2}/\ln(2)$ is the mean-life, i.e., the time interval required to decrease N_{SLR} by a factor $1/e$ (instead of a factor $1/2$, as when considering the half-life).

As presented schematically in Figure 5.1, the history of Solar System matter can be roughly divided into two phases. Phase I represents the contribution of Galactic chemical evolution (GCE) on the long time scale of the age of the Galaxy until the birth of the Sun (of approximately 9 Gyr, since the age of the Universe is $\simeq 13.7$ Gyr and the age of the Sun is 4.6 Gr). Thousands of stars, which belonged to different generations and lived and died before the birth of the Sun, injected chemical elements into the parcel of gas that eventually became the Solar System (see Figure 1.4). Phase II is much shorter, and starts when this pre-solar parcel of gas was incorporated in a star-forming region, or molecular cloud, i.e., a cold and dense region of the interstellar medium (ISM) where stars are born. The timescale of Phase II for the Sun is unknown. We do know that molecular clouds can live short or long lifetimes (from a few to a few tens of Myr), depending on their mass, and that rare stars also form in isolation in sparse regions of the ISM. However, we cannot determine *a priori* in which type of environment the Sun was born. Using a radioactive nucleus we can measure the time, before the birth of the Sun, either of the last stellar addition of the radioactive nucleus, or of when the Solar System matter was incorporated into the star-forming cloud[1].

To apply Eq. 5.3 I need to know $N_{\mathrm{SLR}}(t_0)$ and $N_{\mathrm{SLR}}(t_1)$. The former is provided by meteoritic analysis and in some cases is well known (Section 2.4.3). Note that t_0 here refers specifically to the time of the formation of the first solids in the early Solar System (ESS), the calcium-aluminium-rich inclusions (CAIs). $N_{\mathrm{SLR}}(t_1)$, instead, needs to be determined

---

[1]As discussed in detail in Côté et al. (2019b), if the former or the latter time can be determined depends on the value of τ, and specifically if it is small or large, respectively, relative to the recurrence of the stellar source of the radioactive nucleus.
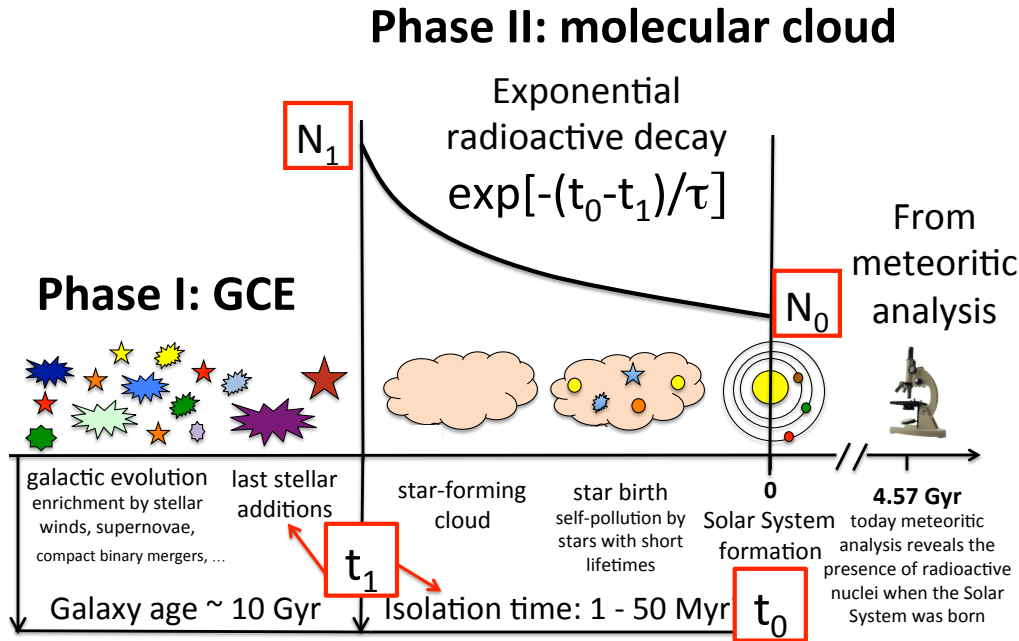
Phase II: molecular cloud

Figure 5.1: Schematic description of the methodology I use to investigate the prehistory of the matter than ended up in the Solar System (see text for details).

using models of stellar nucleosynthesis and of the evolution of the abundances of radioactive nuclei in the Galaxy. We do not have observational constraints on this number, which is, therefore, much more uncertain than $N_{\rm SLR}(t_0)$. One advantage of in Eq. 5.3, nevertheless, is that the dependence of the time interval to the abundances is logarithmic. Therefore, the uncertainties on the abundances are suppressed, relative to the uncertainties on the mean life, which is usually better known than the abundances. The SLRs with half lives of the order of 3 to 100 Myr (Table 2.2) are clocks of the appropriate sensitivity to investigate the length in time of Phase II, and therefore the life time of the star-forming cloud where the Sun was born.

Other information that can help us to investigate the environment of the birth of the Sun are the dynamical properties of the Solar System, such as the fact that planetary orbits are relatively regular, and the presence of Sedna. SLRs with even shorter half lives than those mentioned above (i.e., roughly 1 Myr or less), such as ^{26}Al, have also being used to try to investigate directly the environment of the birth of the Sun (Adams, 2010). These nuclei probably carry the signature of Phase II only, because they decay too fast to carry the signature of their production in Phase I. However, even if the abundance of ^{26}Al in the ESS is very well known (Jacobsen et al., 2008; Luu et al., 2019), it has been very difficult to establish its origin: many theories have been proposed and there is no agreement. Figure 5.2 presents a schematic diagram of the current scenarios suggested in the literature to explain the presence of ^{26}Al in the ESS, together with some example references. Note that these are *stellar* scenarios, which assume that ^{26}Al originated from a star external to the Sun and Solar System itself. There is also a *solar* origin scenario, still currently under investigation, whereby accelerated particles such as fast protons and ^{3}He from the young, active Sun, interacted with material in the proto-planetary disk and produced SLRs via non-thermal spallation reactions

106

within the Solar System itself, without the need of an external source (e.g. Gaches et al., 2020; Gounelle et al., 2006; Jacquet, 2019; Lee et al., 1998). There are two general main problems with this idea. One is that the total amount of energy estimated for the young Sun is not enough to produce the integrated amount of ^{26}Al over the whole Solar System, as is required by the observations that show that ^{26}Al was widespread. Models have shown that the maximum mass of material containing ^{26}Al is predicted to be of the order of a few Earth masses, well below the amount needed to cover the total rocky component of the minimum-mass solar nebula, i.e., the minimum amount of solids necessary to build the planets of the Solar System, of around 50 Earth masses (Duprat & Tatischeff, 2007). The other problem is that spallation reactions produce other SLRs too, specifically significant production of ^{26}Al leads to a strong overproduction of ^{10}Be (e.g. Sossi et al., 2017), which is not typically made in stars and whose origin is mainly attributed to spallation processes. Since the solar scenario does not offer an obvious solution for the origin of ^{26}Al in the ESS, the stellar scenarios shown in Figure 5.2 are still investigated. Note that this figure and the following discussion represent a brief summary, aimed at giving an idea of the complexity of the origin of ^{26}Al in the ESS and of its possible solutions. For details on the different aspects of the problem and more references I refer the reader to Section 5 of the review paper by myself and collaborators, Lugaro et al. (2018b).

First, I distinguish the proposed stellar scenarios on the basis of the number of external stellar sources invoked. The original, traditional idea proposed in the 1970s to address the discovery of ^{26}Al was that of a single supernova source (Cameron & Truran, 1977). Because the likelihood of having a supernova nearby the birth of the Sun was already envisaged to be extremely small, it was suggested that the same supernova should also have triggered the collapse of the pre-solar cloud so that the injection of ^{26}Al would have been an inevitable consequence of the birth of the Sun. Such a scenario has been considered, for example, in a series of papers by Boss et al. (e.g. Boss & Keiser, 2013). More recent work has considered if multiple stellar sources could have enriched the ambient medium of ^{26}Al within a giant molecular cloud comprising different stellar generations (Vasileiadis et al., 2013) or even within the galactic ISM itself (Fujimoto et al., 2018). Such a scenario is supported by observations of ^{26}Al enrichment in star-forming regions, for example, the case of the Scorpius-Centaurus OB association (Krause et al., 2018). It should be noted, that the the estimated ^{26}Al abundance in star forming regions appears to be much lower than that required to explain the ESS value, however, it is difficult to compare the two observations because to do so the mass of the region is needed, which is usually not well known.

The second level of categorisation for the different scenarios is the timing of the pollution. This is connected to the choice of the single or multiple source. In Fig. 5.2, "*Early* injection" refers to pollution of the pre-solar cloud, before its collapse, probably triggering or being somewhat connected to the collapse, while "*Late* injection" refers to pollution into the already formed solar proto-planetary disk. "Initial gas" refers to pollution into the pre-solar cloud before its collapse, but with no causal relation (i.e., no "triggering") between the ^{26}Al pollution and the collapse of the cloud.

The third, and last level of categorisation is related to the specific stellar ejecta source of the polluting material. Here, I consider only possible sources that are short-lived enough
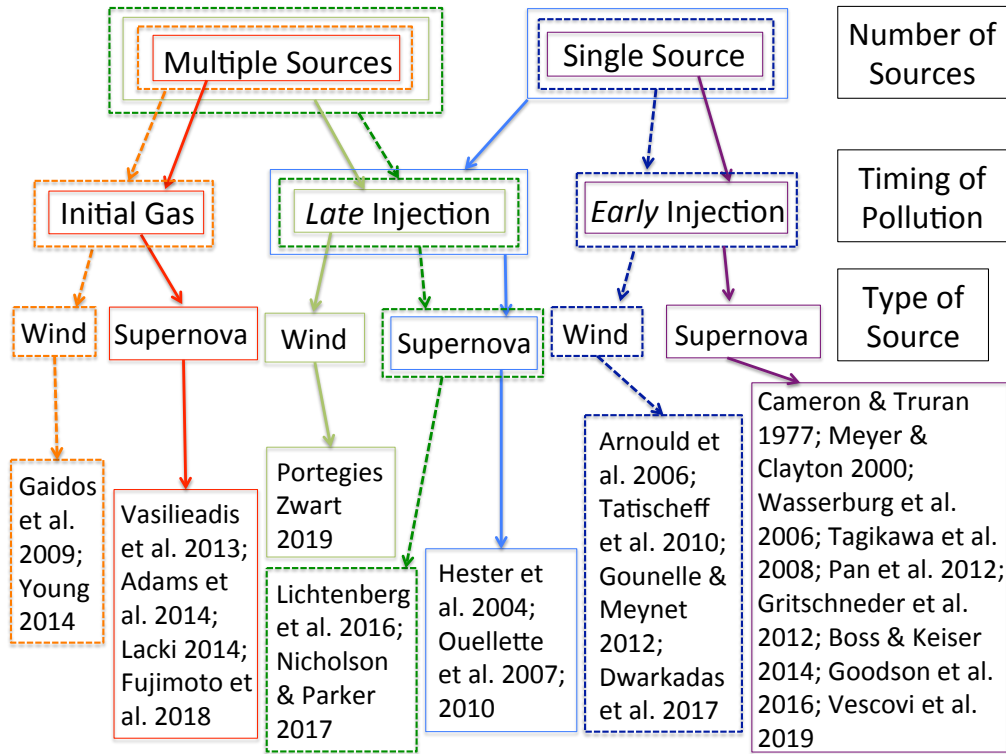
107

Figure 5.2: Schematic summary of the current scenarios proposed to explain the abundance of ^{26}Al in the ESS and selected related references. See text for details.

to be likely found in star-forming regions and have been shown to be the main producers of ^{26}Al in the Galaxy by γ-ray spectroscopy (Diehl, 2013): the winds and the core-collapse supernova (CCSN) explosions of massive stars. Lower mass stars on the AGB phase have also been considered as potential sources of the ^{26}Al in the ESS (Lugaro et al., 2012a; Trigo-Rodríguez et al., 2009; Vescovi et al., 2018; Wasserburg et al., 2006, 2017), however, they are not expected to be found in star-forming regions because they derive from stars of low mass, which live typically longer than those regions. I separated the two possibilities of massive star winds and explosions because it is well known that CCSN sources have problems in explaining the relatively high abundance of ^{26}Al together with the much lower abundance of ^{60}Fe (see Lugaro et al., 2018b, for details) because the explosive ejecta carry both isotopes. Several authors have therefore consider massive star winds as a possible source of ^{26}Al, since ^{60}Fe is not ejected in such winds.

In summary, when considering the three levels of discrimination described above, and their possible combinations as found in the literature, it is possible to encounter seven different relatively plausible, proposed scenarios for the origin of the ^{26}Al in the ESS. These range from multiple (Gaidos et al., 2009; Portegies Zwart et al., 2018; Young, 2014) to single (Arnould et al., 2006; Dwarkadas et al., 2017; Gounelle & Meynet, 2012; Tatischeff et al., 2010) massive star winds, and from multiple CCSN - both for initial (Adams et al., 2014; Fujimoto et al., 2018; Lacki, 2014; Vasileiadis et al., 2013) and late enrichment (Lichtenberg et al., 2016b; Nicholson & Parker, 2017) - to single CCSN, both for early (Boss & Keiser, 2014; Cameron & Truran, 1977; Goodson et al., 2016; Gritschneder et al., 2012; Meyer & Clayton, 2000; Pan

et al., 2012; Takigawa et al., 2008; Vescovi et al., 2018; Wasserburg et al., 2006) and late (Hester et al., 2004; Ouellette et al., 2007, 2010) enrichment. There is currently no consensus in the community on which scenario(s) is(are) favoured.

Interestingly, the probability of each of the different scenarios to occur, imply that the Sun's birth was either a "commonplace" stellar birth, or "rare/special" birth. Single source scenarios typically have lower probabilities of occurrence (Gounelle, 2015; Williams & Gaidos, 2007) than scenarios invoking multiple sources. Jura et al. (2013) showed that other stars should also have been enriched in ^{26}Al, therefore favouring the multiple source scenarios. This conclusion is based on indirect observations derived from elemental compositions produced on the surface of white dwarfs affected by asteroid collisions. Such compositions appear to indicate melting and differentiation driven by the radioactive heat produced by ^{26}Al, as it happened in the ESS. In fact, it is well known that ^{26}Al acted as an energy source in the ESS, heating the interiors of the planetesimals that formed within the first few million of years. In planetesimals that formed beyond the snow line, this resulted in more water escape than it would have occurred for their ^{26}Al-poor counterparts (Lichtenberg et al., 2016a). Because these planetesimals may have significantly contributed to water content of the Earth, the initial amount of ^{26}Al in a proto-planetary disk may ultimately have an impact on the water content of habitable exo-planets (Ciesla et al., 2015) and this effect is relevant also in relation to the water content of these planets (Lichtenberg et al., 2019).

My contribution within this currently, hotly debated, difficult question has been to try to exploit SLRs other than ^{26}Al to measure the timescale of Phase II. This independent information can support or exclude some of the scenarios proposed for the origin of ^{26}Al, and provide us with a clearer view of where our Solar System and the life within it stand in relation to the vast population of extra-solar planetary systems in the Galaxy. I have used SLRs produced by neutron-capture processes (Section 1.3) and by the p process to investigate the timescale of Phase II. My currently running (2017-2022) ERC-CoG-2016 project (RADIOSTAR, *Radioactivities from Stars to Solar Systems*) is focused on this challenge. I report a brief summary of the project achievements so far and the ongoing and future work in Section 5.3.

5.1 Origin of ^{107}Pd and ^{182}Hf from the s process in AGB stars

Lugaro et al. 2014, Science, 345, 650

5.1.1 Motivation

The exploitation of SLRs heavier than iron produced by neutron captures, to measure timescales related to the presolar history of Solar System matter, was hindered until 2014 by our poor knowledge of how these SLRs are produced in stars. Of particular interest here are three SLRs isotopes heavier than iron: ^{107}Pd, ^{129}I, and ^{182}Hf (Table 2.2). The paradigm, before my work in 2014, was that ^{129}I and ^{182}Hf are mostly produced by the r process in mergers of compact objects and peculiar supernovae (see Section 1.3), while ^{107}Pd, in addition to r-process pro-

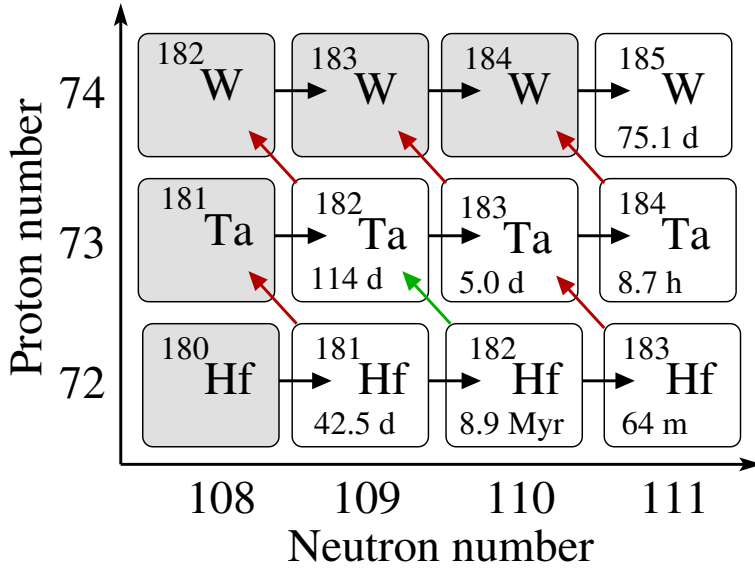## 5.1 Origin of ^{107}Pd and ^{182}Hf from the s process in AGB stars

Figure 5.3: Section of the nuclide chart including Hf, Ta, and W, and showing stable isotopes as grey boxes and unstable isotopes as white boxes (with their terrestrial half-lives). Neutron-capture reactions during the s process are represented as black arrows, β-decay as red arrows, and the radiogenic β-decay of ^{182}Hf as a green arrow. The production of ^{182}Hf is controlled by the half-life of the unstable ^{181}Hf, which precedes ^{182}Hf in the s-process neutron-capture isotopic chain. (Figure from Lugaro et al., 2014b).

duction, is also produced by the s process in AGB stars. Models of the s process in AGB stars prior to 2014 predicted only marginal production of ^{182}Hf (Wasserburg et al., 1994) because the β-decay rate of the unstable isotope ^{181}Hf at stellar temperatures was estimated to be much faster (Takahashi & Yokoi, 1987) than the rate of its neutron captures, which leads to the production of ^{182}Hf (Figure 5.3). For ^{129}I, the case for exclusive r-process production is even stronger because the β-decay half life of its precursor, ^{128}I, is only 2 minutes, therefore, s-process neutron densities never favour neutron captures over decay, even if ^{128}I is produced by neutron captures starting on the stable ^{127}I isotope (see Figure 1.7). Production of ^{182}Hf and ^{129}I by the r process in the Galaxy, however, could not self-consistently explain the measured high-precision meteoritic abundances of these SLRs (Ott & Kratz, 2008; Wasserburg et al., 1996, 2006). The simplest equation for the abundance of a radioactive isotope in the Galaxy, relative to a stable isotope of the same element produced by the same process, and under the assumption of uniform production (hereafter UP, in other words, instantaneous ISM mixing) is given by:

$$\frac{N_{\text{SLR}}}{N_{\text{stable}}} \simeq \frac{P_{\text{SLR}}}{P_{\text{stable}}} \frac{\tau}{T_{\text{Gal}}}, \tag{5.4}$$

where N_{SLR} and N_{stable} are the abundances of the radioactive and stable isotopes, respectively, $P_{\text{SLR}}/P_{\text{stable}}$ is the ratio of their stellar production rates, τ is the mean lifetime of the radioactive isotope, and $T_{\text{Gal}} \sim 10^{10}$ yr is the timescale of the evolution of the Galaxy (Phase I, in Figure 5.1). When applying Eq. 5.3 to ^{129}I and ^{182}Hf, using abundance ratios ^{129}I/^{127}I and ^{182}Hf/^{180}Hf calculated from Eq. 5.4, assuming that both ^{129}I and ^{182}Hf are primarily produced by the r process, inconsistent values of the isolation time (i.e., of the length of Phase II) are obtained. Using ^{129}I the isolation time is 73 Myr, while using ^{182}Hf it is 18 Myr (see Table 5.1 and Ott & Kratz, 2008). This conundrum led Wasserburg et al. (1996) to hypothesise the existence of two types of r-process events to produce the two SLRs separately. Another proposed solution was that the ^{107}Pd, ^{129}I, and ^{182}Hf present in the ESS were produced by the neutron burst that occurs in the He-rich shell of CCSNe (Meyer, 2005; Meyer & Clayton,

5.1 Origin of ^{107}Pd and ^{182}Hf from the s process in AGB stars

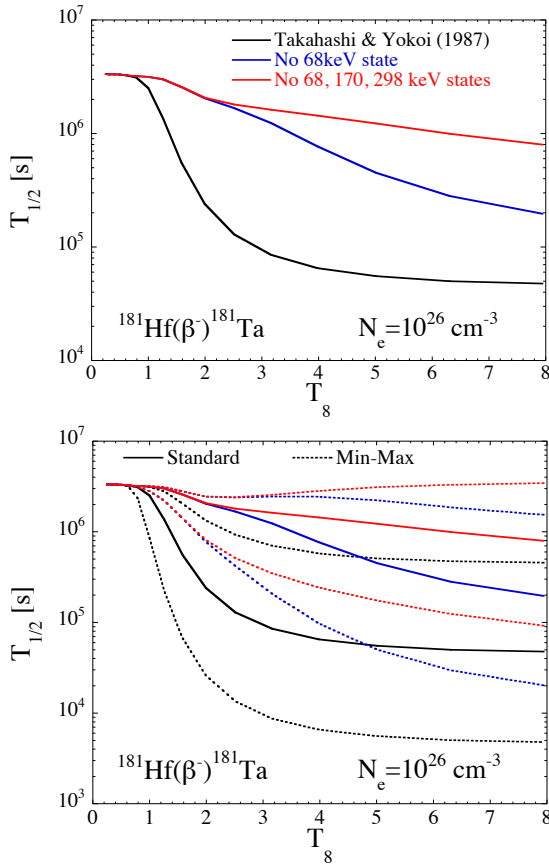Figure 5.4: Three different calculations of the half-life of ^{181}Hf: same as Takahashi & Yokoi (1987) (black line), removing the 68 keV energy state (blue line), and removing the 68, 170, and 298 keV energy states (red line). The lower panel also includes the minimum and maximum half-lives for each computation (dotted lines) allowed when assuming a ±0.5 uncertainty on the unknown transition probabilities, $\log ft$ (Goriely, 1999). Changing the value of the electron density (N_e) does not affect the results. (Figure from Lugaro et al., 2014b, courtesy of Stephan Goriely.)

2000) within the star-forming region of the Sun (i.e, Phase II described above related to the origin of ^{26}Al). While this neutron burst does not result in significant elemental production (in other words, it would not impact the abundances produced in Phase I), the relative isotopic abundances of each element can be modified due to relatively high neutron densities, with values between those of the s and r processes (this is also referred to as the n process, as mentioned in Section 1.3.1.

5.1.2 Methodology and discovery

To reanalyse this problem I planned to update stellar model predictions of the production of ^{182}Hf and other SLR nuclei in stars of initial masses between 1.25 M$_\odot$ and 25 M$_\odot$. The stars of initial mass up to 8.5 M$_\odot$, which evolve onto the AGB phase, were computed using the `Stromlo` and `dppns45` codes by myself, Amanda Karakas, and Carolyn Doherty. Stars of higher mass, which evolve into CCSNe, were computed using the `Kepler` code (Heger & Woosley, 2010; Rauscher et al., 2002) by Alexander Heger. While preparing an analytical formula for the temperature dependence of the β-decay rate of ^{181}Hf based on the population of excited energy states (to be included in the `Kepler` code, which does not read tables for such rates), I stumbled across an unexpected finding. The popular estimates of β-decay rates for the nuclei heavier than Fe by Takahashi & Yokoi (1987) were based on nuclear energy level information from the Table of Isotopes (ToI) database, which included nuclear energy levels for ^{181}Hf located at 68, 170, and 298 keV. The 68 keV level in particular was found to be

111

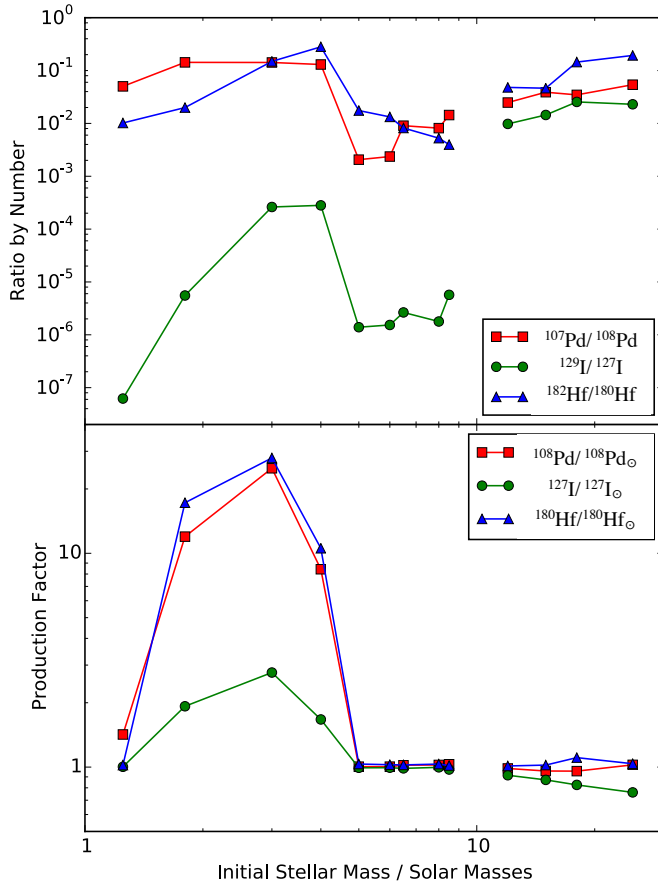## 5.1 Origin of ^{107}Pd and ^{182}Hf from the s process in AGB stars

Figure 5.5: Stellar model predictions as function of the initial stellar mass. The production ratios of the SLRs of interest with respect to the stable reference isotope of the same element are shown in the top panel, the production factors with respect to the initial solar composition of each stable reference isotope are shown in the bottom panel. Stars below 10 M$_\odot$ evolve through the AGB phase and produce both ^{180}Hf and ^{182}Hf via the s process, while stars above 10 M$_\odot$ evolve through a core-collapse supernova and produce only ^{182}Hf via the neutron burst. All the models were calculated using no temperature dependence for the half-life of ^{181}Hf (see Figure 5.4) and with initial solar abundances from Asplund et al. (2009), corresponding to a metallicity $Z = 0.014$. (Figure from Lugaro et al., 2014b, courtesy of Alexander Heger.)

responsible for the strong enhancement of the β-decay rate of ^{181}Hf at s-process temperatures, preventing the production of ^{182}Hf during the s process. However, a more recent experimental evaluation of the level structure of ^{181}Hf by Bondarenko et al. (2002) did not find any evidence for the existence of these states. This literature was subsequently checked and confirmed by my collaborator Kai Zuber. Removing these energy states from the computation performed by Stephan Goriely of the half-life of ^{181}Hf in stellar conditions, resulted in decay rates for ^{181}Hf that do not present any temperature dependence, within the uncertainties, as shown in Figure 5.4. This discovery changed the picture substantially: using a β-decay rate of 30 hours, the value given by Takahashi & Yokoi (1987) at a temperature of 300 MK, neutron densities $> 10^{11}$ cm^{-3} are needed for the probability of ^{181}Hf capturing a neutron and producing ^{182}Hf to be $> 50\%$. Using the terrestrial rate of 42.5 days, instead, to significantly produce ^{182}Hf, much lower neutron densities are needed, i.e, $> 4 \times 10^9$ cm^{-3}. These lower values are more commonly reached in AGB stars than the higher values required by the faster decay rate.

5.1.3 Results

The removal of the temperature dependence of the β-decay rate of ^{181}Hf resulted in an increase by a factor of 4 to 6 of the ^{182}Hf abundance predicted by the AGB s-process models. The effect was milder on the ^{182}Hf abundance predictions from the CCSN neutron burst, increasing between 7% for the 15 M$_\odot$ model, and a factor of 2.6, for the 25 M$_\odot$ model. This is because

5.1 Origin of ^{107}Pd and ^{182}Hf from the s process in AGB stars

the the production of ^{182}Hf in the CCSN neutron burst is already very efficient, with neutron densities much higher than those experienced by AGB stars. Some production of ^{182}Hf, as well as of ^{129}I and ^{107}Pd, is achieved in all the stellar models we considered (top panel of Figure 5.5), with ^{182}Hf/^{180}Hf ratios ranging from ~ 0.001 to ~ 0.3. In terms of absolute, rather than relative to ^{180}Hf, ^{182}Hf abundances, however, only AGB models of mass $\sim 3-4$ M$_\odot$ are major producers of s-process ^{182}Hf in the Galaxy. In these stars only the production factor of the stable ^{180}Hf, with respect to its solar value, is well above unity (bottom panel of Figure 5.5). This is because the s-process is driven by the ^{13}C$(\alpha,$n$)^{16}$O neutron source, which generates the largest total number of neutrons of all the models and efficiently produces the heaviest s-process elements, including Hf. This leads to a high enhancement of ^{180}Hf, which, in turn, leads to high ^{182}Hf production during the secondary neutron burst generated by the ^{22}Ne$(\alpha,$n$)^{25}$Mg neutron source, with a lower total number of neutrons but higher neutron densities than those produced by the ^{13}C$(\alpha,$n$)^{16}$O neutron source (see Section 1.3.2). Stars in the mass range $\sim 3-4$ M$_\odot$ are the most efficient ^{182}Hf producers because in AGB stars of mass lower than ~ 3 M$_\odot$ the ^{22}Ne neutron source is not efficiently activated, whereas in higher mass AGB stars the ^{13}C neutron source is not efficiently activated.

5.1.4   Discussion and conclusions

In Table 5.1 I report timescales calculated using the indicated production ratios, also including the ^{247}Cm/^{235}U ratio, which is known in the ESS (see Table 2.2). This ratio provides a further independent constraint for the r process because actinides such as Cm and U can only be produced by the r process. The production ratios reported in the table and used to derive the timescales were obtained as follows: the s-process production ratios from a single stellar event, $p_{\text{SLR}}/p_{\text{stable}}(s)$, for ^{107}Pd/^{108}Pd and ^{182}Hf/^{180}Hf were taken from the Monash model of a 3 M$_\odot$ AGB star of solar metallicity (Figure 5.5) as representative of an s-process AGB star. The ^{107}Pd/^{108}Pd ratio depends almost exclusively on the inverse ratio of the neutron-capture cross sections of the two isotopes because the neutron flux through them is in equilibrium and there are no branching points affecting their abundances (see Section 1.3.1), therefore, since the neutron-capture cross sections are relatively well known, the uncertainty of the ratio is also small (of the order of 20%). The ^{182}Hf/^{180}Hf ratio, instead, depends on the activation of the branching point at ^{182}Hf (as discussed above, see Figure 5.3), and therefore is affected by model and nuclear uncertainties, including the temperature, the rate of the ^{22}Ne$(\alpha,$n$)^{26}$Mg reaction, the neutron-capture cross sections of ^{180,181,182}Hf, and the β^--decay rate of ^{181}Hf. With my students, Benjamin Soós and Blanka Világos, I am currently analysing the last two listed nuclear uncertainties and finding ^{182}Hf/^{180}Hf ratios in the most conservative, unfavourable (and statistically unlikely) scenario, at most of a factor of two lower than that reported here.

The r-process production ratios from a single stellar event, $p_{\text{SLR}}/p_{\text{stable}}(r)$, for ^{107}Pd/^{108}Pd, ^{129}I/^{127}I, and ^{182}Hf/^{180}Hf were instead derived using the r-process residual method described in Section 1.3.1, under the assumption that the solar r-process abundances are typical of a generic r-process event. To apply this method I considered the r-process residual of the stable reference isotopes, ^{108}Pd, ^{127}I, and ^{180}Hf, and of the daughter nuclei ^{107}Ag, ^{129}Xe, and ^{182}W, respectively for ^{107}Pd, ^{129}I, and ^{182}Hf. This is allowed because the full production flux

5.1 Origin of ^{107}Pd and ^{182}Hf from the s process in AGB stars

Table 5.1: Production ratios and inferred timescales for four SLRs produced by the r and the s processes. All times are given in Myr. $P_{\mathrm{SLR}}/P_{\mathrm{stable}}$ are the ratios of the stellar production rates ($s+r$ processes), $p_{\mathrm{SLR}}/p_{\mathrm{stable}}$ the production ratios of a single stellar event (s or r process, as indicated). The UP and LE ratios are calculated using Eq. 5.4 and Eq. 5.5, respectively, the latter for different values of δ as indicated in brackets. The UP and LE times are the time intervals required to obtain the ESS ratio reported in Table 2.2 starting from the UP and LE ratios, respectively, using Eq. 5.3.

Ratio	$P_{\mathrm{SLR}}/P_{\mathrm{stable}}$	UP ratio	UP time	$p_{\mathrm{SLR}}/p_{\mathrm{stable}}$	LE ratio (δ)	LE time
^{247}Cm/^{235}U^a	0.40	8.8×10^{-3}	113	0.40(r)	3.8×10^{-2}(100)	146
					1.1×10^{-2}(10)	118
^{129}I/^{127}I	1.25	2.9×10^{-3}	73	1.35(r)	1.4×10^{-2}(100)	109
					3.8×10^{-3}(10)	80
^{182}Hf/^{180}Hf	0.29	3.8×10^{-4}	18	0.91(r)	9.1×10^{-3}(100)	59
					1.7×10^{-3}(10)	37
				0.15(s)	1.5×10^{-3}(100)	36
					2.8×10^{-4}(10)	14
^{107}Pd/^{108}Pd	0.65	6.1×10^{-4}	22	2.09(r)	2.1×10^{-2}(100)	55
					3.2×10^{-3}(10)	38
				0.14(s)	1.4×10^{-3}(100)	30
					2.1×10^{-4}(10)	12

^{a}Because ^{235}U is also radioactive, to calculate the ^{247}Cm/^{235}U ratio from Eq. 5.4, T_{Gal} needs to be substituted by the mean lifetime of ^{235}U ($\tau=1020$ Myr), and in Eq. 5.5, δ/T_{Gal} is removed and p_{SLR}/p_{stable} is multiplied instead by the ratio of the exponential terms derived for ^{247}Cm and for ^{235}U. Note also that the UP time and LE time are slightly different in this table from those I published in 2014 because here I have used the better ESS determination of the ^{247}Cm/^{235}U ratio published in 2016 (see Table 2.2).

5.1 Origin of ^{107}Pd and ^{182}Hf from the s process in AGB stars

leading to the r-process abundances of the daughter nuclei proceeds via the corresponding SLRs. The $p_{\text{SLR}}/p_{\text{stable}}(r)$ of the ^{247}Cm/^{235}U ratio, instead, cannot be calculated with the r-process residual method above because there are no stable nuclei directly produced by the decay of these two isotopes. Decay-chains starting at the actinides end up at isotopes of Bi and Pb, however, there are many such decay chains and it is not possible to deduce the initial abundances of the actinides. Therefore, here I used a value for the ^{247}Cm/^{235}U derived from parametric models of the r process (e.g., Goriely & Janka, 2016).

Finally, the stellar production rates $P_{\text{SLR}}/P_{\text{stable}}$, used to derive the UP ratio and the UP times, were obtained for ^{247}Cm/^{235}U directly from the $p_{\text{SLR}}/p_{\text{stable}}(r)$ ratios, since these two isotopes are only produced by the r process. The other three stellar production rate ratios were calculated as an average production ratio weighted by the s- and r-process percent contributions to the solar composition of the stable reference isotope, where the s-process contributions are 65%, 5%, and 75%, respectively, for ^{108}Pd, ^{127}I , and ^{180}Hf from Arlandini et al. (1999), see also Côté et al. (2019a).

When using Eq. 5.4 with the updated $s+r$ production rate ratios, I still found the problem that the time of isolation of the Solar System material from the ISM matter (Phase II in Figure 5.1), calculated using ^{182}Hf, is much shorter than the value calculated using ^{129}I ("UP time" in Table 5.1). In reality, however, this simple uniform production description of the evolution of SLRs in the Galactic ISM is inaccurate because stellar production is not continuous, rather, it is strongly discontinuous as production is linked to stellar events specific in time and space. If a given SLR has a long mean life relative to the recurrence time, δ, between the events that produce it, then we can treat its abundances as if the stellar production rate was continuous. However, for the nuclei under consideration, it is more likely that their mean lives are smaller or similar to the recurrence times of the r- and s-process events that produce them, specifically for the r-process events, which are known to be rare (i.e., compact mergers). In this case, the *granularity* in time and space of the production events controls the abundance ratio, and the best estimate for such a ratio, in the parcel of gas that ended up making the Solar System, is its value just after the last contributing event. Because the cosmic abundances of the nuclei we are considering result from two different types of sources, the r process and the s process, it necessarily follows that the precursor material of the Solar System must have seen one last event (LE) of each type, i.e., one r-process LE and one s-process LE. Following each of these LEs, the abundance of a radioactive isotope in the Galaxy, relatively to a stable isotope of the same element produced by the same process, is given by:

$$\frac{N_{\text{SLR}}}{N_{\text{stable}}} \simeq \frac{p_{\text{SLR}}}{p_{\text{stable}}} \times \frac{\delta}{T_{\text{Gal}}} \times \left(1 + \frac{e^{-\delta/\tau}}{1 - e^{-\delta/\tau}}\right), \tag{5.5}$$

where $p_{\text{SLR}}/p_{\text{stable}}$ are the production ratios of each single stellar event, T_{Gal}/δ is the total number of events that contributed to the abundance of the stable isotope in the Solar System, and the second term of the sum accounts for the memory of all the previous events before the last (Wasserburg et al., 2006). Employing simple considerations on the expansion of stellar ejecta into the ISM, and the resulting contamination of the Galactic disk, Meyer & Clayton (2000) derived $\delta \sim 10$ Myr for supernovae and, using the same method, I derived $\sim$50 Myr

5.1 Origin of ^{107}Pd and ^{182}Hf from the s process in AGB stars

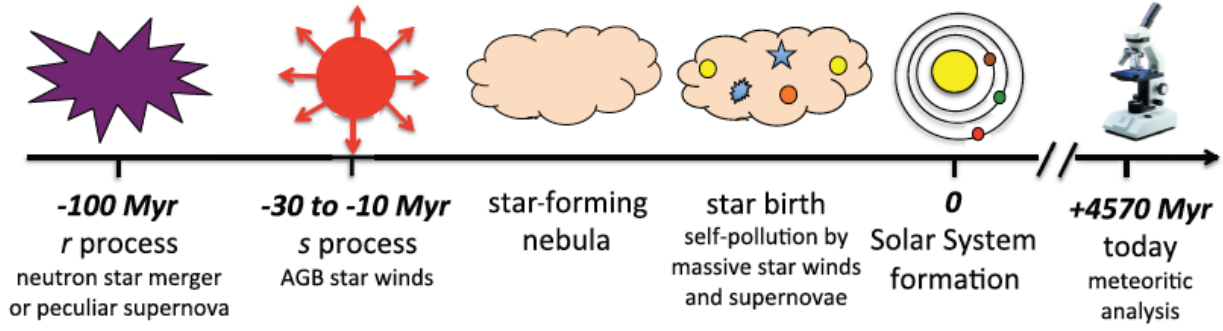Figure 5.6: Adaptation of the schematic timeline of the prehistory of the Solar System matter shown in Figure 5.1. The r-process LE contributed ^{129}I and ^{247}Cm to the ESS, the s-process LE ^{107}Pd and ^{182}Hf. Self-pollution of the star-forming region most likely is responsible for the presence of the lighter SLRs, such as ^{26}Al. (Figure from Lugaro et al., 2014b).

for AGB stars in the mass range 2 - 4 M$_\odot$. Because these values are first approximations, and because the r process most likely occurs in rare events (i.e., high δ), in Table 5.1 I present the results obtained using $\delta = 10$ and 100 Myr. The time of the r-process LE as derived from ^{129}I/^{127}I is 80 - 109 Myr ("LE time" in Table 5.1), similar to the 118 - 146 Myr values derived from the ^{247}Cm/^{235}U ratio, whose initial abundance was confirmed in 2016 (see Section 5.3). Note that here I used typical values for the production ratios as described above, in our more recent work (Côté et al., 2021), we have evaluated this production ratio for the r process for different sites and nuclear physics inputs. These results bring the agreement between the LE time calculated using ^{129}I and using ^{247}Cm closer, with a self-consistent range of 100-200 Myr.

The possible range of r-process LE times derived from ^{129}I and ^{247}Cm is in strong disagreement with the r-process LE times derived from ^{107}Pd/^{108}Pd and ^{182}Hf/^{180}Hf of <60 Myr. If we consider that ^{108}Pd and ^{180}Hf have an important ($\simeq 70\%$) s-process contribution not explicitly included in Eq 5.5, this maximum value decreases by roughly 12 Myr[1]. A natural explanation to solve this mismatch is to invoke a separate s-process LE for ^{107}Pd and ^{182}Hf. When calculating the time of this event, under the approximation that the stable reference isotopes ^{108}Pd and ^{180}Hf are of s-process origin, I derive concordant times from ^{107}Pd and ^{182}Hf of 10 - 30 Myr (Table 5.1). With the r-process component correction to the stable reference isotopes of $\simeq 30\%$, the values decrease by roughly 3.5 Myr[2].

The timeline of the r- and s-process last events that contributed the final addition of elements heavier than Fe to the precursor material of the Solar System is schematically shown in Figure 5.6. The r-process last event occurred significantly earlier than the s-process last event, closer to the time of the formation of the stellar nursery where the Sun was born. Therefore, the timing of this s-process last event has important implications for our understanding of the events that led to the formation of the Sun because it provides us with an upper limit for Phase II (Figure 5.1). Interestingly, the timescale we derived compares well to the total lifetime (from formation to dispersal) of typical giant molecular clouds of 27±12 Myr (Murray, 2011). Therefore, other radioactive nuclei in the ESS of possible stellar origin (Table 2.2),

---

[1]Calculated as $\tau\, ln(1/r)$, where r is the r-process fraction of 0.3, and $\tau \simeq 10$ Myr for these two SLRs.
[2]Calculated as $\tau\, ln(1/s)$, where s is the s-process fraction of 0.7, and $\tau \simeq 10$ Myr for these two SLRs.

e.g., ^{26}Al, probably result from self-pollution of the star-forming region itself (Gounelle & Meynet, 2012; Vasileiadis et al., 2013; Young, 2014). This is not possible for the radioactive nuclei of s-process origin considered here, because their $\simeq 3$ M$_\odot$ parent stars live too long (~ 400 Myr) to evolve within star-forming regions, nor for r-process nuclei which are from rare, late merging events. The scenario I have drawn here also implies that the origin of ^{26}Al and of ^{182}Hf in the ESS was decoupled (unlike the case where they originated from the same CCSNe within Phase II), which is in agreement with meteoritic analysis that demonstrated the presence of ^{182}Hf in an ESS solid that did not contain ^{26}Al (Holst et al., 2013).

5.2 Short-lived radioactive p-process isotopes and ^{53}Mn from Type Ia supernovae

Lugaro et al. 2016, PNAS, 113, 907

5.2.1 Motivation

After considering the origin of the SLRs produced by the s and r processes discussed above, I turned to the investigation of the origin of another two SLRs heavier than Fe whose abundances are well known in the ESS: ^{92}Nb and ^{146}Sm (Table 2.2). These nuclei are proton rich, relative to the stable isotopes of Nb and Sm, which means that they cannot be produced by neutron captures like the vast majority of the nuclei heavier than Fe (see Figure 1.7). Instead, their nucleosynthetic origin has been traditionally ascribed to some flavor of the so-called p process (Arnould & Goriely, 2003; Rauscher et al., 2013). The two main types of the p process are "top-to-bottom" processes proceeding from heavier to lighter nuclei and driven by photon-induced disintegration (the γ process), and "bottom-to-top" processes proceeding from lighter to heavier nuclei and driven by charged particle reactions (e.g., the *rapid, rp* process). The latter type typically reaches only the lighter p-process nuclei, up to Pd-Ag, possibly including ^{92}Nb, but not ^{146}Sm. Not only the nuclear processes but also the astrophysical sites of the p process in the Universe are not well constrained. One further difficulty is that the only observational evidence for p-process abundances is related to their meteoritic abundances. These are so low (typically less than 1% of the total elemental abundance, see Figure 1.7) that it is impossible to observe these isotopes in stars. Below I report a brief summary of the state-of-the-art of this complex topic.

A favoured site for the γ process are the O-Ne-rich zones of the ejecta of core-collapse supernova (CCSN) explosions (Woosley & Howard, 1978). However, CCSN models have never managed to reproduce the complete p-process pattern observed in the bulk of the Solar System material (Prantzos et al., 1990; Rauscher et al., 2002; Rayet et al., 1995), and specifically, the unusually large abundances of the p-only isotopes ^{92,94}Mo and ^{96,98}Ru (representing approximately 25% and 8% of the total solar abundances of Mo and Ru, respectively). Taking into account nuclear uncertainties has not solved the problem (Rapp et al., 2006; Rauscher, 2006), except in the case of a strong increase of the ^{12}C+^{12}C fusion reaction rate (Bennett et al.,

2012; Pignatari et al., 2013b), which remains to be determined experimentally[1]. Another process in CCSNe that can produce the lighter *p*-process nuclei up to Pd-Ag, and including the SLR ^{92}Nb, is the combination of the α, proton, neutron captures, and their reverse reactions that happen in the deep layers of the exploding star during the so-called "α-rich freeze-out" (Woosley & Hoffman, 1992). Another possible site related to CCSNe for the production of the light *p*-process nuclei are the neutrino winds that come out from a forming neutron star (Arcones & Montes, 2011; Farouqi et al., 2009; Hoffman et al., 1996). The so-called νp-process can occur in these winds (Fröhlich et al., 2006), however, this process cannot produce ^{92}Nb because this SLR is shielded by ^{92}Mo against the subsequent β^+-decay chains at mass 92 (Fisker et al., 2009; Rauscher et al., 2013). The same shielding effect occurs in the case of another flavour of a bottom-to-top *p* process, the "rapid" *rp*-process that can occur in X-ray bursts (Dauphas et al., 2003). Other neutrino-induced reactions in CCSNe (the ν-process) can also produce some ^{92}Nb (Hayakawa et al., 2013), but no other *p*-process nuclei. Thermonuclear supernovae (SNeIa) from the explosion of a white dwarf that reached a near Chandrasekhar-mass by accretion of material from a main sequence companion have also been proposed as a site of the γ process (Kusakabe et al., 2011; Travaglio et al., 2015, 2018, 2011). In these models, heavy seed nuclei are produced by the neutron captures during the accretion phase (Battino et al., 2020) and, given such an initial distribution, it is possible to reproduce the high abundances of ^{92,94}Mo and ^{96,98}Ru in the Solar System. However, there are still many uncertainties related to the possibility and occurrence of SNeIa explosions on accreting white dwarfs, and on the features of the neutron-capture processes during the accretion.

Travaglio et al. (2014) analysed in detail the production of ^{92}Nb and ^{146}Sm[2] in SNeIa using multidimensional models and concluded that such an origin is plausible for both radionuclides in the ESS. However, these authors did not check for the self-consistency of the results (i.e., if they produce the same UP and/or LE times as defined in the previous Section 5.1), nor for the consistency of the results with the analysis of another SLR, ^{53}Mn. This nucleus provides us a further, strong constraint because the near Chandrasekhar-mass SNeIa that can produce the *p*-process isotopes are also the major producers of Mn in the Solar System (Seitenzahl et al., 2013). Together with the stable ^{55}Mn, they produce ^{53}Mn, whose abundance is well determined in the ESS (Table 2.2). Therefore, I extended the study of Travaglio et al. (2014) to investigate if an origin of ^{92}Nb and ^{146}Sm from SNeIa is also compatible with that of the ^{53}Mn. I considered the SNeIa results from Claudia Travaglio as well as predictions of the production of *p*-process nuclei in α-rich freeze-out conditions in CCSNe provided by Marco Pignatari to investigate the origin of ^{92}Nb and ^{146}Sm, together with ^{53}Mn, and further constrain the circumstances of the birth of the Sun.

5.2.2 Methodology

Travaglio et al. (2014) included the stellar yields of ^{92}Nb and ^{146}Sm, and of their refer-

---

[1]The ^{12}C+^{12}C fusion reaction is one of the most difficult reactions to measure in the laboratory, and it will take roughly 5 years of data collection for the underground laboratory LUNA to be able to obtain a full data set for this planned experiment.

[2]Travaglio et al. (2014) also presented SNeIa yields for the other two SLR *p*-only isotopes ^{97}Tc ad ^{98}Tc, however, I will not discuss these two isotopes here because their ESS abundances are not well known.

ence isotopes ^{92}Mo and ^{144}Sm, respectively, from their SNIa models into Galactic chemical evolution (GCE) simulations that reproduce the solar abundances of the stable reference isotopes (Travaglio et al., 2015). These authors evaluated the abundance ratios ^{92}Nb/^{92}Mo and ^{146}Sm/^{144}Sm in the ISM at the time of the birth of the Sun, assuming that the production of p nuclei only occurs in SNIa. I reproduced these results using an improved version of Eq. 5.4 and Eq. 5.5, where a free multiplication parameter K is introduced to account for various GCE effects, from the infall of low-metallicity gas, which dilutes the abundances, to the fact that a fraction of the abundances, particularly for stable isotopes, is locked inside stars (Clayton, 1985; Côté et al., 2019a). The value of K may vary depending on whether the isotopes involved are of primary or secondary origin, i.e., respectively, whether they are produced directly from the burning of H and He in a star or whether their production requires the initial presence of CNO elements. These effects are complex to evaluate analytically, but the general result is that $K > 1$ (Huss et al., 2009)[1].

Whether Eq. 5.4 or Eq. 5.5 should be used to compare the analytical approach to the GCE models depends on the mean life of the SLR. Due to the relatively long half lives of ^{92}Nb and ^{146}Sm, the second term of the sum in Eq. 5.5, i.e., the term that keeps the memory of all the events that occurred before the last event, is more important than the first term, representing the last event. For example, using δ=10 Myr the memory term accounts for 82% and 90% of the total amount of ^{92}Nb and ^{146}Sm, respectively. As shown in Table 5.2[2], with Eq. 5.4 I obtain values very close to those calculated by Travaglio et al. (2014) for these two SLRs by using $K = 2$ and T_{Gal}=9200 Myr (the latter being the value reported by Travaglio et al., 2014). The full analysis of GCE uncertainties we reported recently in Côté et al. (2019a) resulted in a value for $K = 2.3^{3.4}_{-0.7}$, consistent with $K = 2$ I used here. Using Eq. 5.5, I recovered similar values to Eq. 5.4 and the GCE models, when considering $K = 2$ and $\delta = 8$ Myr. It should be noted however, that such a comparison is less meaningful than the comparison between the GCE models and the results of Eq. 5.4 because the GCE models are calculated assuming instantaneous mixing. Therefore, by construction they do not account for the granularity of the stellar event as is done by Eq. 5.5. The comparison should be taken with these caveats well in mind. In any case, I was able to recover results for ^{92}Nb and ^{146}Sm very close to those of the detailed GCE models (compare Rows 3, 4, and 5 of Columns 3 and 4 of Table 5.2).

I apply the same method and K, δ, and T_{Gal} values as above to derive self-consistently the ISM ^{53}Mn/^{55}Mn ratio, which was not included in the study of Travaglio et al. (2014). The main difference between ^{53}Mn and the other two SLRs, is that the half life of ^{53}Mn is much shorter (10 to 20 times). This results in a larger difference, of a factor of two, between the ISM ratio calculated using Eq. 5.4 or Eq. 5.5 (compare Rows 4 and 5 of Column 2 of Table 5.2) since the memory term in Eq. 5.5 only contributes 20% of the total abundance, for the example with δ=10 Myr. This means that most of the abundance of ^{53}Mn in the ESS is probably contributed to by the last production event. The final step is to evaluate timescales related to Phase II (the UP or LE time, related to Eq. 5.4 and 5.5, respectively)

---

[1]Since in Section 5.1 I did not consider the parameter K in the evaluation of the ratios, effectively $K = 1$ and the timescales reported in Table 5.1 represent lower limits.

[2]The method and the numbers presented in Table 5.2 are marginally different from those used in Lugaro et al. (2016) because of improvements based on our recent 2019 work (Côté et al., 2019a,b). The main results and conclusion are, however, unchanged.

Table 5.2: Production and ISM ratios, relative to the reference stable isotope, and timescales (in Myr) for the SLR of interest

	SNIa			CCSN[a]
	^{53}Mn	^{92}Nb	^{146}Sm	^{92}Nb
Production ratio	0.108	1.58×10^{-3}	0.347	$8.2(5.5)\times10^{-3}$
ISM ratio GCE[b]		$1.72^{+1.40}_{-0.06}\times10^{-5}$	$7.0^{+9.7}\times10^{-3}$	
ISM ratio Eq. 5.4[c]	1.26×10^{-4}	1.72×10^{-5}	7.4×10^{-3}	$8.9(5.9)\times10^{-5}$
ISM ratio Eq. 5.5[d]	2.4×10^{-4}	1.86×10^{-5}	7.70×10^{-3}	$9.6(6.4)\times10^{-5}$
Timescales	15^e, 19^f	$<5.4^g$	$\leq 244^h$	$51(31)^e$

[a]Values derived from the CCSN 15 M$_\odot$ models with delay and rapid (in brackets) setups.
[b]The value is from Table 2, while the error bars are due to nuclear physics uncertainties from Tables 3 and 4 of Travaglio et al. (2014).
[c]Using $K = 2$ and T_{Gal}=9200 Myr.
[d]Using $K = 2$, $\delta = 8$ Myr, and T_{Gal}=9200 Myr.
[e]UP time calculated using Row 3.
[f]LE time calculated using Row 4.
[g]UP time calculated using the upper limit from Row 2.
[h]UP time calculated using the upper limit from Row 2 and the half life of 68 Myr.

using radioactive exponential decay (Eq. 5.3) and the ISM ratios.

5.2.3 Results

In Table 5.2 all the numbers used and derived from the methodology above are reported assuming that ^{53}Mn, ^{92}Nb, and ^{146}Sm are produced by SNeIa only, Columns 2, 3, and 4. Column 5 reports the same values, for ^{92}Nb only, derived assuming that this SLR is instead only produced by CCSNe.

The SNIa source

The production ratios in the case SNIa for ^{92}Nb/^{92}Mo and ^{146}Sm/^{144}Sm are the average of the ratios from Table 1 of Travaglio et al. (2014) with metallicities from 0.01 to 0.02. For ^{53}Mn/^{55}Mn, they are obtained from the ^{53}Cr abundance given by Travaglio et al. (2011) (all the ^{53}Cr produced in SNIa results from the decay of ^{53}Mn). Different models produce very similar ^{53}Mn/^{55}Mn ratios (Seitenzahl et al., 2013; Travaglio et al., 2004). The ISM ^{92}Nb/^{92}Mo and ^{146}Sm/^{144}Sm ratios are reported in the table together with the error bars derived by Travaglio et al. (2014) via careful analysis of the nuclear uncertainties that affect the production of these isotopes in SNeIa. For the production of ^{92}Nb, (γ,n) reactions play the dominant role with some contribution from proton-induced reactions. Since the rates of some of the most important reactions are constrained experimentally, the nuclear uncertainties on the ^{92}Nb production are moderate, resulting in possible variations in the ISM ratio of less than a factor of two. The ^{146}Sm/^{144}Sm ratio, instead, is determined by $(\gamma,n)/(\gamma,\alpha)$ rate ratios, mainly those from ^{148}Gd. The uncertainty range reported by Travaglio et al. (2014) is based on three choices of the ^{148}Gd$(\gamma,\alpha)^{144}$Sm rate. With respect to two previous estimates (Rauscher & Thielemann, 2000; Somorjai et al., 1998), an updated new rate resulted

in a ^{146}Sm/^{144}Sm ratio higher by a factor of two in SNIa, but lower by at least a factor of two in CCSNe (Rauscher, 2013). The ^{146}Sm/^{144}Sm ratio may have an even higher nuclear uncertainty, possibly up to one order of magnitude, owing to the lack of experimental data at the relevant energies (Gyürky et al., 2014).

It should be noted, however, that recent Monte Carlo sensitivity studies of the impact of reaction rate uncertainties on the production of p-process nuclei in SNIa and CCSNe (Nishimura et al., 2018; Rauscher et al., 2016) indicate that, when varying all the rates randomly, nuclear uncertainty effects cancel each other and the final error bars on the p-nuclei abundances are much lower than the error bars obtained when changing only one rate at a time, as done by Travaglio et al. (2014). According to these new studies, therefore, the central values given in the second line of Table 5.2 are actually correct within roughly 10% (although stellar models may also carry some uncertainties). These recent results need to be considered in relation to the problem of ^{92}Nb and ^{146}Sm in the ESS, and this task is part of our current ERC project work (see Section 5.3).

Within the investigation presented here, for ^{92}Nb/^{92}Mo, if we compare the maximum ISM value from GCE allowed within nuclear uncertainties of 3.12×10^5 to the lower limit of the ESS value, we derive a maximum UP time of 5.4 Myr (Table 5.2). The equivalent upper limit solution for ^{146}Sm/^{144}Sm provides an unrealistically high UP time, but consistent with ^{92}Nb/^{92}Mo, given the very large uncertainties. The value of the half life of ^{146}Sm is also debated between the two values of 68 and 103 Myr (see Table 2.2). Here, I have used the lower value, if I used the higher value I would obtain an even longer UP time than reported in Table 5.2. If I decay the ISM abundance of ^{53}Mn corresponding to ^{53}Mn/^{55}Mn ratios of $1.26 - 2.41 \times 10^4$ by the maximum time of 5.4 Myr, derived from ^{92}Nb, I obtain values in the range $4.63 - 5.82 \times 10^{-5}$, roughly one order of magnitude higher than the ESS value (Table 2.2). A longer UP time of 15 Myr, or LE time of 19 Myr, is required to match the observed ^{53}Mn/^{55}Mn. A three times lower ^{53}Mn/^{55}Mn ratio in SNIa may result from a tenfold increase of the ^{32}S$(\beta^+)^{32}$P decay (Parikh et al., 2013), in which case the times derived from ^{53}Mn would decrease to $\simeq$ 9-13 Myr. This possibility needs to be further investigated also within the context of Monte Carlo nuclear sensitivity studies, which, as mentioned above, appear to strongly reduce the impact of single rates on the final abundances. A suggested longer half life for ^{53}Mn (see discussion in Dressler et al., 2012) would instead further increase the times and therefore the mismatch. Another way to reconcile the ESS ^{92}Nb abundance with an isolation time of 15 Myr is a half life of ^{92}Nb roughly a factor of three higher than it current value. This seems unrealistic as the current half life is the weighted average of two experiments that produced similar results in spite of being based on different normalizations: the first (Makino & Honda, 1977) is normalized to the half life of ^{94}Nb, which is not well known, and the second (Nethaway et al., 1978) to an assumed value of the ^{93}Nb(n,2n)^{92}Nb cross section. Finally, to achieve consistency, the ESS ^{92}Nb/^{92}Mo ratio would need to be at least 50% lower than the current nominal value, which is well outside the error bars of the recently reported, high-precision determination of this ratio (Table 2.2).

Therefore, I conclude that SNIa nucleosynthesis results in a too low production of ^{92}Nb, relative to ^{53}Mn, to explain their ESS abundances.
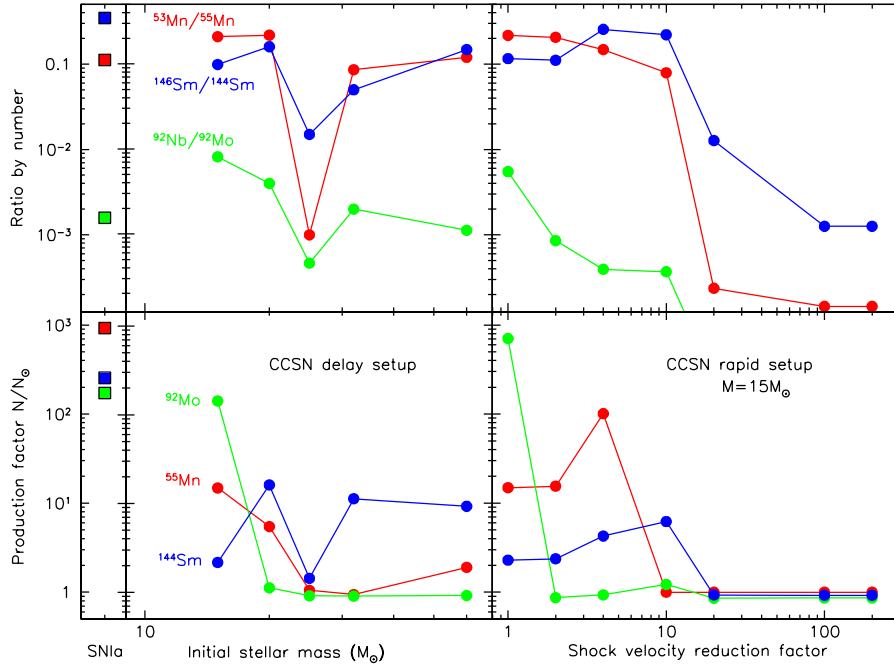
Figure 5.7: Results for the SLR/stable ratios (top panels) and the stable isotope production factors relative to solar (bottom panels) from the SNIa (thin left panels) and CCSN models with different setups, as described in the text (large middle and right panels).

The CCSN source

As described in Section 5.2.1, the γ process in CCSNe does not efficiently produce p-process isotopes in the Mo-Ru region, however, other CCSN nucleosynthesis components may contribute to these isotopes. Pignatari et al. (2016b) computed CCSN models, with initial mass 15 $M_\odot$, that carry an α-rich freeze-out component in the deep layers of the ejecta, where ^{4}He is the most abundant isotope and production of the p-process nuclei up to ^{92}Mo occurs. This is shown by the CCSN models shown in Figure 5.7, together for comparison with the SNIa models of Travaglio et al. (2014, 2011). The CCSN models were computed by Marco Pignatari with solar metallicity $Z = 0.02$ and two setups for the convection-enhanced neutrino-driven explosion (Fryer et al., 2012): the delay setup for all the masses of 15, 20, 25, 32 and 60 $M_\odot$ (left panels of Figure 5.7) and the rapid setup for the 15 $M_\odot$ star with different reduction factors of the standard initial shock velocity used beyond fallback (of 2×10^9 cm s^1, right panels). In comparison to the SNIa models, the CCSN models produce much lower absolute abundances of ^{55}Mn and ^{144}Sm (see bottom panes of the figure), and therefore ^{53}Mn and ^{146}Sm. Significant production of ^{92}Nb and ^{92}Mo occurs, but only in CCSN models of 15 $M_\odot$ with the delay setup and the rapid setup with standard velocity. In these cases, production factors for ^{92}Mo are comparable to those of the SNIa model, and the ^{92}Nb/^{92}Mo ratio is up to five times higher. The reason is that CCSN models with initial mass larger than 15 $M_\odot$ do not eject material exposed to the α-rich freeze-out due to the more extended fallback of the ejecta onto the central compact object. The α-rich freeze-out efficiency also strongly depends on the shock velocity. When its standard value is reduced, even only by a factor of two, the amounts of ^{92}Mo and ^{92}Nb ejected become negligible. This is because for lower shock velocities the bulk of α-rich freeze-out nucleosynthesis is shifted toward lighter elements closer to the Fe

122

group. In summary, the α-rich freeze-out conditions suitable for the production of ^{92}Mo and ^{92}Nb are more likely hosted in CCSNe with initial mass of 15 M$_\odot$ or lower and shock velocities at least as large as those provided by Fryer et al. (2012).

I explored in Table 5.2 the possibility that the ^{92}Nb in the ESS came from the α-rich freeze-out production experienced by these 15 M$_\odot$ CCSN models. Assuming that ^{92}Nb and ^{92}Mo in the Galaxy are produced mainly by these CCSN α-rich freeze-out events, I applied Eq. 5.4 and Eq. 5.5 to calculate the ISM ^{92}Nb/^{92}Mo ratios. Since the ^{92}Nb/^{92}Mo ratios are 2 to 3 times higher than in the SNIa case, the derived timescales are also longer: 31-51 Myr.

5.2.4 Conclusions

The UP and LE times (15 and 19 Myr) derived from ^{55}Mn are consistent with the times of the last r- and s-process events of $\simeq$100 Myr and $\simeq$20 Myr, respectively, derived in Section 5.1 (see Figure 5.6). However, the UP time of <5.4 Myr derived from ^{92}Nb is inconsistent with that derived from ^{53}Mn. One possibility is that the ESS abundance of ^{53}Mn records only the last SNIa event to have occurred 19 Myr before the formation of the Sun, while the ESS abundance of ^{92}Nb (with a 20 times longer half life) records the memory of many events and defines the "true" isolation time, equal to the derived UP time. If I consider the more recent work of Nishimura et al. (2018), who report very small nuclear uncertainties, then, using the central values for the ISM ratios from GCE given in Table 5.2, the UP time derived from ^{92}Nb would be equal to zero and that derived from ^{146}Sm would be 86 Myr, completely incompatible (see also Côté et al., 2019a,b). Another option is that ^{92}Nb may be also, or predominantly, produced in the Galaxy by CCSNe that experienced the α-rich freeze-out, corresponding to the models of Marco Pignatari that have low initial stellar masses and experience a core-collapse with high shock velocities. In the extreme scenario, where all the ^{92}Nb and ^{92}Mo in the ESS came from such events, the UP time would be of the order of 30-50 Myr, still in disagreement with the UP time derived from the ^{53}Mn, as well as those from the s-process isotopes. However, the production of ^{92}Nb in CCSNe is prone to many uncertainties such as shock temperature, mass cut, mixing, etc, and thorough investigations are needed that also take into account information from 3D modelling of core-collapse explosions. Furthermore, light p-process nuclei including ^{92}Nb could have been produced by both SNIa and CCSN events, as indicated also by follow-up GCE models presented for the stable isotopes (Travaglio et al., 2018). In this case the combined SNIa and CCSN production rate would be between the values given in Table 5.2, therefore leading to timescales in potentially better agreement with those coming from the other constraints.

5.3 Implications and outlook

The ERC RADIOSTAR[1] project running from September 2017 to August 2022 is based on the work presented in this chapter as pilot studies. Indeed, since the publication of the material and the theses presented in this chapter, our group made significant advances in both the

---

[1]konkoly.hu/radiostar/

methodologies and the results related to the SLRs in the ESS. We have developed full GCE models of radioactive nuclei and used them to determine the value of K and its uncertainties (Côté et al., 2019a) and to study the full GCE evolution of the s-process SLR ^{107}Pd and ^{182}Hf (Trueman et al. 2021, ApJ, submitted). We have also started to analyse in detail the impact of heterogeneities in the ISM in the SLR abundances. We have started considering temporal granularity of production events and implemented a Monte Carlo method to evaluate statistically the related uncertainties (Côté et al., 2019b; Yagüe López et al., 2021). We have now also moved to the investigation of the spatial granularity of the stellar event, which is complicated because it involves also the impact of the uncertain transport mechanism in the ISM, from possible diffusion to CCSN-driven shocks (Wehmeyer et al., in preparation). We are also implementing the SLRs evolution into a Smooth Particle Hydrodynamics code of the evolution of the Milky Way Galaxy (Kobayashi & Nakasato, 2011). Further, we have used the two well determined SLRs of r-process origin, ^{129}I and ^{247}Cm, to produce the first high-precision isotopic constraint on the last r-process event to contribute to the Solar System matter (Côté et al., 2021). This was achieved as we realised that these two isotopes have an almost identical half lives (Table 2.2), which means that their ratio is preserved since the time of the last r-process event and corresponds directly to the ratio produced in such an event. For the most short-lived nuclei, such as ^{26}Al, ^{36}Cl and ^{41}Cl, we are calculating the effect of a binary companion on their ejection by the winds of massive stars (Brinkman et al., 2019, and Brinkman et al. 2021, ApJ, submitted).

Ultimately, I will be able to apply the tools and expertise built up from the work related to the SLRs to also investigate the cosmic origin and distribution in the Galaxy of the much longer-lived radioactive nuclei ^{40}K, ^{232}Th, and ^{235,238}U (half lives of the order of 1 to 10 Gy), whose decay represents a major source of heat driving the interior mantle convection and surface plate tectonics in terrestrial planets like the Earth (Botelho et al., 2019; Unterborn et al., 2015).

Chapter 6

Summary of the thesis results

1. **The abundance signatures observed in old, metal-poor halo stars, and in post-AGB stars, cannot be explained by the *slow* neutron-capture (*s*) process in AGB stars, nor by a combination of the *s* process and the *rapid* neutron-capture (*r*) processes. This provides evidence that an *intermediate* neutron-capture (*i*) process exists, and its operation can be seen in these stars (Chapter 3).**

   Among the stellar objects showing the signature of *s*-process nucleosynthesis are carbon-enhanced metal-poor (CEMP) and post-AGB stars.

   (a) CEMP stars (with metallicities typically around 1/100 of solar) show high abundances of the elements heavier than iron, which were produced by a former AGB companion and transferred via binary interaction onto the stars now seen as CEMPs. CEMP stars showing excesses in the elements mostly produced by the *s* process (e.g., Ba) have abundance distributions compatible with those predicted by models of AGB stars. CEMP stars showing excesses in elements produced by both the *s* and the *r* processes (e.g., Ba and Eu, respectively) have, instead, abundance distributions incompatible with those predicted by models of AGB stars, even if an initial enhancement of *r*-process elements is included in the models. No combination of the *s* and *r* neutron-capture processes can match their composition, and a different neutron-capture process must be invoked **(Section 3.1, Lugaro et al., 2012b)**.

   (b) Post-AGB stars observed in the Large and Small Magellanic Clouds (with metallicities approximately 1/10 of solar and masses approximately 1.3 M$_\odot$) display extremely high abundances of the elements heavier than iron, however, their abundance patterns cannot be explained by the operation of the *s* process during the former AGB phase. In particular, the Pb abundance is much lower than predicted, while the abundances of the rare-earth elements are higher. This is impossible to produce with the *s* process and points to the operation in nature of a neutron-capture process different from the *s* and *r* processes **(Section 3.2, Lugaro et al., 2015)**.

This thesis was subsequently proven by the *i*-process models of Hampel et al. (2019, 2016).

2. **The stardust silicon carbide (SiC) grains that carry the signature of the *s* process formed in C-rich AGB stars of initial masses between roughly 2 and 4 M$_\odot$ and metallicity from solar up to roughly twice solar. The grain sizes increase, roughly from smaller to larger than a micrometer, with increasing the metallicity of the AGB parent star (Chapter 4, Sections 4.1, 4.2, and 4.3).**

Stardust grains recovered from meteorites originated mostly in AGB stars and their high-precision laboratory analysis shows that they carry the signature of the isotopic compositions of their stellar origin.

(a) The signature of *s*-process nucleosynthesis found in the vast majority of the SiC grains indicates that their parent AGB stars were of initial masses between roughly 2 and 4 M$_\odot$ and metallicity from solar up to roughly twice solar **(Section 4.1, Lugaro et al., 2003a, 2018a, 2014a)**.

(b) Comparison of the grain data to spectroscopic observations of Ba stars, the binary companions of AGB stars at roughly solar metallicity, shows that the size of the SiC grains increases with the metallicity of the parent star. Therefore, AGB stars of metallicity higher than solar are predicted to produce larger grains more favourably than AGB stars of metallicity around solar **(Section 4.2, Lugaro et al., 2020)**.

(c) Using the distribution of the main element silicon in the SiC grains from AGB stars, the age-metallicity relationship of the AGB parent stars can be derived, which shows that the grains must have originated in stars with, on average, higher metallicities than observed in the solar neighbourhood **(Section 4.3, Lewis et al., 2013; Lugaro et al., 1999)**.

This thesis explained why the Earth is observed to be more *s*-process enriched than bodies that formed farther away from the Sun, as the larger SiC grains are the best candidates to have carried *s*-process nucleosynthetic signatures in the proto-planetary disk (Ek et al., 2020).

3. **Stardust oxide and silicate grains showing strong depletion in ^{18}O, known as Group II grains, originated from AGB stars with initial masses above roughly 4 M$_\odot$, where proton captures occur at the base of the convective envelope (Section 4.4, Lugaro et al., 2007, 2017).**

Stardust oxide and silicate grains mostly originate from O-rich AGB stars, but the origin of Group II grains has so far been elusive. Massive AGB stars are predicted and observed to produce vast amounts of O-rich dust, however, no dust grains had been found in the meteoritic stardust inventory that could be interpreted as originating from them. A new rate of the ^{17}O(p,α)^{14}N reaction measured by the LUNA laboratory (located roughly a kilometre underground at the Gran Sasso National Laboratories in Italy) was reported

to be 2 to 2.5 times higher than the previous estimates (Bruno et al., 2016). Using this new rate, models of nucleosynthesis in massive AGB stars that experience the CNO cycle at the base of their envelope are able to match the $^{17}O/^{16}O$ ratios of the Group II grains, together with the predicted depletion of ^{18}O.

4. **The origin of the abundances of radioactive nuclei made by the r- and s-processes in the early Solar System is decoupled, and provides us with independent clocks for the last r-process (a neutron star merger or a rare supernova) and s-process (an AGB star) source that contributed matter to the Solar System. The abundances of the heavy radioactive nuclei of p-process origin should be produced by both Type Ia and core-collapse supernovae (Chapter 5).**

Radioactive nuclei heavier than iron, now extinct, were present at the time when the Sun formed, as inferred from meteoritic analysis. Using their abundances we can measure timescales relating to the history of the Solar System.

(a) The origin of ^{129}I (half life = 15.7 Myr) and ^{182}Hf (half life = 8.90 Myr) in the early Solar System is decoupled. The former is made only by the r process, while the latter is also made by the s process in AGB stars. The s-process origin for ^{182}Hf was revealed by the re-analysis of the temperature dependence of the β-decay of ^{181}Hf, the unstable isotope that precedes ^{182}Hf on the s-process path of neutron captures. Previously, it was believed that ^{181}Hf decays much faster at s-process temperatures (200-300 MK) than at terrestrial temperatures, due to an excited nuclear energy level at 68 keV. However, the existence of this energy level in ^{181}Hf was not confirmed by recent experiments, which means that also in hot stellar environments the decay rate of ^{181}Hf is close to the terrestrial rate. This favours the $^{181}Hf(n,\gamma)^{182}Hf$ reaction and the production of ^{182}Hf in AGB stars. Therefore, ^{129}I and ^{182}Hf have two different origins. The last r-process and s-process events to contribute to the Solar System matter occurred roughly 100 Myr and 30 Myr before the formation of the Sun, respectively **(Section 5.1, Lugaro et al., 2014b)**.

(b) If the p-process radioactive nuclei ^{92}Nb and ^{146}Sm only originated in Type Ia supernovae, there is a discrepancy between timescales relating to the history of the Solar System obtained using ^{92}Nb and those obtained using ^{53}Mn, another main product of Type Ia supernovae. This indicates that ^{92}Nb should also be produced in core-collapse supernovae **(Section 5.2, Lugaro et al., 2016)**.

I used this thesis to prepare my ERC proposal, as proof of concept for the use of radioactive nuclei in understanding the birth of the Sun and its place in the Galaxy as compared to all the other planetary systems currently being discovered.

Acknowledgements

"The one important thing I have learned over the years is the difference between taking one's work seriously and taking one's self seriously. The first is imperative and the second is disastrous." – Margot Fontain

Much has changed since I started working in the field of nuclear astrophysics in 1995. As a community we have solved many puzzles, at the same time we have opened up such a large number of new questions, topics, and interactions, that stellar nucleosynthesis is now one of the most eclectic and far-reaching topics in astrophysics. Today, we can use chemical and isotopic abundances to understand the Big Bang, the first stars, gravitational wave sources, the evolution of galaxies and stellar clusters, and even the formation of solar and extrasolar planets. This success is also due to a vibrant, large community, which I am proud to be part of, including the European ChETEC COST Action and H2020 ChETEC-INFRA project, the USA NSF JINA institute, and the China Institute for Nuclear Astrophysics, as well as the IReNA network of networks and moreover all the colleagues in Japan and Australia, as well as Brazil and India, with whom I enjoy working and discussing. I thank especially the LUNA collaboration, who readily accepted me as a member when I moved back to Europe in 2014.

I would not have learned as much along the way without the support and knowledge exchange I enjoyed at the different institutes I studied, worked, and visited: the University of Torino, my hometown in Italy, Monash University in Melbourne, Australia, the University of Notre Dame in the USA, the Institute of Astronomy in Cambridge in the UK, the University of Utrecht in the Netherlands, and the Institute of Astrophysics of the Canary Islands. I am particularly grateful to the Hungarian Academy of Sciences, who offered me yet another life-changing opportunity, to move to Budapest.

There are truly too many colleagues I need to thank, but first of all are: Roberto Gallino, who taught me to carry out scientific research with tough training and endless enthusiasm, and John Lattanzio, who supported and believed in me all along. I would like to thank Amanda Karakas for her friendship and collaboration, our work together has now exceeded all our expectations. I also thank Michael Wiescher for friendship and support, Marco Pignatari, Chiaki Kobayashi, Alexander Heger, Roland Diehl, Maurizio Busso, Oscar Straniero, Sergio Cristallo,

Appendix A

List of the main acronyms and abbreviations

Table A.1: List of the main acronyms and abbreviations used throughout the thesis.

AGB star	asymptotic giant branch star
CAIs	calcium-aluminium-rich inclusions, the oldest Solar System solids
CEMP star	carbon-enhanced metal-poor star
CCSN	core-collapse supernova
δ (in permil)	isotopic ratio variation relative to solar and multiplied by 1000
δ (in Myr)	time interval between additions of material from a type of stellar source into a given parcel of ISM matter
ESS	early Solar System
GCE	galactic chemical evolution
HBB	hot bottom burning
ISM	interstellar medium
LE	last event to have contributed to the ESS matter
LUNA	Laboratory for Underground Nuclear Astrophysics
NSE	nuclear statistical equilibrium
PMZ	partial mixing zone leading to the formation of the ^{13}C pocket
p process	any process responsible for producing p-rich isotopes heavier than Fe
r process	*rapid* neutron-capture process
s process	*slow* neutron-capture process
SLR	short-lived radionuclide
SNIa	Type Ia (thermonuclear) supernova
T_{Gal}	time elapsed from the birth of the Milky Way Galaxy to the birth of the Sun
$T_{1/2}$	half life of a radioactive nucleus
τ (in Myr)	mean life of a radioactive nucleus
τ (in mbarn^{-1})	time-integrated neutron flux
TDU	third dredge-up
TP	thermal pulse
UP	uniform production (continuous stellar production rates) and instantaneous ISM mixing
Z	stellar metallicity, i.e., total abundance of all the elements except H and He

Appendix B

List of nuclear species in the `dppns45` network

Table B.1: List of nuclear species up to sulphur (S) included in the 328 species network with the element symbol in the first column (where n on first row is for neutrons) and the atomic number in the second column. In the third column, the isotopes in the network are listed for each element. Masses in bold refer to stable or long-lived ($T_{1/2} \sim$ Gyr) isotopes, followed by their solar abundance by number in the format, e.g., 7.15e-01, which stands for 7.15×10^{-1}. Masses in italics refer, instead, to unstable isotopes, with laboratory half lives given in seconds (s), minutes (m), hours (h), days (d), years (y), or million years (My). All the elements listed here are also included in the 77 species network, with one added isotope for P (of mass 34) and one removed isotope of S (at mass 36), in the 77 network relative to the 328 network, indicated in square brackets by plus and minus, respectively. Note that for ^{26}Al, both the ground (g) and isomeric (i) states are included and treated separately.

n	0	*1 10.3m*
H	1	**1** 7.15e-01, **2** 0
He	2	**3** 0, **4** 6.78e-02
Li	3	**7** 1.30e-09
Be	4	*7 53d*
B	5	*8 770ms*
C	6	**12** 2.09e-04, **13** 2.33e-06, *14 5700yr*
N	7	*13 9.965m*, **14** 5.29e-05, **15** 1.21e-07
O	8	*14 70.62s, 15 122.24s*, **16** 3.78e-04, **17** 1.44e-07, **18** 7.56e-07, *19 28.88s*
F	9	*17 64.49s, 18 109.77m*, **19** 2.06e-08, *20 11.07s*
Ne	10	*19 17.22s*, **20** 6.20e-05, **21** 1.49e-07, **22** 4.56e-06, *23 37.24s*
Na	11	*21 22.49s, 22 2.60y*, **23** 1.46e-06, *24 15h*
Mg	12	*23 11.317s*, **24** 2.47e-05, **25** 3.12e-06, **26** 3.43e-06, *27 9.458m*
Al	13	*25 7.183s, 26(g) 0.717My, 26(i) 6.346s*, **27** 2.11e-06, *28 2.245m*
Si	14	*27 4.15s*, **28** 2.34e-05, **29** 1.19e-06, **30** 7.83e-07
P	15	**31** 2.11e-07, *32 14.268d, 33 25.35d* [plus *34 12.43s*]
S	16	**32** 9.81e-06, **33** 7.86e-08, **34** 4.44e-07, *35 87.37d*, [minus **36** 2.07e-09]

Table B.2: Same as Table B.1, but for the elements up to the Fe peak and through the first *s*-process peak (magic number of neutrons = 50, Sr, Y, and Zr). Note that only Fe, Co, and Ni are also included in the 77 species network, with more (plus) or less (minus) isotopes, as indicated in the square brackets. For ^{85}Kr, both the ground (g) and isomeric (i) states are included and treated separately.

Cl	17	**35** 9.21e-08, *36 0.301My*, **37** 2.94e-08
Ar	18	**36** 1.67e-06, *37 35.04d*, **38** 3.03e-07, *39 269y*, **40** 4.85e-10
K	19	**39** 8.01e-08, **40** 1.26e-11, **41** 5.78e-09
Ca	20	**40** 1.35e-06, *41 0.10My*, **42** 9.03e-09, **43** 1.88e-09
		44 2.91e-08, *45 162.61d*, **46** 5.58e-11, *47 4.536d*, **48** 2.61e-09
Sc	21	**45** 8.03e-10, *46 83.79d*, *47 3.35d*, *48 43.67h*
Ti	22	**46** 4.80e-09, **47** 4.33e-09, **48** 4.29e-08, **49** 3.15e-09, **50** 3.01e-09
V	23	**51** 6.51e-09
Cr	24	**52** 2.62e-07, **53** 2.97e-08, **54** 7.39e-09
Mn	25	**55** 2.16e-07
Fe	26	**54** 1.45e-06, *55 2.744y*, **56** 2.28e-05, **57** 5.26e-07
		58 6.99e-08, *59 44.495d*, *60 2.62My*, [plus *61 5.98m*]
Co	27	**59** 5.30e-08, *60 5.27y* [plus *61 1.649h*]
Ni	28	**58** 7.72e-07, *59 0.076My*, **60** 2.97e-07, **61** 1.29e-08
		62 4.12e-08, *63 101.2y*, **64** 1.05e-08 [minus *63*, **64**]
Cu	29	**63** 8.80e-09, *64 17.701h*, **65** 3.92e-09
Zn	30	**64** 1.48e-08, *65 243.93d*, **66** 8.51e-09, **67** 1.25e-09, **68** 5.72e-09, *69 13.756h*
		70 1.89e-10
Ga	31	**69** 5.17e-10, *70 21.14m*, **71** 3.43e-10
Ge	32	**70** 5.67e-10, *71 11.43d*, **72** 7.49e-10, **73** 2.10e-10, **74** 9.87e-10
As	33	**75** 1.43e-10
Se	34	**76** 1.47e-10, **77** 1.19e-10, **78** 3.72e-10, *79 0.326My*, **80** 7.76e-10
Br	35	**79** 1.26e-10, *80 17.68m*, **81** 1.22e-10
Kr	36	**80** 2.96e-11, *81 0.229My*, **82** 1.48e-10, **83** 1.47e-10, **84** 7.24e-10
		85(g) 10.739y, *85(i) 4.48h*, **86** 2.19e-10
Rb	37	**85** 1.16e-10, *86 18.642d*, **87** 4.78e-11
Sr	38	**86** 5.35e-11, **87** 3.74e-11, **88** 4.49e-10, *89 50.563d*, *90 28.90y*
Y	39	**89** 1.06e-10, *90 64.053h*, *91 58.51d*
Zr	40	**90** 1.25e-10, **91** 2.72e-11, **92** 4.16e-11, *93 1.61My*, **94** 4.21e-11, *95*
		96 6.79e-12
Nb	41	**93** 1.84e-11, *94 0.02My*, *95 34.991d*
Mo	42	**94** 5.70e-12, **95** 9.87e-12, **96** 1.04e-11, **97** 5.98e-12, **98** 1.52e-11
Tc	43	*99 0.21My*
Ru	44	**99** 5.25e-12, **100** 5.19e-12, **101** 7.02e-12, **102** 1.30e-11
Rh	45	**103** 8.21e-12
Pd	46	**104** 3.56e-12, **105** 7.14e-12, **106** 8.73e-12, *107 6.5My*, **108** 8.45e-12
Ag	47	**107** 5.88e-12, *108 2.382m*, **109** 5.46e-12

Table B.3: Same as Table B.2, but for the elements through the second *s*-process peak (magic number of neutrons = 82, Ba, La, Ce, Pr, Nd, Sm) and up to the third peak (magic number of neutrons = 126, Pb and Bi).

Cd	48	**108** 3.26e-13, *109 461.4d*, **110** 4.58e-12, **111** 4.70e-12, **112** 8.85e-12 **113** 4.48e-12, **114** 1.05e-11
In	49	**115** 3.94e-12
Sn	50	**116** 1.22e-11, **117** 6.45e-12, **118** 1.95e-11, **119** 7.22e-12, **120** 2.74e-11
Sb	51	**121** 4.19e-12
Te	52	**122** 2.76e-12, **123** 9.64e-13, **124** 5.13e-12, **125** 7.65e-12, **126** 2.04e-11
I	53	**127** 2.54e-11, *128 24.99m, 129 15.7My*
Xe	54	**128** 2.72e-12, **129** 3.39e-11, **130** 5.44e-12, **131** 2.70e-11, **132** 3.30e-11 *133 5.2475d*, **134** 1.22e-11
Cs	55	**133** 8.60e-12, *134 2.0652y, 135 2.3My, 136 13.04d, 137 30.08y*
Ba	56	**134** 2.62e-12, **135** 7.14e-12, **136** 8.50e-12, **137** 1.23e-11, **138** 7.76e-11
La	57	**139** 1.06e-11
Ce	58	**140** 2.41e-11, *141 32.511d*, **142** 3.02e-12
Pr	59	**141** 4.12e-12
Nd	60	**142** 5.45e-12, **143** 2.42e-12, **144** 4.78e-12, **145** 1.77e-12, **146** 3.45e-12 *147 10.98d*, **148** 1.15e-12
Pm	61	*147 2.6534y, 148 5.368d*
Sm	62	**147** 9.34e-13, **148** 7.00e-13, **149** 8.61e-13, **150** 4.60e-13, *151 90y* **152** 1.67e-12
Eu	63	**151** 1.11e-12, *152 13.517y*, **153** 1.21e-12, *154 8.601y, 155 4.753y*
Gd	64	**152** 1.60e-14, *153 240.4d*, **154** 1.75e-13, **155** 1.19e-12, **156** 1.64e-12 **157** 1.25e-12, **158** 1.99e-12, *159 18.479h*, **160** 1.75e-12
Tb	65	**159** 1.49e-12, *160 72.3d, 161 6.89d*
Dy	66	**160** 2.25e-13, **161** 1.82e-12, **162** 2.46e-12, **163** 2.40e-12, **164** 2.73e-12
Ho	67	**165** 2.11e-12
Er	68	**166** 1.99e-12, **167** 1.36e-12, **168** 1.61e-12, *169 9.392d*, **170** 8.87e-13
Tm	69	**169** 9.43e-13, *170 128.6d, 171 1.92y*
Yb	70	**170** 1.77e-13, **171** 8.38e-13, **172** 1.29e-12, **173** 9.58e-13, **174** 1.91e-12
Lu	71	**175** 8.55e-13, **176** 2.48e-14, *177 6.647d*
Hf	72	**176** 1.91e-13, **177** 6.82e-13, **178** 1.00e-12, **179** 5.00e-13, **180** 1.29e-12 *181 42.39d, 182 8.9My*
Ta	73	**181** 5.42e-13, *182 114.74d, 183 5.1d*
W	74	**182** 8.47e-13, **183** 4.57e-13, **184** 9.79e-13, *185 75.1d*, **186** 9.08e-13
Re	75	**185** 4.64e-13, *186 3.7186d*, **187** 8.38e-13
Os	76	**186** 2.56e-13, **187** 2.04e-13, **188** 2.14e-12, **189** 2.60e-12, **190** 4.23e-12 *191 15.4d*, **192** 6.58e-12
Ir	77	**191** 5.57e-12, *192 73.829d*, **193** 9.37e-12
Pt	78	**192** 2.33e-13, *193 50y*, **194** 9.83e-12, **195** 1.01e-11, **196** 7.53e-12
Au	79	**197** 4.51e-12
Hg	80	**198** 1.05e-12, **199** 1.79e-12, **200** 2.44e-12, **201** 1.39e-12, **202** 3.16e-12
Tl	81	**203** 1.24e-12, *204 3.783y*, **205** 2.97e-12
Pb	82	**204** 1.57e-12, *205 17.3My*, **206** 1.46e-11, **207** 1.61e-11, **208** 4.62e-11
Bi	83	**209** 3.20e-12, *210 5.012d*
Po	84	*210 138.376d*

Bibliography

Abate, C., Pols, O. R., Karakas, A. I., & Izzard, R. G. 2015, *A&A*, 576, A118 62

Abate, C., Pols, O. R., & Stancliffe, R. J. 2018, *A&A*, 620, A63 62

Abia, C., Domínguez, I., Gallino, R., et al. 2002, *ApJ*, 579, 817 32, 35, 38

Adams, F. C. 2010, *Ann. Rev. Astron. Astrophys.*, 48, 47 106

Adams, F. C., Fatuzzo, M., & Holden, L. 2014, *ApJ*, 789, 86 108

Adsley, P., Battino, U., Best, A., et al. 2021, *Phys. Rev. C*, 103, 015805 19

Alpher, R. A., Bethe, H., & Gamow, G. 1948, *Phys. Rev.*, 73, 803 iv, 3

Amari, S. 2009, *Publ. Astron. Soc. Austr.*, 26, 266 14

Amari, S., Hoppe, P., Zinner, E., & Lewis, R. S. 1995, *Meteoritics*, 30, 679 86

Amari, S., Lewis, R. S., & Anders, E. 1994, *Geochim. Cosmochim. Acta*, 58, 459 65, 80, 85

Amari, S., Nittler, L. R., Zinner, E., et al. 2001a, *ApJ*, 546, 248 43, 88

Amari, S., Nittler, L. R., Zinner, E., Lodders, K., & Lewis, R. S. 2001b, *ApJ*, 559, 463 43

Amari, S., Zinner, E., & Gallino, R. 2014, *Geochim. Cosmochim. Acta*, 133, 479 44

Amari, S., Zinner, E., & Lewis, R. S. 2000, Meteoritics and Planetary Science, 35, 997 80, 85, 86

Amelin, Y., Kaltenbach, A., Iizuka, T., et al. 2010, *Earth Planet. Sci. Lett.*, 300, 343 45, 104

Anders, E., & Grevesse, N. 1989, *Geochim. Cosmochim. Acta*, 53, 197 2, 4, 66

Angulo, C., Arnould, M., Rayet, M., et al. 1999, *Nucl. Phys. A*, 656, 3 97

Aoki, W., Beers, T. C., Christlieb, N., et al. 2007, *ApJ*, 655, 492 49, 51

Arcones, A., & Montes, F. 2011, *ApJ*, 731, 5 118

Arlandini, C., Käppeler, F., Wisshak, K., et al. 1999, *ApJ*, 525, 886 12, 61, 115

Arnould, M., & Goriely, S. 2003, *Phys. Rep.*, 384, 1 117

Arnould, M., Goriely, S., & Meynet, G. 2006, *A&A*, 453, 653 108

Asplund, M. 2005, *Ann. Rev. Astron. Astrophys.*, 43, 481 2, 35

Asplund, M., Grevesse, N., Sauval, A. J., & Scott, P. 2009, *Ann. Rev. Astron. Astrophys.*, 47, 481 3, 28, 50, 59, 60, 66, 84, 112

Ávila, J. N., Ireland, T. R., Gyngard, F., et al. 2013a, *Geochim. Cosmochim. Acta*, 120, 628 85

Ávila, J. N., Ireland, T. R., Lugaro, M., et al. 2013b, *ApJL*, 768, L18 65

Banerjee, P., Qian, Y.-Z., & Heger, A. 2018, *ApJ*, 865, 120 19, 62

Bao, Z. Y., Beer, H., Käppeler, F., et al. 2000, *Atom. Data Nucl. Data Tables*, 76, 70 61, 69

Battino, U., Pignatari, M., Travaglio, C., et al. 2020, *MNRAS*, 497, 4981 118

Battino, U., Pignatari, M., Ritter, C., et al. 2016, *ApJ*, 827, 30 33

Battino, U., Tattersall, A., Lederer-Woods, C., et al. 2019, *MNRAS*, 489, 1082 18, 33, 59, 76, 77, 82

Beers, T. C., & Christlieb, N. 2005, *Ann. Rev. Astron. Astrophys.*, 43, 531 48

Bennett, M. E., Hirschi, R., Pignatari, M., et al. 2012, *MNRAS*, 420, 3047 117

Bensby, T., Feltzing, S., & Oey, M. S. 2014, *A&A*, 562, A71 86

Bernatowicz, T. J., Cowsik, R., Gibbons, P. C., et al. 1996, *ApJ*, 472, 760 44

Bethe, H. A. 1939, Physical Review, 55, 434 iv

Bethe, H. A., & Critchfield, C. L. 1938, *Phys. Rev.*, 54, 248 iv

Binns, W. R., Israel, M. H., Christian, E. R., et al. 2016, *Science*, 352, 677 46

Bisterzo, S., Gallino, R., Straniero, O., Cristallo, S., & Käppeler, F. 2010, *MNRAS*, 404, 1529 49, 61

—. 2011, *MNRAS*, 418, 284 39, 57, 61

Bisterzo, S., Travaglio, C., Gallino, R., Wiescher, M., & Käppeler, F. 2014, *ApJ*, 787, 10 84

Bisterzo, S., Gallino, R., Käppeler, F., et al. 2015, *MNRAS*, 449, 506 19, 80

Black, D. C., & Pepin, R. O. 1969, *Earth Planet. Sci. Lett.*, 6, 395 40

Blöcker, T. 2001, *A&SS*, 275, 1 59

Boeche, C., Chiappini, C., Minchev, I., et al. 2013, *A&A*, 553, A19 92

Bondarenko, V., Berzins, J., Prokofjevs, P., et al. 2002, *Nucl. Phys. A*, 709, 3 112

Boss, A. P., & Keiser, S. A. 2013, *ApJ*, 770, 51 107

—. 2014, *ApJ*, 788, 20 108

Botelho, R. B., Milone, A. d. C., Meléndez, J., et al. 2019, *MNRAS*, 482, 1690 9, 124

Boujibar, A., Howell, S., Zhang, S., et al. 2021, *ApJL*, 907, L39 95

Brasser, R., & Mojzsis, S. J. 2020, *Nature Astronomy*, 8 40, 102

Breitschwerdt, D., Feige, J., Schulreich, M. M., et al. 2016, *Nature*, 532, 73 46

Brinkman, H. E., Doherty, C. L., Pols, O. R., et al. 2019, *ApJ*, 884, 38 124

Bruno, C. G., Scott, D. A., Aliotta, M., et al. 2016, *Phys. Rev. Lett.*, 117, 142502 97, 98, 99, 127

Buckner, M. Q., Iliadis, C., Kelly, K. J., et al. 2015, *Phys. Rev. C*, 91, 015812 98

Buntain, J. F., Doherty, C. L., Lugaro, M., et al. 2017, *MNRAS*, 471, 824 33, 34

Burbidge, E. M., Burbidge, G. R., Fowler, W. A., & Hoyle, F. 1957, *Rev. Mod. Phys.*, 29, 547 iv, 1, 3, 6

Burkhardt, C., Kleine, T., Oberli, F., et al. 2011, *Earth Planet. Sci. Lett.*, 312, 390 46

Busso, M., Gallino, R., Lambert, D. L., Travaglio, C., & Smith, V. V. 2001, *ApJ*, 557, 802 32, 38

Cameron, A. G. W. 1957, *PASA*, 69, 201 iv

Cameron, A. G. W., & Truran, J. W. 1977, *Icarus*, 30, 447 107, 108

Campbell, S. W., & Lattanzio, J. C. 2008, *A&A*, 490, 769 54, 59

Campbell, S. W., Lugaro, M., & Karakas, A. I. 2010, *A&A*, 522, L6 19

Cannon, R. C. 1993, *MNRAS*, 263, 817 23, 27

Carollo, D., Beers, T. C., Bovy, J., et al. 2012, *ApJ*, 744, 195 49

Casagrande, L., Schönrich, R., Asplund, M., et al. 2011, *A&A*, 530, A138 78, 91

Choi, B.-G., Wasserburg, G. J., & Huss, G. R. 1999, *ApJL*, 522, L133 44

Ciesla, F. J., Mulders, G. D., Pascucci, I., & Apai, D. 2015, *ApJ*, 804, 9 109

Clarkson, O., Herwig, F., & Pignatari, M. 2018, *MNRAS*, 474, L37 20, 62

Clayton, D. D. 1968, Principles of stellar evolution and nucleosynthesis (New York: McGraw-Hill) 6

Clayton, D. D. 1985, in Nucleosynthesis: Challenges and New Developments, ed. W. D. Arnett & J. W. Truran, 65 119

—. 1988, *MNRAS*, 234, 1 69, 79

—. 2003, *ApJ*, 598, 313 89

Clayton, D. D., & Nittler, L. R. 2004a, *Ann. Rev. Astron. Astrophys.*, 42, 39 41

Clayton, D. D., & Nittler, L. R. 2004b, in Origin and Evolution of the Elements, ed. A. McWilliam & M. Rauch, 297 42

Clayton, D. D., & Timmes, F. X. 1997, *ApJ*, 483, 220 89, 92

Clément, D., Mutschke, H., Klein, R., & Henning, T. 2003, *ApJ*, 594, 642 43

Cohen, J. G., Shectman, S., Thompson, I., et al. 2005, *ApJ*, 633, L109 49

Connelly, J. N., Bizzaro, M., Krot, A. N., et al. 2012, *Science*, 338, 651 104

Cook, C. W., Fowler, W. A., Lauritsen, C. C., & Lauritsen, T. 1957, *Phys. Rev.*, 107, 508 7

Côté, B., Lugaro, M., Reifarth, R., et al. 2019a, *ApJ*, 878, 156 115, 119, 123, 124

Côté, B., Yagüe, A., Világos, B., & Lugaro, M. 2019b, *ApJ*, 887, 213 105, 119, 123, 124

Côté, B., Eichler, M., Arcones, A., et al. 2019c, *ApJ*, 875, 106 11

Côté, B., Eichler, M., Yagüe López, A., et al. 2021, *Science*, 371, 945 116, 124

Cowan, J. J., & Rose, W. K. 1977, *ApJ*, 212, 149 14, 19, 62

Cristallo, S., Nanni, A., Cescutti, G., et al. 2020, *A&A*, 644, A8 86

Cristallo, S., Piersanti, L., Straniero, O., et al. 2009a, *Publ. Astron. Soc. Austr.*, 26, 139 19, 54

Cristallo, S., Straniero, O., Gallino, R., et al. 2009b, *ApJ*, 696, 797 23, 32, 33, 34, 49, 66, 76

Cristallo, S., Straniero, O., Piersanti, L., & Gobrecht, D. 2015, *ApJ Suppl. Ser.*, 219, 40 34, 82, 99

Cristallo, S., Piersanti, L., Straniero, O., et al. 2011, *ApJ Suppl. Ser.*, 197, 17 37, 38, 66, 85

Croat, T. K., Bernatowicz, T., Amari, S., Messenger, S., & Stadermann, F. J. 2003, *Geochim. Cosmochim. Acta*, 67, 4705 44

Cseh, B., Lugaro, M., D'Orazi, V., et al. 2018, *A&A*, 620, A146 18, 34, 35, 38, 39, 63, 77, 79, 81

Cyburt, R. H. e. a. 2010, *ApJ Suppl. Ser.*, 189, 240 81

Dauphas, N., & Chaussidon, M. 2011, *Ann. Rev. Earth Planet. Sci.*, 39, 351 47, 104

Dauphas, N., Davis, A. M., Marty, B., & Reisberg, L. 2004, *Earth Planet. Sci. Lett.*, 226, 465 42

Dauphas, N., Rauscher, T., Marty, B., & Reisberg, L. 2003, *Nucl. Phys. A*, 719, 287c 118

de Castro, D. B., Pereira, C. B., Roig, F., et al. 2016, *MNRAS*, 459, 4299 35, 39, 63, 77, 78, 79

De Marco, O., & Izzard, R. G. 2017, *Publ. Astron. Soc. Austr.*, 34, e001 38

De Smedt, K., Van Winckel, H., Kamath, D., et al. 2014, *A&A*, 563, L5 58, 60

De Smedt, K., Van Winckel, H., Karakas, A. I., et al. 2012, *A&A*, 541, A67 35, 58

Dell'Agli, F., Ventura, P., Schneider, R., et al. 2015, *MNRAS*, 447, 2992 64

Demyk, K., Dartois, E., Wiesemeyer, H., Jones, A. P., & d'Hendecourt, L. 2000, *A&A*, 364, 170 43

den Hartogh, J. W., Hirschi, R., Lugaro, M., et al. 2019, *A&A*, 629, A123 18, 34, 76, 77

Denissenkov, P. A., Truran, J. W., Herwig, F., et al. 2015, *MNRAS*, 447, 2696 62

Diehl, R. 2013, *Reports on Progress in Physics*, 76, 026301 108

Diehl, R., Hartmann, D. H., & Prantzos, N., eds. 2018, Astrophysics with Radioactive Isoptopes, Vol. 453 (Springer ASSL), 3–27 104

Dillmann, I., Heil, M., Käppeler, F., et al. 2006, in American Institute of Physics Conference Series, Vol. 819, Capture Gamma-Ray Spectroscopy and Related Topics, ed. A. Woehr & A. Aprahamian, 123–127 31

Dinerstein, H. L. 2001, *ApJ*, 550, L223 38

Doherty, C. L., Gil-Pons, P., Lau, H. H. B., Lattanzio, J. C., & Siess, L. 2014a, *MNRAS*, 437, 195 20

—. 2014b, *MNRAS*, 437, 195 24

Doherty, C. L., Gil-Pons, P., Lau, H. H. B., et al. 2014c, *MNRAS*, 441, 582 24

Doherty, C. L., Gil-Pons, P., Siess, L., Lattanzio, J. C., & Lau, H. H. B. 2015, *MNRAS*, 446, 2599 24

Dressler, R., Ayranov, M., Bemmerer, D., et al. 2012, *Jour. Phys. G*, 39, 105201 121

Duprat, J., & Tatischeff, V. 2007, *ApJ*, 671, L69 107

Dwarkadas, V. V., Dauphas, N., Meyer, B., Boyajian, P., & Bojazi, M. 2017, *ApJ*, 851, 147 108

Efron, B. 1979, *Ann. Statist.*, 7, 1 84

Eggleton, P. P. 1972, *MNRAS*, 156, 361 55

Ek, M., Hunt, A. C., Lugaro, M., & Schönbächler, M. 2020, *Nature Astronomy*, 4, 273 10, 40, 42, 102, 126

Farouqi, K., Kratz, K. L., & Pfeiffer, B. 2009, *Publ. Astron. Soc. Austr.*, 26, 194 118

Fenner, Y., Gibson, B. K., Lee, H.-c., et al. 2003, *Publ. Astron. Soc. Austr.*, 20, 340 89

Ferrarotti, A. S., & Gail, H. P. 2006, *A&A*, 447, 553 64

Fimiani, L., Cook, D. L., Faestermann, T., et al. 2016, *Phys. Rev. Lett.*, 116, 151104 46

Fishlock, C. K., Karakas, A. I., Lugaro, M., & Yong, D. 2014, *ApJ*, 797, 44 17, 33, 63

Fisker, J. L., Hoffman, R. D., & Pruet, J. 2009, *ApJ*, 690, L135 118

Frebel, A., Christlieb, N., Norris, J. E., et al. 2007, *ApJ*, 660, L117 104

Fröhlich, C., Hix, W. R., Martínez-Pinedo, G., et al. 2006, *New Astron. Rev.*, 50, 496 118

Fryer, C. L., Belczynski, K., Wiktorowicz, G., et al. 2012, *ApJ*, 749, 91 122, 123

Fujimoto, Y., Krumholz, M. R., & Tachibana, S. 2018, *MNRAS*, 480, 4025 107, 108

Fuller, G. M., Fowler, W. A., & Newman, M. J. 1982, *ApJ Suppl. Ser.*, 48, 279 32

Gaches, B. A. L., Walch, S., Offner, S. S. R., & Münker, C. 2020, *ApJ*, 898, 79 107

Gaidos, E., Krot, A. N., Williams, J. P., & Raymond, S. N. 2009, *ApJ*, 696, 1854 108

Gail, H.-P., Zhukovska, S. V., Hoppe, P., & Trieloff, M. 2009, *ApJ*, 698, 1136 86, 91, 95, 96

Gallino, R., Arlandini, C., Busso, M., et al. 1998, *ApJ*, 497, 388 34, 79, 87

Gallino, R., Busso, M., & Lugaro, M. 1997, in American Institute of Physics Conference Series, Vol. 402, American Institute of Physics Conference Series, ed. E. K. Zinner & T. J. Bernatowicz, 115–153 79

Garcia-Hernandez, D. A., Garcia-Lario, P., Plez, B., et al. 2006, *Science*, 314, 1751 18, 34, 35, 36

García-Hernández, D. A., Zamora, O., Yagüe, A., et al. 2013, *A&A*, 555, L3 34

García-Hernández, D. A., Manchado, A., Lambert, D. L., et al. 2009, *ApJ*, 705, L31 18

Goodson, M. D., Luebbers, I., Heitsch, F., & Frazer, C. C. 2016, *MNRAS*, 462, 2777 108

Goriely, S. 1999, *A&A*, 342, 881 19, 111

Goriely, S., & Janka, H.-T. 2016, *MNRAS*, 459, 4174 115

Goriely, S., & Siess, L. 2004, *A&A*, 421, L25 34

Gounelle, M. 2015, *A&A*, 582, A26 109

Gounelle, M., & Meynet, G. 2012, *A&A*, 545, A4 108, 117

Gounelle, M., Shu, F. H., Shang, H., et al. 2006, *ApJ*, 640, 1163 107

Grawe, H., Langanke, K., & Martínez-Pinedo, G. 2007, Reports on Progress in Physics, 70, 1525 11

Gritschneder, M., Lin, D. N. C., Murray, S. D., Yin, Q.-Z., & Gong, M.-N. 2012, *ApJ*, 745, 22 108

Groenewegen, M. A. T., van den Hoek, L. B., & de Jong, T. 1995, *A&A*, 293, 381 91

Groopman, E., Zinner, E., Amari, S., et al. 2015, *ApJ*, 809, 31 85

Guber, K. H., Koehler, P. E., Derrien, H., et al. 2003, *Phys. Rev. C*, 67, 062802 90

Guo, B., Li, Z. H., Lugaro, M., et al. 2012, *ApJ*, 756, 193 31

Gyngard, F., Amari, S., Zinner, E., & Ott, U. 2009, *ApJ*, 694, 359 90

Gyngard, F., Zinner, E., Nittler, L. R., et al. 2010, *ApJ*, 717, 107 100

Gyürky, G., Fülöp, Z., Halász, Z., Kiss, G. G., & Szücs, T. 2014, *Phys. Rev. C*, 90, 052801 121

Hampel, M., Karakas, A. I., Stancliffe, R. J., Meyer, B. S., & Lugaro, M. 2019, *ApJ*, 887, 11 20, 62, 81, 126

Hampel, M., Stancliffe, R. J., Lugaro, M., & Meyer, B. S. 2016, *ApJ*, 831, 171 20, 62, 81, 126

Hayakawa, T., Nakamura, K., Kajino, T., et al. 2013, *ApJ*, 779, L9 118

Hayden, M. R., Bovy, J., Holtzman, J. A., et al. 2015, *ApJ*, 808, 132 78, 86

Heck, P. R., Greer, J., Kööp, L., et al. 2020, *Proc. Natl. Acad. Sci. USA*, 117, 1884 78, 90

Heger, A., Langer, N., & Woosley, S. E. 2000, *ApJ*, 528, 368 26

Heger, A., & Woosley, S. E. 2010, *ApJ*, 724, 341 111

Heil, M., Detwiler, R., Azuma, R. E., et al. 2008, *Phys. Rev. C*, 78, 025803 31

Herwig, F., Langer, N., & Lugaro, M. 2003, *ApJ*, 593, 1056 18

Herwig, F., Pignatari, M., Woodward, P. R., et al. 2011, *ApJ*, 727, 89 19, 27, 62

Herwig, F., Woodward, P. R., Lin, P.-H., Knox, M., & Fryer, C. 2014, *ApJ*, 792, L3 55

Hester, J. J., Desch, S. J., Healy, K. R., & Leshin, L. A. 2004, *Science*, 304, 1116 109

Hoffman, R. D., Woosley, S. E., Fuller, G. M., & Meyer, B. S. 1996, *ApJ*, 460, 478 118

Höfner, S., & Olofsson, H. 2018, *A&A Rev.*, 26, 1 37

Holmberg, J., Nordström, B., & Andersen, J. 2007, *A&A*, 475, 519 91

Holst, J. C., Olsen, M. B., Paton, C., et al. 2013, *Proc. Natl. Acad. Sci. USA*, 110, 88198823 117

Hoppe, P., Amari, S., Zinner, E., Ireland , T., & Lewis, R. S. 1994, *ApJ*, 430, 870 85

Hoppe, P., Amari, S., Zinner, E., & Lewis, R. S. 1995, *Geochim. Cosmochim. Acta*, 59, 4029 44

Hoppe, P., Annen, P., Strebel, R., et al. 1997, *ApJL*, 487, L101 43, 88

Hoppe, P., Leitner, J., & Kodolányi, J. 2018, *ApJ*, 869, 47 95

Hoppe, P., Leitner, J., Meyer, B. S., et al. 2009, *ApJL*, 691, L20 90

Hoppe, P., & Ott, U. 1997, in American Institute of Physics Conference Series, Vol. 402, American Institute of Physics Conference Series, ed. T. J. Bernatowicz & E. Zinner, 27–58 43, 64

Hoppe, P., Strebel, R., Eberhardt, P., Amari, S., & Lewis, R. S. 1996, *Geochim. Cosmochim. Acta*, 60, 883 80, 85

Howard, W. M., Meyer, B. S., & Clayton, D. D. 1992, *Meteoritics*, 27, 404 14

Hoyle, F. 1946, *MNRAS*, 106, 343 iv

Huss, G. R., Meyer, B. S., Srinivasan, G., Goswami, J. N., & Sahijpal, S. 2009, *Geochim. Cosmochim. Acta*, 73, 4922 119

Hynes, K. M., & Gyngard, F. 2009, in Lunar and Planetary Science Conference, Vol. 40, Lunar and Planetary Science Conference, 1198 43, 89

Iliadis, C. 2007, Nuclear Physics of Stars (Wiley-VCH Verlag, Wenheim, Germany) 6

Iliadis, C., Angulo, C., Descouvemont, P., Lugaro, M., & Mohr, P. 2008, *Phys. Rev. C*, 77, 045802 97, 98

Iliadis, C., Longland, R., Champagne, A. E., & Coc, A. 2010, *Nucl. Phys. A*, 841, 323 31, 96, 98, 99, 101

Ireland, T. R., Ávila, J. N., Lugaro, M., et al. 2018, *Geochim. Cosmochim. Acta*, 221, 200 86

Jacobsen, B., Yin, Q.-Z., Moynier, F., et al. 2008, *Earth Planet. Sci. Lett.*, 272, 353 106

Jacquet, E. 2019, *A&A*, 624, A131 107

Jadhav, M., Amari, S., Marhas, K. K., et al. 2008, *ApJ*, 682, 1479 95

Janka, H.-T. 2012, *Ann. Rev. Nucl. Part. Sci.*, 62, 407 8

Jones, S., Ritter, C., Herwig, F., et al. 2016, *MNRAS*, 455, 3848 19, 62

Jonsell, K., Barklem, P. S., Gustafsson, B., et al. 2006, *A&A*, 451, 651 49, 57

Jorissen, A., Boffin, H. M. J., Karinkuzhi, D., et al. 2019, *A&A*, 626, A127 35

José, J., Halabi, G. M., & El Eid, M. F. 2016, *A&A*, 593, A54 43

Jura, M., Xu, S., & Young, E. D. 2013, *ApJ*, 775, L41 109

Justtanont, K., Barlow, M. J., Blommaert, J., et al. 2015, *A&A*, 578, A115 100

Kamath, D., Karakas, A. I., & Wood, P. R. 2012, *ApJ*, 746, 20 25, 66

Karakas, A. I. 2010, *MNRAS*, 403, 1413 25, 50, 66

—. 2014, *MNRAS*, 445, 347 23, 24, 25, 66

Karakas, A. I., García-Hernández, D. A., & Lugaro, M. 2012, *ApJ*, 751, 8 34, 50

Karakas, A. I., & Lattanzio, J. C. 2003, *Publ. Astron. Soc. Austr.*, 20, 393 52

—. 2014, *Publ. Astron. Soc. Austr.*, 31, id. e030 15, 85

Karakas, A. I., & Lugaro, M. 2016, *ApJ*, 825, 26 24, 33, 34, 63, 66, 76, 85, 99

Karakas, A. I., Lugaro, M., Carlos, M., et al. 2018, *MNRAS*, 477, 421 63

Karakas, A. I., Lugaro, M., Wiescher, M., Goerres, J., & Ugalde, C. 2006, *ApJ*, 643, 471 19

Kerschbaum, F., Maercker, M., Brunner, M., et al. 2017, *A&A*, 605, A116 15

Kilpatrick, C. D., Foley, R. J., Kasen, D., et al. 2017, *Science*, 358, 1583 11

Kinoshita, N., Paul, M., Kashiv, Y., et al. 2012, *Science*, 335, 1614 46

Kleine, T., Budde, G., Burkhardt, C., et al. 2020, *Space Science Reviews*, 216, 55 42, 102

Kobayashi, C., Karakas, A. I., & Lugaro, M. 2020, *ApJ*, 900, 179 63

Kobayashi, C., Karakas, A. I., & Umeda, H. 2011, *MNRAS*, 414, 3231 50, 85, 89

Kobayashi, C., & Nakasato, N. 2011, *ApJ*, 729, 16 86, 92, 124

Krause, M. G. H., Burkert, A., Diehl, R., et al. 2018, *A&A*, 619, A120 107

Kruijer, T. S., Burkhardt, C., Budde, G., & Kleine, T. 2017, *Proc. Natl. Acad. Sci. USA*, 114, 6712 40, 102

Kusakabe, M., Iwamoto, N., & Nomoto, K. 2011, *ApJ*, 726, 25 118

Lacki, B. C. 2014, *MNRAS*, 440, 3738 108

Lattanzio, J., Frost, C., Cannon, R., & Wood, P. R. 1996, *Mem. Soc. Astron. It.*, 67, 729 23

Lattanzio, J. C. 1986, *ApJ*, 311, 708 24

—. 1989, *ApJL*, 344, L25 24

—. 1991, *ApJ Suppl. Ser.*, 76, 215 23

Lau, H. H. B., Stancliffe, R. J., & Tout, C. A. 2009, *MNRAS*, 396, 1046 54

Lederer, M. T., & Aringer, B. 2009, *A&A*, 494, 403 59

Lee, T., Papanastassiou, D. A., & Wasserburg, G. J. 1977, *ApJ*, 211, L107 47

Lee, T., Shu, F. H., Shang, H., Glassgold, A. E., & Rehm, K. E. 1998, *ApJ*, 506, 898 107

Lewis, K. M., Lugaro, M., Gibson, B. K., & Pilkington, K. 2013, *ApJL*, 768, L19 43, 85, 87, 89, 90, 91, 93, 126

Li, K. A., Lam, Y. H., Qi, C., Tang, X. D., & Zhang, N. T. 2016, *Phys. Rev. C*, 94, 065807 19, 74

Lichtenberg, T., Golabek, G. J., Burn, R., et al. 2019, *Nature Astronomy*, 3, 307 36, 109

Lichtenberg, T., Golabek, G. J., Gerya, T. V., & Meyer, M. R. 2016a, *Icarus*, 274, 350 109

Lichtenberg, T., Parker, R. J., & Meyer, M. R. 2016b, *MNRAS*, 462, 3979 108

Liu, N., Gallino, R., Bisterzo, S., et al. 2014a, *ApJ*, 788, 163 65, 66, 67, 70, 71

Liu, N., Gallino, R., Cristallo, S., et al. 2018a, *ApJ*, 865, 112 65, 76, 77, 79, 80, 84

Liu, N., Nittler, L. R., Alexander, C. M. O. D., & Wang, J. 2018b, *Science Advances*, 4, eaao1054 43

Liu, N., Nittler, L. R., Pignatari, M., O'D. Alexander, C. M., & Wang, J. 2017a, *ApJL*, 842, L1 43

Liu, N., Savina, M. R., Davis, A. M., et al. 2014b, *ApJ*, 786, 66 65, 72

Liu, N., Savina, M. R., Gallino, R., et al. 2015, *ApJ*, 803, 12 65, 66, 70, 72, 73, 74, 79

Liu, N., Stephan, T., Boehnke, P., et al. 2017b, *ApJL*, 844, L12 43

Liu, N., Stephan, T., Cristallo, S., et al. 2019, *ApJ*, 881, 28 43

Lodders, K. 2010, *Astrophys. Space Sci. Proceedings*, 16, 379 3

—. 2020, Oxford Research Encyclopedia of Planetary Science, Oxford University Press, arXiv:1912.00844 3

Lodders, K., & Fegley, Bruce, J. 1997, *ApJL*, 484, L71 35

Lodders, K., Palme, H., & Gail, H.-P. 2009, Landolt-Börnstein, New Series VI/4B, 34, Chapter 4.4. 46

Longland, R., Iliadis, C., & Karakas, A. I. 2012, *Phys. Rev. C*, 85, 065809 19

Lucatello, S., Beers, T. C., Christlieb, N., et al. 2006, *ApJL*, 652, L37 49

Lucatello, S., Tsangarides, S., Beers, T. C., et al. 2005, *ApJ*, 625, 825 49

Ludwig, P., Bishop, S., Egli, R., et al. 2016, *Proc. Natl. Acad. Sci. USA*, 113, 9232 46

Lugaro, M. 2005, Stardust from meteorites. An introduction to presolar grains (World Scientific Series in Astronomy and Astrophysics, Vol. 9, New Jersey, London, Singapore: World Scientific) 41, 64

Lugaro, M., Campbell, S. W., & de Mink, S. E. 2009, *Publ. Astron. Soc. Austr.*, 26, 322 49, 57

Lugaro, M., Campbell, S. W., Van Winckel, H., et al. 2015, *A&A*, 583, A77 60, 125

Lugaro, M., & Chieffi, A. 2018, Chapter 3 of Astrophysics with Radioactive Isotopes, ed. R. Diehl, D. H. Hartmann, & N. Prantzos, Lecture Notes in Physics, Berlin Springer Verlag 17, 28

Lugaro, M., Davis, A. M., Gallino, R., et al. 2003a, *ApJ*, 593, 486 29, 30, 64, 65, 69, 70, 76, 126

Lugaro, M., Doherty, C. L., Karakas, A. I., et al. 2012a, *Meteorit. Planet. Sci.*, 47, 1998 vi, 20, 108

Lugaro, M., Herwig, F., Lattanzio, J. C., Gallino, R., & Straniero, O. 2003b, *ApJ*, 586, 1305 18, 33

Lugaro, M., Karakas, A. I., Nittler, L. R., et al. 2007, *A&A*, 461, 657 96, 97, 100, 126

Lugaro, M., Karakas, A. I., Pető, M., & Plachy, E. 2018a, *Geochim. Cosmochim. Acta*, 221, 6 67, 70, 72, 73, 77, 126

Lugaro, M., Karakas, A. I., Stancliffe, R. J., & Rijs, C. 2012b, *ApJ*, 747, 2 24, 33, 51, 53, 56, 62, 63, 125

Lugaro, M., Liffman, K., Ireland, T. R., & Maddison, S. T. 2012c, *ApJ*, 759, 51 vi

Lugaro, M., Ott, U., & Keresztúri, Á. 2018b, *Progr. Part. Nucl. Phys.*, 102, 1 36, 46, 47, 107, 108

Lugaro, M., Pignatari, M., Ott, U., et al. 2016, *Proc. Natl. Acad. Sci. USA*, 113, 907 119, 127

Lugaro, M., Tagliente, G., Karakas, A. I., et al. 2014a, *ApJ*, 780, 95 31, 65, 69, 70, 126

Lugaro, M., Ugalde, C., Karakas, A. I., et al. 2004, *ApJ*, 615, 934 vi

Lugaro, M., Zinner, E., Gallino, R., & Amari, S. 1999, *ApJ*, 527, 369 43, 64, 85, 86, 87, 89, 92, 94, 126

Lugaro, M., Heger, A., Osrin, D., et al. 2014b, *Science*, 345, 650 110, 111, 112, 116, 127

Lugaro, M., Karakas, A. I., Bruno, C. G., et al. 2017, *Nature Astronomy*, 1, 0027 96, 98, 99, 100, 126

Lugaro, M., Cseh, B., Világos, B., et al. 2020, *ApJ*, 898, 96 75, 78, 82, 126

Luu, T.-H., Hin, R. C., Coath, C. D., & Elliott, T. 2019, *Earth Planet. Sci. Lett.*, 522, 166 106

Madonna, S., Bautista, M., Dinerstein, H. L., et al. 2018, *ApJL*, 861, L8 38

Makino, T., & Honda, M. 1977, *Geochim. Cosmochim. Acta*, 41, 1521 121

Marigo, P., Cummings, J. D., Curtis, J. L., et al. 2020, *Nature Astronomy*, 4, 1102 25, 91

Marks, N. E., Borg, L. E., Hutcheon, I. D., Jacobsen, B., & Clayton, R. N. 2014, *Earth Planet. Sci. Lett.*, 405, 15 45, 46

Masseron, T., Johnson, J. A., Plez, B., et al. 2010, *A&A*, 509, A93 51

Merrill, S. P. W. 1952, *ApJ*, 116, 21 iv

Meyer, B. 2012, in Nuclei in the Cosmos (NIC XII), ed. J. Lattanzio, A. Karakas, M. Lugaro, & G. Dracoulis, 96 81

Meyer, B. S. 2005, in Astronomical Society of the Pacific Conference Series, Vol. 341, Chondrites and the Protoplanetary Disk, ed. A. N. Krot, E. R. D. Scott, & B. Reipurth, 515 110

Meyer, B. S., & Clayton, D. D. 2000, *Space Sci. Rev.*, 92, 133 108, 110, 115

Mishenina, T., Pignatari, M., Gorbaneva, T., et al. 2019, *MNRAS*, 484, 3846 92

Mishenina, T. V., Pignatari, M., Korotin, S. A., et al. 2013, *A&A*, 552, A128 86

Mostefaoui, S., & Hoppe, P. 2004, *ApJL*, 613, L149 90, 95

Murray, N. 2011, *ApJ*, 729, id. 133 116

Nanne, J. A. M., Nimmo, F., Cuzzi, J. N., & Kleine, T. 2019, *Earth Planet. Sci. Lett.*, 511, 44 40

Nanni, A., Bressan, A., Marigo, P., & Girardi, L. 2013, *MNRAS*, 434, 2390 64

Nethaway, D. R., Prindle, A. L., & van Konynenburg, R. A. 1978, *Phys. Rev. C*, 17, 1409 121

Nguyen, A. N., Nittler, L. R., Stadermann, F. J., Stroud, R. M., & Alexander, C. M. O. 2010, *ApJ*, 719, 166 90, 95

Nguyen, A. N., Stadermann, F. J., Zinner, E., et al. 2007, *ApJ*, 656, 1223 45

Nguyen, A. N., & Zinner, E. 2004, *Science*, 303, 1496 43

Nicholson, R. B., & Parker, R. J. 2017, *MNRAS*, 464, 4318 108

Nicolussi, G. K., Pellin, M. J., Lewis, R. S., et al. 1998, *ApJ*, 504, 492 69

Nishimura, N., Rauscher, T., Hirschi, R., et al. 2018, *MNRAS*, 474, 3133 121, 123

Nissen, P. E., Christensen-Dalsgaard, J., Mosumgaard, J. R., et al. 2020, *A&A*, 640, A81 78, 102, 103

Nittler, L. R. 2005, *ApJ*, 618, 281 85, 89, 92, 94, 95

Nittler, L. R., & Alexander, C. M. O. 1999, *ApJ*, 526, 249 89

Nittler, L. R., Alexander, C. M. O., Gallino, R., et al. 2008, *ApJ*, 682, 1450 95, 101

Nittler, L. R., Alexander, O., Gao, X., Walker, R. M., & Zinner, E. 1997, *ApJ*, 483, 475 44, 95

Nittler, L. R., & Ciesla, F. 2016, *Ann. Rev. Astron. Astrophys.*, 54, 53 41

Nittler, L. R., Hoppe, P., Alexander, C. M. O., et al. 1995, *ApJL*, 453, L25 44

Nollett, K. M., Busso, M., & Wasserburg, G. J. 2003, *ApJ*, 582, 1036 97

Nucci, M. C., & Busso, M. 2014, *ApJ*, 787, 141 97

Ott, U., & Begemann, F. 1990, *ApJL*, 353, L57 79

Ott, U., & Kratz, K.-L. 2008, *New Astron. Rev.*, 52, 396 110

Ouellette, N., Desch, S. J., & Hester, J. J. 2007, *ApJ*, 662, 1268 109

—. 2010, *ApJ*, 711, 597 109

Palmerini, S., La Cognata, M., Cristallo, S., & Busso, M. 2011, *ApJ*, 729, 3 97

Palmerini, S., Trippella, O., Busso, M., et al. 2018, *Geochim. Cosmochim. Acta*, 221, 21 77

Pan, L., Desch, S. J., Scannapieco, E., & Timmes, F. X. 2012, *ApJ*, 756, 102 108

Parikh, A., José, J., Seitenzahl, I. R., & Röpke, F. K. 2013, *A&A*, 557, A3 121

Pereira, C. B., Sales Silva, J. V., Chavero, C., Roig, F., & Jilinski, E. 2011, *A&A*, 533, A51 39, 78, 79

Pérez-Mesa, V., Zamora, O., García-Hernández, D. A., et al. 2017, *A&A*, 606, A20 35

Piersanti, L., Cristallo, S., & Straniero, O. 2013, *ApJ*, 774, 98 18, 76

Pignatari, M., Göbel, K., Reifarth, R., & Travaglio, C. 2016a, *Int. Jour. Mod. Phys. E*, 25, 1630003 10

Pignatari, M., Wiescher, M., Timmes, F. X., et al. 2013a, *ApJ*, 767, L22 43, 44

Pignatari, M., Hirschi, R., Wiescher, M., et al. 2013b, *ApJ*, 762, 31 118

Pignatari, M., Herwig, F., Hirschi, R., et al. 2016b, *ApJ Suppl. Ser.*, 225, 24 122

Pilkington, K., Gibson, B. K., Brook, C. B., et al. 2012, *MNRAS*, 425, 969 92

Podosek, F. A., Prombo, C. A., Amari, S., & Lewis, R. S. 2004, *ApJ*, 605, 960 79, 80

Poole, G. M., Rehkämper, M., Coles, B. J., Goldberg, T., & Smith, C. L. 2017, *Earth Planet. Sci. Lett.*, 473, 215 1

Portegies Zwart, S., Pelupessy, I., van Elteren, A., Wijnen, T. P. G., & Lugaro, M. 2018, *A&A*, 616, A85 108

Prantzos, N., Hashimoto, M., Rayet, M., & Arnould, M. 1990, *A&A*, 238, 455 117

Prombo, C. A., Podosek, F. A., Amari, S., & Lewis, R. S. 1993, *ApJ*, 410, 393 80

Ramírez, I., Allende Prieto, C., & Lambert, D. L. 2013, *ApJ*, 764, 78 92

Rapp, W., Görres, J., Wiescher, M., Schatz, H., & Käppeler, F. 2006, *ApJ*, 653, 474 117

Ratzel, U., Arlandini, C., Käppeler, F., et al. 2004, *Phys. Rev. C*, 70, 065803 31

Rauscher, T. 2006, *Phys. Rev. C*, 73, 015804 117

—. 2012, *ApJ*, 755, L10 19

—. 2013, *Phys. Rev. Lett.*, 111, 061104 121

Rauscher, T., Dauphas, N., Dillmann, I., et al. 2013, *Reports on Progress in Physics*, 76, 066201 117, 118

Rauscher, T., Heger, A., Hoffman, R. D., & Woosley, S. E. 2002, *ApJ*, 576, 323 111, 117

Rauscher, T., Nishimura, N., Hirschi, R., et al. 2016, *MNRAS*, 463, 4153 121

Rauscher, T., & Thielemann, F.-K. 2000, *Atom. Data Nucl. Data Tables*, 75, 1 120

Raut, R., Tonchev, A. P., Rusev, G., et al. 2013, *Phys. Rev. Letters*, 111, 112501 31

Rayet, M., Arnould, M., Hashimoto, M., Prantzos, N., & Nomoto, K. 1995, *A&A*, 298, 517 117

Reimers, D. 1975, Circumstellar envelopes and mass loss of red giant stars (Problems in stellar atmospheres and envelopes.), 229–256 50, 90

Reyniers, M., & Van Winckel, H. 2003, *A&A*, 408, L33 58

Reyniers, M., Van Winckel, H., Gallino, R., & Straniero, O. 2004, *A&A*, 417, 269 38, 58

Reynolds, J. H., & Turner, G. 1964, *Jour. Geophys. Res.*, 69, 3263 40, 43

Robert, F., Tartese, R., Lombardi, G., et al. 2020, *Nature Astronomy*, 2 64

Savina, M. R., Pellin, M. J., Tripa, C. E., et al. 2003, *Geochim. Cosmochim. Acta*, 67, 3215 44, 65

Seitenzahl, I. R., Cescutti, G., Röpke, F. K., Ruiter, A. J., & Pakmor, R. 2013, *A&A*, 559, L5 118, 120

Shetye, S., Van Eck, S., Goriely, S., et al. 2020, *A&A*, 635, L6 37

Siess, L. 2006, *A&A*, 448, 717 24

Siess, L., Goriely, S., & Langer, N. 2004, *A&A*, 415, 1089 18

Simonucci, S., Taioli, S., Palmerini, S., & Busso, M. 2013, *ApJ*, 764, 118 32

Skúladóttir, Á., Hansen, C. J., Salvadori, S., & Choplin, A. 2019, *A&A*, 631, A171 10

Sloan, G. C., Kraemer, K. E., Wood, P. R., et al. 2008, *ApJ*, 686, 1056 93

Sneden, C., Cowan, J. J., & Gallino, R. 2008, *Ann. Rev. Astron. Astrophys.*, 46, 241 9, 12, 48, 49, 50

Somorjai, E., Fülöp, Z., Kiss, A. Z., et al. 1998, *A&A*, 333, 1112 120

Sossi, P. A., Moynier, F., Chaussidon, M., et al. 2017, *Nature Astronomy*, 1, 0055 107

Speck, A. K., & Hofmeister, A. M. 2004, *ApJ*, 600, 986 43

Speck, A. K., Hofmeister, A. M., & Barlow, M. J. 1999, *ApJL*, 513, L87 43

Speck, A. K., Thompson, G. D., & Hofmeister, A. M. 2005, *ApJ*, 634, 426 64

Spina, L., Meléndez, J., Karakas, A. I., et al. 2018, *MNRAS*, 474, 2580 10

Spitoni, E., Romano, D., Matteucci, F., & Ciotti, L. 2015, *ApJ*, 802, id. 129 86, 92

Srinivasan, B., & Anders, E. 1978, *Science*, 201, 51 14, 65

Stancliffe, R. J. 2009, *MNRAS*, 394, 1051 49

Stancliffe, R. J., Dearborn, D. S. P., Lattanzio, J. C., Heap, S. A., & Campbell, S. W. 2011, *ApJ*, 742, 121 55

Stancliffe, R. J., Izzard, R. G., & Tout, C. A. 2005, *MNRAS*, 356, L1 25

Stancliffe, R. J., Izzard, R. G., Tout, C. A., & Pols, O. R. 2004, *Mem. Soc. Astron. It.*, 75, 670 50

Stephan, T., Trappitsch, R., Davis, A. M., et al. 2016, *Int. Jour. Mass Spectr.*, 407, 1 44, 65

Sterling, N. C., & Dinerstein, H. L. 2008, *ApJ Suppl. Ser.*, 174, 158 38

Straniero, O., Imbriani, G., Strieder, F., et al. 2013, *ApJ*, 763, 100 101

Suda, T., & Fujimoto, M. Y. 2010, *MNRAS*, 405, 177 54

Suess, H. E., & Urey, H. C. 1956, *Rev. Mod. Phys.*, 28, 53 2

Tagliente, G., Milazzo, P. M., Fujii, K., et al. 2008a, *Phys. Rev. C*, 78, 045804 70

Tagliente, G., Fujii, K., Milazzo, P. M., et al. 2008b, *Phys. Rev. C*, 77, 035802 70

Tagliente, G., Milazzo, P. M., Fujii, K., et al. 2010, *Phys. Rev. C*, 81, 055801 70

—. 2011a, *Phys. Rev. C*, 84, 055802 70

—. 2011b, *Phys. Rev. C*, 84, 015801 70

Takahashi, K., & Yokoi, K. 1987, *Atom. Data Nucl. Data Tables*, 36, 375 19, 32, 110, 111, 112

Takigawa, A., Miki, J., Tachibana, S., et al. 2008, *ApJ*, 688, 1382 109

Tatischeff, V., Duprat, J., & de Séréville, N. 2010, *ApJ*, 714, L26 108

Timmes, F. X., & Clayton, D. D. 1996, *ApJ*, 472, 723 85, 88, 89

Trappitsch, R., Stephan, T., Savina, M. R., et al. 2018, *Geochim. Cosmochim. Acta*, 221, 87 35, 75, 76

Travaglio, C., Gallino, R., Amari, S., et al. 1999, *ApJ*, 510, 325 44

Travaglio, C., Gallino, R., Rauscher, T., et al. 2014, *ApJ*, 795, 141 118, 119, 120, 121, 122

Travaglio, C., Gallino, R., Rauscher, T., Röpke, F. K., & Hillebrandt, W. 2015, *ApJ*, 799, 54 118, 119

Travaglio, C., Hillebrandt, W., Reinecke, M., & Thielemann, F.-K. 2004, *A&A*, 425, 1029 120

Travaglio, C., Rauscher, T., Heger, A., Pignatari, M., & West, C. 2018, *ApJ*, 854, 18 118, 123

Travaglio, C., Röpke, F. K., Gallino, R., & Hillebrandt, W. 2011, *ApJ*, 739, 93 118, 120, 122

Treffers, R., & Cohen, M. 1974, *ApJ*, 188, 545 43

Trigo-Rodríguez, J. M., García-Hernández, D. A., Lugaro, M., et al. 2009, *Meteorit. Planet. Sci.*, 44, 627 20, 108

Trippella, O., Busso, M., Palmerini, S., Maiorca, E., & Nucci, M. C. 2016, *ApJ*, 818, 125 76

Unterborn, C. T., Johnson, J. A., & Panero, W. R. 2015, *ApJ*, 806, 139 9, 124

van Aarle, E., Van Winckel, H., De Smedt, K., Kamath, D., & Wood, P. R. 2013, *A&A*, 554, A106 58

van Raai, M. A., Lugaro, M., Karakas, A. I., García-Hernández, D. A., & Yong, D. 2012, *A&A*, 540, A44 17, 34, 50, 53, 80

Van Winckel, H., & Reyniers, M. 2000, *A&A*, 354, 135 58

Vasileiadis, A., Nordlund, A., & Bizzarro, M. 2013, *ApJ*, 769, L8 107, 108, 117

Vassiliadis, E., & Wood, P. R. 1993, *ApJ*, 413, 641 24, 50

Ventura, P., Di Criscienzo, M., Carini, R., & D'Antona, F. 2013, *MNRAS*, 431, 3642 96, 99

Vescovi, D., Busso, M., Palmerini, S., et al. 2018, *ApJ*, 863, 115 20, 108, 109

Wallerstein, G., Iben, Jr., I., Parker, P., et al. 1997, *Rev. Mod. Phys.*, 69, 995 6

Wallner, A., Bichler, M., Buczak, K., et al. 2016, *Phys. Rev. C*, 93, 045803 17, 46

Wasserburg, G. J., Busso, M., & Gallino, R. 1996, *ApJ*, 466, L109 110

Wasserburg, G. J., Busso, M., Gallino, R., & Nollett, K. M. 2006, *Nucl. Phys. A*, 777, 5 20, 108, 109, 110, 115

Wasserburg, G. J., Busso, M., Gallino, R., & Raiteri, C. M. 1994, *ApJ*, 424, 412 110

Wasserburg, G. J., Karakas, A. I., & Lugaro, M. 2017, *ApJ*, 836, 126 20, 108

Waters, L. B. F. M., Molster, F. J., de Jong, T., et al. 1996, *A&A*, 315, L361 43

Watson, D., Hansen, C. J., Selsing, J., et al. 2019, *Nature*, 574, 497 11

Wehmeyer, B., Pignatari, M., & Thielemann, F.-K. 2015, *MNRAS*, 452, 1970 11

Wilde, S. A., Valley, J. W., Peck, W. H., & Graham, C. M. 2001, *Nature*, 409, 175 104

Williams, J. P., & Gaidos, E. 2007, *ApJ*, 663, L33 109

Wood, P. R., Bessell, M. S., & Fox, M. W. 1983, *ApJ*, 272, 99 96

Woosley, S. E., & Hoffman, R. D. 1992, *ApJ*, 395, 202 118

Woosley, S. E., & Howard, W. M. 1978, *ApJ Suppl. Ser.*, 36, 285 117

Xu, Y., Goriely, S., Jorissen, A., Chen, G. L., & Arnould, M. 2013, *A&A*, 549, A106 32

Yagüe López, A., Côté, B., & Lugaro, M. 2021, *ApJ*, 915, 128 124

Yan, S. Q., Li, Z. H., Wang, Y. B., et al. 2017, *ApJ*, 848, 98 19, 31

Young, E. D. 2014, *Earth Planet. Sci. Lett.*, 392, 16 108, 117

Zhukovska, S., Petrov, M., & Henning, T. 2015, *ApJ*, 810, 128 96

Zinner, E. 2014, in Meteorites and Cosmochemical Processes. Vol. 1 Treatise on Geochemistry, 2nd Ed. Elsevier, Oxford, ed. A. M. Davis, H. D. Exec. Eds. Holland, & T. K. K., 181–213 41, 64

Zinner, E., Amari, S., Guinness, R., et al. 2003, *Geochim. Cosmochim. Acta*, 67, 5083 44

Zinner, E., Amari, S., & Lewis, R. S. 1991, *ApJL*, 382, L47 79

Zinner, E., Nittler, L. R., Gallino, R., et al. 2006, *ApJ*, 650, 350 43, 88, 89, 90, 92